

Dissertation
submitted to the
Combined Faculties of the Natural Sciences and Mathematics
of the Ruperto-Carola-University of Heidelberg, Germany
for the degree of
Doctor of Natural Sciences

Put forward by
Anna Therese Phoebe Schauer
born in: Munich, Germany
Oral examination: 25 October 2017

DELAYING THE FORMATION OF THE FIRST STARS

THE IMPACT OF STREAMING VELOCITIES AND LYMAN-WERNER RADIATION

IN COSMOLOGICAL HYDRODYNAMICAL SIMULATIONS

Referees: Prof. Dr. Ralf Klessen
Prof. Dr. Volker Springel

ABSTRACT

In this thesis, we study which effects can delay the formation of the first stars in the Universe. These Population III stars were the first luminous objects emerging after recombination, starting to end the dark ages. They form in minihaloes or first galaxies, and the minimum mass of these objects is strongly related to the number of Population III stars that formed. In some regions of the Universe, there is an offset velocity between baryons and dark matter, the so-called streaming velocity. In this thesis, we show that in regions with large streaming velocities, the halo masses necessary to form the first stars increase. These regions are the perfect environment for the formation of direct collapse black holes. Feedback in the form of Lyman-Werner radiation emitted by the first stars can destroy molecular hydrogen and prevent the primordial gas cloud from cooling and collapsing. This also leads to an offset in time and halo mass for Population III star formation. To account for the strength of the Lyman-Werner background, we performed simulations that study the escape fraction from minihaloes and the first galaxies. With these results, we provide a piece of the jigsaw of the star formation history of the Universe.

ZUSAMMENFASSUNG

Diese Doktorarbeit handelt davon, welche Effekte die Entstehung der ersten Sterne im Universum verzögern. Diese Population III-Sterne waren die ersten Objekte nach der Rekombination des Universums, von denen Licht ausging und die somit anfangen, das Dunkle Zeitalter des Universums zu beenden. Sie entstanden in Minihalos oder ersten Galaxien, und die Mindestmasse dieser Halos korreliert mit der Anzahl an gebildeten Population III-Sternen. In einigen Regionen des Universums gibt es große relative Geschwindigkeiten zwischen den Baryonen und der dunklen Materie, die sogenannten Strömungsgeschwindigkeiten. In dieser Arbeit zeigen wir, dass die Mindest-Halomasse, oberhalb derer Population III-Sterne entstehen können, in Regionen mit großen Strömungsgeschwindigkeiten zunimmt. Außerdem bilden diese Bereiche die perfekte Umgebung für schwarze Löcher, die in einem direkten Kollaps der Gaswolke entstehen. Die allerersten Sterne strahlen auch in den Lyman-Werner Bändern und erzeugen dadurch einen negativen Rückkopplungsmechanismus für weitere Sternentstehung. Diese Strahlung zerstört molekularen Wasserstoff, ohne den Gaswolken nicht kühlen können, was zu einer Verzögerung der weiteren Sternentstehung und einem Übergang zu Sternentstehung in massiveren Halos führt. Um die Stärke des Lyman-Werner Strahlungshintergrundes besser bestimmen zu können, haben wir mit Simulationen den prozentualen Anteil der Strahlung, der die Haloumgebung verlassen kann, bestimmt. Damit können wir einen kleinen Teil zur Sternentstehungsgeschichte des Universums beitragen.

Contents

1	Introduction	1
1.1	Cosmology	2
1.2	From Recombination to Reionization - a short story about the Dark Ages of the Universe	4
1.3	Structure Formation	6
1.3.1	Initial fluctuations	6
1.3.2	The Jeans mass	8
1.4	Primordial chemistry	10
1.5	Population III stars	13
1.5.1	Lyman-Werner radiation	17
1.5.2	Streaming velocities	19
1.5.3	X-rays	21
1.6	Supermassive black holes	23
1.6.1	Black holes from stellar seeds	23
1.6.2	Direct collapse black holes	25
1.7	Observational prospects	27
1.7.1	Stellar archaeology	27
1.7.2	21 cm observations	28
1.7.3	Gravitational waves	30
2	Astrophysical codes	33
2.1	ZEUS-MP	34
2.2	AREPO	37
3	Lyman-Werner UV Escape Fractions from Primordial Haloes	39
3.1	Introduction	40
3.2	Method	43
3.2.1	ZEUS-MP	44
3.2.2	Halo Models	45

3.2.3	HII Region Simulation Setup	45
3.2.4	LW Escape Fractions	47
3.3	Results	54
3.3.1	Evolution of the HII Region	54
3.3.2	LW Escape Fractions in the Near-Field Limit	57
3.3.3	Far-Field Limit	59
3.4	Conclusion	61
4	Lyman-Werner Escape Fractions from the First Galaxies	65
4.1	Introduction	67
4.2	Method	69
4.2.1	ZEUS-MP	69
4.2.2	Semi-analytical post-processing	70
4.3	Parameter Space	72
4.3.1	Haloed	72
4.3.2	Spectral energy distribution	72
4.3.3	Star Formation Efficiencies	77
4.4	Results	78
4.4.1	Individual ionisation front behaviour	79
4.4.2	Time-averaged escape fractions in the near-field	86
4.4.3	LW flux-averaged escape fractions in the near-field	89
4.4.4	Time-averaged escape fractions in the far-field	91
4.4.5	Lower limits for ionising escape fractions	91
4.5	Discussion and Conclusion	92
5	DCBH formation under streaming velocities	97
5.1	Introduction	98
5.2	Simulations	101
5.2.1	Numerical method	101
5.2.2	Initial conditions	102
5.3	Results	103
5.3.1	Masses and collapse redshifts of haloed containing cold dense gas	103
5.3.2	Gas properties within the collapsed haloed	106
5.4	Conclusions	110
6	Streaming velocities at first star formation	113
6.1	Introduction	114
6.2	Method	116
6.2.1	Numerical method	116
6.2.2	Initial conditions	117

6.2.3	Halo selection	118
6.3	Results	119
6.3.1	No streaming velocities	119
6.3.2	Streaming velocities	124
6.4	Discussion and Conclusion	129
6.A	Updates to the chemical model	130
6.B	Numerical convergence of box sizes	131
6.C	Comparison of friends-of-friends results with subfind	132
6.D	Cold mass - halo mass relation	133
7	Conclusion and Outlook	135
	List of Publications	141
	References	167

Listing of Figures

1.2.1	History of the Universe. Image credit: ESA - Christophe Carreau	5
1.3.1	Cosmic microwave background. Image credit: ESA and the Planck Collaboration	6
1.3.2	Variance of the relative streaming velocity as a function of wave number. Image credit: Figure 1 of Tseliakhovich and Hirata (2010)	8
1.3.3	Large-scale density and velocity fluctuations at redshift $z = 20$. Image credit: Figure 5 of Fialkov et al. (2013)	9
1.4.1	Cooling rates as a function of temperature. Image credit: Figure 12 of Barkana and Loeb (2001)	11
1.5.1	Masses of the protostars over time. Image credit: left panel taken from Figure 10 of Greif et al. (2012) , right panel taken from Figure 13a from Stacy et al. (2016)	14
1.5.2	Halo mass as function of collapse redshift for haloes with and without streaming velocity. Image credit: Figure 3 of Greif et al. (2011b)	20
1.6.1	DCBH formation with synchronized halo pairs	25
1.7.1	Gravitational waves spectrum. Image credit: NASA Goddard Space Flight Center	30
3.2.1	Initial densities, temperatures, radial velocities and species mass fractions for the three halos	46
3.2.2	Evolution of the I-front of the $60 M_{\odot}$ star in halo 1.	51
3.3.1	Escape fractions as a function of time for a 9 and $80 M_{\odot}$ star in halo 1	57
3.3.2	Time-averaged escape fractions in the near-field	59
3.3.3	Time-averaged escape fractions in the far-field	60
4.3.1	Number density, temperature, H_2 abundance and velocity profiles at startup	73
4.3.2	SEDs for a SFE of 0.5% in Halo A	75
4.3.3	Ionising and Lyman-Werner photon production rates for all SEDs for a SFE of 0.5% in Halo A	76
4.4.1	Position of the I-front and LW escape fraction in the near-field as a function of time for a 1.0% SFE with a Salpeter IMF in Halo B	79

4.4.2	Abundances of the primordial species as a function of radius for four output times for a 1.0% SFE with a Salpeter IMF in Halo B	80
4.4.3	Position of the I-front and LW escape fraction in the near-field as a function of time for a 1.0% SFE with a flat IMF in Halo B	82
4.4.4	Abundances of the primordial species as a function of radius for six output times for a 1.0% SFE with a flat IMF in Halo B.	83
4.4.5	Position of the I-front and LW escape fraction in the near-field as a function of time for a 0.1% SFE with Salpeter IMF in Halo A	84
4.4.6	Abundances of the primordial species as a function of radius for six output times for a 0.1% SFE with a Salpeter IMF in Halo A.	85
4.4.7	Flux-averaged LW escape fractions in the near-field for our parameter space .	90
5.3.1	Masses of haloes containing cold dense gas, plotted at their redshift of collapse z_{coll}	104
5.3.2	Number density and temperature slices of the collapsed halo with $M_{\text{halo}} = 3 \times 10^7 M_{\odot}$ in the SB simulation at redshift $z = 14$	105
5.3.3	Properties of the collapsed halo with $M_{\text{halo}} = 3 \times 10^7 M_{\odot}$ in the SB simulation at redshift $z = 14$	107
5.3.4	Two dimensional histograms of all gas cells in $\log(n)$ – $\log(T)$ space at redshift $z = 14$	109
6.3.1	Cumulative halo mass function for all haloes and cold haloes for the simulation without streaming velocity.	120
6.3.2	Cold gas mass M_{cold} plotted as a function of halo mass M_{halo} for the simulation without streaming velocity at $z = 15$	120
6.3.3	Cold gas mass M_{cold} plotted as a function of halo mass M_{halo} for the simulation without streaming velocity at redshifts in the range $14 \leq z \leq 24$	121
6.3.4	Cold gas fraction $M_{\text{cold}}/M_{\text{halo}}$ plotted as a function of halo mass M_{halo} for the simulation without streaming velocity at $z = 15$	122
6.3.5	Cold gas fraction $M_{\text{cold}}/M_{\text{halo}}$ plotted as a function of halo mass M_{halo} for the simulation without streaming velocity for redshifts in the range $14 \leq z \leq 24$	122
6.3.6	Fraction of haloes that contain cold gas plotted as function of halo mass for different redshifts in the range $14 \leq z \leq 22$	123
6.3.7	Minimum halo mass $M_{\text{halo,min}}$ for a halo to contain cold gas and halo mass $M_{\text{halo,50\%}}$ above which more than 50% of all haloes harbour cold, dense gas plotted as a function of redshift. Data from the literature are included.	124
6.3.8	Baryon fraction a function of redshift for different streaming velocity values.	125
6.3.9	Cumulative halo mass function $N(> M_{\text{halo}})$ at redshift $z = 15$ for all simulation in the small box and streaming velocities of 0, 1, 2 and $3 \sigma_{\text{rms}}$	126
6.3.10	Cold gas fraction $M_{\text{cold}}/M_{\text{halo}}$ as a function of halo mass for the simulation with a streaming velocity of 1σ for redshifts in the range $14 \leq z \leq 20$	126

6.3.11	Cold gas fraction $M_{\text{cold}}/M_{\text{halo}}$ as a function of halo mass for the simulation with a streaming velocity of 2σ for redshifts in the range $14 \leq z \leq 18$	127
6.3.12	Cold gas fraction $M_{\text{cold}}/M_{\text{halo}}$ as a function of halo mass for the simulation with a streaming velocity of 3σ in the small box for redshifts in the range $14 \leq z \leq 16$	127
6.3.13	Halo mass of the first halo to contain cold gas and halo threshold mass above which more than 50% of all haloes contain cold gas as a function of redshift for all different streaming velocities.	128
6.B.1	Resolution test: different number of particles and Voronoi cells for a cosmological box with the side length of 500 ckpc/h.	132
6.C.1	Cold gas mass against halo mass for the simulation without LWBG or streaming at redshift $z = 15$: comparison of fof with subfind.	133

Listing of tables

3.2.1	Virial radii and total (dark matter + baryon) masses of the three halos . . .	49
3.2.2	Pop III stellar properties (Schaerer, 2002)	49
3.3.1	Near-field escape fractions, H ₂ self-shielding	60
3.3.2	Near-field escape fractions, H ₂ and H shielding	60
3.3.3	Far-field escape fractions, H ₂ self-shielding	61
3.3.4	Far-field escape fractions, H ₂ and H shielding	61
4.3.1	Summary of all spectral energy distributions used in this study	72
4.3.2	Star formation efficiencies and the corresponding stellar masses for both haloes	78
4.4.1	Time-averaged LW escape fractions in the near-field, averaged over the run- time of the simulation	87
4.4.2	Time-averaged LW escape fractions in the near-field, averaged over the first two Myr	87
4.4.3	LW flux averaged LW escape fractions in the near-field, averaged over the total LW flux of the simulation	89
4.4.4	Time-averaged LW escape fractions in the far-field	91
4.4.5	Time-averaged ionising escape fractions in the near-field	92
5.2.1	Dark matter particle mass and initial mesh cell gas mass in our two simulations	103
6.2.1	Overview of our simulations.	118
6.D.1	Cold gas mass - halo mass relation for all simulations at redshifts 15 and 20.	134

1

Introduction

When, how and where did the first stars in the Universe form? These questions involve many studies and are of fundamental interest. Without stars, the Universe would consist of only hydrogen and helium, as heavier elements are bred in stars and supernovae. We would like to understand how the first stars and black holes formed, to derive a consistent picture from the Big Bang until the present day.

We are now on the edge of a new era. Currently, observations of the high-redshift regime of $z \sim 15 - 40$ are not yet possible, but will come closer in the next decade with direct and indirect observation techniques. Now, we can run simulations and models and predict properties of these first stars and black holes that can be tested soon.

In contrast to simulations of present-day star-forming regions, these computer simulations of the first stars have the fundamental advantage that we can build them on a well-established theory, cosmology. In addition, we have a good understanding of the underlying chemistry of the gas which has primordial composition, consisting of hydrogen and helium and the isotopes and molecules these two elements can form. These two fundamental blocks are incorporated in present-day simulation codes. We can now run massively parallelized simulations that are able to predict the fundamental properties of the early Universe.

In this introduction, I will briefly review the cosmological model we are building our assumptions upon, followed by a more detailed summary of the evolution of the Universe in the “Dark Ages”, before the Universe was reionized. During that time, structure formed in a hierarchical way from smaller to larger objects, starting from tiny fluctuations emerging from the CMB. After discussing these linear and nonlinear modes of structure formation in Section 1.3, I will give a short overview of the chemical reactions taking place in the first objects, minihaloes and atomic cooling haloes, in Section 1.4.

In Section 1.5, I will then describe properties of minihaloes and atomic cooling haloes, which are the building blocks of structure at these redshifts. Following that, I will also tell the reader about the two types of objects that form in these haloes, the first stars and black holes. Three non-linear effects will influence the birth of these so-called Population III (Pop III) stars: streaming velocities, a Lyman-Werner background (LWBG) and X-rays. The first two delay the formation of the first stars, whereas the latter has been found to accelerate it. Thus the combination of these effects plays a role in understanding the star formation history of the Universe. I will review their contribution and influence and point to open questions that we hope to target with future studies.

Observations of massive quasars at high redshift put strong constraints on the formation mechanism of black holes. In Section 1.6, I will explain which challenges these observations cause and review the two possible formation channels via stellar seed black holes and so-called direct collapse black holes (DCBH). Finally, in Section 1.7, I will show how these objects will become detectable in the coming decade and how we might test our theories with these observations.

1.1 COSMOLOGY

The model that describes the nature of the Universe best is currently the Λ CDM theory. It is based on the cosmological principle that the Universe is homogeneous and isotropic on large scales.

The velocity $v(x, t)$ of a source at position x relative to the observer is related to its position via the Hubble law $v(t) = H(t) \cdot x(t)$. The Universe is expanding and objects that are further away move with a higher velocity. The Hubble parameter $H(t)$ changes with time.

The metric corresponding to an homogeneous and isotropic Universe is the

Friedmann–Lemaître–Robertson–Walker metric (Friedmann, 1922):

$$ds^2 = c^2 dt^2 - a(t)^2 (dr^2 + \bar{r}^2 d\Omega^2). \quad (1.1)$$

Here, c is the speed of light, t the time, $a(t)$ the time dependent scale factor of the Universe, r the radius, Ω the two dimensional angle and \bar{r} the covariant distance that incorporates the curvature of the Universe. The Hubble can be related to the scale factor as $H(t) \equiv \frac{\dot{a}}{a}$.

Light emitted by a source which is moving relative to the observer is shifted in frequency. As the Universe is expanding, the observed wavelength is redshifted, $z = \frac{\lambda_{\text{obs}} - \lambda_{\text{em}}}{\lambda_{\text{em}}}$, where z is the redshift, λ_{em} is the emitted wavelength and λ_{obs} the observed wavelength. The metric relates the time- to the space dependence. One can derive the relation between the wavelength and the scale factor $\frac{\lambda_{\text{obs}}}{\lambda_{\text{em}}} = \frac{a_{\text{obs}}}{a_{\text{em}}}$. As we observe the Universe at the present day, the scale factor $a_{\text{obs}} = a_0 = 1$ is often set to one by convention. With this, we can relate the redshift to the scale factor $a = \frac{1}{1+z}$. Since the redshift is a monotonically decreasing function of time, it is often used as a measure for time that has passed since the Big Bang.

From Einstein's field equations, the Friedmann equations can be derived. They describe the large-scale evolution of the Universe:

$$H(t)^2 = \frac{8\pi G}{3}\rho - \frac{k}{a^2} + \frac{\Lambda}{3} \quad (1.2)$$

$$\frac{\ddot{a}}{a} = -\frac{4\pi G}{3}\left(\rho + \frac{3p}{c^2}\right) + \frac{\Lambda}{3} \quad (1.3)$$

Here, G is the gravitational constant, ρ and p are the density and pressure fields, and Λ is the cosmological constant. The density ρ is the sum of its contribution from radiation and matter, $\rho = \rho_m + \rho_r$.

The different components, radiation, matter and the cosmological constant, have different equations of state $p = p(\rho)$ that relate their pressure to their density. For non-relativistic matter, $p_m = 0$, while for radiation or relativistic matter, $p_r = \frac{c^2}{3}\rho_r$. For the cosmological constant, $p_\Lambda = -c^2\rho_\Lambda$. The components therefore evolve differently with redshift: $\rho_m(z) = \rho_{m,0}(1+z)^3$, $\rho_r(z) = \rho_{r,0}(1+z)^4$, $\rho_\Lambda(z) = \rho_{\Lambda,0}$. The subscript 0 denotes present day, and the convention is $a_0 = 1$.

The critical density ρ_{crit} necessary for a flat Universe,

$$\rho_{\text{crit}} \equiv \frac{3H^2}{8\pi G}, \quad (1.4)$$

can be used to abbreviate the 1st Friedmann equation. We can introduce the dimensionless quantities $\Omega \equiv \frac{\rho}{\rho_{\text{crit}}}$, and rewrite the equations as follows:

$$\Omega_{\text{r}} \equiv \frac{\rho_{\text{r}}}{\rho_{\text{crit}}} \qquad \Omega_{\text{m}} \equiv \frac{\rho_{\text{m}}}{\rho_{\text{crit}}} \qquad \Omega_{\Lambda} \equiv \frac{\Lambda c^2}{3H_0^2} \qquad (1.5)$$

Modern measurements of the cosmic microwave background find that the curvature k is approximately zero and hence the Universe is flat ([Planck Collaboration et al., 2013](#)),

$$\Omega_{\text{K}} = 1 - \Omega_{\text{r},0} - \Omega_{\text{m},0} - \Omega_{\Lambda} \sim 0. \qquad (1.6)$$

$$H^2 = H_0^2 [\Omega_{\text{r},0} a^{-4} + \Omega_{\text{m},0} a^{-3} + \Omega_{\Lambda} + \Omega_{\text{K}} a^{-2}] \qquad (1.7)$$

We can divide the time evolution into three sections: radiation domination, matter domination and the domination of the cosmological constant Λ . At early times, radiation dominates. Matter-radiation equality takes place when $\Omega_{\text{r}}(z_{\text{rm}}) = \Omega_{\text{m}}(z_{\text{rm}})$. This transition happens at redshift $z_{\text{rm}} \approx 5900$, long before the cosmic microwave background (CMB) emerges. The contribution from the cosmological constant starts to dominate at $\Omega_{\text{m}}(z_{\text{m}\Lambda}) = \Omega_{\Lambda}(z_{\text{m}\Lambda})$, with the corresponding redshift of matter- Λ equality $z_{\text{m}\Lambda} \approx 0.4$.

1.2 FROM RECOMBINATION TO REIONIZATION - A SHORT STORY ABOUT THE DARK AGES OF THE UNIVERSE

Figure 1.2.1 illustrates the history of the Universe schematically. After the Big Bang, the Universe expanded exponentially, in the so-called inflation period. During that time, the first fluctuations form and get amplified. As the Universe expands and cools, particles start forming, producing the elements responsible for most of today's structure: hydrogen, deuterium, helium and free electrons as well as traces of lithium.

The Universe continues to cool as it expands further, allowing first ionized helium and later ionized hydrogen to recombine to their neutral states. The photons are strongly coupled to all baryonic matter until the moment of last scattering which emerges as the CMB at a redshift of $z \approx 1100$.

After recombination, the Universe is neutral and dark. No light source is available, the only structures are small fluctuations in density and the velocity field. This period is called the ‘‘Dark Ages’’.

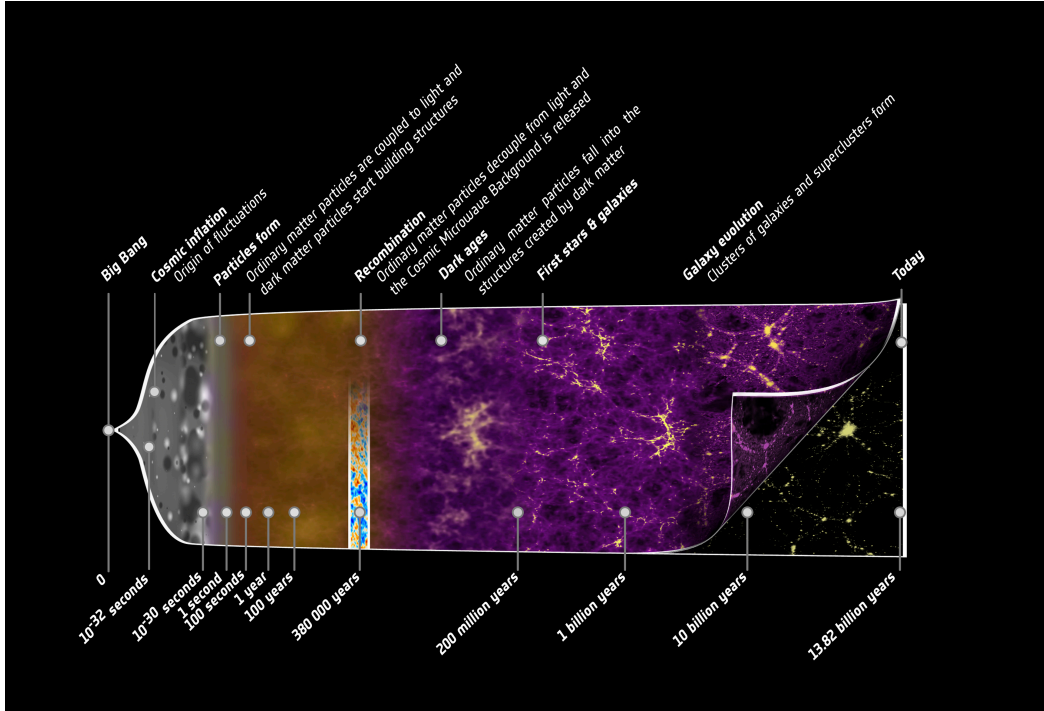


Figure 1.2.1: Sketch of the history of the Universe. Image credit: ESA - Christophe Carreau.

The tiny density fluctuations, however, grow. First, collapse proceeds along sheets, that then continue to form filaments and later haloes. The smallest objects form first, leading to hierarchical growth of all structures.

The first stars form in so-called minihaloes. Depending on their mass and rotation, they end their lives as black holes or as (superluminous) supernovae. These supernovae can spread metals to the host halo or even further, giving rise to the next generation of stars, Pop II stars. The minihaloes accrete mass and merge, leading to the formation of the first galaxies.

More and more radiation sources emerge, including quasars and binaries that emit X-rays, helping to reionize the Universe. The Universe we observe today is mostly ionized and a big open question is when this transition occurs and how smooth it is. The number of ionizing photons per baryon required depends on many factors like the ionizing escape fraction from minihaloes and first galaxies, the average binary fraction and the clumpiness of the interstellar medium and is the subject of many large-scale simulations. The redshift of this transition is still under debate. Lower limits are given by the Gunn-Peterson trough at $z \gtrsim 6$ (Becker et al., 2001), upper limits by the latest Planck results of $z \lesssim 10$ (Planck

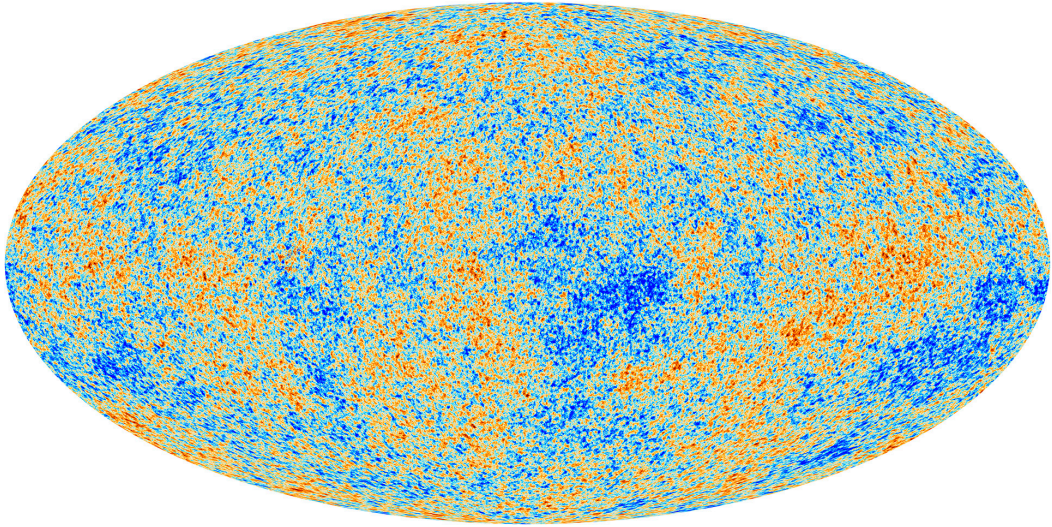


Figure 1.3.1: CMB measured by Planck. Image credit: ESA and the Planck Collaboration.

Collaboration et al., 2016a). This transition ends the Dark Ages.

1.3 STRUCTURE FORMATION

In this section, we will take a closer look at how the structures formed and evolved. We start with discussing the density and baryon-dark matter offset velocities emerging from the CMB, followed by a simple standard model for halo growth.

1.3.1 INITIAL FLUCTUATIONS

The cosmic microwave background (CMB) is a almost perfect black-body spectrum with effective temperature $T_{\text{eff}} = 2.73 \text{ K}$, and contains fluctuations at the order of 10^{-5} (Fixsen et al., 1996). These tiny fluctuations, however, are the sources for all structure that forms in the Universe.

Before recombination, photons were coupled to the baryons, while dark matter could stream freely and assemble in the first bound structures. Baryons would fall into the potential wells of the dark matter structures, but when the density became too large, pressure would take over and lead to repulsion of the baryons. At recombination, these fluctuations are frozen-in and become visible as temperature fluctuations in the CMB.

Quantitatively, all these fluctuations can be written as perturbations of the density and velocity in the continuity equation, the Euler equation and the Poisson

equation. The density fluctuations δ are defined with respect to the cosmic mean density $\bar{\rho}$ via $\delta = \frac{\rho - \bar{\rho}}{\bar{\rho}}$. The three equations can be written as

$$\frac{\partial \delta_i}{\partial t} + \frac{1}{a} \mathbf{v}_i \cdot \nabla \delta_i = -\frac{1}{a} (1 + \delta_i) \nabla \cdot \mathbf{v}_i \quad (1.8)$$

$$\frac{\partial \mathbf{v}_i}{\partial t} + \frac{1}{a} (\mathbf{v}_i \cdot \nabla) \mathbf{v}_i = -\frac{1}{a} \nabla \Phi - H \mathbf{v}_i - \delta_{ib} \frac{1}{a} c_s^2 \nabla \delta_b \quad (1.9)$$

$$\frac{1}{a^2} \nabla^2 \Phi = 4\pi G \bar{\rho}_m \delta_m \quad (1.10)$$

(Fialkov, 2014). Here, the subscript i can be b for the baryonic and c for the cold dark matter component. (Note: the 3rd term of the right hand side of the Euler equation only applies to baryons, and the Kronecker delta δ_{ib} is zero for $i = c$ and one for $i = b$.) The baryonic sound speed, c_s , depends on the temperature T and its evolution,

$$c_s = \frac{dp}{d\rho} = \frac{dp/da}{d\rho/da} = \frac{k_b T}{\mu} \left(1 - \frac{1}{3} \frac{\partial \log T}{\partial \log a} \right). \quad (1.11)$$

In 2010, Tseliakhovich and Hirata (2010) re-evaluated a 2nd order effect and found it to make significant contributions: the offset between baryon- and dark matter velocity, $\mathbf{v}_{bc} = \mathbf{v}_b - \mathbf{v}_c$, the so-called streaming velocities. Before recombination, photons were coupled to the baryons, while dark matter particles could stream freely and start to accumulate in larger overdensities. The baryons were gravitationally attracted to the centers of the dark matter potential, and therefore streaming in, but subsequently the pressure grew and they were pushed outwards. This resulted in a relative velocity of the baryons with respect to the dark matter.

Figure 1.3.2 from Tseliakhovich and Hirata (2010) shows the variance of the streaming velocities per mode k that is an inverse measure for angular distances on the sky. The streaming velocities are coherent on larger scales than the density fluctuations, with a coherence length of ~ 3 cMpc, where c stands for comoving (Fialkov, 2014).

The relative motions are distributed in the form of the Maxwell-Boltzmann distribution function:

$$P_{\text{MB}}(v) = \left(\frac{3}{2\pi\sigma_{\text{rms}}^2} \right) 4\pi v^2 \exp\left(-\frac{3v^2}{2\sigma_{\text{rms}}^2}\right). \quad (1.12)$$

The root mean squared value σ_{rms} of the distribution has the initial value of $\sigma_{\text{rms}} \approx 30 \text{ km s}^{-1}$ at recombination, which is highly supersonic at that time (Tseliakhovich and Hirata, 2010). The velocity decays as $(1+z)$ as the Universe is expanding and

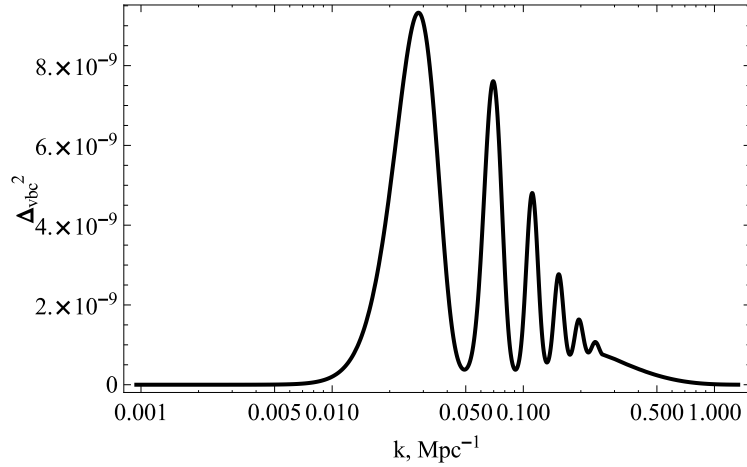


Figure 1.3.2: Variance of the relative streaming velocity per $\ln k$, Δ_{vbc}^2 , as a function of k . Image credit: Figure 1 of [Tseliakhovich and Hirata \(2010\)](#).

reaches values of $\sigma_{\text{rms}} \approx 6 \text{ km s}^{-1}$ at redshift $z = 200$ and $\sigma_{\text{rms}} \approx 3 \text{ km s}^{-1}$ at redshift $z = 100$.

In Figure 1.3.3 taken from [Fialkov et al. \(2013\)](#), we see results from a large-scale numerical simulation with a box size of $(384 \text{ cMpc})^3$ and a resolution of 3 cMpc that was evolved down to redshift $z = 20$. Colours show the velocity deviation (on the left panel) in units of the standard deviation σ_{rms} or the density fluctuations with respect to the cosmic mean (on the right panel).

We can see that the majority of the volume actually does have a non-zero streaming velocity, since the Figure has only small regions that are coloured dark blue, corresponding to a streaming velocity of zero. Simulations that target a representative volume of the Universe should therefore better be run with a small streaming velocity. When comparing the left and the right panel, we notice that the structure of the density is much finer and the structure of the velocity coarser. We can thus see that the streaming velocities are indeed coherent over larger scales.

1.3.2 THE JEANS MASS

The Jeans mass gives a simple estimate for the mass needed for an object to collapse due to its own gravitational force. If the free-fall time, $t_{\text{ff}} \sim (G\rho)^{-1}$, is larger than the sound crossing time $t_{\text{sound}} \sim R/c_s$, gravity dominates over pressure and the halo can undergo gravitational collapse. Here, ρ is the density, c_s is the sound speed and R is the diameter of the object.

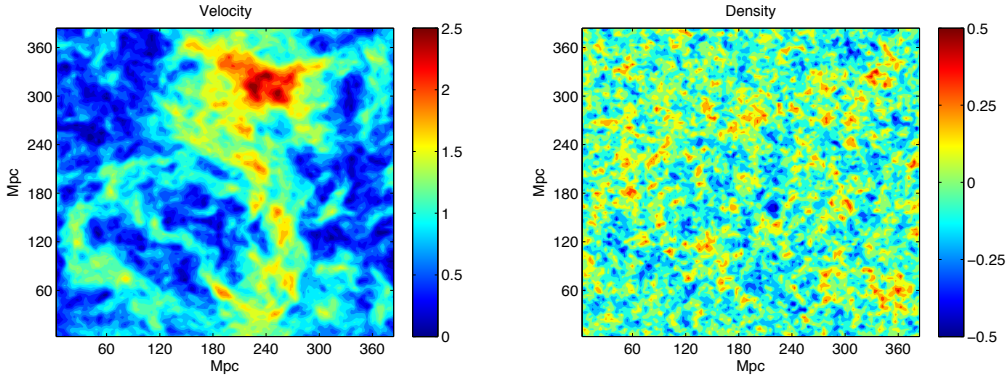


Figure 1.3.3: Large-scale density and velocity fluctuations in units of σ_{rms} at redshift $z = 20$, smoothed over 3 Mpc. Image credit: Figure 5 of [Fialkov et al. \(2013\)](#).

This condition can be expressed in terms of the Jeans length

$$\lambda_J = c_s \sqrt{\frac{\pi}{G\rho_0}}. \quad (1.13)$$

In objects that are larger than λ_J , gravity dominates over the pressure and pressure cannot halt the collapse.

The corresponding Jeans mass can be derived to be, assuming a sphere with radius $\lambda_J/2$ ([Barkana and Loeb, 2001](#)):

$$M_J = \frac{4\pi}{3} \rho_0 \left(\frac{\lambda_J}{2} \right)^3. \quad (1.14)$$

Objects exceeding the Jeans mass will undergo gravitational collapse. As in Equation 1.13, the Jeans mass only represents the forces the gas experiences due to pressure and gravity and neglects effects like rotation, magnetic fields or streaming velocities.

The Jeans mass depends on the sound speed of the gas. Assuming an ideal gas, $T \propto c_{\text{sound}}^2$. Before redshift $z \gtrsim 100$, the baryonic temperature was coupled to the radiation through Compton scattering, leading to $T_b \propto T_\gamma \propto (1+z)$.

Later, as the density drops, the coupling becomes inefficient and the temperature of the baryons evolves adiabatically, $T_b \propto \rho^{\gamma-1}$, where $\gamma = 5/3$ is the adiabatic index for monoatomic gas. As the density of the Universe scales with $\rho \propto (1+z)^3$, this leads to a temperature dependence of $T_b \propto (1+z)^2$. Using linear perturbation theory in Equation 1.9, the Jeans mass can be derived directly.

In the high-redshift regime, the Jeans mass

$$M_J = 1.35 \times 10^5 \left(\frac{\Omega_m h^2}{0.15} \right)^{-1/2} M_\odot \quad (1.15)$$

is independent of redshift. When the gas expands adiabatically,

$$M_J = 5.73 \times 10^5 \left(\frac{\Omega_m h^2}{0.15} \right)^{-1/2} \left(\frac{\Omega_b h^2}{0.022} \right)^{-3/5} \left(\frac{1+z}{10} \right)^{3/2} M_\odot \quad (1.16)$$

there is a strong redshift dependence (Barkana and Loeb, 2001).

This analytic, one dimensional estimate gives an first approximation of the formation of structures in the early Universe. For more detailed calculations, we need to take many non-linear effects into account, such as hydrodynamics and a reaction network for primordial chemistry. For these calculations, we have to rely on simulations that treat these accurately. In the next section, I will sum up the most important chemical processes that concern heating, cooling and ultimately star formation in a metal-free Universe.

1.4 PRIMORDIAL CHEMISTRY

The gas composition of the early Universe is primordial, with the majority of mass in hydrogen (75%) and helium (25%). The only other elements with fractional abundances of more than 10^{-12} (Alizadeh and Hirata, 2011), are deuterium (D) with $D/H = 2.5 \times 10^{-5}$ and lithium (Li) with $Li/H = 5 \times 10^{-10}$ (Cyburt et al., 2008). After recombination, a small amount of H and D is ionized, with $H^+/H = 2.5 \times 10^{-3}$ (Wong et al., 2008) and $D^+/D \simeq H^+/H$.

Heavier elements such as carbon or oxygen that play an important role in present day star formation theory do not exist yet as they first have to be bred in stars and supernovae. Therefore, many of the cooling and molecule formation processes that are important nowadays are not present in the primordial Universe.

In the previous section, we have discussed an analytical formalism that describes the early collapse stage of the first objects that form in the primordial Universe, minihaloes and first galaxies. To understand their inner structure and their properties, we need to study the cooling processes that enable higher densities and complex structures.

In Figure 1.4.1, we see the cooling curve for a number density of $n = 0.045 \text{ cm}^{-3}$, which is typical for the early-collapse state of a minihalo. At temperatures above

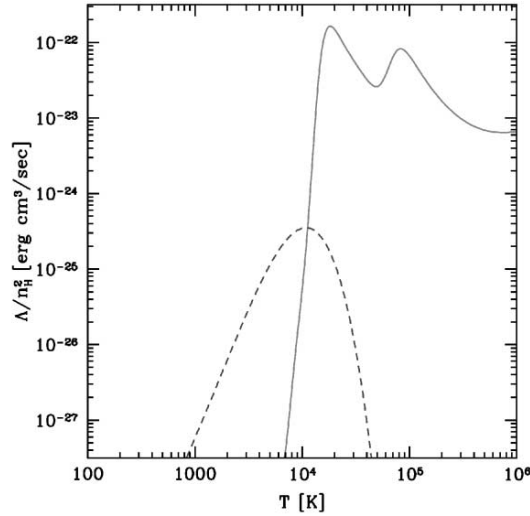


Figure 1.4.1: Cooling rates as a function of temperature for hydrogen and helium (solid line) and molecular hydrogen (dashed line). Image credit: Figure 12 of [Barkana and Loeb \(2001\)](#).

$T > 8000$ K, cooling can proceed efficiently via atomic hydrogen and helium. At lower temperatures, the lowest accessible hydrogen line from the ground state, Lyman- α , cannot be excited, leading to a sharp drop in the cooling function due to neutral hydrogen. In this temperature regime, cooling from molecular hydrogen (H_2) dominates. Since H_2 lacks a dipole moment, transitions from the first to the zeroth rotational level ($J = 1 \rightarrow 0$) are strongly forbidden. The lowest accessible transition is from the second to the zeroth rotational state ($J = 2 \rightarrow 0$), which corresponds to a transition energy of $E_{20}/k \approx 512$ K. Due to the tail of the Maxwellian velocity distribution, this enables cooling down to temperatures of about 150-200 K.

Since molecular hydrogen plays a crucial role in cooling haloes to low temperatures, it is important to understand its formation and destruction processes. These reactions depend on density and temperature. In the following, I will sum up the important processes following the collapse of a halo, from low to high densities.

H_2 lacks a dipole moment, thus its direct formation is strictly forbidden and occurs at negligible rate ([Gould and Salpeter, 1963](#)). At low densities, it forms through two different formation channels. The H^- channel usually dominates:



However, some H_2 can also form via the H^+ channel:



where the $h\nu$ stands for photons that are released in the course of this reaction.

In both cases, the rate equation is determined by the first part of the reaction, the radiative association to form H^- or H_2^+ , while the formation of H_2 then follows rapidly. The free electron e^- or proton H^+ acts as a catalyst.

Mutual neutralization, that would destroy the constituent of the molecular hydrogen formation channel,



is only important in regions with a high ionization fraction of a few percent (Glover, 2005), $x = n_{\text{H}^+}/n_{\text{H}} \geq 0.03$. This can be reached in regions, in which all hydrogen has been ionized by radiation that is e.g. coming from a star. In the intergalactic medium, however, the mean ionization fraction is more than two orders of magnitude lower, $x \sim 2 \times 10^{-4}$ (Schleicher et al., 2008) and mutual neutralization is not important. We can conclude that in regions of first star formation, mutual neutralization plays a minor role compared to H_2 formation.

For cooling below 200 K, hydrogen deuteride (HD) becomes efficient. Other molecules that could in principle contribute to the cooling of minihaloes have been found to be unimportant such as LiH (Mizusawa et al., 2005) or H_2^+ and H_3^+ (Glover and Savin, 2009). HD formation proceeds exothermically by converting H_2 into HD:



HD cooling becomes important when the gas is already quite cold, with temperatures around $T \sim 150$ K (Glover and Abel, 2008). At these temperatures, HD produced by reaction 1.22 cannot easily be converted back to H_2 by the inverse reaction owing to its endothermicity. Consequently, the HD/ H_2 ratio can become much larger than the ratio of elemental D to elemental H. Unlike H_2 , HD has a weak dipole moment, and thus the transition between the first excited state and the ground state is possible. Due to the larger mass of HD compared to H_2 , the rotational energy levels of HD are lower, resulting in a transition energy of $E_{10}^{\text{HD}}/k = 128$ K. In practice, HD cooling has been found to be important only in minihaloes that are strongly shocked or cooling from an initially ionized state, or ones in which the gravitational

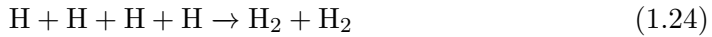
collapse of the gas is unusually slow (Bromm et al., 2002; Johnson and Bromm, 2006).

At densities of $n_{\text{crit}} \sim 10^4 \text{ cm}^{-3}$, the formation of H_2 becomes ineffective. On the one hand, above this critical density, the rotational and vibrational levels of H_2 reach their local thermal equilibrium values. This results in a linear dependence of the cooling rate on the density and therefore a density-independent H_2 cooling time. On the other hand, the free-fall time still decreases with increasing density. Overall, cooling by H_2 becomes less important when the critical density of $n \sim 10^4 \text{ cm}^{-3}$ is exceeded.

At even higher densities, of around $n > 10^8 \text{ cm}^{-3}$, three-body interactions become important and H_2 can form via



and



(Palla et al., 1983). When these densities are reached, the gas has passed the point of no return. These reactions can turn all neutral hydrogen into molecular hydrogen and enable star formation. We do not look into the details of the further evolution of the gas in this thesis and therefore end our summary at this point. For more details, I would like to refer the reader to reviews by Bromm (2013) and Glover (2013) that describe the evolution of the central gas to even higher densities.

1.5 POPULATION III STARS

The dark ages end with the birth of Pop III stars, the first compact objects in the Universe. They form inside minihaloes whose centres collapsed to high densities as described in the previous section.

For the sites of first star formation, one distinguishes between minihaloes and atomic cooling haloes, both of which are sometimes also referred to as protogalaxies. Atomic cooling haloes are massive enough that their virial temperature, T_{vir} , lies above the atomic cooling threshold of $T \sim 8000 \text{ K}$. Minihaloes are less massive, and they can only be cooled by molecular hydrogen.

The relation between the mass of a halo and its temperature can be derived from the virial theorem $W = -2K$, where W is the potential energy and K is the thermal energy of the halo. The overdensity of a virialized halo compared to the

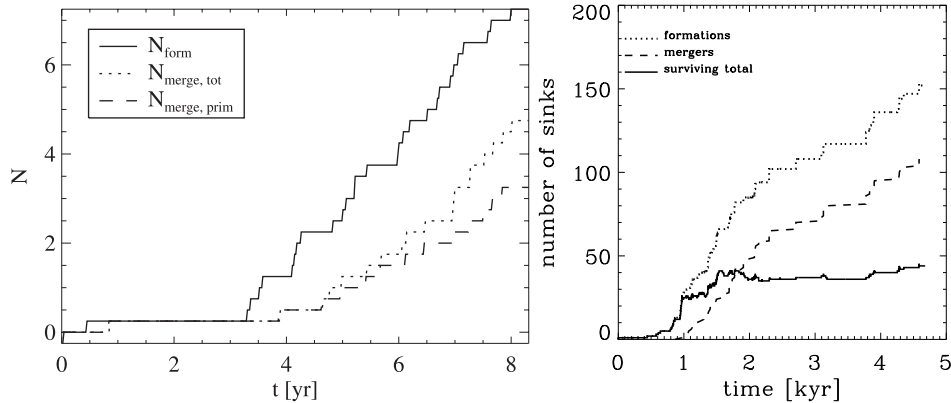


Figure 1.5.1: Protostar masses as a function of time. Image credit: left panel taken from Figure 10 of Greif et al. (2012), right panel taken from Figure 13a from Stacy et al. (2016).

critical density in an Einstein-de Sitter Universe can be derived to be $\Delta_c \sim 200$. With this, the virial radius R_{vir} and subsequently the virial temperature can be derived as a function of the halo mass (assuming Einstein-de Sitter),

$$R_{\text{vir}} = 0.784 \left(\frac{M}{10^8 M_{\odot}/h} \right)^{1/3} \left(\frac{1+z}{10} \right)^{-1} h^{-1} \text{kpc} \quad (1.25)$$

$$T_{\text{vir}} = \frac{\mu m_p v_c^2}{2k} = 1.98 \times 10^4 \left(\frac{\mu}{0.6} \right) \left(\frac{M}{10^8 M_{\odot}/h} \right)^{2/3} \left(\frac{1+z}{10} \right) \text{K}, \quad (1.26)$$

where μ is the mean molecular weight ($\mu \approx 0.6$ for ionized gas and $\mu \approx 1.2$ for neutral atomic gas, Barkana and Loeb, 2001).

The first star ever to be born is estimated to form in the rarest high-density peak in the early Universe at a redshift of about $z \sim 65$ (Fialkov et al., 2012). The majority of Pop III star formation happens later, at redshifts $z \leq 30$ (see e.g. Machacek et al. 2001; Yoshida et al. 2003; Hirano et al. 2015, Schauer et al. in prep.).

The mass of these first stars is highly uncertain. Early simulations show that a significant fraction of the mass in a central clump of $\sim 10^4 M_{\odot}$ can collapse to form a massive $\geq 100 M_{\odot}$ Pop III star (Abel et al., 2002; Bromm et al., 2002). These simulations, however, were not using a very high resolution and could not resolve fragmentation of the central accretion disk.

More recent work focuses on the high-resolution inner part of the minihalo that will collapse into one or several stars, resolving spatial scales of 5% of the solar radius and densities up to $n \approx 10^{19} \text{ cm}^{-3}$. Such ground-breaking simulations have been

performed by Greif et al. (2012). Instead of relying on sink particles, they resolve the forming protostars. Unfortunately, these calculations are computationally very expensive and the study could only span a range of 10 yr. Nevertheless, the results are very interesting: over the course of the simulated 10 yr, Greif et al. (2012) find a number of protostars forming in a Keplerian disk. About half of these objects experience strong gravitational torques that redistribute their angular momentum and enables them to migrate to the centre, to eventually merge with the central protostar. Even though other protostars also merge, the number of survivors (about 1/3 of the total amount) increases monotonically with time as can be seen in the left hand panel of Figure 1.5.1. After 10 yr, the mass of the most massive protostar in each halo approaches $\approx 1 M_{\odot}$. On average, 7 protostars have formed by this point, although most of these have already merged with the central object. For predicting the final masses of Pop III stars, simulations of these kind would need to run for several orders of magnitude longer time intervals.

To run simulations of Pop III star formation for longer times, techniques for limiting the computational cost are required. One popular technique involves the use of sink particles. When a certain density threshold is crossed, a normal particle is converted into a sink particle. It accretes nearby particles as long as they are gravitationally bound to the sink and do not have a large angular momentum with respect to the sink particle. The mass, angular and linear momentum from the swallowed particles are added to the sink particle. Sometimes, subgrid physics is included into the sink particle and it serves as e.g. a radiation source that provides feedback to the surrounding gas. This method reduces the computational costs, as it avoids the need to resolve particles beyond the density of the sink particle creation and therefore puts a limit to the resolution. The disadvantage is that sink particles cannot resolve hydrodynamics close to the accretion radius and therefore might artificially increase / decrease fragmentation. In addition, sink particles might gain a lot of kinetic energy and could subsequently be expelled from their host halo due to sink-sink interactions, when in reality gravitational torques might dissipate that energy.

A recent example of the use of sink particles in simulations of Pop III star formation can be found in Stacy et al. (2016). They perform zoom-in simulations similar to the ones of Greif et al. (2012), but introduce sink particles when the number density exceeds $n = 10^{16} \text{ cm}^{-3}$. Their goal is to start to constrain the initial mass function for Pop III stars. They run their simulations for 5000 yr. The total, merging and surviving number of fragments can be seen in the right panel of

Figure 1.5.1. Within the first 2000 yr, they find the same survival rate of $\approx 1/3$ as in Greif et al. (2012). After that time, the number of sinks stays relatively constant at ~ 40 , with ~ 30 having a sub-solar mass and the most massive sink having a mass of $20 M_{\odot}$. About one third of the sinks have a velocity exceeding the escape velocity of the minihalo, allowing them to escape from the centre of the host gas reservoir. When such a protostar is ejected, it might move to regions of very low density in which it cannot substantially accrete mass and therefore remains with a subsolar mass.

In contrast to Greif et al. (2012) and Stacy et al. (2016), in numerical simulations from Hosokawa et al. (2016), one star forms per minihalo with masses in the range of 10 to $1000 M_{\odot}$. Hosokawa et al. (2016) perform their simulations on a spherical grid centred around the high density peak of the halo and run them for 10^5 yr. The central cell is a sink cell, and is used as a radiation source of ionizing and photodissociating feedback. In their work, Hosokawa et al. (2016) also find fragmentation, but all fragments merge with the central protostar. As the number of fragments depends on the resolution, is it not clear if the radiation feedback is responsible for forming only one object in the halo or the method or the resolution. Conclusive results can only be drawn if the subject is revisited with a converged resolution.

Hirano et al. (2014) study the formation of Pop III stars in a sample of 100 minihaloes, the largest sample considered to date. They find only one star per minihalo with masses ranging from 10 to $2000 M_{\odot}$ after a simulation runtime of $\sim 10^5$ yr. However, as their simulations are performed in 2D, fragmentation is suppressed and these masses may instead only represent the mass of the most massive star forming in each halo (Stacy et al., 2016).

We can conclude that the initial mass function of the first stars or even the typical mass of a Pop III star is very difficult to predict and highly dependent on the method employed. Simulating the inner regions of star-forming objects with extremely high resolution is one pathway to better understand the early Universe.

Interesting results can also be found by focusing on the larger scales and studying the build up of the host haloes of Pop III stars, minihaloes and atomic cooling haloes. These larger structures are the building blocks of the Universe we observe today.

The minimum halo mass for Pop III star formation to take place can be estimated from simulations or by semi-analytic modelling. Glover (2013) derives a critical temperature of $T_{\text{crit}} \sim 1000$ K, above which the gas will cool with less than the Hubble time. With the virial theorem, this translates into a critical mass M_{crit}

given by the equation:

$$M_{\text{crit}} \simeq 6 \times 10^5 / h \left(\frac{\mu}{1.2} \right)^{-3/2} \Omega_m^{-1/2} \left(\frac{1+z}{10} \right)^{-3/2} M_{\odot}. \quad (1.27)$$

The same methodology of comparing the Hubble time with the H_2 cooling time is used by [Trenti and Stiavelli \(2009\)](#). They find a lower minimum mass with a stronger redshift dependence, $M_{\text{tH-cool}}$,

$$M_{\text{tH-cool}} \simeq 1.54 \times 10^5 \left(\frac{1+z}{31} \right)^{-2.074} M_{\odot}. \quad (1.28)$$

[Yoshida et al. \(2003\)](#) determine the minimum halo mass for forming cold gas clumps to be $\sim 5 \times 10^5 / h M_{\odot}$ from a set of cosmological simulations. This minimum halo mass depends only weakly on redshift. There seems to be light tension between the semi-analytic estimates and the simulations. It is thus necessary to revisit the simulations with present day astrophysical codes that allow the minihalo to be studied with higher resolution and a complex chemical treatment than was possible one decade ago. This is addressed in Chapter 6.

1.5.1 LYMAN-WERNER RADIATION

The key molecule for Pop III star formation is H_2 . Without its presence, cooling below $T \leq 8000 \text{ K}$ would not be possible.

Since H_2 does not have a dipole moment, it is difficult to destroy. Processes like direct excitation of the vibrational ground state and photoionization or excitation to the vibrational continuum of an excited state are strongly forbidden or proceed at energies exceeding 13.6 eV and can thus only take place in HII regions ([Glover and Brand, 2001](#)).

The main pathway to the destruction of molecular hydrogen is the two-step photodissociation process (the Solomon process) ([Stecher and Williams, 1967a](#)):



In the first step, photons in the Lyman or Werner lines excite molecular hydrogen to the 2nd or 3rd electronic state. From there, about 15% of the molecules decay to the vibrational continuum and are dissociated ([Field et al., 1966](#); [Stecher and Williams, 1967b](#)). There are 76 Lyman-Werner (LW) bands between 11.2 and 13.6 eV. Radiation in this range is referred to as LW radiation.

When molecular hydrogen is destroyed, the gas can only cool via atomic hydrogen emission and therefore stays at high temperatures. This can influence the process of first star formation, or, as will be described in the next section, support the formation of supermassive black holes.

With energies below the ionisation limit of atomic hydrogen, LW radiation can travel large distances in the primordial Universe and a global LWBG can build up. However, if the column densities are large, molecular and neutral hydrogen can shield LW radiation. Pop III formation therefore becomes an multi-scale, multi-physics problem.

In a first step, one needs to know how many LW photons from stellar sources are available to form the LWBG. In Chapter 3, I present the results from a series of one dimensional simulations with the code ZEUS-MP to determine the LW escape fraction of Pop III stars from minihaloes. I find that this escape fraction can be very low for stars in the lower mass regime, $9 - 40 M_{\odot}$ or in our most massive halo with $2 \times 10^7 M_{\odot}$. I furthermore find that in this massive object, shielding by neutral hydrogen plays a role and cannot be neglected.

These LW escape fractions are important to determine the build-up of the LWBG in unresolved large-scale simulations or in semi-analytic modelling. For example, the results from this Chapter have been used in a merger-tree code used to determine Pop III supernovae rates (Magg et al., 2016).

In a follow-up study, presented in Chapter 4, I have investigated the LW escape fractions of time-dependent stellar populations. Here, the escape fractions are generally close to 100% except for extreme initial mass functions and a very low star formation efficiency. If future simulations show that the Pop III star formation efficiency is very low, it will be necessary to revisit the calculations for the global LWBG and incorporate the escape fractions derived in this chapter.

Haiman et al. (2000) perform semi-analytical modelling to determine the global shape of the LWBG without considering the LW escape fractions from the sources. The effect of absorption of LW radiation in the intergalactic medium by H_2 is small (see also Glover and Brand, 2001). When LW radiation redshifts into the Lyman-lines of neutral hydrogen, it is absorbed. The Lyman-lines of Lyman β and higher lie in the LW range. Neutral hydrogen is the predominant constituent of the early Universe, and when radiation redshifts in one of these lines, it is completely absorbed. As a result, the global shape of the LWBG looks like a sawtooth. Haiman et al. (2000) furthermore find that the effect of the LWBG on minihaloes is large and can suppress H_2 cooling completely.

Machacek et al. (2001) perform a set of cosmological simulations, studying protogalaxies in the mass range of $10^5 - 10^7 M_{\odot}$. Their simulations contain a primordial chemistry network, but neglect H_2 self-shielding. The minimum halo masses is shifted to higher values in the presence of a LWBG:

$$M_{\text{crit}} = 1.25 \times 10^5 + 8.7 \times 10^5 \left(\frac{F_{\text{LW}}}{10^{-21}} \right)^{0.47}, \quad (1.30)$$

where F_{LW} is given in $\text{erg s}^{-1} \text{cm}^{-2} \text{Hz}^{-1}$. (Note that $F_{\text{LW}} = J_{\text{LW}} \times 4\pi$ is the LW flux and not the LW intensity that we use elsewhere in this thesis.)

Wise and Abel (2007) and O’Shea and Norman (2008) follow up on this study, and consider LWBGs with a larger range of strengths. Both studies agree that even with the highest considered LWBG, H_2 cooling can lead to star formation in minihaloes below the atomic cooling limit, but that a LWBG shifts the minimum halo mass to larger values. However, both studies again neglect self-shielding and it is debatable whether the absolute numbers they derive will remain unchanged when self-shielding is properly accounted for.

Safranek-Shrader et al. (2012b) studied the effects of a very strong LWBG with a strength $J = 100 J_{21}$. Unlike previous studies, they include self-shielding and are furthermore able to follow the collapsing halo to very high densities, inserting sink particles above $n > 10^8 \text{cm}^{-3}$. However, their LWBG is unusually strong, delaying the collapse of the first object in a 1cMpc^3 box to redshift $z \sim 12$ with a mass of $M_{\text{halo}} = 3 \times 10^7 M_{\odot}$. This study therefore can be regarded as prototype for the very late evolution of a fraction of the Universe and not for the standard minihalo.

In the future, we plan to run cosmological simulations with different LWBGs, targeting a large sample of minihaloes. With high resolution and incorporated H_2 self-shielding, we want to find the offset in halo mass and redshift for an average minihalo. The details of this project are elaborated on in Chapter 7.

1.5.2 STREAMING VELOCITIES

In parts of the Universe that are exposed to a high streaming velocity, an additional pressure term is added to the baryons. The effect on the resulting structure formation is largest on scales similar to the mode associated with the Jeans length, $k \sim 200 \text{cMpc}^{-1}$, lowering the power spectrum by 15% (Tseliakhovich and Hirata, 2010; Fialkov, 2014) in that regime. Semi-analytic modelling and first simulations show that the baryon fraction in haloes in these regions are therefore lower and the

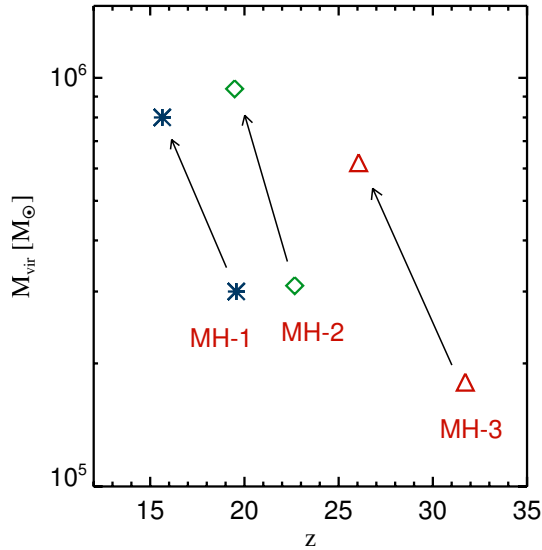


Figure 1.5.2: Halo mass as a function of redshift at collapse. The lower symbols show the three haloes in initial conditions without streaming velocity, the upper symbols with $1\sigma_{\text{rms}}$ streaming velocity. Image credit: Figure 3 of Greif et al. (2011b).

halo mass function decreases (Tselikhovich and Hirata, 2010; Tselikhovich et al., 2011).

The formation time of the first star is also delayed because of the systematically lower halo mass function for streaming velocity regions. In a universe without streaming velocities, the first star would probably form at redshift $z \sim 70$ instead of at redshift $z \sim 65$ (Fialkov et al., 2012).

Greif et al. (2011b) studied the first collapsing halo in three different cosmological boxes each with and without a streaming velocity of $1\sigma_{\text{rms}}$. Figure 1.5.2 sums up their two main results: on the one hand, the halo mass of the collapsed object increases by a factor of about 3, on the other hand the collapse is delayed by $\Delta z \sim 4$ (Greif et al., 2011b).

Stacy et al. (2011) also perform simulations targeting the difference of star formation in regions with and without streaming velocities. They do not find a substantial difference in formation redshift or halo mass for their $1\sigma_{\text{rms}}$ streaming simulation compared to a run without streaming. For their $> 3\sigma_{\text{rms}}$ streaming simulation, the collapse time is delayed by a few 10^8 yr and the halo mass increases by a factor of about ~ 10 .

Fialkov et al. (2012) perform semi-analytic modelling based on the simulations of Greif et al. (2011b) and Stacy et al. (2011). They define a fitting formula for

the required circular velocity above which the halo can undergo cooling and term it v_{cool} . It takes into account streaming velocities and adds them in a quadratic way to the circular velocity of the halo to enable a smooth transition,

$$v_{\text{cool}} = [(3.17 \text{ km s}^{-1})^2 + (4.015 v_{\text{bc}})^2]^{1/2}, \quad (1.31)$$

where the first term corresponds to fits for the circular velocity without streaming velocity and the second term takes into account the relative motion between baryons and dark matter, v_{bc} . This formula fits both simulations from Greif et al. (2011b) and Stacy et al. (2011) well, and Fialkov et al. (2012) suggest the apparent discrepancy might result from different numerical resolutions, different numerical algorithms or cosmic scatter.

Naoz et al. (2012, 2013) simulate cosmological volumes with high resolution and study many objects within. As predicted by Tselikhovich et al. (2011), they find lower baryon fractions in haloes in regions of higher streaming velocities, lowering the halo mass function. They also find that the gas fraction in haloes in non-zero streaming velocity regions is reduced, reaching values below half the cosmic mean for high streaming velocity regions. However, they lack a treatment of the primordial chemistry that is necessary to infer star formation properties.

We are still lacking an understanding of how the average minihalo is influenced by streaming velocities when taking the relevant chemical reactions into account. To close this gap, we ran cosmological simulations using the code AREPO with an accurate treatment of primordial chemistry. We include simulations with 0, 1, 2 and $3\sigma_{\text{rms}}$ streaming velocity. As expected, we find an increase in the halo mass required for the formation of cold, dense gas. However, we do not find a direct redshift dependence. This project is in preparation for publication and is described in Chapter 6.

1.5.3 X-RAYS

X-rays may counterbalance the photodissociating effect of LW radiation: they produce many free electrons. Molecular hydrogen forms indirectly via the H^- or H_2^+ channels and depends on the amount of free electrons (or protons, in the case of the H_2^+ channel), available as these act as catalysts for H_2 formation. X-rays can therefore increase the amount of molecular hydrogen formed within a minihalo (Haiman et al., 2000; Oh, 2001). In addition, their mean free path is large and they can travel great distances, reaching minihaloes far from the source and triggering H_2 formation

there.

X-rays in the early Universe can originate from quasars or star formation. High mass X-ray binaries consist of one massive star and a compact companion, a neutron star or a stellar mass black hole. X-rays are emitted during a short time interval after the formation of the compact object by accretion of material from the massive star onto the compact companion.

Present-day starburst galaxies have a clear relation between X-ray and infrared luminosity, hinting at a linear relation to the star formation rate in starbursts (Helfand and Moran, 2001; Glover and Brand, 2003). Another source for X-rays comes from supernovae and photons that experience inverse Compton scattering or originate from bremsstrahlung.

Glover and Brand (2003) show that X-rays from X-ray binaries are strong enough to partially offset the LWBG-induced effects in larger protogalaxies with $T_{\text{vir}} > 1000$ K. However, the initial mass function and the binary fraction of Pop III stars are still unknown, leading to large uncertainties in the model. The results for small protogalaxies are more conclusive: for $T_{\text{vir}} < 1000$ K, none of the considered X-ray backgrounds are able to counterbalance the LWBG. The X-ray background also leads to an increase of the temperature of the intergalactic medium by ~ 100 K, which might result in suppression of the smallest scales of structure formation.

Machacek et al. (2003) repeated their study published as Machacek et al. (2001) under the consideration of a soft X-ray background that could originate from quasars or very massive stars. They find that the halo mass necessary for efficient cooling decreases and the redshift increases, but that both effects are rather mild. In agreement with Glover and Brand (2003), they find X-rays of any strength inefficient to counterbalance the LWBG in small protogalaxies of $M_{\text{vir}} < 10^6 M_{\odot}$ (equivalent to $T_{\text{vir}} \sim 1000$ K from Glover and Brand (2003) at these redshifts).

In a more recent study, Ricotti (2016) investigates which of the stellar sources plays the major role in promoting H_2 formation and Pop III star formation. He finds that super- and hypernovae play the dominant role in providing X-rays. He furthermore studies the effect of heating the intergalactic medium and subsequent structure formation suppression. A too large X-ray background would increase the Jeans mass for structure formation, and a too low X-ray background is not enough to counterbalance photodissociation of H_2 . When the energy emitted by X-rays is 1% of the mean LWBG energy emitted by UV photons, the number of Pop III stars reaches its maximum of a number density of about 400 cMpc^{-3} . This number is comparable to the energy ratios of 20-40 M_{\odot} stars that explode as hypernovae.

Since current simulations are consistent with Pop III stars in this mass regime, this maximum Pop III star density could well be reached.

1.6 SUPERMASSIVE BLACK HOLES

The other type of object that forms during the first billion years of the Universe are black holes. Very luminous quasars have been observed at high redshift, e.g. a quasar with bolometric luminosity of $6 \times 10^{13} L_{\odot}$ at redshift $z = 7.1$ by [Mortlock et al. \(2011\)](#) or a quasar with bolometric luminosity of $4 \times 10^{14} L_{\odot}$ at redshift $z = 6.30$ by [Wu et al. \(2015\)](#). The corresponding black hole masses can be estimated from the width of the magnesium II line ([McLure and Dunlop, 2004](#); [Vestergaard and Osmer, 2009](#)) and are $M = 2 \times 10^9 M_{\odot}$ and $M = 1.2 \times 10^{10} M_{\odot}$, respectively. To put these numbers in perspective, we can compare them to local galaxies at the present day. The central black hole of our Milky Way is three orders of magnitude less massive, $M_{\text{BH,MW}} \approx 4.3 \times 10^6 M_{\odot}$ ([Gillessen et al., 2009](#)) and the black hole of the giant elliptical galaxy M87 at the centre of the Virgo cluster is just in a similar mass range as the high redshift quasars with $M_{\text{BH,M87}} \approx 6.6 \times 10^9 M_{\odot}$ ([Gebhardt et al., 2011](#)).

These luminous quasars are not only fascinating objects by themselves, but also very rare. The observed number density of high-redshift quasars at redshift $z = 6$ is about 1cGpc^{-3} ([Fan et al., 2006](#)). There needs to be a pathway to form these objects, but only very rarely. We therefore need to explain how these very massive objects have formed during the first billion years of the Universe and why they are so rare. Two possible pathways have been suggested that will be discussed in the subsequent sections.

1.6.1 BLACK HOLES FROM STELLAR SEEDS

One possibility is that these supermassive black holes observed at redshift $z \approx 6 - 7$ originate from remnants of Pop III stars. Models suggest that Pop III stars with masses in the range of $25 M_{\odot} < M < 140 M_{\odot}$ do not explode as supernovae, but undergo collapse to a black hole directly ([Heger and Woosley, 2002](#)), leaving behind a black hole of the order of $100 M_{\odot}$. If these stellar remnants accreted a lot of gas between their formation at redshift $z \sim 15 - 25$ and their detection at redshift $z \sim 6$, they could be the seeds for the observed supermassive black holes at high redshift.

One limit to their growth is given by the Eddington luminosity, where the outwards pointing force exerted by radiation balances the inwards pointing gravitational

force:

$$\frac{GM_{\text{BH}}m_p}{r^2} = \frac{L_{\text{E}}}{4\pi r^2 c} \sigma_{\text{T}}. \quad (1.32)$$

After inserting all constants such as the proton mass m_p , the speed of light c and the electron cross section of Thomson scattering of a photon σ_{T} , one obtains an relation between the Eddington luminosity L_{E} and the mass of the black hole M_{BH} :

$$L_{\text{E}} = \frac{4\pi GM_{\text{BH}}cm_p}{\sigma_{\text{T}}} = 1.3 \times 10^{44} \left(\frac{M_{\text{BH}}}{10^6 M_{\odot}} \right) \text{erg s}^{-1}. \quad (1.33)$$

The luminosity L is related to the mass accretion rate \dot{M} via:

$$L = \epsilon \dot{M} c^2, \quad (1.34)$$

where ϵ is the radiative efficiency of accreting gas onto the black hole. The standard value for the radiative efficiency is $\epsilon \approx 0.1$ for a non-rotating black hole. If we assume accretion at the Eddington limit, the maximum mass accretion rate can be directly related to the black hole mass, as the black hole accretion rate equals the mass that is not converted to radiation $\dot{M}_{\text{BH}} = (1 - \epsilon)\dot{M}$:

$$\dot{M}_{\text{BH}} = \frac{1 - \epsilon}{\epsilon} \frac{4\pi GM_{\text{BH}}m_p}{c\sigma_{\text{T}}}. \quad (1.35)$$

The mass of the black hole $M_{\text{BH}}(t)$ grows exponentially in time. When accreting at the Eddington rate, the black hole mass grows as

$$M_{\text{BH}}(t) = M_{\text{BH}}(0) \exp\left(\frac{1 - \epsilon}{\epsilon} \cdot \frac{t}{t_{\text{Edd}}}\right) \quad (1.36)$$

Here, $t_{\text{Edd}} = 0.45 \times 10^9 \text{ yr}$ is the e-folding time of the Eddington accretion (see e.g. [Volonteri, 2010](#)). The time for a black hole to grow from $100 M_{\odot}$ to $10^9 M_{\odot}$ or to $10^{10} M_{\odot}$ when accreting at Eddington rate is $\approx 0.8 \times 10^9 \text{ yr}$ or $\approx 0.9 \times 10^9 \text{ yr}$, respectively.

At redshift $z = 6$, the Universe is only $\approx 0.93 \times 10^9 \text{ yr}$ old. The central black hole would need to accrete at Eddington rate for the lifetime of the Universe to arrive at these masses. This is very unlikely, as the progenitor Pop III star will have first formed an HII region around itself, and the resulting gas heating is sufficient to drive most of the gas out of the host minihaloes ([Whalen et al., 2004](#); [Johnson and Bromm, 2007](#)). The BH seed is therefore cut off from its fuel supply.

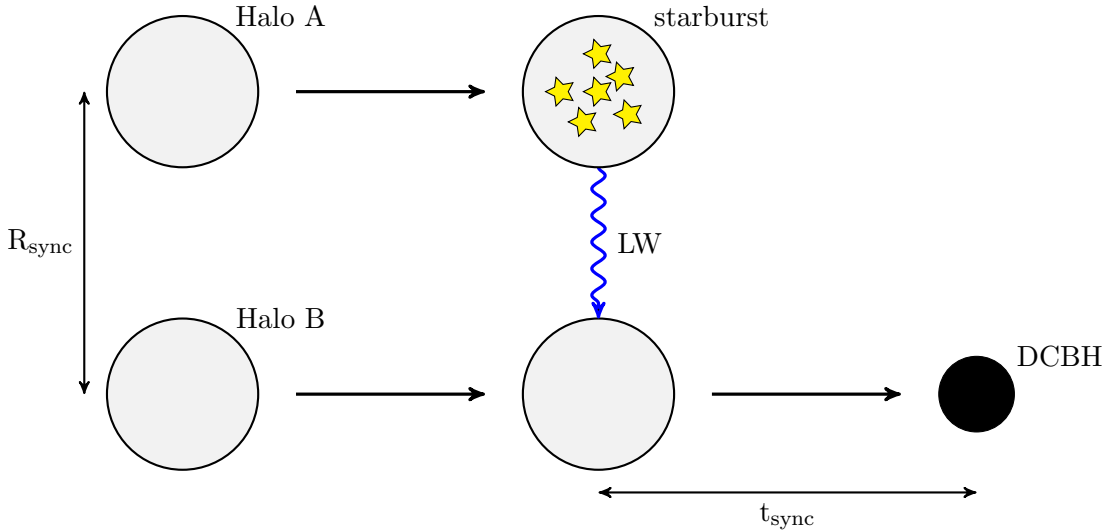


Figure 1.6.1: Direct collapse black hole formation with synchronized halo pairs.

1.6.2 DIRECT COLLAPSE BLACK HOLES

A second pathway to supermassive black holes is given by the so-called direct collapse black hole (DCBH) scenario that can be achieved by the synchronized halo mechanism (see e.g. [Dijkstra et al., 2008](#); [Agarwal et al., 2012, 2014](#); [Regan et al., 2016a](#)). The underlying idea is quite simple and illustrated in Figure 1.6.1: Two haloes, Halo A and Halo B, with masses just above the atomic cooling limit have a small separation R_{sync} . Halo A collapses first and forms many Pop III stars, which emit a large LW flux. The amount of LW radiation is large enough to destroy H_2 in the centre of Halo B. Therefore, Halo B cannot cool via molecular hydrogen, its core cannot fragment and form stars. If the timing is right, Halo B quickly collapses to a supermassive star that will subsequently collapse to a $10^{4-6} M_{\odot}$ black hole seed ([Haehnelt and Rees, 1993](#); [Oh and Haiman, 2002](#)). For this model to work, the time between the collapse of Halo A and Halo B, t_{sync} , needs to be less than the time that metals ejected from stars and supernovae in Halo A take to reach Halo B and Halo B needs to be completely primordial. Calculations show that Haloes A and B need to be well synchronized in time and space with t_{sync} typically a few kyr to Myr and R_{sync} on the order of 200-500 kpc ([Regan et al., 2017](#)).

To destroy the molecular hydrogen core in Halo B completely, a large flux of LW radiation of $J \geq 10^3 J_{21}$ is required ([Latif et al., 2014b](#); [Regan et al., 2016a](#)) for a 10^5 K black body spectrum (The value for J depends on the spectral shape, see e.g.

Agarwal and Khochfar 2015; Agarwal et al. 2016; Wolcott-Green et al. 2017). This flux is orders of magnitude larger than the estimated LWBG (values for the LWBG range from $\approx 0.01 J_{21}$ to $\approx 1 J_{21}$, see e.g. Johnson et al. 2008; Hartwig et al. 2015a) and can only be reached in the vicinity of a strong LW source. This is why Halo A is required.

The number density of synchronized halo pairs is small. Visbal et al. (2014b) find 2 pairs in their simulation volume of $\approx 1.7 \times 10^4 \text{ cMpc}^3$. But unlike black holes from stellar seeds, they are robust to effects like photoevaporation or tidal disruption (Visbal et al., 2014b).

A further complication arises from the fact that minihaloes of lower mass start to form stars before the star-forming halo of the synchronized halo pair does. In the minihalo, the first Pop III stars can explode as supernovae and spread metals that can pollute the synchronized pair. Due to the hierarchical nature of structure formation, the more massive atomic cooling haloes, Haloes A and B, form later. Therefore, in order to circumvent the metal enrichment of the region of interest, star formation in minihaloes in this region needs to be suppressed. This can be achieved if the region is illuminated by a LWBG with $J \sim 100 J_{21}$ that is able to suppress Pop III star formation in minihaloes completely (Regan et al., 2017). However, while this radiation background is not as extreme as the one required to suppress H_2 cooling in atomic cooling haloes, it is still much higher than the typical global LWBG.

Another pathway to DCBH formation might exist in regions of the Universe with a high streaming velocity. As a part of this thesis, we (Schauer et al., 2017b) have recently shown that in a region of the Universe with $3\sigma_{\text{rms}}$ streaming velocity, no halo below the atomic cooling limit (corresponding to a virial temperature of $\sim 8000 \text{ K}$) reaches high densities in its centre and can thus form stars. The high streaming velocity value of $3\sigma_{\text{rms}}$ or higher is only present in a volume fraction of 5.9×10^{-6} of the Universe. Combined with an estimate to find two synchronized halo pairs in a volume of $\approx 1.7 \times 10^4 \text{ cMpc}^3$ (Visbal et al., 2014b), we obtain a number density of 0.7 cGpc^{-3} . Our theoretical prediction matches the observed quasar number density of 1 cGpc^{-3} almost perfectly (Fan, 2006). These results are presented in Chapter 5.

This is an excellent example of why it is important to study the combination of different non-linear effects in the early Universe. I will provide an outlook at the end of this thesis on how we plan to elaborate on this topic of combined LWBG and streaming velocities further.

1.7 OBSERVATIONAL PROSPECTS

The astronomical community is awaiting the launch of the James Webb Space Telescope (JWST) in 2018, which will be able to observe much fainter objects. However, even with JWST, the detection of a single or a small cluster of Pop III stars will not be possible (Greif et al., 2009), not even if these objects are observed through a gravitational lens that magnifies the luminosity of the source (Rydberg et al., 2013).

The science mission for JWST does include understanding the early Universe and its first light sources, but it targets the first galaxies instead of the first Pop III stars. One key project suggested for JWST’s Cycle 1 or 2 would target star forming galaxies at redshift $z \sim 14$ with stellar masses of $M_{\star} \sim 2 \times 10^7 M_{\odot}$ as well as post-starburst galaxies at redshift $z \sim 7$ with stellar masses of $M_{\star} \sim 2 \times 10^9 M_{\odot}$ (Finkelstein et al., 2015). The suggested plan is expensive in observing time, requesting more than 2000 hours. We might witness this program performed over the five year mission duration, taking up 4-8% of the total hours of JWST available. With JWST, however, we will not observe star forming minihaloes at high redshift.

However, we might be able to indirectly constrain the formation scenarios of more massive haloes at redshifts as high as $z \sim 14$ with JWST if our simulations explain the growth and composition of these structures. If JWST can disentangle the contributions of the light from different stellar populations, we may learn how many stars form as Pop III, Pop II or even Pop I. These massive, early galaxies are expected to be rare. Their number density should provide constraints on when and in which haloes the first stars form. In addition, there are a few possibilities to indirectly measure properties of the first stars that we will discuss in the following subsections.

1.7.1 STELLAR ARCHAEOLOGY

One possibility to observe Pop III stars is to look for them in the Galactic halo or satellite galaxies with low metallicity. Stars with masses of $0.8 M_{\odot}$ and below have lifetimes longer than the current age of the Universe (see e.g. Kippenhahn et al., 2012). If such low mass Pop III stars exist, they would be still alive today and could be observed.

The hunt for metal-poor and metal-free stars is called stellar archaeology. So far, no metal free star has been found in the Milky Way. With a semi-analytical merger tree code, Hartwig et al. (2015a) studied the build-up of Milky Way like galaxies and their Pop III stars. They determine the minimum sample size of a survey in

halo stars to exclude Pop III survivors. They find that if no Pop III star is found in 4 million stars with masses below $0.8 M_{\odot}$, their existence can be excluded at the 66.7% level, and that a sample size of 20 million stars is necessary to exclude Pop III survivors at a 99% level.

Another explanation for the lack of observed metal-free stars could be that metal enriched material was accreted later onto a Pop III star. Some of the metal-poor stars show a different composition and are strongly carbon enhanced. They have been proposed to belong to a new class, the so-called carbon enhanced metal poor (CEMP) stars (Beers and Christlieb, 2005). The fraction of CEMP stars increases with decreasing metallicity, suggesting that this might be a feature of Pop III stars. However, the high velocities of the observed metal-poor stars (Frebel et al., 2009) or stellar winds (Tanaka et al., 2017) might prevent significant metal accretion onto the surface of a Pop III star. We therefore need to continue the search for the truly metal-free stars in the Milky Way.

1.7.2 21 CM OBSERVATIONS

Hydrogen is by far the most abundant element in the Universe. The 21 cm line of H originates from the hyperfine splitting of the ground state into a singlet and a triplet state. The energy difference of the two levels is $\Delta E = T_{\star} \times k_B = 5.9 \times 10^{-6}$ eV, where k_B is the Boltzmann constant and $T_{\star} \approx 68$ mK. Because of the large abundance of neutral hydrogen at high redshifts, the 21cm line is a good tracer for structures in the early Universe.

The occupation of the excited state is characterized by the spin temperature, T_s , that is defined via $n_1/n_0 = (g_1/g_0) \exp(-T_{\star}/T_s)$. Here, n_i denotes the number density and i can take the value of 0 (representing the singlet state) or 1 (representing the triplet state), g_0 and g_1 are the degeneracy factors with $g_1/g_0 = 3$. We can observe the spin temperature in emission and absorption relative to the CMB as the brightness temperature.

As the Universe expands, photons are redshifted by factors of $(1+z)$. Observing the 21 cm line at different redshifts therefore corresponds to observing it at different wavelengths and allows us to construct three dimensional picture of neutral hydrogen in the early Universe. As a consequence, we can derive fundamental properties of the early Universe at different times.

The measured brightness temperature depends on different effects that relate to the redshift, the ionization fraction, the temperature and density of the gas, and

the Lyman- α flux. As e.g. reviewed by [Pritchard and Loeb \(2012\)](#), at very high redshifts $z \gtrsim 200$, the Universe is very dense and the spin temperature can couple to the kinetic gas temperature. As the Universe expands, the gas temperature decreases adiabatically. T_s therefore decreases below T_{CMB} , and the 21 cm line becomes visible in absorption down to a redshift of $z \gtrsim 40$. At lower redshifts, the coupling weakens due to the decreasing density and the spin temperature instead couples to the CMB, eliminating signals in the brightness temperature around $z \lesssim 40$.

At later redshifts, the 21 cm signal starts to probe structure and radiation source formation. Two types of radiation have a strong influence of the 21 cm signal. On the one hand, energetic radiation such as X-rays can heat up the intergalactic medium. On the other hand, Lyman- α photons can induce a spin flip in neutral hydrogen and pump electrons to the triplet state via the so-called Wouthuysen-Field effect. As a consequence, the spin temperature couples once again to the kinetic temperature of the gas. Therefore, after redshift $z \lesssim 30$, the spin temperature couples to the cold gas, allowing the line to be visible in absorption. Later, when the gas is heated by hard radiation like X-rays, the gas temperature increases and therefore the spin temperature increases as well. It eventually exceeds the CMB temperature, and the line becomes visible in emission. Finally, the 21 cm signal will fade as the ionization fraction of the Universe increases, and we will be able to tell when and how smooth the process of reionization finished. With this information, many simulations that rely on subgrid models will finally have good constraints for the global parameters such as the ionization fraction of the Universe as a function of redshift or the times when Lyman- α emission or X-ray heating become important.

Several current experiments are trying to measure the global, sky-averaged 21cm signal. Unfortunately, the noise (including many man-made radio signals) is several orders of magnitude larger than the expected signal. One of the radio telescopes targeting the cosmological 21 cm line is the Precision Array to Probe the Epoch of Reionization (PAPER) ([Parsons et al., 2010](#)). It consists of many simple antennas located in the USA and South Africa, remote from civilisation and trying to avoid man-made noise. A second radio telescope, the LOw requency ARray (LOFAR) ([van Haarlem et al., 2013](#)), takes a different approach by having many antennas distributed over many places in Europe, all of them relatively close to cities and well-accessible. These radio telescopes start giving first constraints on the reionization history, but the signals they detect are still weak and 2σ upper limits. The results are, however, a good tool to better constrain the employed noise models ([Ali et al., 2015](#); [Patil et al., 2017](#)).

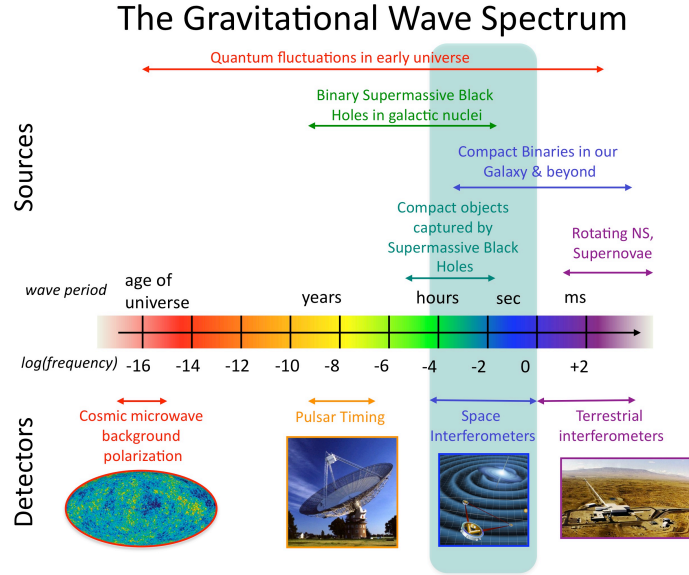


Figure 1.7.1: The spectrum of gravitational waves accessible by different instruments. Image credit: NASA Goddard Space Flight Center.

A future facility, the Square Kilometer Array (SKA), is already under construction. It will be able to provide spatially resolved maps of neutral hydrogen out to redshifts of $z \sim 28$ already with the first phase of SKA, SKA1 (Koopmans et al., 2015). Observations of the 21 cm signal of a single region of clustered Pop III / Pop II stars at high redshifts ($z \sim 13$ to $z \sim 19$) could be possible that would then allow to determine e.g. the ratio of emitted X-rays to UV photons of the source (Ahn et al., 2015). With this telescope, we will be able to put constraints on the evolution and end of the Dark Ages.

1.7.3 GRAVITATIONAL WAVES

The recent discovery of the first gravitational wave signal GW150914 in September 2015 has opened a new observational opportunity for astronomers. The Advanced Laser Interferometer Gravitational Wave Observatory (aLIGO) has detected a pair of inspiralling and subsequently merging black holes with masses of $M_{\text{BH},1} = 36_{-4}^{+5} M_{\odot}$ and $M_{\text{BH},2} = 29_{-4}^{+4} M_{\odot}$ at redshift $z \approx 0.08$ (Abbott et al., 2016a), merging to a combined black hole mass of $M_{\text{BH}} = 62 M_{\odot}$. Since then, two more black hole mergers have been detected, with combined masses of $21 M_{\odot}$ (Abbott et al., 2016b) and $49 M_{\odot}$ (Abbott et al., 2017).

This topic of gravitational waves is not only very interesting in itself as it allows us to test general relativity, but it is also related to the early Universe. The observed gravitational wave GW150914 could originate from the merger of a pair of black holes from Pop III star remnants, with a probability of $\sim 1\%$ (Hartwig et al., 2016). The expectation to measure a gravitational wave signal from Pop III stars with a combined mass of $M > 300 M_{\odot}$ is about once per decade, if we assume a log-normal IMF in the mass range from 0.1 to $300 M_{\odot}$. The centre of a galaxy is the most likely part to host such a merging black hole pair originating from Pop III seeds (Pacucci et al., 2017).

The current instrument aLIGO is sensitive to objects of combined masses in the range $10\text{-}1000 M_{\odot}$ out to a few thousand Mpc. Even more interesting for the high redshift Universe, another instrument called Laser Interferometer Space Antenna (LISA) will be able to detect gravitational waves emerging from more massive objects at very high redshifts (see Figure 1.7.1). LISA is planned to consist of three spacecraft orbiting the sun with baselines of 5×10^6 km. It will be sensitive to $10^4 - 10^7 M_{\odot}$ black hole binaries out to redshifts of $z = 15$ and higher (Baker et al., 2007).

With this new instrument, we will be able to place constraints on black hole masses at redshifts that go far beyond current possibilities of observing high-redshift quasars. This will help us to study the high-redshift structure formation and to disentangle the formation theory of supermassive black holes.

2

Astrophysical codes

The very first astrophysical simulation in 1941 did not yet run on a computer, but instead involved light bulbs ([Holmberg, 1941](#)). This ‘simulation’ contained 74 light bulbs, representing the collision of two ‘nebulae’ (galaxies). At the position of each light bulb, the incident light from the 73 surrounding candles was determined and used as a measure of the acceleration that each point experienced.

As in many areas of astronomy, the progress that has been made in less than a hundred years is stunning. Present day computer simulations are massively parallelised to run on supercomputers, being able to target cosmological simulations with over a hundred billion particles (as e.g. the Magneticum Pathfinder simulations; [Bocquet et al. 2016](#), [Dolag et al. in prep.](#)) or highly resolved disk galaxies originating from cosmological conditions with ten million dark matter particles and a few million gas cells (the Auriga simulations; [Grand et al., 2017](#)).

These advances have been possible not only because of the invention and improvement of computers, but also because many well-suited astrophysical simulation codes have been developed. In general, there are two fundamental types of codes currently used in hydrodynamical astrophysical simulations: smoothed particle hydrodynamics (SPH), which is a Lagrangian method, or Eulerian mesh codes. Famous and commonly used examples for SPH are e.g. Gadget-2 ([Springel and Hernquist,](#)

2002) or Gasoline (Wadsley et al., 2004), for mesh codes RAMSES, (Teyssier, 2002) or FLASH (Fryxell et al., 2000).

In SPH, the gas is represented by discrete elements (particles), that are smoothed over a kernel with a smoothing length. Quantities like density or pressure are not tied to the particle, but calculated over an ensemble of particles. Single particles can carry e.g. the velocity and mass information, and also other physical properties like their chemical composition. Problems arise as SPH can suppress mixing or fluid instabilities on small scales (see e.g. Marri and White, 2003). It is also difficult to increase the resolution locally (e.g. by particle splitting techniques), as this introduces numerical artefacts.

In mesh codes, the gas is distributed over a grid, often in combination with an adaptive refinement technique that allows smaller grid cells in regions that require high resolution. Grid codes are usually Eulerian, as in general, the grid does not move with the fluid. They are much better at resolving small scale mixing and instabilities. The grid structure, however, can lead to problems, as e.g. galaxies tend to align with a Cartesian grid in large cosmological simulations or spherical grids favour infall to their centres.

In this thesis, I make use of two different simulation codes: ZEUS-MP and AREPO. I briefly introduce both codes in the following sections.

2.1 ZEUS-MP

ZEUS-MP is an Eulerian grid code (Hayes et al., 2006) that is an updated and improved version of the ZEUS-2D code developed by Stone and Norman (1992). We use this code for the projects described in Chapters 3 and 4. ZEUS-MP is a finite difference code that solves the equations of hydrodynamics on a structured mesh¹. Quantities such as density, internal energy etc. are determined at cell centres while velocities are determined at cell edges. The hydrodynamical equations are solved using a second-order monotonic advection scheme (van Leer, 1977).

ZEUS-MP allows simulations to be carried out in 1D, 2D or 3D, and supports the use of cylindrical and spherical grids in addition to the usual Cartesian grid. In the simulations presented in Chapters 3 and 4, we use a 1D spherical grid.

We use a version of ZEUS-MP modified by (Whalen and Norman, 2006) to model the propagation of ionizing and photodissociating radiation from point sources using

¹ZEUS-MP can also be used to simulate magneto-hydrodynamical flows, but in our simulations we assume $B = 0$.

photon conserving radiative transfer. This version of ZEUS-MP couples the hydrodynamical fluid equations to a network of primordial chemistry network. Different boundary conditions can be employed that are treated with ghost-cells outside the regular grid.

After problem set-up, a potential is calculated to balance the gas and keep it in hydrostatic equilibrium. This potential does not change in time, as it is assumed that the lifetime of the problem we are interested in is much shorter than the free-fall time of the halo. This is indeed true for our set-ups.

After creating the associated initial conditions, the code evolves the fluid dynamics equations by splitting them into source terms and advection terms that are evolved separately. Both the source terms (corresponding to the gradients in the equations) and the advection terms (corresponding to the divergence terms) are evolved in three or two sub steps, respectively. After each hydrodynamical step, baryon and charge conservation are enforced.

A chemical network for nine primordial species, H, H⁺, He, He⁺, He²⁺, H⁻, H₂, H₂⁺, e⁻, is included, using the reactions from [Anninos et al. \(1997\)](#). Each of them is evolved using its own continuity equation. They are assumed to move with the flow of the gas and share the same velocity field. The advection terms are included in the hydrodynamic cycle, while the reactions are evolved on a separate step. Heating and cooling rates that lead to changes in the internal energy are included in the code. It treats reactions like photoionization of neutral hydrogen and different cooling processes such as recombinational, Compton, collisional ionization, collisional excitation cooling and cooling via H₂. A full list of the chemical reactions and heating and cooling processes included can be found in [Whalen and Norman \(2006\)](#), and references therein.

Radiation is included by a radiative transfer from a central source in a spherical-polar geometry. The rates for ionizing photons are sub cycled on a chemical time step.

Radiation is transported in a photon-conserving way, where the number of photons exiting a cell per second equals the number of photons entering the cell per second minus the ionizing rate in that cell. The photons are transported in 120 energy bins, ranging from 0.755 eV (the H⁻ photodissociation energy) to 90 eV (the extreme ultraviolet). Between 0.755 eV and 13.6 eV (the photoionization energy of H), energy is transported in 40 linearly spaced bins. Between 13.6 eV and 90 eV, it is transported in logarithmically spaced bins.

For transporting radiation through the cells, the on-the-spot approximation ([Os-](#)

terbrock, 1989) is employed. The underlying assumption is that case A (spontaneous) recombination photons are reabsorbed in a cell before leaving that cell where the number of ionizations per zone per time is equal to the difference of the number of ionizing photons entering to the number of ionizing photons exiting the cell. Like that, radiative transfer has to be calculated with only one radiation source in the centre instead of each cell being a new source. This reduces the computational costs by a lot, since radiative transfer along many lines of sight gets very expensive. Other reactions that are included are case B (stimulated) recombination rates, photoionization and electron collisional ionization of hydrogen.

In general, photon conservation is employed, except for H_2 . Instead, the self-shielding functions from [Draine and Bertoldi \(1996\)](#) are used to account for photodissociation from LW radiation from the central source; He^+ and He^{2+} two photon emissions can be in this wavelength range, but are neglected as they play only a minor role.

The chemical time step is sub cycled over the hydrodynamical time step, the reactions of the species are performed until the hydrodynamical time step is reached. The hydrodynamical time step is the minimum of the Courant time (the sound crossing time in the smallest cell) and a tenth of the heating time. The chemical time step is a tenth of the electron number density over the change in electron density. If the hydrodynamical time step is smaller than the chemical time step, the chemistry is not sub-cycled, but both updates are performed on an equal time step. Therefore, both fast changes in the heating and cooling and chemistry can be accounted for.

We use ZEUS-MP in spherical symmetry in a one dimensional grid with an inflowing boundary condition towards the centre and out flowing boundary conditions at large radii. Our code version does not include adaptive mesh refinement. This can cause problems because a thin shell of highly abundant molecular hydrogen builds up in the outer part of the ionization front that provides as large fraction of the shielding and is very important for the LW escape fraction calculations (see [Chapters 3 and 4](#)). This is especially challenging if the ionization front moves slowly. We overcome this issue by sampling a 10 pc region around the front with a resolution of 0.1 pc for the LW escape fractions from first galaxies (see [Chapter 4](#)). Before the I-front moves out of this region, we halt the code and resample the region around the I-front. This process therefore employs an external adaptive mesh refinement.

2.2 AREPO

AREPO is a moving mesh code. We use it to run cosmological simulations with different streaming velocities, the projects presented in Chapters 5 and 6. The code AREPO uses a new method that combines the advantages of SPH and adaptive mesh refinement grid code simulations and is described in detail by [Springel \(2010\)](#). It evolves dark matter as particles and gas as cells that are allowed to move with the gas flow.

The gas cells are constructed from mesh-generation points as an unstructured mesh via Voronoi tessellation that is constructed from a Delaunay triangulation of these points. This alone gives the advantage that structures do not align with the Cartesian grid or inflow is favoured in a spherical grid. The hydrodynamical equations are solved using a Lagrangian formulation with a Runge-Kutta integration scheme ([Pakmor et al., 2016](#)). The gas can flow from grid cell to grid cell, and in addition, the cells themselves can move. The cells are reconstructed on the hydrodynamical time step with an improved grid regularization method ([Mocz et al., 2015](#)).

Gravity is included using the TreePM method ([Springel and Hernquist, 2002](#)) with a hierarchical oct-tree algorithm ([Barnes and Hut, 1986](#)) for short-range forces and a Fast Fourier Transform method for long-range forces.

In our setup, we include a primordial chemistry network, that evolves the rate equations of all relevant reactions for H_2 and HD formation and that are important for DCBH formation ([Glover, 2015](#)). The chemical network is subcycled at the end of each step. The species that are evolved by the code are H, H^+ , H_2 , D, D^+ , HD, He, He^+ , He^{++} . Several heating and cooling processes are included in the network, with the most important contribution coming from H_2 line cooling. Furthermore, line cooling by HD is included, as well as cooling by collisional ionization of H, He and He^+ , recombination cooling of H^+ , He^+ and He^{++} , H^- formation cooling, Compton and bremsstrahlung cooling. A description of the chemical network can be found in [Hartwig et al. \(2015b\)](#), which builds upon earlier work from [Glover and Jappsen \(2007\)](#), [Glover and Abel \(2008\)](#) and [Clark et al. \(2011\)](#). In contrast to [Hartwig et al. \(2015b\)](#), we have now implemented HD chemistry and the latest changes are described in Chapter 6.

3

Lyman-Werner UV Escape Fractions from Primordial Haloes

Distribution of work Anna T. P. Schauer has used a version of ZEUS-MP modified by Daniel J. Whalen to perform all simulations that have been used in this study. She performed the analysis and interpretation of the results with the help of Daniel J. Whalen, Simon C. O. Glover and Ralf S. Klessen. She has written most of the text, and Daniel J. Whalen contributed to the text in the introduction, Simon C. O. Glover to the method section of the near- and far-field. All authors provided comments and ideas to the project.

The content of this chapter has been published as:

Schauer, A. T. P., Whalen, D. J., Glover, S. C. O., and Klessen, R. S.
“Lyman-Werner UV escape fractions from primordial haloes”.
MNRAS, 454:2441–2450, December 2015.
doi: 10.1093/mnras/stv2117.

Authors Anna T. P. Schauer¹, Daniel J. Whalen^{1,2}, Simon C. O. Glover¹, Ralf S. Klessen¹

¹Universität Heidelberg, Zentrum für Astronomie, Institut für Theoretische Astrophysik, Albert-Ueberle-Str. 2, 69120 Heidelberg, Germany

²Institute for Cosmology and Gravitation, University of Portsmouth, Portsmouth, PO1 3FX, UK

Abstract Population III stars can regulate star formation in the primordial Universe in several ways. They can ionize nearby halos, and even if their ionizing photons are trapped by their own halos, their Lyman-Werner (LW) photons can still escape and destroy H₂ in other halos, preventing them from cooling and forming stars. LW escape fractions are thus a key parameter in cosmological simulations of early reionization and star formation but have not yet been parametrized for realistic halos by halo or stellar mass. To do so, we perform radiation hydrodynamical simulations of LW UV escape from 9–120 M_⊙ Pop III stars in 10⁵ to 10⁷ M_⊙ halos with ZEUS-MP. We find that photons in the LW lines (i.e. those responsible for destroying H₂ in nearby systems) have escape fractions ranging from 0% to 85%. No LW photons escape the most massive halo in our sample, even from the most massive star. Escape fractions for photons elsewhere in the 11.18–13.6 eV energy range, which can be redshifted into the LW lines at cosmological distances, are generally much higher, being above 60% for all but the least massive stars in the most massive halos. We find that shielding of H₂ by neutral hydrogen, which has been neglected in most studies to date, produces escape fractions that are up to a factor of three smaller than those predicted by H₂ self-shielding alone.

Keywords early universe – cosmic background radiation – dark ages, reionization, first stars – stars: Population III – radiation: dynamics.

3.1 INTRODUCTION

The first stars form at $z \sim 20$ –30, or about 200 Myr after the big bang. Early numerical simulations suggested that Pop III stars are very massive, 100 - 500 M_⊙, and form in isolation, one per halo (Bromm et al., 1999, 2002; Abel et al., 2000, 2002; Nakamura and Umemura, 2001; Glover, 2005). More recent models indicate that most Pop III stars form in binaries (Turk et al., 2009) or in small clusters (Stacy

et al. 2010; Clark et al. 2011a,b; Greif et al. 2011a, 2012; Smith et al. 2011; Dopcke et al. 2013; Glover 2013; Stacy and Bromm 2014) with a wide range of masses, all the way from the sub-solar regime to $\sim 10^3 M_{\odot}$. These calculations suggest that the final mass of a star is either limited by dynamical processes (Clark et al. 2011a; Greif et al. 2012; Smith et al. 2012) or by radiative feedback (McKee and Tan, 2008; Hosokawa et al., 2011, 2012; Stacy et al., 2012; Hirano et al., 2014).

If any Pop III stars formed with masses below $\sim 0.8 M_{\odot}$, they will have survived until the present day, and they may therefore be detectable in surveys targeting extremely metal-poor stars in the Galactic bulge and halo as well as in nearby satellite galaxies (see the reviews by Beers and Christlieb 2005, or Frebel 2010). This could potentially allow us to set limits on the low mass end of the primordial stellar initial mass function (IMF, see e.g. Tumlinson, 2006; Salvadori et al., 2007; Hartwig et al., 2015a). Unfortunately, the direct detection of Pop III stars in the high redshift Universe is unlikely even with future 30 meter telescopes (although see Rydberg et al., 2010). As massive stars are very short lived, the upper end of the Pop III IMF is thus more difficult to constrain. This can only be done indirectly, for example by observing and analyzing the supernovae (SNe) that mark the end of the lives of very massive stars. These may indeed be visible to the *James Webb Space Telescope* (*JWST*), the Thirty-Meter Telescope (TMT), the Extremely Large Telescope (ELT) and the *Giant Magellan Telescope* (*GMT*) (e.g., Whalen et al., 2013a,b, 2014; Smidt et al., 2014). Another promising possibility is again Galactic archeology. The comparison of the nucleosynthetic yields of Pop III SNe to the chemical abundances of extremely metal-poor stars observed in our Milky Way suggests that many Pop III stars may had masses in the range $15 - 40 M_{\odot}$ (e.g., Beers and Christlieb, 2005; Frebel et al., 2005, 2008; Joggerst et al., 2010).

In this Chapter, we focus on the high-mass end of the Pop III IMF. Massive Pop III stars had the capability to profoundly transform their environment due to the strong radiative, chemical, and mechanical feedback they provide. They can evaporate the gas from their dark matter (DM) halos, engulf nearby halos with both ionizing and LW band UV radiation (Whalen et al., 2004; Alvarez et al., 2006; Abel et al., 2007; Whalen et al., 2008), and alter their composition with the metal they produced and expelled. LW photons lie in a series of discrete lines located in the energy range $11.18 - 13.6$ eV (corresponding to a wavelength range of $1110 \text{ \AA} - 912 \text{ \AA}$) and can travel great distances in the primeval universe because they lie below the ionization threshold of atomic hydrogen. They can delay or suppress star formation in nearby halos because they photodissociate H_2 and prevent the gas from cooling

(see e.g. Haiman et al., 1997, 2000; Glover and Brand, 2001, 2003; Machacek et al., 2001; Susa and Umemura, 2006; Susa, 2007; O’Shea and Norman, 2007; Wise and Abel, 2008). How Pop III stars regulate subsequent star formation is central to the rise of stellar populations in the first galaxies (Ciardi and Ferrara, 2005; Johnson et al., 2009; Greif et al., 2010; Jeon et al., 2012; Pawlik et al., 2013; Wise et al., 2012). This begins with understanding how the strength of the LW background changes over time, which depends on the masses of Pop III stars and the halos in which they reside.

Over the past two decades, many studies have examined the influence of LW and ionizing radiation on the formation of stars at high redshift. They found that a photodissociating background cannot halt Pop III star formation but can delay it (e.g., Machacek et al., 2001; Wise and Abel, 2007; O’Shea and Norman, 2007; Safranek-Shrader et al., 2012a). An early X-ray background created by accretion onto stellar remnants and by emission from supernovae can catalyze additional H₂ formation that offsets the effects of LW radiation to some extent, but radiative feedback overall is dominated by the LW background (Glover and Brand, 2003; Machacek et al., 2003). The evolution of this background over time in general seems to play only a minor role if it changes less rapidly with redshift z than $10^{-z/5}$ (Visbal et al., 2014c). Simulations suggest that Pop III stars forming in halos illuminated by significant LW backgrounds will be more massive because their host halos must grow to larger masses before beginning to cool (O’Shea and Norman, 2007; Hirano et al., 2015; Latif et al., 2014b). When they do begin to cool, collapse rates at their centers are higher and lead to more massive stars.

The effect of a single Pop III star on a nearby halo has been examined in much greater detail than in large cosmological boxes. Radiation hydrodynamical simulations by Susa and Umemura (2006) find that star formation in the vicinity of a source star is possible if the star forming region exceeds a density threshold (see also Glover and Brand, 2001). Other studies in this vein show that star formation can be either promoted or suppressed depending on the mass of the halo, the mass of the star, and the proximity of the halo to the star (Susa, 2007; Whalen et al., 2008, 2010; see also Shapiro et al., 2004; Iliev et al., 2005; Hasegawa et al., 2009; Susa et al., 2009).

In some cases the H II region of a Pop III star may fail to break out from a halo because of large central gas densities. In such cases, LW photons might still exit the halo because their energies lie below the ionization limit of hydrogen, even if H₂ self-shields against this flux to some degree. Most simulations of radiative feedback

with Pop III stars in cosmological boxes simply assume uniform LW backgrounds. A parametrization of LW escape fractions from primordial halos as a function of halo and stellar mass could provide the strength of this background from first principles in future simulations. However, almost no work has been done to produce such a parametrization. In the only previous study on this topic of which we are aware, [Kitayama et al. \(2004\)](#) examined LW escape fractions from Pop III star-forming halos with a [Navarro et al. \(1997\)](#) radial density profile, varying the mass of the halo and central star.

In an effort to improve on this previous study, we perform radiation hydrodynamical calculations of LW escape from Pop III minihalos with the ZEUS-MP code. We then post-process the simulations with semi-analytical methods and calculate escape fractions in two limits, the near-field and the far-field. In the near-field case – the only scenario considered by [Kitayama et al. \(2004\)](#) – we compute the escape fraction of photons in the LW lines themselves. This is the value that is relevant if we are interested in the effect of radiation from the halo on H_2 in its immediate vicinity. In the far-field case, on the other hand, we are interested in the total fraction of the photons lying between 13.6 eV and 11.2 eV that can escape from the halo. This is the important quantity if we are interested in the effect of radiation from the halo on H_2 located at cosmological distances.

In both cases, we account not only for H_2 self-shielding but also for shielding from the Lyman series lines of atomic hydrogen, which were not considered by [Kitayama et al. \(2004\)](#). In some circumstances, this can significantly affect the LW escape fraction.

This Chapter is structured as follows. In Section 2 we describe our numerical models. In Section 3 we tabulate LW escape fractions by halo and stellar masses and we conclude in Section 4.

3.2 METHOD

To calculate LW escape fractions for a given star and halo we first evolve the H II region of the star with the radiation hydrodynamics simulation code ZEUS-MP. We then post-process the profiles for the ionization front (I-front) and the surrounding halo with semi-analytic calculations to determine how many LW photons exit the halo. LW escape fractions in both the near-field and far-field approximations are considered, as described below.

3.2.1 ZEUS-MP

ZEUS-MP is an astrophysical radiation-hydrodynamics code that self-consistently couples photon-conserving raytracing UV transport and nonequilibrium primordial gas chemistry to gas dynamics to evolve cosmological I-fronts (Whalen and Norman, 2006, 2008a,b). We evolve mass fractions for H, H⁺, He, He⁺, He²⁺, H⁻, H₂⁺, H₂, and e⁻ with nine additional continuity equations and the nonequilibrium rate equations of Anninos et al. (1997) in which the species are assumed to share a common velocity distribution. Mass and charge conservation, which are not formally guaranteed by either the network or advection steps, are enforced at every update of the reaction network. Heating and cooling due to photoionization and chemistry are coupled to the gas energy density with an isochoric update that is operator-split from the fluid equations. Cooling due to collisional ionization and excitation of H and He, recombinations of H and He, inverse Compton scattering (IC) from the CMB, bremsstrahlung emission, and H₂ cooling are all included in our models. The chemical and cooling rate coefficients are the same as those used in Anninos et al. (1997), with one important exception: we use case B rates to describe the recombination of hydrogen and helium, rather than case A as used in Anninos et al. (1997).

We use 120 energy bins in our photon-conserving UV transport scheme, 40 bins that are uniform in energy from 0.755 to 13.6 eV and 80 bins that are logarithmically spaced from 13.6 eV to 90 eV. We normalize photon rates in each bin by the time-averaged ionizing photon rates and surface temperatures for Pop III stars from Tables 3 and 4 of Schaerer (2002). The radiative reactions in our simulations are listed in Table 1 of Whalen and Norman (2008a), and the momentum imparted to the gas by ionizations of H and He is included in the photon transport. Photon conservation is not used to calculate H₂ photodissociation rates. They are derived along radial rays from the star with the self-shielding functions of Draine and Bertoldi (1996, hereafter DB96) modified for thermal broadening as a proxy for the effects of gas motion (equations 9 and 10 in Whalen and Norman, 2008a), with r^{-2} attenuation taken into account.

Two-photon emission from recombining He⁺ and He²⁺ can produce photons capable of photo-dissociating H₂. However, we do not account for the effects of this nebular emission, as it is unimportant in comparison to the effects of the direct stellar emission.

3.2.2 HALO MODELS

We adopt the one-dimensional (1D) spherically-averaged halo profiles used in Whalen et al. (2010), which were based on the results of cosmological simulations carried out with the Enzo adaptive mesh refinement (AMR) code (Bryan et al., 2014). Their masses are $6.9 \times 10^5 M_{\odot}$, $2.1 \times 10^6 M_{\odot}$ and $1.2 \times 10^7 M_{\odot}$. This corresponds to the range of halo masses in which Pop III stars are expected to form via H_2 cooling, and all three halos form at $z \sim 20$. Densities, velocities, temperatures and mass fractions for all nine primordial species are mapped from these profiles onto a 1D spherical grid in ZEUS-MP. We summarize the properties of these halos in Table 3.2.1 and plot their initial densities, velocities, temperatures, and species mass fractions in Figure 3.2.1.

The gas densities have nearly a power-law profile with slopes around -2.1, with the most massive halo having the highest densities. Temperatures vary from a few hundred K to several thousand K and generally increase with halo mass. This is to be expected since the virial temperature of a halo scales with the halo mass as $T_{\text{vir}} \propto M^{2/3}$. Virial shocks are visible in all three profiles at ~ 100 pc, where infall velocities abruptly decrease as accretion flows crash into increasingly dense regions of the halo. Shock heating at these radii is also evident in the temperature profiles, and is almost strong enough to collisionally ionize atomic hydrogen in halo 3.

ZEUS-MP does not evolve DM particles as in cosmological codes such as Enzo or GADGET; instead, an additional gravitational potential is implemented as a proxy for the DM potential of the halo. We take its potential to be that required to keep the baryons in hydrostatic equilibrium on the grid. The mass associated with this potential is nearly the same as that of the halo. We interpolate this precomputed potential onto the grid at the beginning of the run but it does not evolve thereafter. Taking the potential to be static is a reasonable approximation because merger and accretion timescales at $z \sim 20$ are on the order of 20 Myr, significantly longer than the lifetimes of most of the stars that we consider in this study (see Table 3.2.2). We therefore do not expect the dark matter distribution to evolve much over the lifetime of the star.

3.2.3 HII REGION SIMULATION SETUP

We center the Pop III star at the origin of a 1D spherically-symmetric grid that has 500 ratioed zones in radius. The inner boundaries are at 2.0×10^{17} cm (halos 1 and 2) or 4.0×10^{17} cm (halo 3) and the outer boundaries are at slightly more than

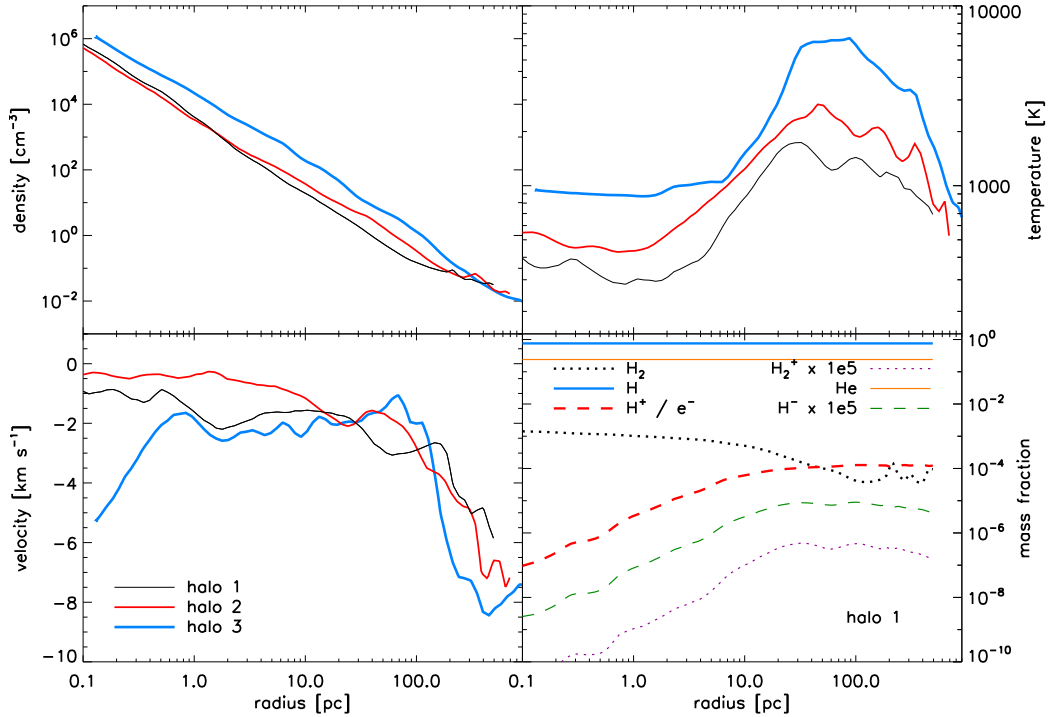


Figure 3.2.1: Initial densities (upper left), temperatures (upper right), radial velocities (lower left) and species mass fractions (lower right) for the three halos.

twice the virial radius of the halo. Reflecting and outflow conditions are imposed on the inner and outer boundaries, respectively. Densities, energies, velocities and species mass fractions from our Enzo profiles are mapped onto the ZEUS-MP grid with a simple linear interpolation of the logarithm of the given variable. We consider Pop III stars with masses 9, 15, 25, 40, 60, 80 and 120 M_{\odot} in all three halos, leading to a total of 21 models. The properties of these stars are listed in Table 2 (Schaerer, 2002). Each simulation is run out to the end of the life of the star.

In two of the 21 simulations (the 15 M_{\odot} star in halos 1 and 2) the I-front is confined to small radii that require a finer grid in order to be resolved. We therefore use a grid of 1000 zones with two contiguous blocks: a very finely spaced uniform grid with 600 cells to resolve the I-front followed by a ratioed grid with 400 cells that again extends to twice the virial radius of the halo. We ensure that the length of the innermost zone of the outer block is within 20% of that of the outermost zone of the inner block to avoid spurious reflections of shocks at the interface of the two blocks.

3.2.4 LW ESCAPE FRACTIONS

Molecular hydrogen has no dipole moment and is therefore destroyed in a two-step photodissociation process, the Solomon-process (Stecher and Williams, 1967b): $\text{H}_2 + \gamma \rightarrow \text{H}_2^* \rightarrow 2\text{H}$. Incident radiation can excite the molecule from the ground state to an electronically excited state. Two of these excited states, $\text{B}^1\Sigma_u^+$ (known as the Lyman state) and $\text{C}^1\Pi_u$ (the Werner state), are separated from the electronic ground state by less than 13.6 eV, and transitions to these states can therefore be brought about by photons with energies below the Lyman limit of atomic hydrogen. Within the Lyman and Werner states, a variety of bound rotational or vibrational levels are accessible, and so transitions from the ground state to the Lyman or Werner states occur through a series of discrete lines, known as the Lyman-Werner band system, or simply as the Lyman-Werner lines. Once excited by a photon in one of these lines (a LW photon), the H_2 molecule remains in the Lyman or Werner state for only a very short time $\Delta t \sim 10^{-8}$ s, before decaying back to the electronic ground state. Most of the time, the H_2 molecule decays to a bound ro-vibrational level in the ground state. However, a small fraction of the time, the decay occurs to the vibrational continuum, resulting in the dissociation of the H_2 molecule. The dissociation probability depends on the details of the incident spectrum and the density and temperature of the gas (which fix the initial rotational and vibrational level populations), but is typically around 15% (DB96). The remaining 85% of LW photon absorptions result in decay back to a bound state. In a small fraction of cases, this results in a photon with the same energy as the original LW photon (albeit with a random direction). However, the majority of the time, the re-emitted photon has too small an energy to bring about photodissociation (Glover and Brand, 2001, for more details, see the discussion in Section 3.4 of).

When the H_2 column density is large, the gas becomes optically thick in the LW lines. This can prevent radiation from an external source from reaching the center of a halo or LW flux from the center of a halo from escaping it. The gas therefore self-shields against LW radiation. In addition, LW photons can also be absorbed by most of the Lyman series lines of atomic hydrogen ¹.

In the immediate vicinity of a halo, the photons responsible for photodissociating

¹The exception is Lyman- α , which is located at too low an energy. However, because the frequencies of the LW lines of H_2 do not coincide particularly closely with those of the Lyman series lines of H, this effect only becomes important when the atomic hydrogen column density is very high, $N_{\text{H}} \simeq 10^{23} \text{ cm}^{-2}$ or above, so that the Lyman series lines are strongly Lorentz-broadened (Wolcott-Green and Haiman, 2011).

H_2 are those emitted in the LW lines in the rest-frame of the halo. The absorption of these photons by H_2 and H within the halo can be conveniently parameterized by a simple self-shielding function (see e.g. DB96; [Wolcott-Green and Haiman 2011](#), hereafter simply WH11). The escape fraction of photons in this limit, which we term the near-field limit, is then simply given by the value of this self-shielding function evaluated at the virial radius of the halo. At larger, cosmological distances, the LW flux is redshifted by the expanding Universe or Doppler shifted due to relative velocities between halos. As a consequence, the LW lines in the source frame may not coincide with LW absorption lines in the local frame of a halo. A simple estimate of the escape fraction in this limit, which we term the far-field limit, is given by the fraction of the LW range 11.2 – 13.6 eV not lying inside the combined equivalent width of the absorption lines. In the sections below, we describe in more detail how we compute the LW escape fractions in both limits.

NEAR-FIELD LIMIT

A LW photon escapes a halo if it does not photodissociate an H_2 molecule or is not absorbed and re-emitted as lower-energy photons. The LW escape fraction, f_{esc} , can therefore be equated to the fraction of H_2 molecules that are shielded from either process. The factors by which H_2 is shielded from LW photons by other H_2 molecules and by H atoms are $f_{\text{shield}}^{\text{H}_2}$ and $f_{\text{shield}}^{\text{H}}$, respectively. Both factors account for all processes by which LW photons are absorbed, not just those that result in a photodissociation. The total factor by which H_2 is shielded can be taken to be the product of these two factors (see the commentary on equation 13 in WH11),

$$f_{\text{esc}} = f_{\text{shield}}^{\text{H}_2} f_{\text{shield}}^{\text{H}}. \quad (3.1)$$

To construct $f_{\text{shield}}^{\text{H}_2}$ we first determine the column density of H_2 ,

$$N_{\text{H}_2} = \sum_{i=1}^{r_i \leq R_{200}} n_i \chi_{\text{H}_2,i} (r_i - r_{i-1}), \quad (3.2)$$

where n_i is the number density of all particles and r_i is the outer radius of the i^{th} cell, where r_0 is zero. $\chi_{\text{H}_2,i} = N_{\text{H}_2,i}/N_{\text{total},i}$ is the H_2 particle fraction with $N_{\text{H}_2,i}$ the number of H_2 molecules and $N_{\text{total},i}$ the total number of particles in bin i . The

halo	R_{200} (pc)	mass (M_{\odot})
1	256.8	6.9×10^5
2	339.6	2.1×10^6
3	495.2	1.2×10^7

Table 3.2.1: Virial radii and total (dark matter + baryon) masses of the three halos.

M (M_{\odot})	lifetime (Myr)	$\log L$ (L_{\odot})	$\log T_{\text{eff}}$ (K)
9	20.2	3.709	4.622
15	10.4	4.324	4.759
25	6.46	4.890	4.850
40	3.86	5.420	4.900
60	3.46	5.715	4.943
80	3.01	5.947	4.970
120	2.52	6.243	4.981

Table 3.2.2: Pop III stellar properties (Schaerer, 2002).

sum extends out to the virial radius of the halo,

$$R_{200} = R(\rho = 200 \Omega_{b,0} \rho_{\text{crit}}), \quad (3.3)$$

where ρ is the gas density and $\rho_{\text{crit}} = 3H^2(z = 20)/(8\pi G) \sim 2.349 \times 10^{-26} \text{g cm}^{-3}$ is the critical overdensity of the Universe at $z = 20$. The virial radii are listed for all three halos in Table 3.2.1.

The Doppler broadening of lines must be taken into account in $f_{\text{shield}}^{\text{H}_2}$. The thermal component of the Doppler broadening parameter, $b_{\text{D,T}}$, is associated with the Maxwellian velocity distribution of the atoms and molecules,

$$P_v(v)dv = \sqrt{\frac{m}{2\pi k_B T}} \exp\left(-\frac{mv^2}{2k_B T}\right). \quad (3.4)$$

From DB96, the Doppler broadening parameter is defined by $b = \text{FWHM}/(4 \ln 2)^{1/2}$, where FWHM is the full-width half maximum of $P_v(v)$ and is related to the standard deviation, σ , of $P_v(v)$ by $\text{FWHM} = 2\sqrt{2 \ln 2} \sigma$. This yields

$$b_{\text{D,T}} = \sqrt{\frac{2k_B T}{m_{\text{H}_2}}}, \quad (3.5)$$

where k_B is the Boltzmann constant and m_{H_2} is the mass of an H_2 molecule. The temperature T in equation (3.5) is the H_2 -weighted mean temperature T_{eff} of the

gas

$$\begin{aligned}
 T_{\text{eff}} &= \frac{\sum_{i=1}^{r_i \leq R_{200}} n_i \chi_{\text{H}_2, i} T_i V_i}{\sum_{i=1}^{r_i \leq R_{200}} n_i \chi_{\text{H}_2, i} V_i} \\
 &= \frac{\sum_{i=1}^{r_i \leq R_{200}} n_i \chi_{\text{H}_2, i} T_i \frac{4\pi}{3} (r_i^3 - r_{i-1}^3)}{\sum_{i=1}^{r_i \leq R_{200}} n_i \chi_{\text{H}_2, i} \frac{4\pi}{3} (r_i^3 - r_{i-1}^3)}, \tag{3.6}
 \end{aligned}$$

where T_i is the temperature and V_i is the volume in cell i .

The bulk motion of the gas can also affect whether or not a fluid element is shifted into the line of an outgoing LW photon. We account for this in an approximate way with an additional component to the Doppler broadening parameter,

$$b_{\text{D}, \text{T}, \text{v}} = \sqrt{b_{\text{D}, \text{T}}^2 + b_{\text{D}, \text{v}}^2} = \sqrt{\frac{2k_B T}{m_{\text{H}_2}} + 2\sigma_{\text{mt}}^2}, \tag{3.7}$$

where σ_{mt} is taken to be the microturbulent velocity dispersion, which is approximated as the H_2 -weighted velocity dispersion of the halo in analogy to T_{eff} . We then calculate $f_{\text{shield}}^{\text{H}_2}$ with the fitting function in WH11

$$\begin{aligned}
 f_{\text{shield}}^{\text{H}_2}(N_{\text{H}_2}, b_{\text{D}, \text{T}, \text{v}}) &= \frac{0.9379}{(1 + x/D_{\text{H}_2})^{1.879}} \\
 &+ \frac{0.03465}{(1 + x)^{0.473}} \times \exp[-2.293 \times 10^{-4} \sqrt{1 + x}], \tag{3.8}
 \end{aligned}$$

where $x = N_{\text{H}_2}/(8.465 \times 10^{13} \text{cm}^{-2})$ and $D_{\text{H}_2} = b_{\text{D}, \text{T}, \text{v}}/(10^5 \text{cm s}^{-1})$.

We construct $f_{\text{shield}}^{\text{H}}$ from the fitting function in WH11,

$$f_{\text{shield}}^{\text{H}}(N_{\text{H}}) = \frac{1}{(1 + x_{\text{H}})^{1.62}} \exp(-0.149 x_{\text{H}}), \tag{3.9}$$

where $x_{\text{H}} = N_{\text{H}}/(2.85 \times 10^{23} \text{cm}^{-2})$. Escape fractions in the near-field limit are calculated for each profile of the HII region and surrounding halo as they evolve throughout the run, typically 1000 times during the simulation.

FAR-FIELD LIMIT

In the far-field approximation, we begin by calculating the dimensionless equivalent width of all the LW lines, \widetilde{W}' . It cannot exceed the total dimensionless width of the LW range 11.2 – 13.6 eV: $W'_{\text{max}} = \ln(1110/912) \simeq 0.2$. The escape fraction in the far-field limit is then one minus the fraction of these two quantities, $f_{\text{esc}} = 1 - \widetilde{W}'/W'_{\text{max}}$.

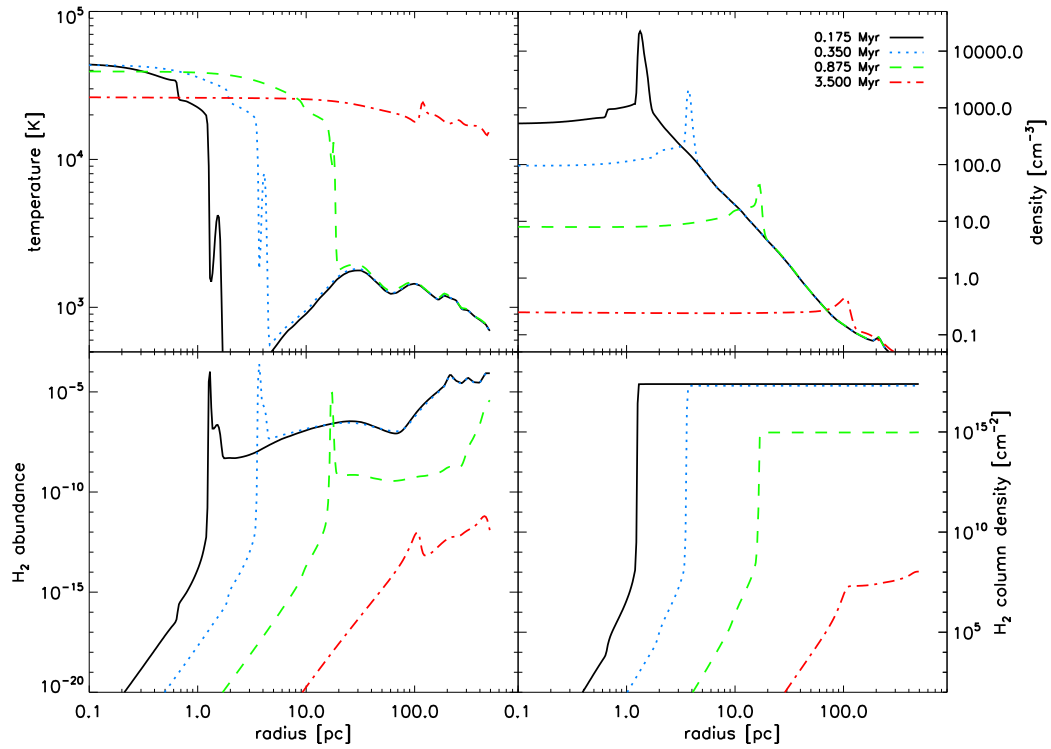


Figure 3.2.2: Evolution of the I-front of the $60 M_{\odot}$ star in halo 1. The times are 0.175 Myr (black solid line), 0.35 Myr (blue dotted line), 0.875 Myr (green dashed line) and 3.5 Myr, the end of the life of the star (red dash-dotted line).

The transition from a lower level l (with vibrational quantum number v and rotational quantum number J) to an upper level u (with v' and J' , respectively) depends on the photoabsorption cross-section σ_{ul} and column density N_l . In a first step, we show the calculation for a single line. Later, we combine them to obtain the total equivalent width. We follow the notation of DB96. The equivalent width of the l to u transition can be written as

$$W_{ul}(N_l) = \int [1 - \exp(-N_l\sigma_{ul})]d\nu. \quad (3.10)$$

If $N_l\sigma_{ul} \ll 1$ we can treat the line width in the weak-line limit, in which $\exp(-N_l\sigma_{ul}) \simeq 1 - N_l\sigma_{ul}$. The photodissociation cross section can also be written in terms of the cross section at line center, $\sigma_{ul}(\nu_0)$, and a frequency dependent line profile function that is normalized to one. Therefore, we have

$$W_{ul,w}(N_l) \simeq N_l\sigma_{ul}(\nu_0). \quad (3.11)$$

The shape of the equivalent width needs to be accounted for in the general case. Two processes determine the shape, Lorentz and Doppler broadening.

Lorentz broadening, also known as natural broadening, is intrinsic to the line and is a consequence of the Uncertainty Principle: a quantum state with a lifetime Δt has an uncertainty associated with its energy ΔE such that $\Delta E\Delta t \geq \hbar/2$. Consequently, radiative transitions to or from this state do not have a precise energy but instead occur with a range of energies with a distribution with a width $\sim \Delta E$. Doppler broadening, also known as thermal broadening, is a consequence of the thermal motion of molecules and atoms. The Doppler shifts associated with this motion again lead to a spread in the frequency of the transition in the laboratory frame. If the gas particles have a Maxwell-Boltzmann velocity distribution, the line profile is a simple Gaussian when Doppler broadening dominates.

Doppler broadening usually dominates near the center of the line ν_0 . However, the Doppler line profile function falls off exponentially away from the line center while the Lorentz profile falls off only as $(\nu - \nu_0)^{-2}$. Lorentz broadening therefore always dominates far enough from the centre of the line. Lorentz broadening can often be ignored far from the centre of the line because the line is so weak there that the optical depth due to that region of the line profile is $\ll 1$. However, if N_l is very large this may no longer be true and we need to account for both Lorentz and Doppler broadening.

When both effects are important, the line profile becomes a convolution of the Lorentz and Doppler profiles known as the Voigt profile. Instead of calculating the Voigt profile directly, we follow the approach of [Rodgers and Williams \(1974\)](#), hereafter RW74) and approximate the equivalent width of a single line to be

$$W_{ul} = [W_{ul,L}^2 + W_{ul,D}^2 - (W_{ul,L} * W_{ul,D} / W_{ul,W})^2]^{1/2} \quad (3.12)$$

(equation 3 of RW74). Here, W_L is the equivalent width of the line, assuming only Lorentz broadening, W_D is the equivalent width for only the Doppler effect taken into account, while W_W is the equivalent width in the weak line limit (equation 10).

We use the approximation in RW74 to calculate W_D ,

$$W_D = \Delta\nu_D D(z), \quad (3.13)$$

where $\Delta\nu_D = b_{D,T,v}\nu_0/c$ includes the Doppler broadening parameter $b_{D,T,v}$, as defined in Equation (6). The function D is a seventh-order polynomial given in the Appendix of RW74 and $z = \sigma_{ul}(\nu_0)N_l/(\Delta\nu_D\pi^{1/2})$.

We take the expression for W_L given in [Belafhal \(2000\)](#), which is more accurate than the one from RW74,

$$W_L = 2\pi\Delta\nu_L L(z), \quad (3.14)$$

where $\Delta\nu_L = \Gamma/2$ is the Lorentz half-width of the line with the total de-excitation rate Γ , $z = \sigma_{ul}(\nu_0)N_l/(2\pi\Delta\nu_L)$, and L is the Ladenburg-Reiche function used by [Belafhal \(2000\)](#). To combine the individual lines we first find their dimensionless equivalent widths. As the width of the line is small compared to its frequency, it can be written as

$$W'_{ul} = \frac{W_{ul}}{\nu_0}. \quad (3.15)$$

We assume an ortho-to-para ratio of 3:1 for molecular hydrogen, so $N_{\text{ortho}} = 0.75 \times N_{\text{H}_2}$ and $N_{\text{para}} = 0.25 \times N_{\text{H}_2}$. Applying the transition rules, only one upper rotational level can be reached: $J' = 1$. We further limit our calculations to transition energies below the ionization limit of hydrogen, $E \geq [13.6]eV$, because we assume that any photon with $E \geq [13.6]eV$ ionizes a hydrogen atom.

For each transition, we take the molecular data required to compute the dimensionless equivalent width – the oscillator strength and frequency of the transition, and the total radiative de-excitation rate of the excited state – from the papers by [Abgrall and Roueff \(1989\)](#) and [Abgrall et al. \(1992\)](#).

In the case of no line overlap, the total dimensionless equivalent width can be calculated by a sum over all individual lines,

$$W' = \sum_l \sum_u W'_{ul}. \quad (3.16)$$

If there is overlap we account for it in the same way as DB96. To ensure that the total dimensionless equivalent width of our set of lines satisfies this constraint, we write it as

$$\tilde{W}' = W'_{\max} [1 - \exp(-W'/W'_{\max})]. \quad (3.17)$$

Therefore, since $f_{\text{esc}} = 1 - f_{\text{abs}} = 1 - \tilde{W}'/W'_{\max}$, we have

$$f_{\text{esc}} = \exp(-W'/W'_{\max}). \quad (3.18)$$

As in the near-field case, we consider shielding by neutral hydrogen in addition to self shielding by H_2 . All Lyman lines starting from $\text{Ly}\beta$ fall into the LW range and can therefore reduce the LW escape fraction. Like WH11, we consider Lyman transitions ($l = 1$) from $u = 2$ up to $u = 10$. We calculate W'_{H} with data from [Wise and Fuhr \(2009\)](#) in analogy to W' . The two dimensionless equivalent widths are then summed and the total escape fraction becomes

$$f_{\text{esc,H}_2\&\text{H}} = \exp\left(-\frac{W' + W'_{\text{H}}}{W'_{\max}}\right). \quad (3.19)$$

3.3 RESULTS

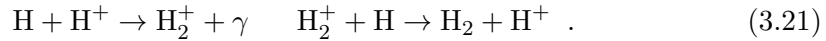
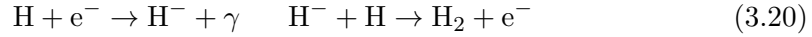
We first examine the evolution of the I-front and H II region in a halo and then present our results for f_{esc} in the near-field and far-field limits.

3.3.1 EVOLUTION OF THE H II REGION

The evolution of the I-front and H II region depends on the mass of the star and its host halo. At early times the I-front propagates very rapidly, leaving the gas behind it essentially undisturbed (an R-type front). It then decelerates as it approaches the Strömngren radius of the halo. If the halo is massive and the star is not very luminous the I-front stalls at the Strömngren radius and advances no further. If the star is bright, the front may briefly loiter at the Strömngren radius, but it then resumes its expansion driving a shock in front of it (a D-type front). As it descends the steep

density gradient of the halo, the front can break through the shell and revert to R-type, flash ionizing the halo out to radii of 2.5–5 kpc. The I-front may be preceded by an H_2 photodissociation front driven by LW photons (see e.g. studies by [Ricotti et al. 2001, 2002](#)). This second radiation front is often at first confined to the halo because the rate of H_2 formation in the photodissociation region (PDR) exceeds the rate at which LW photons are emitted by the star.

The hard UV spectra of hot high-mass Pop III stars increases the thickness of the I-front because of the larger range of mean free paths of the ionizing photons in the neutral gas. The outer layers of the front can have temperatures of just a few thousand K and free electron fractions of $\sim 10\%$, ideal conditions for the formation of H_2 in the gas phase via the H^- and H_2^+ channels:



An H_2 layer may thus form in the outer shell of the front, with a molecular mass that greatly exceeds the one in the surrounding PDR. In the HII region itself nearly all H_2 is collisionally dissociated by free electrons. Beyond the I-front much of the H_2 in the halo that existed before the star was born may have been destroyed by the PDR. The total H_2 column density in the halo may therefore be dominated by the H_2 sandwiched between the I-front and the shell of gas plowed up by the front after becoming D-type. Since this thin layer may govern LW escape from the halo, it is essential that it is well resolved in our numerical simulations.

We show in [Figure 3.2.2](#) profiles for the I-front, HII region and PDR for the $60 M_\odot$ star in halo 1 at 0.175, 0.35, 0.875 and 3.5 Myr, the lifetime of the star. At 0.175 Myr it is evident from the temperature plot that the I-front has become D-type: an ionized region with a temperature of 4.5×10^4 K extends out to the position of the front at 1.2 pc, after which the temperature drops to 1400 K, rises to 4000 K at 1.5 pc and then falls to below 500 K at 1.7 pc. The 4000 K gas is the plowed up, shocked material. The temperature falls to 1400 K in the region between the fully ionized gas and the dense shell because of H_2 cooling in the outer layers of the I-front. The shock has fully detached from the front and is at ~ 1.7 pc. The density spike at 1.3 pc marks the center of the plowed up shell, which has ten times the density of the ambient halo. H_2 mass fractions reach 10^{-4} between the I-front and the dense shell

and then fall to 10^{-7} just beyond it, marking the beginning of the PDR. The latter extends out to ~ 100 pc, beyond which the H_2 mass fractions gradually rise to $\sim 10^{-4}$, those that were in the halo prior to the birth of the star. Note the extremely low H_2 mass fractions within the H II region that are due to collisional dissociation.

At 0.35 Myr, the I-front has advanced to ~ 4 pc, but remains D-type and continues to move behind the shock front. The structures of the PDR beyond the I-front are virtually identical to the ones at 0.175 Myr, as shown in the H_2 mass fractions. Note that at each stage the rise of the H_2 column density to its peak value coincides with the position of the H_2 layer just ahead of the front. The thin layer in which most of the H_2 forms has a peak H_2 abundance of over 10^{-4} , slightly higher than at 0.175 Myr. It is also somewhat wider, but the peak density in the layer is roughly an order of magnitude lower than at 0.175 Myr. Together, these factors lead to the H_2 column density at 0.35 Myr being little changed from its value at 0.175 Myr.

The H II region remains D-type until about 0.875 Myr, when the dense shell is barely visible in the temperature profile at ~ 20 pc. The peak H_2 abundance in the shell at this point has fallen to 10^{-5} because of the smaller densities there, resulting in a substantially lower H_2 column density. As the halo becomes more and more ionized, more LW photons pass through the I-front and decrease the H_2 abundance in the PDR. This also increases the radius of the PDR, from 100 pc at 0.375 Myr to 250 pc at 0.875 Myr. The peak density behind the shock front has fallen to $\sim 75 \text{ cm}^{-3}$, but this is still 10 times higher than the density immediately ahead of the shock.

Later on, the I-front becomes R-type, overruns the PDR and breaks out of the halo. As the density of the H_2 layer falls with the expansion of the I-front, the H_2 column density decreases.

At the end of the lifetime of the star, 3.5 Myr, the whole halo is ionized, while the shock front is still moving outwards. Nearly all molecular hydrogen is destroyed in the H II region due to collisional dissociations, resulting in a very low H_2 column density which is not able to shield against LW radiation.

This case is an example of delayed breakout, in which the star eventually ionizes the halo, but only after a large fraction of its lifetime. In our grid of models some I-fronts loiter at the Strömgren radius until the death of the star. For the $9 M_\odot$ star in the $1.7 \times 10^7 M_\odot$ halo the Strömgren radius is below the grid resolution and the H II region remains hypercompact until the death of the star. In these models the halo is essentially undisturbed by UV radiation from the star.

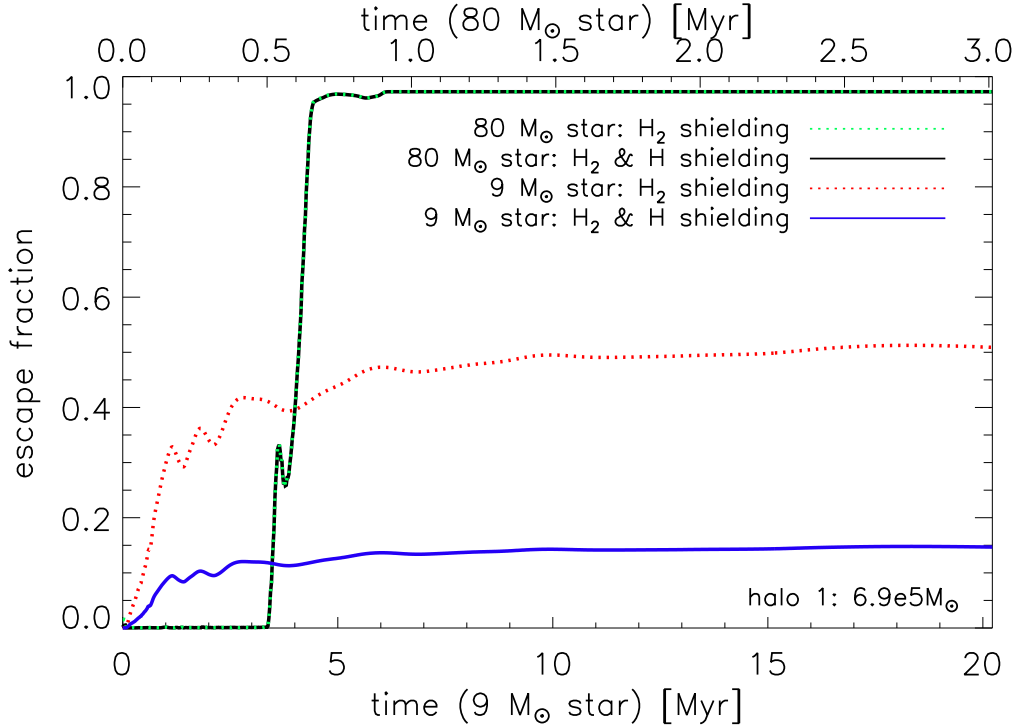


Figure 3.3.1: Smoothed escape fractions for a $9 M_{\odot}$ star (black solid and green dotted lines, overlying) and a $80 M_{\odot}$ star (blue solid and red dotted lines) in halo 1 as a function of time. Escape fractions with shielding by H_2 only (dotted lines) and by H_2 and neutral hydrogen (solid lines) are shown.

3.3.2 LW ESCAPE FRACTIONS IN THE NEAR-FIELD LIMIT

The escape fraction evolves as the $H\text{II}$ region of the star expands in the halo and the H_2 column density and neutral H fraction change. In Figure 3.3.1, we show how f_{esc} evolves over time with H_2 self-shielding alone (dotted lines) and with both H_2 and H shielding (solid lines) for the $9 M_{\odot}$ and $80 M_{\odot}$ stars in halo 1. With the $9 M_{\odot}$ star, the I-front is trapped and ionizing UV photons never break out of the halo. With the $80 M_{\odot}$ star, the I-front breaks out of the halo and fully ionizes it. Here, the escape fraction is essentially zero until the I-front changes to R-type at 0.6 Myr. Before this transition, the H_2 column density is high enough to prevent most LW photons from escaping the halo, due to the dense shell driven by the I-front. After the front breaks through the dense shell and accelerates down the steep density gradient of the halo, the column density of H_2 rapidly decreases, owing to the rapid decrease in the post-shock density. Because the density decreases so rapidly with radius, most

of the H_2 is destroyed by the front well before it reaches the virial radius of the halo at a time ~ 0.9 Myr.

The rapid initial increase in f_{esc} with the $9 M_{\odot}$ star is due to the lower luminosity of the star, which creates less H_2 in the dense shell plowed up by the I-front. The dense shell therefore has a lower H_2 column density and hence traps LW photons less effectively than in the case of the $80 M_{\odot}$ star. However, the smaller UV flux also prevents the I-front from overrunning the entire halo, leading to it remaining trapped for the lifetime of the star. Consequently, the H_2 column density in the post-shock shell varies only slightly over the lifetime of the star, and the LW escape fraction tends towards a roughly constant value. If we account only for H_2 self-shielding, then the LW escape fraction at late times is around 51%. On the other hand, if we also account for absorption in the Lyman series lines of atomic hydrogen, we recover instead an escape fraction of around 15% at late times. We see therefore that shielding due to neutral H is especially important in this case. This is because most of the halo is not ionized, and the presence of atomic hydrogen reduces f_{esc} by more than two thirds compared to the value based on H_2 alone. We conclude that shielding by neutral hydrogen cannot be neglected for stars with $M \sim 10 M_{\odot}$ in cosmological halos.

We list near-field escape fractions that are averaged over the lifetime of the star in Tables 3.3.1 and 3.3.2. Table 3.3.1 shows the values that we obtain if we only account for H_2 self-shielding, while Table 3.3.2 shows the corresponding values for the case where we account for shielding by both H and H_2 . We see that on the whole, we recover similar values in both cases, unless the mass of the star is low, or the mass of the halo is large.

Our time-averaged values for the near-field escape fraction are also plotted for all three halos as a function of stellar mass in Figure 3.3.2. For a given star, f_{esc} falls with increasing halo mass because a smaller fraction of the halo becomes ionized. In halos 1 and 2, f_{esc} increases with stellar mass, because the higher luminosities of the more massive stars ionize more of the halo. None of the stars in our study can ionize halo 3, which is not only the most massive halo but is also the densest (see Figure 3.2.1). All LW photons are also trapped, even for the $120 M_{\odot}$ star. With more massive stars in halo 3, the H II region does expand, but the star dies before the I-front can reach the virial radius.

Note that escape fractions for small stars (the $9 M_{\odot}$ star in halo 1, the $9 M_{\odot}$ and $15 M_{\odot}$ stars in halo 2 and the $25 M_{\odot}$ star in halo 3) can actually be larger than for more massive stars in the same halo. The lower luminosities of these less

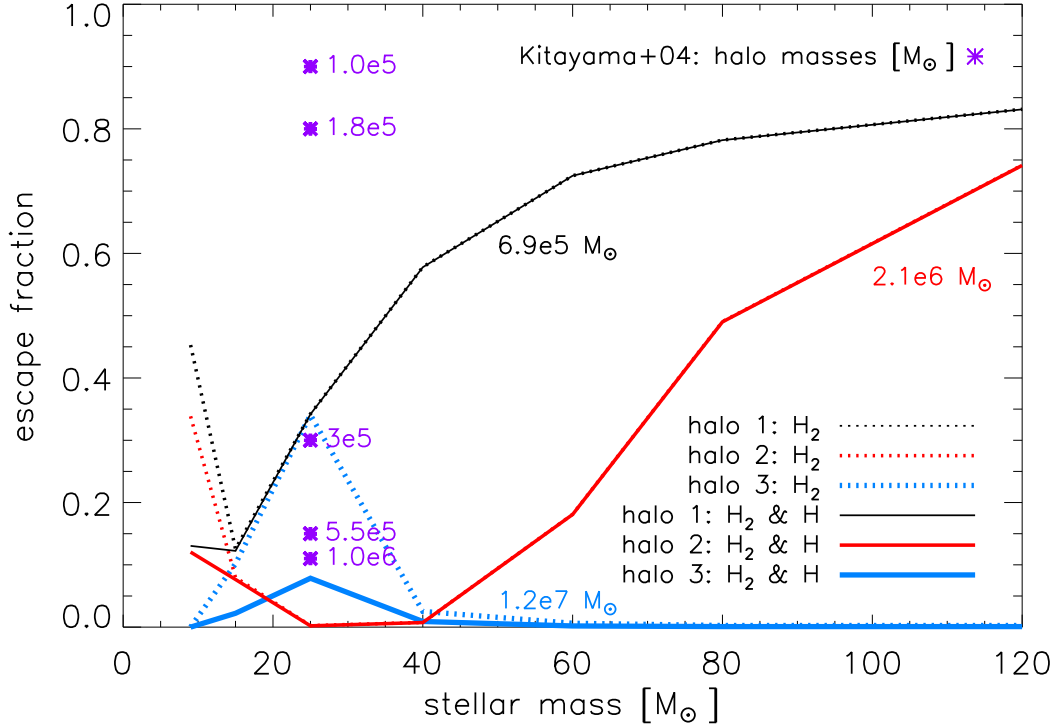


Figure 3.3.2: Time-averaged escape fractions for all our models as a function of stellar mass for halo 1 (black thin line), halo 2 (red normal line), and halo 3 (blue thick line). Escape fractions with just shielding by H_2 (dotted lines) and by H_2 and neutral hydrogen (solid lines) are shown, together with some values from [Kitayama et al. \(2004\)](#) (purple stars).

massive stars produce less H_2 in the dense shell surrounding the HII region so more LW photons can escape the halo. We can compare our numbers with the study by [Kitayama et al. \(2004\)](#). However, we note that they are using an earlier self-shielding function from DB96 and the overlap in parameter space is quite limited. They find the escape fraction for a $25 M_\odot$ star in a $5.5 \times 10^5 M_\odot$ halo to be about half the value for our $6.9 \times 10^5 M_\odot$ halo. As [Kitayama et al. \(2004\)](#) consider their escape fractions to be lower limits, and given the differences in halo structure between our models and theirs, we conclude that the two approaches yield consistent results.

3.3.3 FAR-FIELD LIMIT

As expected, escape fractions in the far-field limit are generally much higher than in the near-field. We show time-averaged escape fractions with self-shielding due to H_2 only for all our runs in [Table 3.3.3](#) and the upper panel of [Figure 3.3.3](#), and for shielding by H_2 and H in [Table 3.3.4](#) and the lower panel of [Figure 3.3.3](#), respectively.

M [M_{\odot}]	9	15	25	40	60	80	120
halo 1	45	13	34	58	72	78	83
halo 2	34	8	< 1	< 1	18	49	74
halo 3	< 1	10	34	3	< 1	< 1	< 1

Table 3.3.1: Near-field escape fractions (in percent) averaged over the lifetime of the stars, accounting only for H_2 self-shielding

M [M_{\odot}]	9	15	25	40	60	80	120
halo 1	13	12	34	58	72	78	83
halo 2	12	8	< 1	< 1	18	49	74
halo 3	< 1	2	8	< 1	< 1	< 1	< 1

Table 3.3.2: Near-field escape fractions (in percent) averaged over the lifetime of the stars, accounting for shielding by both H_2 and H

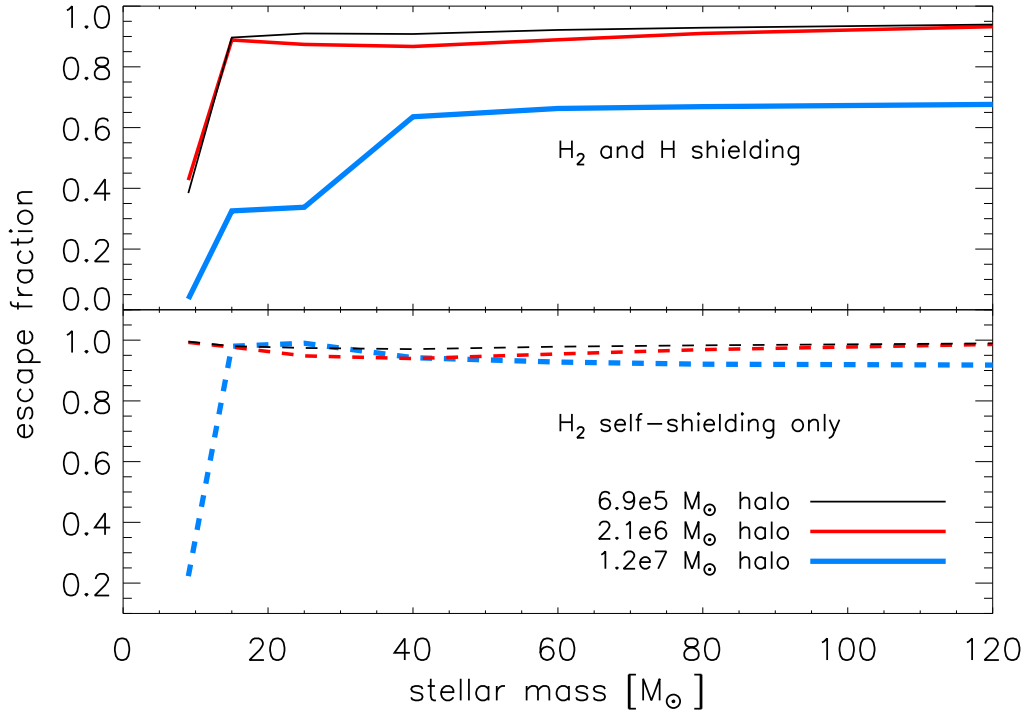


Figure 3.3.3: Time-averaged escape fractions in the far field limit for all the models in our study, plotted as a function of stellar mass (halo 1: black thin line, halo 2: red normal line, halo 3: blue thick line). In the lower panel, escape fractions for self-shielding by H_2 alone are shown (dashed lines). In the upper panel, escape fractions that account for shielding by H and H_2 (solid lines).

M [M_{\odot}]	9	15	25	40	60	80	120
halo 1	99	98	97	97	98	98	99
halo 2	99	98	95	94	95	97	99
halo 3	22	98	99	94	93	92	92

Table 3.3.3: Far-field escape fractions (in percent) averaged over the lifetime of the star, accounting only for H_2 self-shielding.

M [M_{\odot}]	9	15	25	40	60	80	120
halo 1	38	90	91	91	92	93	94
halo 2	43	89	87	87	89	91	93
halo 3	4	33	34	64	66	67	68

Table 3.3.4: Far-field escape fractions averaged over the lifetime of the stars, accounting for shielding by both H_2 and H.

When considering only shielding by H_2 , for halos 1 and 2, the escape fraction is always higher than 90% and nearly all LW photons escape the halo. In halo 3, most of the LW radiation from the $9 M_{\odot}$ star is trapped in the halo, and only a quarter of the photons can escape. The higher mass stars all have larger luminosities so their radiation eventually escapes halo 3.

As in the near-field limit, including shielding by atomic hydrogen reduces the escape fraction. Less than half of the LW photons from the $9 M_{\odot}$ star escape any halo. In particular the escape fraction in halo 3 is only $f_{\text{esc}} \approx 4\%$. LW escape fractions in halos 1 and 2 for more massive stars are above 85%, and they rise slightly with halo mass. In halo 3, the picture is different: for the 9, 15 and $25 M_{\odot}$ stars, the I-front is static and ionizing photons are trapped in the halo. The Strömgren radii of the I-fronts of the 15 and $25 M_{\odot}$ stars are similar, 0.13 pc and 0.14 pc respectively, which explains the step in escape fraction over that mass range. With more massive stars the I-front eventually advances beyond the Strömgren radius, but the star dies before it can reach the virial radius. The final radii of the $H\text{II}$ regions increase only slightly with the mass of the star, because although they are more luminous these stars also have shorter lives. The radii vary from 12 to 20 pc for 40–120 M_{\odot} stars, resulting in escape fractions of 64% to 68%.

3.4 CONCLUSION

We have calculated LW escape fractions for 9–120 M_{\odot} Pop III stars in three different primordial halos ranging in mass from 6.9×10^5 to $1.2 \times 10^7 M_{\odot}$. We have considered

two limiting cases. The near-field limit is relevant for objects close to the halo that do not have a significant velocity relative to it, so that the LW absorption lines in the rest-frame of the object coincide with those in the rest-frame of the halo. In this limit, the escape fraction can be approximated by the product of the self-shielding function of H_2 and the shielding function of H_2 by neutral hydrogen which have been developed by WH11. The far-field limit is valid for objects that are significantly redshifted or blue-shifted with respect to the halo, usually at cosmological distances. In this limit, we can estimate the escape fraction by calculating the ratio of the equivalent width of the LW absorption lines to the width of the entire LW frequency range.

In both limits, we consider self-shielding by molecular hydrogen alone as well as the combined effects of molecular and atomic gas together. We find that it is important to consider both types of shielding.

In the near-field, the escape fraction generally rises with increasing mass of the central star. In the $6.9 \times 10^5 M_\odot$ halo, it grows from about 10% to about 85% and for the $2.1 \times 10^6 M_\odot$ halo to about 75%. None of the stars in our study are bright enough to fully ionize the $1.2 \times 10^7 M_\odot$ halo and escape fractions from this halo are nearly zero in the near-field. For some stars with masses close to $10 M_\odot$, escape fractions can be higher than for slightly more massive stars because their lower luminosities cannot build up as large an H_2 column density, e.g. 12% of the LW photons are able to escape the $2.1 \times 10^6 M_\odot$ halo for a $9 M_\odot$ star, but only 8% for a $15 M_\odot$ star.

In the far-field, the escape fractions are generally higher. Only in the case of the $9 M_\odot$ star do fewer than 50% of its LW photons exit all of our halos. In the most massive halo, this is also true for the 15 and $25 M_\odot$ stars. For higher stellar masses, the escape fraction rises to above 90% for the less massive halos and to above 60% for the $1.2 \times 10^7 M_\odot$ halo.

If shielding by neutral H is neglected, the escape fractions are overpredicted. Therefore, the additional shielding function of neutral hydrogen from WH11 provides an important improvement to the older model from DB96. This is especially severe for stars with masses up to $25 M_\odot$ in the near-field, where shielding by neutral H reduces the escape fraction by as much as a factor of three. In the far-field, less than 50% of the LW radiation from a $9 M_\odot$ star can exit any halo, but if neutral hydrogen shielding is neglected up to 99% can exit the halo. The $1.2 \times 10^7 M_\odot$ halo is not ionized by any of the central stars considered, so its large neutral hydrogen column density plays a major role in shielding, reducing the escape fraction from

about 90% to about 60% for stars with masses of $40 M_{\odot}$ and higher.

Our models assume 1D spherical symmetry. In reality, both ionizing and LW photons can break out of the halo along lines of sight with lower optical depths, so our escape fractions should be taken to be lower limits. We note in particular that shielding by neutral H, which has largely been ignored in studies until now, can play a large role in LW escape fractions, especially those of lower-mass Pop III stars. This latter point is important because of the relative contributions of lower-mass and higher-mass Pop III stars to the LW background. It has recently been found that more realistic stellar spectra that contain a lower-mass Pop III star component may be less efficient at photodissociating H_2 in primordial halos than previously thought (Agarwal and Khochfar, 2015). Shielding by H in the host halos of such lower-mass Pop III stars may reinforce this trend by allowing fewer LW photons to escape into the cosmos.

Finally, we note that star formation in the vicinity of a halo hosting a low-mass Pop III star may be less influenced by the star than by the global LW background because of low escape fractions from the halo in the near field. Conversely, smaller LW escape fractions from low-mass Pop III stars have less of an effect on the LW background on cosmological scales because escape fractions in the far-field limit are generally much larger.

ACKNOWLEDGMENTS

We thank the anonymous referee for a careful review of our paper. We thank Volker Bromm, Andreas Burkert, Andrea Ferrara, Tilman Hartwig and Jan-Pieter Paardekooper for useful discussions. The authors acknowledge support from the European Research Council under the European Community’s Seventh Framework Programme (FP7/2007 - 2013) via the ERC Advanced Grant “STARLIGHT: Formation of the First Stars” (project number 339177). SCOG and RSK also acknowledge support from the Deutsche Forschungsgemeinschaft via SFB 881, “The Milky Way System” (sub-projects B1, B2 and B8) and SPP 1573 , “Physics of the Interstellar Medium” (grant number GL 668/2-1).

4

Lyman-Werner Escape Fractions from the First Galaxies

Distribution of work Anna T. P. Schauer performed all simulations with a version of ZEUS-MP modified by Daniel J. Whalen. She wrote the python routines for always resolving the I-front with high resolution and performed the analysis. The haloes we used in this work are cut out of a cosmological simulation by Muhammad A. Latif, the spectra used here are from Bhaskar Agarwal, Lluís Mas-Ribas, Claes-Erik Rydberg and Erik Zackrisson. The text was mainly written by Anna T. P. Schauer and Simon C. O. Glover, with contributions from the other authors. In detail, Muhammad A. Latif contributed with text to the section describing the host haloes, and Bhaskar Agarwal, Lluís Mas-Ribas, Claes-Erik Rydberg and Erik Zackrisson wrote the paragraphs describing the spectra. All authors contributed with comments and ideas.

The content of this chapter has been published as:

Schauer, A. T. P., Agarwal, B., Glover, S. C. O., Klessen, R. S., Latif, M. A., Mas-Ribas, L., Rydberg, C.-E., Whalen, D. J., and Zackrisson, E.

“Lyman-Werner escape fractions from the first galaxies”.

MNRAS, 467:2288–2300, May 2017a.

doi: 10.1093/mnras/stx264.

Authors Anna T. P. Schauer¹, Bhaskar Agarwal^{1,2}, Simon C. O. Glover¹, Ralf S. Klessen¹, Muhammad A. Latif^{3,4}, Lluís Mas-Ribas⁵, Claes-Erik Rydberg¹, Daniel J. Whalen⁶, Erik Zackrisson⁷

¹Universität Heidelberg, Zentrum für Astronomie, Institut für Theoretische Astrophysik, Albert-Ueberle-Str. 2, 69120 Heidelberg, Germany

²Department of Astronomy, 52 Hillhouse Avenue, Steinbach Hall, Yale University, New Haven, CT 06511, USA

³Sorbonne Universités, UPMC Univ Paris 06 et CNRS, UMR 7095, Institut d’Astrophysique de Paris, 98 bis bd Arago, 75014 Paris, France

⁴Department of Physics, COMSATS Institute of Information Technology, Park Road, Islamabad, Pakistan

⁵Institute of Theoretical Astrophysics, University of Oslo, P. O. Box 1029 Blindern, NO 03015 Oslo, Norway

⁶Institute of Cosmology and Gravitation, Portsmouth University, Dennis Sciana Building, Portsmouth PO1 3FX, UK

⁷Department of Physics and Astronomy, Uppsala University, Box 515, SE-751 20 Uppsala, Sweden

Abstract Direct collapse black holes forming in pristine, atomically-cooling haloes at $z \approx 10 - 20$ may act as the seeds of supermassive black holes (BH) at high redshifts. In order to create a massive BH seed, the host halo needs to be prevented from forming stars. H_2 therefore needs to be irradiated by a large flux of Lyman-Werner (LW) UV photons in order to suppress H_2 cooling. A key uncertainty in this scenario is the escape fraction of LW radiation from first galaxies, the dominant source of UV photons at this epoch. To better constrain this escape fraction, we have performed radiation-hydrodynamical simulations of the growth of H II regions and their associated photodissociation regions in the first galaxies using the ZEUS-MP code. We find that the LW escape fraction crucially depends on the propagation of the ionisation front (I-front). For an R-type I-front overrunning the halo, the LW escape fraction is always larger than 95%. If the halo recombines later from the outside-in, due to a softened and weakened spectrum, the

LW escape fraction in the rest-frame of the halo (the near-field) drops to zero. A detailed and careful analysis is required to analyse slowly moving, D-type I-fronts, where the escape fraction depends on the microphysics and can be as small as 3% in the near-field and 61% in the far-field or as large as 100% in both the near-field and the far-field.

Keywords early universe – cosmic background radiation – dark ages, reionisation, first stars – stars: Population III – radiation: dynamics.

4.1 INTRODUCTION

In recent years, several highly luminous quasars have been observed, for example a $1.2 \times 10^{10} M_{\odot}$ BH at redshift $z \approx 6.3$ (Wu et al., 2015) and a $9 \times 10^9 M_{\odot}$ BH at redshift $z \approx 7.1$ (Mortlock et al., 2011). These objects provide a stern challenge for current structure formation models as it is not clear yet how BHs can assemble so much mass during the first billion years of the Universe (see a review by Volonteri, 2010).

In addition, the luminous Ly α emitter CR7 (Sobral et al., 2015), recently discovered at $z = 6.6$, is found to have a unique structure. A deep HST image shows it consists of three clumps, separated by ≈ 5 kpc. The most luminous clump does not show any metal lines, but the two smaller, accompanying clumps do. CR7 is not only very luminous, but also shows a strong He II 1640 Å line and therefore a hard spectrum. Sobral et al. (2015) interpreted this object as a chemically pristine protogalaxy forming a large cluster of Population III (Pop III) stars, but other authors have argued that it is more likely to be a massive accreting BH (Hartwig et al. 2015c; Agarwal et al. 2015; Pallottini et al. 2015; Dijkstra et al. 2016, but see Bowler et al. 2016).

Explaining these observations and understanding how supermassive black holes (SMBHs) form and grow at high redshift is a topic of active research. On the one hand, SMBH seeds have been suggested to be remnants from Pop III stars (Madau and Rees, 2001; Fryer et al., 2001; Inayoshi et al., 2016) with relatively low masses ($10^{2-3} M_{\odot}$) that accrete close to the Eddington limit for large fractions of their lifetime. On the other hand, very massive seeds ($10^{4-6} M_{\odot}$) could be created by the direct collapse of primordial gas (Loeb and Rasio 1994b; Eisenstein and Loeb 1995; Koushiappas et al. 2004; Begelman et al. 2006; Lodato and Natarajan 2006; Latif

et al. 2013, see Volonteri 2010 for a review).

A necessary condition for the direct collapse scenario is a very massive and hot ($T > 10^4$ K) halo in which gas contracts quasi-isothermally without cooling and fragmenting. The central clump, to which the halo compresses, contains $\geq 10\%$ of the total gas mass (Bromm and Loeb, 2003). The fate of this clump is not entirely clear: it may form a massive BH directly, or may form a supermassive star that subsequently collapses to form a BH. To keep the collapsed gas at high temperatures, the gas must be metal-free (Omukai et al., 2008) and molecular hydrogen has to be prevented from forming or must be destroyed in that system, as it would otherwise cool a pristine halo down to temperatures of 150 K and encourage fragmentation (Bromm and Loeb, 2003). For this, a critical level of external LW flux is crucial (e.g. Omukai, 2001; Shang et al., 2010; Wolcott-Green et al., 2011; Agarwal et al., 2012).

Current work (Smidt, Whalen & Johnson, in prep.) favours the direct collapse scenario (but see Alexander and Natarajan 2014). Unlike BH seeds originating from Pop III stars, direct collapse BH (DCBH) seeds are not born starving (Whalen et al., 2004), but instead retain their fuel supply (Alvarez et al., 2009; Park and Ricotti, 2011). Lower-mass BH seeds are often kicked out of their host halo (Whalen and Fryer, 2012). As the metal-free clump of CR7 is accompanied by two other clumps, the question arises whether this is an observed formation place of such a direct collapse BH.

With this study, we impose additional constraints to the DCBH seed formation scenario from simulations (see Dijkstra et al. 2014 who show that the number density of DCBH seeds is highly dependent on the LW escape fraction). The questions we address in this work are: How much LW radiation can actually escape an atomically cooling halo and contribute to the LW background? Is shielding by neutral hydrogen an important mechanism to prevent the built up of the LW background?

We have recently performed a study on LW escape fractions from minihaloes (Schauer et al. 2015, from here on S15; see also Kitayama et al. 2004), finding the escape fraction varying with halo- and stellar mass from 0 to 95%. We adopted two limiting cases: the near-field and the far-field. In the near-field case, we examine what would be seen by an observer in the rest-frame of the host halo. This is a good approximation for when the relative velocity is smaller than the typical width of the LW lines. In the far-field case, we consider an observer who is significantly Doppler shifted with respect to the halo, either due to a large peculiar velocity or simply due to the Hubble flow. This is the relevant case if we are interested in the

global build-up of the LW background.

In this new study, we use our existing framework presented in S15 but focus on more massive haloes ($10^7 - 10^8 M_{\odot}$), typical hosts of the first galaxies. Here, instead of single stars, we focus on radiation from stellar clusters with time-varying spectral energy distributions (SEDs). We consider several different star formation efficiencies (SFEs) and stellar cluster masses, meant to be descriptive of the first galaxies at $z \approx 10$.

Our paper is structured as follows. In Section 2, we briefly summarize the semi-analytic methods described in S15 and introduce our numerical simulations. Details of our parameter space, including the choice of haloes, SEDs and SFEs are described in Section 3. We present our results in Section 4, where we show the dependence of the LW escape fractions for all halo, SED and SFE combinations over time in both near- and far-field. In addition, we provide tabulated results with values averaged over the lifetime of stellar populations. Finally, we discuss our findings and conclude in Section 5.

4.2 METHOD

In this section, we describe the methods used to calculate the LW escape fractions in the near- and far-field limits. The influence of radiation from a central stellar cluster on the gas in a surrounding protogalaxy is modelled in 1D using the ZEUS-MP hydrodynamical code (Section 2.1). The simulation results are then post-processed to derive the LW escape fraction (Section 2.2).

4.2.1 ZEUS-MP

Our simulations are run with the radiation-hydrodynamics code ZEUS-MP (Whalen and Norman, 2006). A full description of the code can be found in more detail in S15. Here, we only give a short overview of the most important features.

The version of ZEUS-MP used in this study couples photon-conserving ionising UV transport self consistently to non-equilibrium primordial chemistry and hydrodynamics to model the growth of cosmological ionisation fronts (I-fronts; Whalen and Norman, 2006). We include a network of nine chemical species (H, H^+ , He, He^+ , He^{2+} , H^- , H_2^+ , H_2 and e^-). Heating and cooling processes like photoionisation, collisional ionisation, excitation and recombination, inverse Compton scattering from the CMB, bremsstrahlung emission and H_2 cooling mostly following the implementation in Anninos et al. (1997). Details of the radiative reactions can be found in

Table 1 of [Whalen and Norman \(2008a\)](#).

The spectra are tabulated as a function of time, in 120 energy bins with 40 uniform bins from 0.755 to 13.6 eV and 80 uniform logarithmically spaced bins from 13.6 eV to 90.0 eV. Since single stars were analysed in S15, we used SEDs that were constant in time. However, in this work as we are focusing on stellar populations, we consider time-varying SEDs as described in Section 3.2.

For the simulation, we assume spherical symmetry. The volume is divided into 1000 radial cells, reaching out to about twice the virial radius. We use a logarithmically spaced grid, allowing us to have high resolution within the inner regions of the halo without compromising the running time. For 8 out of a total of 30 simulations, we additionally refine a 20 pc region around the I-front with 20000 cells to achieve numerical convergence. For all setups, we run comparison simulations with half the number of cells. In all cases, the results from the comparison simulations differ by less than 1% from the original simulations, demonstrating that our results have converged numerically.

4.2.2 SEMI-ANALYTICAL POST-PROCESSING

After the simulations have run, we calculate escape fractions of LW photons in two limiting cases, the near-field (Section 2.2.1) and the far-field (Section 2.2.2). For a detailed discussion of these two limits, we refer the reader to S15. We summarize the calculations in the sections below.

NEAR-FIELD

The near-field limit applies in the vicinity of the halo and is the escape fraction that would be measured by an observer who is at rest with respect to the halo, or moving with only a low velocity relative to it. In this limit, H_2 within the halo can potentially provide effective self-shielding of the LW lines.

[Draine and Bertoldi \(1996\)](#) and [Wolcott-Green and Haiman \(2011, hereafter WH11\)](#), have calculated the effects of H_2 self-shielding in the low density and LTE limits, respectively. They provide simple fitting functions describing the shielding as a function of H_2 column density and temperature. LW photons that do not dissociate H_2 molecules or are not absorbed and re-emitted as lower-energy photons, can escape the halo. For high column densities, H_2 can shield itself against LW radiation, or can be shielded by H. We can therefore equate the escape fraction to the shielding fraction of molecular, or molecular and neutral hydrogen.

For the optically thick case ($N_{\text{H}_2} > 10^{13} \text{ cm}^{-2}$), we use the shielding functions from WH11, which depend on the column density N_{H_2} and, via the Doppler width, on temperature and velocity dispersion of the gas in the halo. We consider two cases: one in which only H_2 contributes, and another where we additionally account for shielding from neutral hydrogen. In the H_2 -only case, we use the shielding functions given in Equation (8) of WH11. When we account for shielding from atomic hydrogen, we additionally use equations (11) and (12) from the same paper. For small column densities ($N_{\text{H}_2} < 10^{13} \text{ cm}^{-2}$), we set the escape fraction to 1.

FAR-FIELD

The far-field limit corresponds to the escape fraction that would be measured by an observer located far away from the halo, moving with a large peculiar velocity or Hubble flow velocity with respect to it. In this limit, the LW lines in the restframe of the observer are Doppler shifted and do not coincide with the LW lines in the halo.

To calculate the escape fraction in this limit, we choose the LW range 11.2 – 13.6 eV (corresponding to a wavelength range of 912 – 1110 Å) and calculate what fraction of the light in this range will be absorbed by H_2 or H in the halo. If we denote this fraction as f_{abs} , then the far-field escape fraction is simply $f_{\text{esc}} = 1 - f_{\text{abs}}$.

To calculate f_{esc} , we first compute the dimensionless equivalent width of the full set of accessible LW lines. To do this, we follow [Rodgers and Williams \(1974\)](#) and calculate the equivalent width of every line, accounting for both Lorentz broadening and Doppler broadening.

We then sum the equivalent widths of the individual lines and add to them the dimensionless equivalent width of all Lyman series transitions of atomic hydrogen that lie within the energy range of interest, including transitions up to $n = 10$. [Abgrall and Roueff \(1989\)](#) and [Abgrall et al. \(1992\)](#) provide data on the total radiative de-excitation rates of the excited states, oscillator strengths and transition frequencies of molecular hydrogen. [Wise and Fuhr \(2009\)](#) give simulated data for atomic hydrogen. In a final step, we combine the dimensionless equivalent widths and follow the prescription in [Draine and Bertoldi \(1996\)](#), and divide by the total width of the LW band. This yields f_{abs} , from which f_{esc} follows trivially.

M_{\min} [M_{\odot}]	M_{\max} [M_{\odot}]	runtime [Myr]	shape
50	500	3.6	Salpeter
9	500	20.2	flat
1	500	20.2	log-normal
0.1	100	20.2	Kroupa
0.1	100	20.2	Kroupa + nebula

Table 4.3.1: Summary of all spectral energy distributions used in this study.

4.3 PARAMETER SPACE

In this section, we present our parameter space. We consider two haloes with masses of 5.6×10^7 (Halo A) and $4 \times 10^8 M_{\odot}$ (Halo B), three SFEs and five SEDs that evolve over time for a given total stellar mass in the halo. The haloes in our study are taken from cosmological simulations by [Latif and Volonteri \(2015\)](#).

4.3.1 HALOES

We perform our simulations with data from cosmological simulations from [Latif and Volonteri \(2015\)](#). All three dimensional quantities are mapped onto one dimensional radial profiles. In Halo A, we smooth out a region at radius ≈ 20 pc, where a substructure is falling into the halo. In our one dimensional picture, this provides a more physical result. In [Figure 4.3.1](#), we show the temperature, density and velocity profiles as well as the initial H_2 abundance. Both haloes follow a similar density profile, but Halo A shows a higher abundance of molecular hydrogen and therefore lower temperatures in the centre. Both haloes are selected at redshift $z = 10$ and assumed to be metal free. The virial radii of the objects are 1.3 and 4.3 physical kpc, respectively.

4.3.2 SPECTRAL ENERGY DISTRIBUTION

We study SEDs derived from direct sums of individual Pop III stars and from spectral synthesis models of Pop III and Pop III / Pop II stellar populations calculated with the Yggdrasil and Starburst99 codes. As the IMF of first stars is still very uncertain ([Clark et al., 2008](#); [Stacy et al., 2010](#); [Clark et al., 2011](#); [Stacy and Bromm, 2014](#); [Hirano et al., 2014](#); [Stacy et al., 2016](#)), we consider different descriptions that cover the range currently discussed in the literature. A total of 5 initial mass functions (IMFs) for the stars are considered. We use different methods for creating the

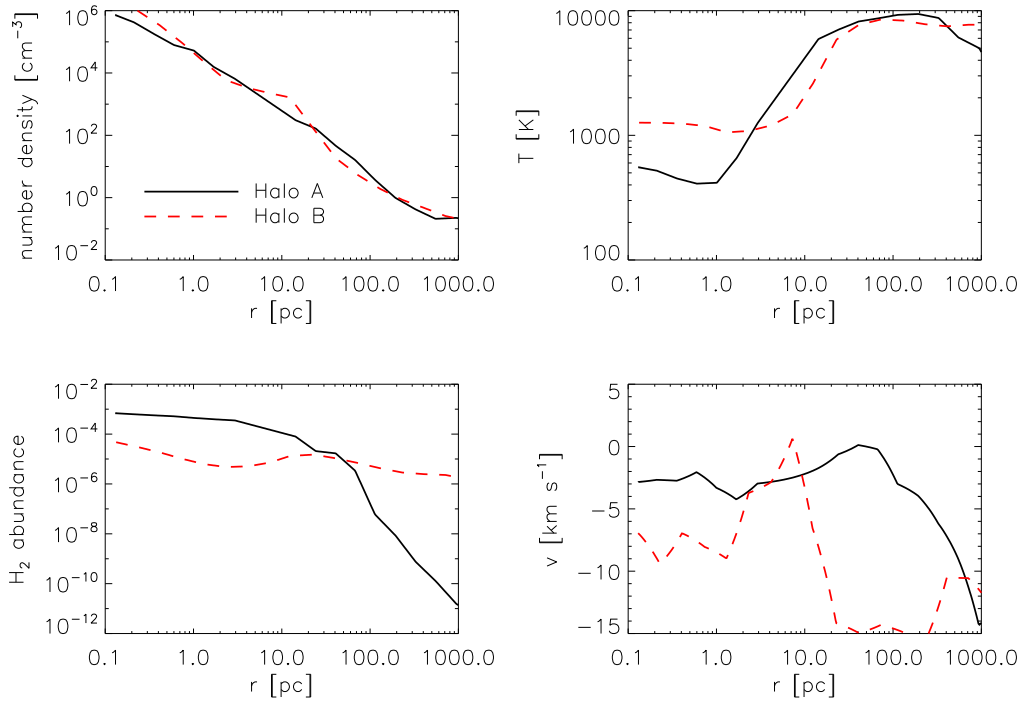


Figure 4.3.1: Number density (upper left panel), temperature (upper right panel), H_2 abundance (lower left panel) and velocity (lower right panel) profiles at startup. Halo A (black solid line) has a total mass of $5.6 \times 10^7 M_\odot$, Halo B (red dashed line) has a total mass of $4 \times 10^8 M_\odot$.

time-dependent SEDs; for a flat IMF ($9 - 500 M_{\odot}$) we use spectra from Pop III stars alone, for a Salpeter slope IMF ($50 - 500 M_{\odot}$) and a lognormal IMF ($1 - 500 M_{\odot}$), we make use of the code Yggdrasil and for Kroupa IMFs ($0.1 - 100 M_{\odot}$), we use a combination of Yggdrasil and Starburst 99; all details can be found in the following subsections. For all SEDs, we assume an instantaneous starburst at the beginning. When the runtime exceeds the lifetime of a star, that star does not explode in a supernova, but is simply removed from the spectrum. We discuss the validity of this assumption in Section 4.3. We show the SED for our fiducial halo-SFE case in Figure 4.3.2 for the first and last moment of the simulation for all five SEDs in terms of dQ/dE , where dQ/dE is the number of photons emitted per second and per eV. Depending on the SED, the simulation runtimes differ. The SED with a Salpeter slope ranging from $50 - 500 M_{\odot}$ lasts for 3.6 Myr, corresponding to the lifetime of the least massive star. For all other SEDs, we adopt a runtime given by the lifetime of a $9 M_{\odot}$ star, 20.2 Myr (Schaerer, 2002). A summary of the SEDs can be seen in Figure 4.3.3, where we show the number of ionising photons and LW photons produced as a function of time.

FLAT SLOPE IMF FROM POP III STELLAR SPECTRA

We create a stellar population from a flat slope IMF within the mass range $9 - 500 M_{\odot}$, using the stellar SEDs and same methodology as in Mas-Ribas et al. (2016); we refer the reader to that work for a detailed description of the calculations. These authors used parameters from Schaerer (2002) and Marigo et al. (2001), and assumed the stars to be metal-free and to reside on the main sequence. We account for the stellar evolution over time by simply removing from the calculation the stars that reach the end of their lives. This SED is considered a radiation source until the least massive star disappears, $t_{\text{end}} = t_{9M_{\odot}} = 20.2$ Myr.

SALPETER AND LOGNORMAL IMF CREATED WITH YGGDRASIL

To generate SEDs for Pop III star clusters with the Yggdrasil spectral synthesis code, we sum the spectra of its constituent stars (Zackrisson et al., 2011; Rydberg et al., 2015). The cluster is assumed to form instantaneously. In summing the spectra of individual stars to obtain an SED we consider two top-heavy IMFs. One is a Salpeter-like extremely top-heavy IMF ranging from $50 - 500 M_{\odot}$ with a typical mass of $100 M_{\odot}$ (Schaerer, 2002). The second is a log-normal distribution IMF with a typical mass of $10 M_{\odot}$ and the standard deviation of the underlying normal

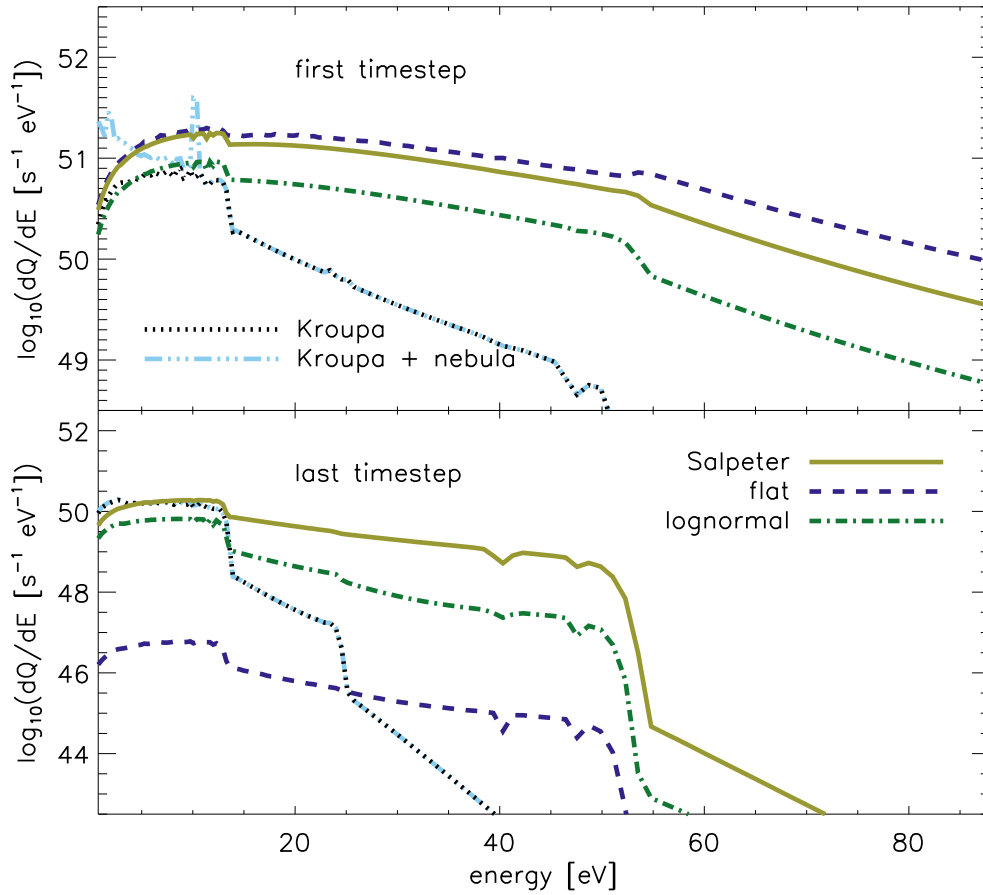


Figure 4.3.2: SEDs for a SFE of 0.5% in Halo A. Different colours and linestyles mark different SEDs: a Salpeter IMF (olive solid line), a flat IMF (dark blue dashed line), a lognormal IMF (green dot-dashed line), a Kroupa IMF without nebular emission (black dotted line) and a Kroupa IMF with nebular emission (light blue dot-dot-dot-dashed line). The upper panel shows the initial spectrum, the lower panel, shows the final spectrum at the cut-off of the simulation at 3.6 and 20.2 Myr, for the Salpeter and other IMFs, respectively.

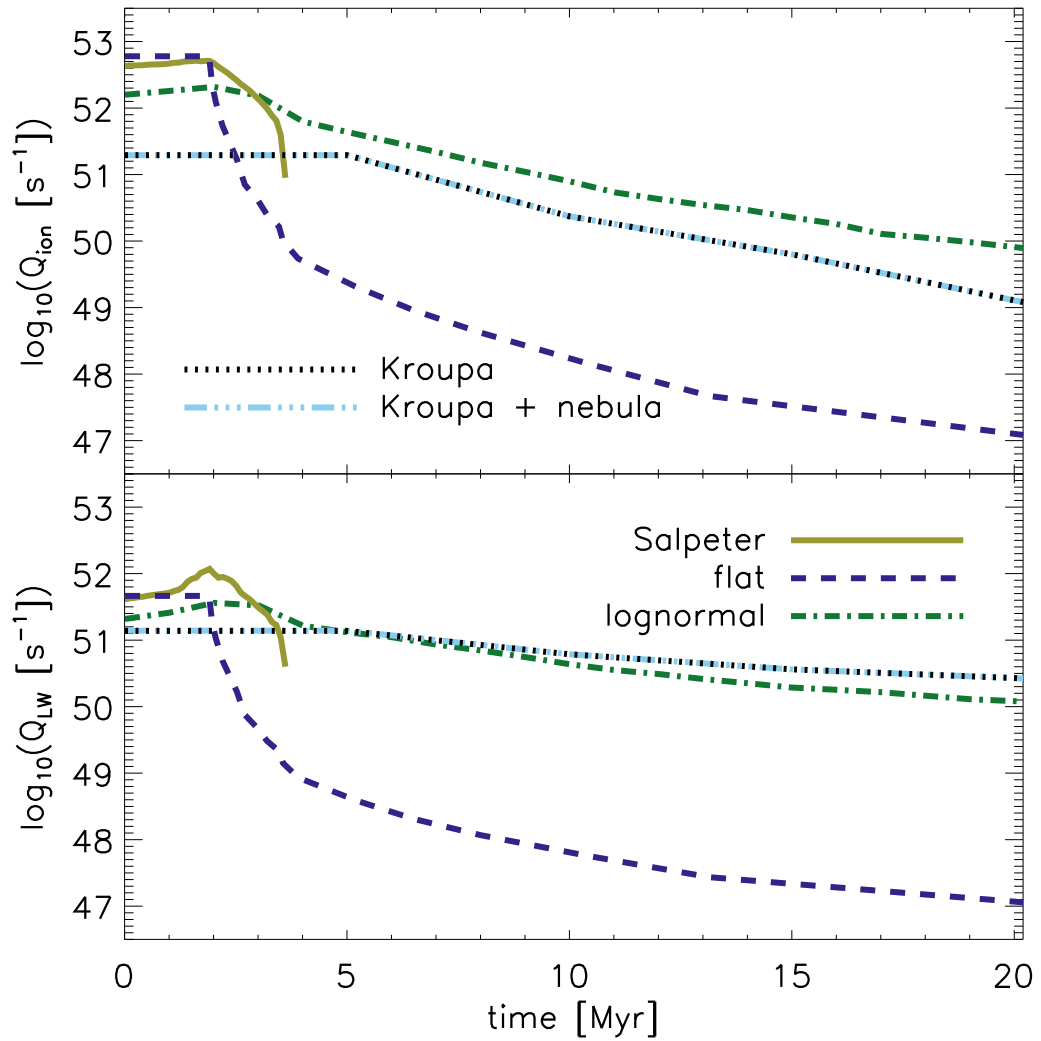


Figure 4.3.3: Ionising (upper panel) and Lyman-Werner (lower panel) photon production rates for all SEDs for a SFE of 0.5% in Halo A. The colour-coding is the same as in Figure 4.3.2.

distribution $\sigma = 1.0$, ranging from $1 M_{\odot}$ to $500 M_{\odot}$ (Raiter et al. 2010, see Tumlinson 2006). Yggdrasil provides spectra for star clusters for ages of up to 3.6 Myr for the extremely top-heavy IMF, which is the lifetime of the longest-lived star in the cluster. The log-normal distribution is turned off after 20.2 Myr.

KROUPA IMF WITH AND WITHOUT NEBULAR EMISSION CREATED WITH YGGDRASIL / STARBURST99

The purely stellar SEDs are based on synthetic spectra from Raiter et al. (2010) for absolute metallicities $Z = 10^{-7}$ and $Z = 10^{-5}$ and Starburst99 (Leitherer et al., 1999) with Geneva high mass-loss tracks in the case of $Z = 0.001, 0.004, 0.008$ and 0.020 . Nebular emission has been added using the Cloudy photoionisation code (Ferland et al., 2013) with parameters as in Zackrisson et al. (2011), under the assumption of no Lyman continuum leakage and no dust. The stellar SEDs have been rescaled in all cases to be consistent with the Kroupa (2001) stellar initial mass function.

We point out here that there are some physical limitation of the Kroupa plus nebular emission case. In principle, the radiation in the halo would be a mixture of starlight and nebular emission. No datasets of mixed SED grids are available at this time, and we simply add the nebular to the stellar emission. Thus we urge the reader to treat this case as an extreme limit where the nebular emission has been maximised. Excluding the Kroupa plus nebular emission case from our work does not qualitatively change our results.

4.3.3 STAR FORMATION EFFICIENCIES

The SEDs from the previous section are normalised to a total number of stars, calculated for each halo. For the fiducial case, we adopt the stellar to virial mass ratio from O’Shea et al. (2015)

$$f_{\star} = 1.26 \times 10^{-3} (M_{\text{vir}}/10^8 M_{\odot})^{0.74}, \quad (4.1)$$

which is valid in the mass range $10^7 M_{\odot} \leq M_{\text{vir}} \leq 10^{8.5} M_{\odot}$. Our most massive halo, Halo B with $M_{\text{vir}} = 10^{8.6} M_{\odot}$, is slightly outside this range and we overestimate the stellar mass by a small amount.

	$M_{\text{vir}} [M_{\odot}]$	$M_{\text{b}} [M_{\odot}]$	$M_{\star} [M_{\odot}]$	$f_{\star} [\%]$	SFE [%]
Halo A, fiducial	5.6×10^7	9.4×10^6	4.6×10^4	0.082	0.5
Halo A, lower limit			9.4×10^3	0.015	0.1
Halo A, upper limit			9.4×10^4	0.15	1.0
Halo B, fiducial	4.0×10^8	6.7×10^7	1.4×10^6	0.35	2.1
Halo B, lower limit			6.7×10^5	0.16	1.0
Halo B, upper limit			3.3×10^6	0.79	5.0

Table 4.3.2: Star formation efficiencies and the corresponding stellar masses for both haloes. The fiducial SFEs are calculated using a formula relating the mass in stars to the total mass from O’Shea et al. (2015); see Equation 1.

The stellar mass, $M_{\star} = f_{\star} \times M_{\text{vir}}$, relates to a star formation efficiency:

$$\text{SFE} = \frac{M_{\star}}{M_{\text{b}}}, \quad (4.2)$$

where M_{b} is the baryonic mass in a halo approximated by $M_{\text{b}} = \Omega_{\text{b}}/\Omega_0 \times M_{\text{vir}}$. Using the values from Jarosik et al. (2011), $\Omega_{\text{b}} = 0.0456$ and $\Omega_0 = 0.2726$, we derive SFEs of 0.5% (Halo A) and 2.1% (Halo B). In addition, we adopt an upper and a lower SFE limit on each halo, ranging from 0.1% to 5.0%. All properties are listed in Table 4.3.2.

For our lower limit SFE of 0.1% in Halo A we get a total of $\approx 10^4 M_{\odot}$ in stars. Mas-Ribas et al. (2016) show that for a total stellar mass of $10^3 M_{\odot}$, there is a factor of few difference in the LW flux for different stochastically sampled IMFs, but this is much reduced for $\approx 10^4 M_{\odot}$ in stars.

4.4 RESULTS

Consistent with S15, we find that the LW escape fraction depends on the evolution of the ionisation front (I-front). In a completely ionised halo, the escape fraction is 100%, but when the I-front retreats or only slowly expands, molecular hydrogen production is enhanced, allowing it to self-shield. The propagation of the I-front is therefore an important quantity for the calculation of the escape fraction. We identify three different ways the I-front can behave and discuss one prominent example of each type in detail in Section 4.1. In the following subsections we will tabulate the time-averaged escape fractions in both near-field (Section 4.2) and far-field (Section 4.4) as well as the escape fraction averaged over the LW flux (Section 4.3). We also present estimates for the ionising escape fractions based on the position of

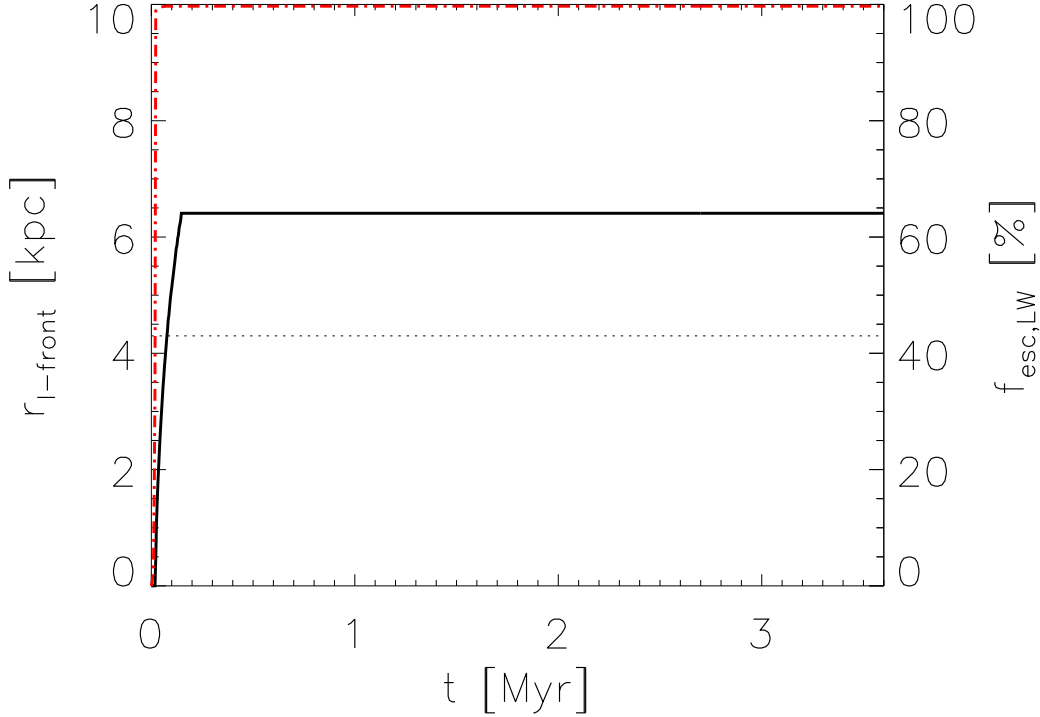


Figure 4.4.1: Position of the I-front (black solid line; left axis) and LW escape fraction in the near-field (red dot-dashed line; right axis) as a function of time for a 1.0% SFE with a Salpeter IMF in Halo B. The virial radius is shown by a black dotted line.

the I-front in Section 4.5. The escape fractions we provide are lower limits: our one dimensional simulations cannot capture asymmetric break-out along directions of minimum column density and we expect radiation to break out faster in some low-density regions.

4.4.1 INDIVIDUAL IONISATION FRONT BEHAVIOUR

OUTBREAKING IONISATION FRONT

In the case of a strong radiation source, the ionisation front quickly breaks out of the halo. Simultaneously, the escape fraction jumps up to 100% because there is no molecular hydrogen within the ionised region. The lower limit case SFE (1%) for our Salpeter SED in Halo B provides a prominent example. Figure 4.4.1 displays the position of the I-front and the LW escape fraction in the near-field as a function of time.

The abundances of the main chemical species can be seen in Figure 4.4.2 for

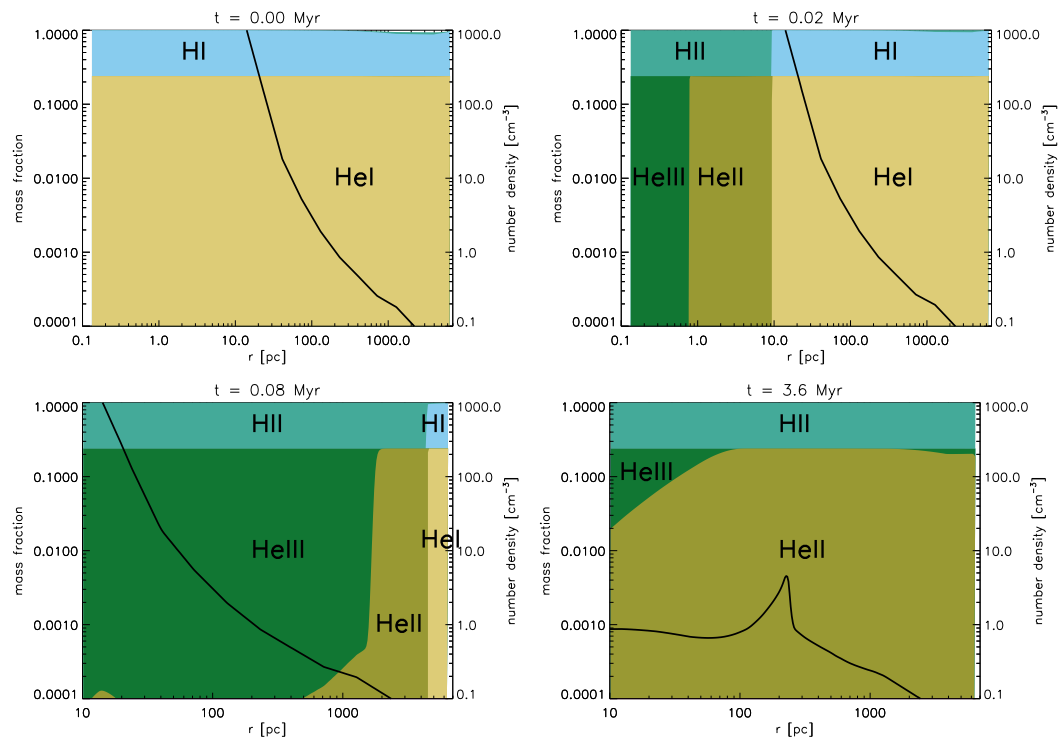


Figure 4.4.2: Abundances of the primordial species as a function of radius for four output times for a 1.0% SFE with a Salpeter IMF in Halo B. The black solid line shows the number density of the gas against radius (corresponding to the label on the right side of the plots).

four different output times. All species are colour coded. The black solid line shows the number density in cm^{-3} . Initially (upper left panel), the halo is mostly neutral with only a small amount of ionised hydrogen outside 200 pc. Already at 0.02 Myr (upper right panel), a very steep I-front has advanced out to 9 pc, indicated by the turquoise H II region that has a sharp transition to the light blue neutral H outer region. The I-front continues to proceed as an R-type I-front through the halo and crosses the virial radius at 0.08 Myr (lower left panel). Helium is doubly ionised out to 1000 pc. The density still shows its initial profile. At the end of the simulation, at 3.6 Myr (lower right panel), the halo is still completely ionised. The expansion of the ionised gas has started to drive a shock front outwards, but this has only reached 200 pc. It is therefore well within the H II region and hence is not relevant for our LW escape fraction calculation. Throughout the simulation, the H_2 abundance remains much smaller than 10^{-4} and the halo is optically thin to LW radiation. The time-averaged LW escape fraction in the near-field therefore is 99% in this case. In general,

$$f_{\text{esc,LW}}^{(o)} \geq 0.95 \quad (4.3)$$

for both the near-field and far-field limit in all models with I-front breakout (indicated by the superscript (o)).

OUTBREAKING AND RETURNING IONISATION FRONT

Similar to the case just mentioned, here, the ionisation front quickly advances through the halo, leading to a sudden increase in the LW near-field escape fraction from 0 to 100% at the beginning of the simulation. However, after some time, the radiation source weakens and produces fewer ionising photons. As a result, these haloes quickly recombine in an outside-in fashion, triggering the production of molecular hydrogen. The near-field escape fraction drops to 0% when recombination sets in.

This can be clearly observed in the lower limit SFE case of a flat IMF in Halo B. In Figure 4.4.3, a fast outbreak of the I-front yields a LW escape fraction of 100% almost immediately after the simulation starts. The abundances and number density are displayed in Figure 4.4.4. At 2.6 Myr (upper left panel), the halo is still completely ionised, but as the spectrum weakens, at 3.0 Myr (upper right panel), the outer part of the halo partly recombines. One can observe that at 3.4 Myr (middle left panel), the recombination proceeds outside-in. At 4.0 Myr (middle right panel), the I-front has moved back to the shock-front position. Here, the high

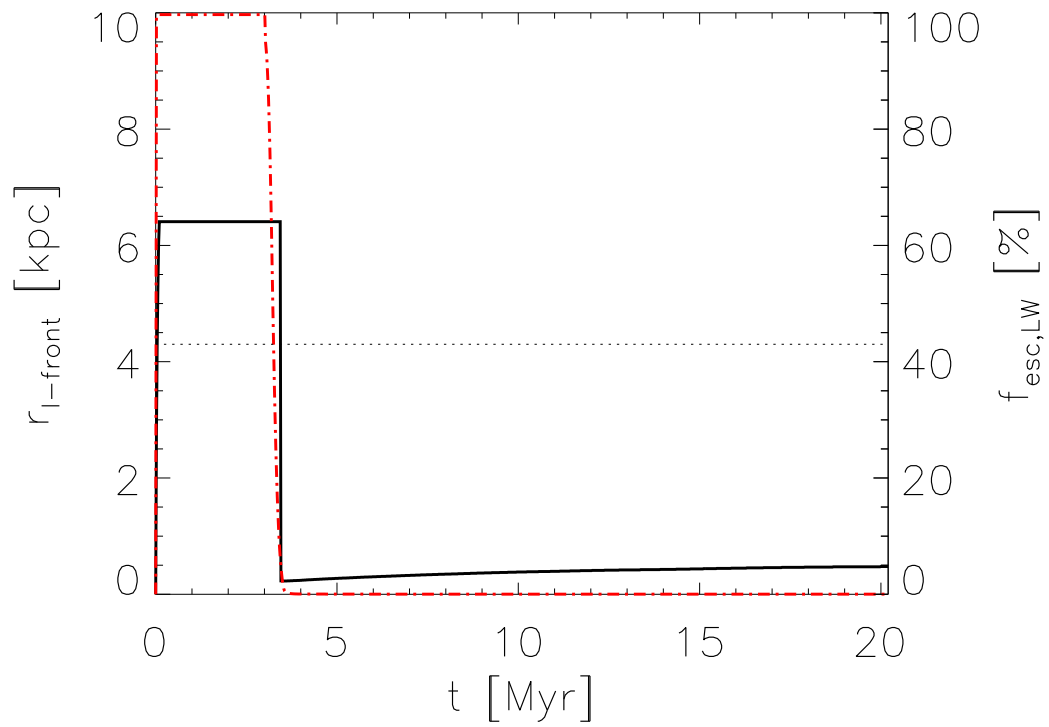


Figure 4.4.3: Position of the I-front (black solid line) and LW escape fraction in the near-field (red dot-dashed line) as a function of time for a 1.0% SFE with a flat IMF in Halo B.

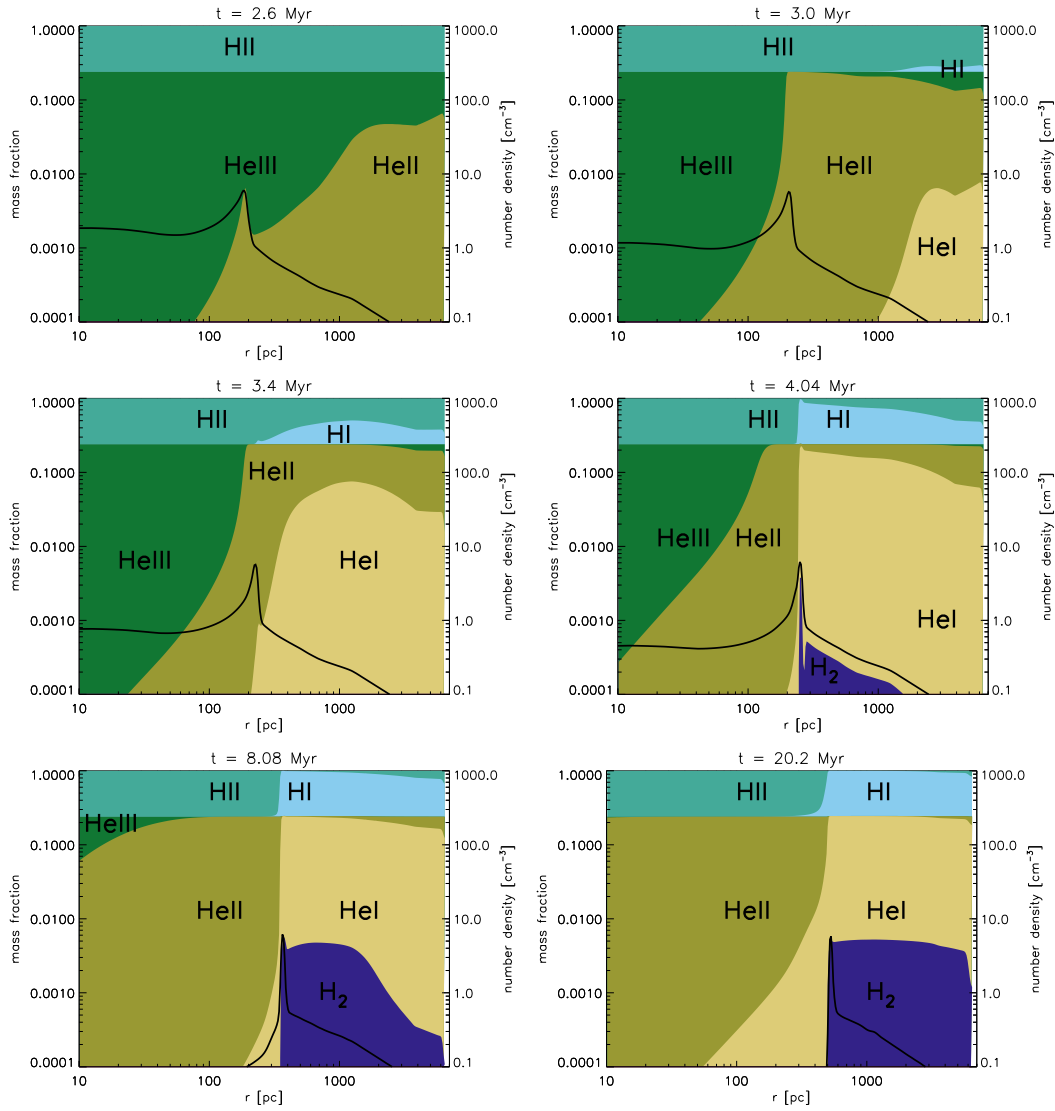


Figure 4.4.4: Abundances of the primordial species as a function of radius for six output times for a 1.0% SFE with a flat IMF in Halo B.

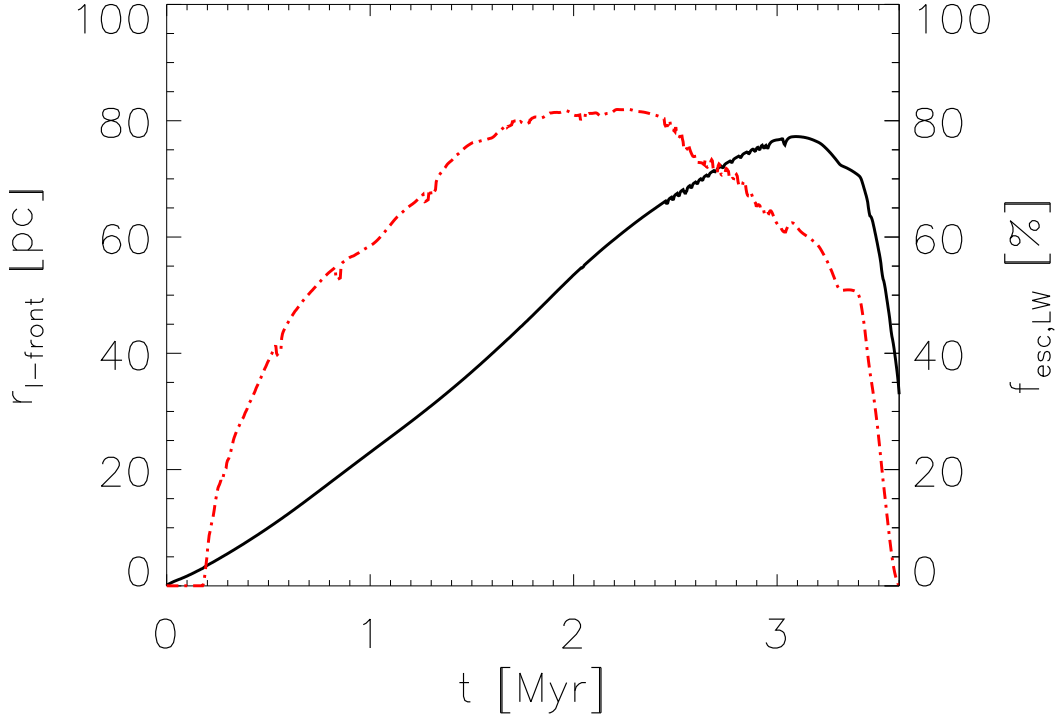


Figure 4.4.5: Position of the I-front (black solid line) and LW escape fraction in the near-field (red dot-dashed line) as a function of time for a 0.1% SFE with Salpeter IMF in Halo A.

density and the large fraction of free electrons produce the ideal environment for the formation of molecular hydrogen. The H_2 abundance peaks close to 0.01 and hinders all LW photons from escaping in the near-field. Molecular hydrogen continues to form outside of the shock-front of the halo at later times (8.1 Myr, lower left panel) until the end of the simulation (at 20.2 Myr, lower right panel). The time-averaged near-field escape fraction is only 16%, as after the outside-in recombination in the halo, LW photons are blocked completely. The LW near-field escape fraction can be approximated in simulations of returning I-fronts (indicated by the superscript $^{(r)}$) as

$$f_{\text{esc,LW}}^{(r)} = \frac{t_{\text{return}}}{t_{\text{total}}}, \quad (4.4)$$

where t_{return} is the point in time when the I-front starts moving backwards through the halo and t_{total} is the total runtime of the simulation.

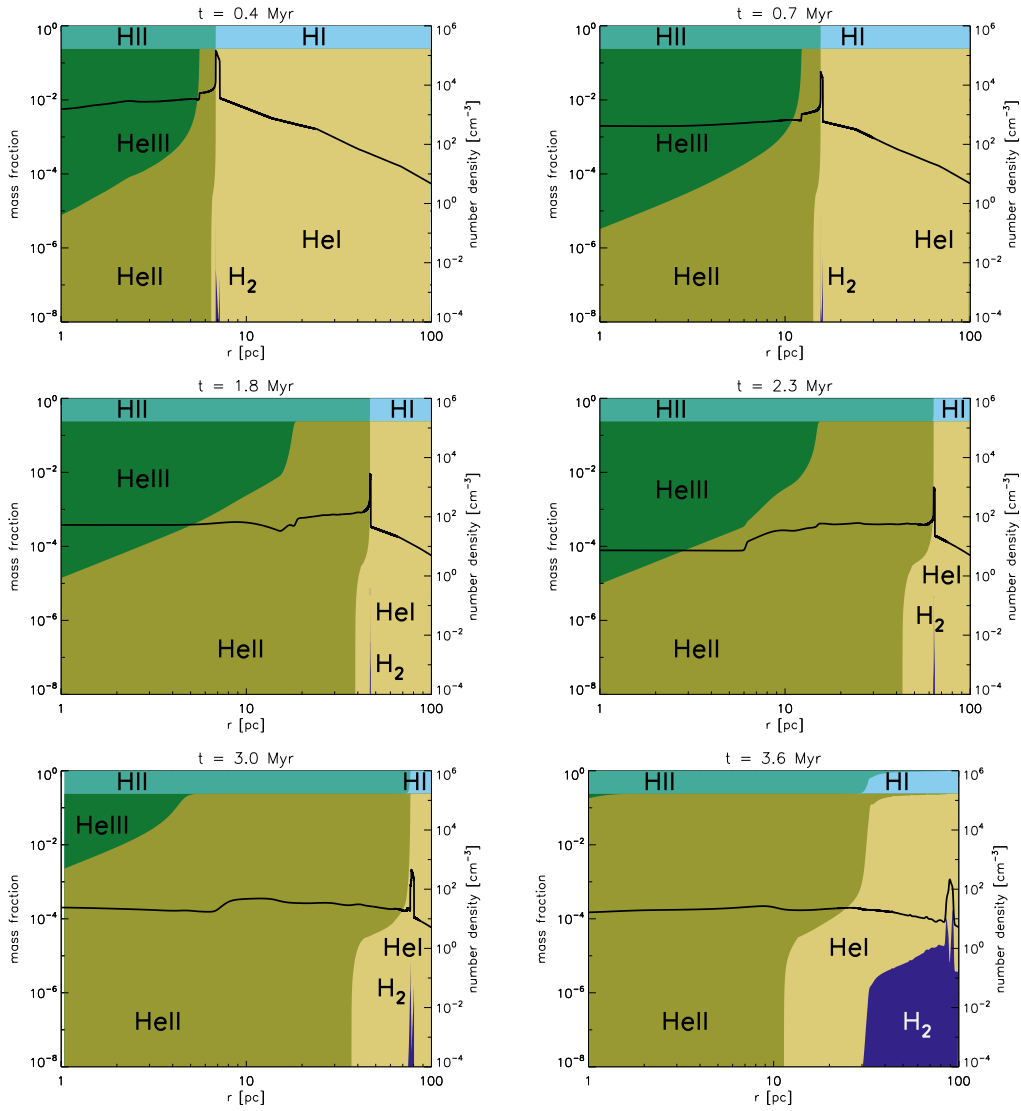


Figure 4.4.6: Abundances of the primordial species as a function of radius for six output times for a 0.1% SFE with a Salpeter IMF in Halo A.

SLOWLY MOVING IONISATION FRONT

In the case of a weak radiation source, a D-type I-front advances slowly through the halo. At its border, the many free electrons trigger massive production of H_2 and the dense thin shell that builds up reaches optical depths that can shield the LW radiation (see also Ricotti et al. 2001). Our calculations depend critically on the thickness and peak abundance of the H_2 shell. This requires specific consideration and we have to implement a region of high numerical resolution at the position of the I-front. We adopt a challenging technique where we resolve a 20 pc wide region that is bracketing and moving with the I-front with a resolution of 0.001 pc. In order to keep the computational time manageable, the first 5% of the simulations are run with our standard resolution, introducing a maximum error of 5% in the time-averaged LW escape fraction.

As an example, in Figure 4.4.5 we show the I-front position and the escape fraction as a function of time for a 0.1% SFE and Salpeter IMF in Halo A. The initial 5% of the simulation had to be run without the refinement around the I-front and therefore shows a LW near-field escape fraction that is probably too low. In the upper left panel of Figure 4.4.6 we show the abundances of all species at 0.4 Myr. The I-front and the shock front move together. A thin shell of molecular hydrogen with peak abundances reaching above 10^{-6} forms at the position of the I-front that is able to shield some of the LW radiation. The thin H_2 shell continues moving with the I-front and shock front (upper right panel and middle left panel). From 2.3 Myr on (middle right panel), the spectrum starts to weaken and the molecular hydrogen shell starts to get stronger, preventing more LW radiation from escaping the halo. At 3.0 Myr (lower left panel), the He^{2+} abundance decreases and the I-front starts to turn back. The shell of molecular hydrogen gets thicker, and at the end of the simulation at 3.6 Myr (lower right panel), all LW radiation is prevented from escaping the halo (in the near-field approximation). Averaged over the runtime of the simulation, the LW escape fraction in this example is 63%. For a slowly moving I-front, we cannot give a simple approximation, in contrast to the outbursting or returning I-front cases.

4.4.2 TIME-AVERAGED ESCAPE FRACTIONS IN THE NEAR-FIELD

For all SFE, SED and halo combinations, we average the LW escape fraction over the runtime of the simulation, 20.2 Myr (or 3.6 Myr for the Salpeter IMF). We list the corresponding escape fractions in Table 4.4.1.

SFE	Salpeter	flat	log-normal	Kroupa	Kroupa + nebula	shielding
	50–500 M_{\odot}	9–500 M_{\odot}	1–500 M_{\odot}	0.1–100 M_{\odot}	0.1–100 M_{\odot}	
0.1	63 (s)	3 (s)	38 (s)	58 (s)	63 (s)	H ₂ only
0.5	93 (r)	11 (r)	26 (r)	88 (s)	90 (s)	
1.0	99 (o)	13 (r)	44 (r)	90 (s)	92 (s)	
0.1	59 (s)	3 (s)	37 (s)	47 (s)	51 (s)	H ₂ and H
0.5	93 (r)	11 (r)	26 (r)	84 (s)	86 (s)	
1.0	99 (o)	13 (r)	44 (r)	88 (s)	89 (s)	
1.0	100 (o)	16 (r)	61 (r)	66 (r)	70 (r)	H ₂ only
2.1	100 (o)	18 (r)	78 (r)	86 (r)	88 (r)	
5.0	100 (o)	20 (r)	94 (r)	96 (r)	97 (r)	
1.0	99 (o)	16 (r)	61 (r)	64 (r)	68 (r)	H ₂ and H
2.1	100 (o)	18 (r)	78 (r)	84 (r)	86 (r)	
5.0	100 (o)	20 (r)	94 (r)	95 (r)	96 (r)	

Table 4.4.1: Time-averaged LW escape fractions in the near-field, averaged over the runtime of the simulation. All values are given in percent. The upper six rows refer to Halo A, the lower six rows to Halo B. The upper three rows of haloes A and B, respectively, are calculated with H₂ shielding only, the lower three rows with H and H₂ shielding. The letter in parentheses refers to the case of I-front behaviour: (o) stands for outbreking I-front, (r) for returning I-front and (s) for slowly moving I-front.

SFE	Salpeter	flat	log-normal	Kroupa	Kroupa + nebula	shielding
	50–500 M_{\odot}	9–500 M_{\odot}	1–500 M_{\odot}	0.1–100 M_{\odot}	0.1–100 M_{\odot}	
0.1	54 (s)	27 (s)	29 (s)	41 (s)	48 (s)	H ₂ only
0.5	87 (r)	94 (r)	45 (r)	57 (s)	64 (s)	
1.0	97 (o)	100 (r)	85 (r)	66 (s)	72 (s)	
0.1	54 (s)	27 (s)	28 (s)	40 (s)	47 (s)	H ₂ and H
0.5	87 (r)	93 (r)	44 (r)	56 (s)	63 (s)	
1.0	97 (o)	99 (r)	84 (r)	65 (s)	71 (s)	
1.0	99 (o)	100 (r)	97 (r)	46 (r)	58 (r)	H ₂ only
2.1	100 (o)	100 (r)	99 (r)	70 (r)	76 (r)	
5.0	100 (o)	100 (r)	100 (r)	92 (r)	93 (r)	
1.0	99 (o)	99 (r)	96 (r)	45 (r)	58 (r)	H ₂ and H
2.1	99 (o)	99 (r)	98 (r)	69 (r)	75 (r)	
5.0	99 (o)	99 (r)	99 (r)	91 (r)	92 (r)	

Table 4.4.2: Time-averaged LW escape fractions in the near-field, averaged over the first two Myr. All values are given in percent. The upper six rows refer to Halo A, the lower six rows to Halo B. The structure of the rows is as in Table 4.4.1.

Shielding by neutral hydrogen only makes a slight difference: the LW escape fractions are at most 16% higher if we only consider H_2 self-shielding compared to the case where we also account for shielding from H. In many cases the difference is negligible. This result is in contrast to S15, where we found significantly lower LW escape fractions when including shielding by neutral hydrogen.

As expected, a higher SFE increases the LW escape fraction. This can be observed in both haloes and for all SEDs. Outbreaking I-fronts lead to LW escape fractions $\geq 95\%$. For slowly moving or returning I-fronts, the values can be as small as 3%. This is mostly observed for the case of a flat SED ranging from 9 to $500 M_\odot$ where many massive stars die at the beginning of the simulation leading to a much weaker ionising source of photons later on. As soon as the more massive stars have died, the production of molecular hydrogen sets in and the halo becomes optically thick for the majority of the runtime of the simulations. In all other simulations, the change in spectrum is not as extreme and ionising photons are produced for a longer period, leading to higher LW escape fractions.

Our simulations assume that no stars explode as supernovae. Instead, at the end of their lives, we simply remove their contributions from the SED. We made this simplifying assumption for several reasons. First, we expect the dynamics of the supernova remnant to be highly sensitive to the 3D matter distribution in the protogalaxy (see e.g. [Mac Low and Ferrara 1999](#)). It is therefore questionable how well we can represent their effects in the simplified geometry of a 1D model. Second, considerable uncertainties still exist regarding the final masses and explosion energies of Pop III stars. In particular, the effects of rotation-driven mass loss may be significant but not yet fully understood ([Ekström et al., 2008](#)). Finally, the supernovae that explode may be unable to clear all of the gas from the protogalaxy, thus resulting in a system polluted by metals and dust. Our assumption of a primordial gas composition may then become highly inaccurate, depending on the final metallicity of the gas.

Nevertheless, once stars begin to explode as supernovae, it is possible that they will rapidly drive gas out of the protogalaxy, leading to escape fractions quickly reaching 100%. To account for this possibility, we have computed LW near-field escape fractions that are averaged over only the first 2 Myr, rather than over the lifetime of the longest-lived massive star (Table 4.4.2). Two Myr corresponds to the lifetime of stars of a few hundred solar masses ([Schaerer, 2002](#)) and we can safely assume that no supernovae exploded earlier.

Most LW escape fractions averaged over 2 Myr are high; for SFEs with a flat

	Salpeter	flat	log-normal	Kroupa	Kroupa + nebula	shielding
SFE	50–500 M_{\odot}	9–500 M_{\odot}	1–500 M_{\odot}	0.1–100 M_{\odot}	0.1–100 M_{\odot}	
0.1	66	27	50	55	60	H ₂ and H
0.5	92	92	61	82	85	
1.0	99	99	82	86	88	
1.0	100	100	91	74	78	H ₂ and H
2.1	100	100	96	89	90	
5.0	100	100	99	97	97	

Table 4.4.3: LW flux averaged LW escape fractions in the near-field, averaged over the total LW flux of the simulation. All values are given in percent. The upper three rows refer to Halo A, the lower three rows refer to Halo B. Shielding by H₂ only and by the combination of H and H₂ yields the same results.

IMF in Halo B this behaviour is most pronounced. The four outbreking I-front cases show slightly reduced LW escape fractions, but only down to 97%. This change occurs because the initial few timesteps until outbreak with escape fractions smaller than 100% now carry a slightly larger weight. For slowly moving I-fronts, the LW escape fraction decreases (with the exception of a 0.1 SFE flat IMF in Halo A). Here, the LW escape fraction slowly increases over time as the I-front moves through the halo. These last results need to be taken as lower limits as we have to run the slowing moving I-front simulations with higher resolution, but can do so only after 1 Myr (0.18 Myr for the Salpeter IMF) due to the high computational costs of the required refinement technique. LW escape fractions of returning I-fronts decrease or increase depending on when the I-front first breaks out (in the case of a Kroupa IMF quite late) and starts to return. We therefore cannot give a general trend.

4.4.3 LW FLUX-AVERAGED ESCAPE FRACTIONS IN THE NEAR-FIELD

The LW flux of the SED is decreasing over time (compare Figure 4.3.3) by factors of up to 4×10^4 in the case of the flat IMF. We therefore provide the LW escape fraction weighted by the LW flux emitted by the stellar source rather than averaged over time. We list these values in Table 4.4.3 and show them in Figure 4.4.7. Except for a SFE of 0.1%, the escape fraction is always larger than 75%. The difference to the time-averaged LW escape fraction from Section 3.2 is most significant for the flat IMF, as in that case, the LW escape fraction drops when the LW flux drops and the overall contribution is small. Additional shielding by atomic hydrogen does

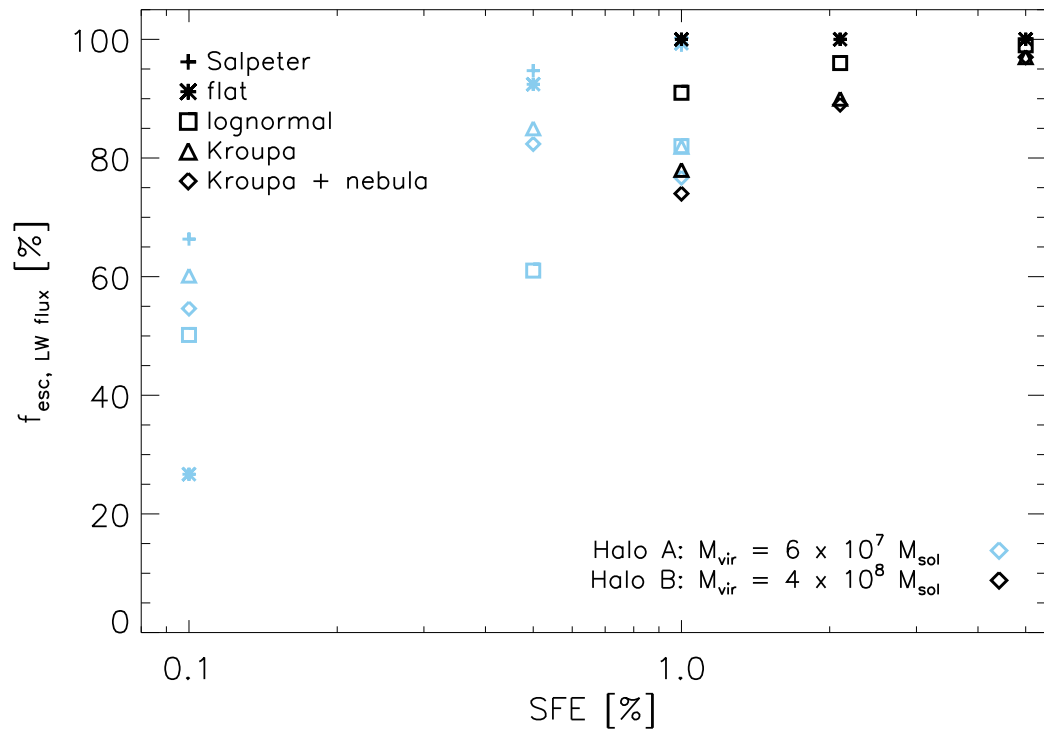


Figure 4.4.7: Flux-averaged LW escape fractions in the near-field for our parameter space. Different SEDs are shown by different symbols, Halo A is colour-coded in light blue, Halo B in black.

SFE	Salpeter	flat	log-normal	Kroupa	Kroupa + nebula	shielding
	50–500 M_{\odot}	9–500 M_{\odot}	1–500 M_{\odot}	0.1–100 M_{\odot}	0.1–100 M_{\odot}	
0.1	98	73	96	99	100	H ₂ only
0.5	99	85	96	100	100	
1.0	100	84	98	100	100	
0.1	79	61	83	68	68	H ₂ and H
0.5	91	78	88	84	84	
1.0	94	79	90	86	86	
1.0	100	85	99	99	100	H ₂ only
2.1	100	86	100	100	100	
5.0	100	88	100	100	100	
1.0	97	76	91	87	87	H ₂ and H
2.1	98	78	93	90	90	
5.0	99	80	95	93	93	

Table 4.4.4: Time-averaged LW escape fractions in the far-field. All values are given in percent. The upper six rows refer to Halo A, the lower six rows to Halo B. The upper three rows of haloes A and B, respectively, are calculated with H₂ shielding only, the lower three rows with H and H₂ shielding.

not decrease the LW escape fraction in this limit by more than 0.5%. Therefore we only provide the escape fraction obtained by considering both H₂ and H shielding together.

4.4.4 TIME-AVERAGED ESCAPE FRACTIONS IN THE FAR-FIELD

In the far-field, the LW escape fractions are generally larger than in the near-field, varying from 59% to 100%. Our values are listed in Table 4.4.4. Including shielding by neutral hydrogen can reduce the LW escape fraction by up to 29% (comparing 0.1% SFE with a Kroupa SED in Halo A) and thus should not be forgotten in simulations. For the fiducial SFE, all LW escape fractions are higher than 75% and we conclude that the host haloes of the first galaxies do not suppress the build-up of the LW background by a large factor.

4.4.5 LOWER LIMITS FOR IONISING ESCAPE FRACTIONS

Since we track the position of the I-front through the halo, we are able to calculate the escape fractions of ionising photons as well. The values need to be taken as a first order approximation only, since our one dimensional setup prevents us from

SFE	Salpeter	flat	log-normal	Kroupa	Kroupa + nebula
	50–500 M_{\odot}	9–500 M_{\odot}	1–500 M_{\odot}	0.1–100 M_{\odot}	0.1–100 M_{\odot}
0.1	0	0	0	0	0
0.5	85	10	18	0	0
1.0	96	13	36	0	0
1.0	98	17	54	26	26
2.1	99	19	66	42	42
5.0	100	22	84	58	58

Table 4.4.5: Time-averaged ionising escape fractions in the near-field. All values are given in percent. The upper three rows refer to Halo A, the lower three rows to Halo B. All values are derived from the position of the I-front and provide lower limits.

seeing the outbreak of ionised cones like authors recently do with high-resolution three dimensional studies (Ritter et al., 2012; Paardekooper et al., 2015; Stacy et al., 2016).

The escape fraction of ionising photons is determined by the position of the I-front alone. For each simulation-output, we check if the I-front has crossed the virial radius, in which case we take $f_{\text{esc,ion}}(t) = 1$; otherwise, $f_{\text{esc,ion}}(t) = 0$. Averaging these values over the runtime of the simulation yields the ionising escape fractions $f_{\text{esc,ion}}$, listed in Table 4.4.5.

The values of $f_{\text{esc,ion}}$ are similar to $f_{\text{esc,LW}}$ in the near-field for the case of an outbreking or a returning I-front, since the LW escape fractions depend critically on the position of the I-front. For the case of a slowly moving I-front that never crosses the virial radius, we obtain ionising escape fractions of zero while the LW escape fractions vary from 3% to 85% in the near-field. In these cases, the outer halo is optically thick to ionising photons, but optically thin to LW photons.

4.5 DISCUSSION AND CONCLUSION

We studied a multidimensional grid of parameters to calculate the LW escape fractions in both the near-field and the far-field limit. We consider two haloes of 5.6×10^7 and $4.0 \times 10^8 M_{\odot}$, that are irradiated by a stellar population in their centre. Different SEDs, ranging from a Salpeter IMF between 50 and 500 M_{\odot} to a Kroupa IMF between 0.1 and 100 M_{\odot} , combined with SFEs between 0.1% and 5.0% are taken into account.

We find that the near-field LW escape fraction depends on the motion of the

I-front and we therefore group our results into three different ways the I-front can behave:

- For an outbreaking I-front, the LW escape fraction in the near-field is $f_{\text{esc}}^{(o)} \geq 95\%$. This is obtained for SFEs greater than 0.5% with a Salpeter slope IMF ranging from 50 to 500 M_{\odot} : the I-front overruns the halo and all gas is ionised for the rest of the simulation.
- In the case of a spectrum that weakens substantially over time, haloes recombine outside-in. Large numbers of free electrons still present in the outer parts of the halo lead to the aforementioned molecular hydrogen formation in the outer part of the halo. The halo becomes optically thick. The LW escape fraction can be approximated by $f_{\text{esc}}^{(r)} \approx t_{\text{return}}/t_{\text{total}}$, where t_{return} is the time when the recombination sets in and t_{total} is the runtime of the simulation.
- For a slowly moving I-front, the LW escape fraction can be as small as 3% and as large as 88%, depending on a thin shell of molecular hydrogen that builds up at the position of the I-front. In this case, the stellar radiation acts as an agent of negative feedback that enhances the abundance of molecular hydrogen and suppresses the LW background (see also [Ricotti et al. 2001](#), discussing H_2 -shell formation in the IGM).

Out of 30 simulations, we find 4 overrunning, 17 returning and 9 slowly moving I-fronts.

In the far-field, all LW escape fractions are much larger than in the near-field, as we are shifting out of the line centres and average the LW escape fraction over the whole LW energy range. Here, shielding by neutral hydrogen starts to play a role since Lyman lines of $\text{H}\beta$ and higher, that lie inside the LW range, become very broad ([Haiman et al., 2000](#)). Neutral hydrogen is able to reduce the LW escape fraction in the far-field by up to 29%. In general, all LW escape fractions in the far-field are higher than 75% in the fiducial case and the halo only slightly hinders the build-up of the LW background.

We also tabulated values of the ionising escape fractions for our parameter space, depending on the position of the I-front relative to the virial radius. For slowly moving I-fronts, this value equals zero, since the I-front does not reach out to the virial radius at any time in our simulation. For simulations where the I-front quickly breaks out of the halo, the ionising escape fractions are larger than 95%. If the I-front first breaks out and later returns due to outside-in recombination of the halo,

the escape fraction ranges from 10% to 85%.

The biggest drawback of this study is our 1D approach. In 3D simulations, ionising photons break cones into the haloes, following low-density regions. We expect our LW escape fractions to be close to 1 in these directions, leading to an overall higher $f_{\text{esc,LW}}$. We therefore consider our LW escape fractions to be lower limits.

Additionally, our UV source is placed in the centre of our 1D halo and all relative velocities of the contributing stars are neglected. For the slowly moving I-front cases, the LW near-field escape fractions are underestimated in this work. For outbursting or returning I-fronts, the abundance of molecular hydrogen is either too low or too high to be influenced by relative motions at the centre of the halo.

We have shown in this study that the LW escape fraction from the first galaxies is high. Unless a protogalaxy harbours a star cluster with flat IMF or forms stars with a low $\sim 0.1\%$ SFE, a large fraction of its LW radiation can escape from the host halo. The LW escape fractions in the far-field exceeds 60% in all cases. We thus conclude that the gas present in the host halo of a stellar cluster with $10^4 M_{\odot}$ to a few times $10^6 M_{\odot}$ in stars cannot prevent the build-up of the LW background.

The recently observed Ly α system CR7 at $z = 6.6$ (Sobral et al., 2015) is comprised of two star-forming components and one seemingly metal-poor component (however see Bowler et al., 2016). Agarwal et al. (2015) showed that the star-forming components can easily produce the LW radiation field required for DCBH formation in the metal-poor clump. For an exponentially declining star formation history, they find that DCBH formation can occur in similar systems as early as $z \sim 20$, if the star-forming component consists of a DM halo or haloes of $M_{\text{DM}} \sim 5 \times 10^8 M_{\odot}$ and a SFE of 8% or larger (Agarwal et al. in preparation). This closely matches our case of Halo B forming stars at its upper limit of SFE $\sim 5\%$ with the same underlying IMF and stellar mass cut-offs. Given the separation between the star-forming component and the metal-poor component of CR7 over which the LW feedback allows for DCBH formation (Agarwal et al. 2016), we can apply our near-field limit. Thus we can conclude that the star-forming component of CR7 type systems could have an escape fraction as high as 96% at onset of DCBH formation.

In general, the near-field can be applied to neighbouring systems that move with no or only a small velocity relative to the halo emitting LW radiation. The critical relative velocity separating the two regimes depends on the strength of the LW absorption lines in the emitting halo. When the lines are weak and dominated by thermal broadening, $v_{\text{crit}} \simeq v_{\text{th,H}_2}$, the thermal velocity of the H₂, which in our

simulated haloes is typically $7\text{--}15\text{ km s}^{-1}$. On the other hand, if the main LW lines are strong and dominated by Lorentz broadening (i.e. if the near-field LW escape fraction is very small), then the linewidths and hence the critical relative velocity can both be much larger.

ACKNOWLEDGMENTS

We would like to thank Mordecai-Marc Mac Low, Mattis Magg and Massimo Ricotti for useful discussions. Furthermore, we would like to thank the anonymous referee for his / her valuable comments. A. T. P. S., B. A., C.-E. R. and D. J. W. acknowledge support from the European Research Council under the European Community's Seventh Framework Programme (FP7/2007 - 2013) via the ERC Advanced Grant "STARLIGHT: Formation of the First Stars" (project number 339177). B. A. acknowledges support of a TCAN postdoctoral fellowship at Yale. S. C. O. G. and R. S. K. also acknowledge support from the Deutsche Forschungsgemeinschaft via SFB 881, "The Milky Way System" (sub-projects B1, B2 and B8) and SPP 1573 , "Physics of the Interstellar Medium" (grant number GL 668/2-1). M. L. acknowledges funding from European Union's Horizon 2020 research and innovation programme under the Marie Skłodowska-Curie grant agreement No 656428. E. Z. acknowledges funding from the Swedish Research Council (project number 2011-5349). All simulations were run on the Sciama Supercomputer at the Institute of Cosmology and Gravitation at the University of Portsmouth.

5

The formation of direct collapse black holes under the influence of streaming velocities

Distribution of work Anna T. P. Schauer has performed the cosmological simulations used in this chapter and the analysis thereof. John Regan wrote the introduction, Simon C. O. Glover wrote the method section and Anna T. P. Schauer wrote the rest of the text, including all figures. All authors contributed with ideas and comments. This work has been performed during a visit of John Regan to Heidelberg.

The content of this chapter has been published as:

Schauer, A. T. P., Regan, J., Glover, S. C. O., and Klessen, R. S.

“The formation of direct collapse black holes under the influence of streaming velocities”.

ArXiv e-prints 1705.02347, accepted by MNRAS, May 2017b

doi: 10.1093/mnras/stx1915.

Authors Anna T. P. Schauer¹, John Regan^{2,1}, Simon C. O. Glover¹, Ralf S. Klessen^{1,3}

¹ Universität Heidelberg, Zentrum für Astronomie, Institut für Theoretische Astrophysik, Albert-Ueberle-Str. 2, 69120 Heidelberg, Germany

² Centre for Astrophysics & Relativity, School of Mathematical Sciences, Dublin City University, Glasnevin, D09 W6Y4, Dublin, Ireland

³ Universität Heidelberg, Interdisziplinäres Zentrum für Wissenschaftliches Rechnen, Im Neuenheimer Feld 205, 69120 Heidelberg, Germany

Abstract We study the influence of a high baryonic streaming velocity on the formation of direct collapse black holes (DCBHs) with the help of cosmological simulations carried out using the moving mesh code AREPO. We show that a streaming velocity that is as large as three times the root-mean-squared value is effective at suppressing the formation of H₂-cooled minihaloes, while still allowing larger atomic cooling haloes (ACHs) to form. We find that enough H₂ forms in the centre of these ACHs to effectively cool the gas, demonstrating that a high streaming velocity by itself cannot produce the conditions required for DCBH formation. However, we argue that high streaming velocity regions do provide an ideal environment for the formation of DCBHs in close pairs of ACHs (the “synchronised halo” model). Due to the absence of star formation in minihaloes, the gas remains chemically pristine until the ACHs form. If two such haloes form with only a small separation in time and space, then the one forming stars earlier can provide enough ultraviolet radiation to suppress H₂ cooling in the other, allowing it to collapse to form a DCBH. Baryonic streaming may therefore play a crucial role in the formation of the seeds of the highest redshift quasars.

Keywords black hole physics – stars: Population III – (cosmology:) early Universe – (galaxies:) quasars: supermassive black holes.

5.1 INTRODUCTION

Massive black hole seeds that can form through gravitational collapse of very massive progenitors, ([Chandrasekhar, 1964](#)), can be invoked to explain the observations of quasars at very early times in the Universe ([Wu et al., 2015](#); [Mortlock et al., 2011](#);

Fan et al., 2006). The direct collapse (DC) model (Loeb and Rasio, 1994a; Oh and Haiman, 2002; Bromm and Loeb, 2003; Begelman et al., 2006; Regan and Haehnelt, 2009a,b) of super-massive black hole (SMBH) formation requires that massive objects form in near pristine atomic cooling haloes in which Population III (Pop III) star formation has been suppressed. The suppression of previous episodes of star formation means that metal enrichment is obviated. Pop III star formation can be restrained by removing the primary gas coolant, H_2 , or alternatively by increasing the minimum halo mass required for collapse due to the impact of streaming motions as we shall see.

One avenue that has been explored by many authors to suppress H_2 formation is radiative feedback from the surrounding galaxies in the Lyman-Werner (LW) band (Shang et al., 2010; Agarwal et al., 2012; Regan et al., 2014; Latif et al., 2014a; Agarwal et al., 2014; Agarwal and Khochfar, 2015; Hartwig et al., 2015b; Regan et al., 2016a). LW radiation readily dissociates H_2 through the two step Solomon process (Field et al., 1966; Stecher and Williams, 1967a). For high star formation efficiencies or single, massive Pop III stars, most of the LW radiation can escape the host galaxy or minihalo (Schauer et al., 2015, 2017a). If the intensity of the LW radiation is sufficient, H_2 is dissociated and cooling is suppressed in low mass minihaloes. The halo then continues to accrete mass all the way up to and beyond the atomic line cooling limit. Halo collapse can then begin once Lyman- α line cooling becomes effective and contraction proceeds isothermally at approximately $T_{\text{gas}} \sim 8000$ K. In this case, the strength of the background required depends both on the spectral shape of the sources and on their proximity with respect to the target halo (Dijkstra et al., 2008; Sugimura et al., 2014; Agarwal et al., 2016). There is general consensus within the literature that the critical value of the background required to suppress H_2 formation throughout the entire halo is $J_{\text{crit}} \sim 1000 J_{21}$ for a background dominated by emission from stars with an effective temperature $T_{\text{eff}} \sim 5 \times 10^4$ K, where $J_{21} = 10^{-21} \text{ erg cm}^{-2} \text{ s}^{-1} \text{ Hz}^{-1} \text{ sr}^{-1}$. If there is also a non-negligible X-ray background, then the required value can be even higher (Inayoshi and Tanaka, 2015; Glover, 2016; Regan et al., 2016b). A much milder intensity level, say $J \lesssim 100 J_{21}$, is enough to delay Pop III formation until a halo reaches the atomic cooling limit, but in this case H_2 readily forms in the self-shielded core of the ACH, resulting in rapid Pop III formation (e.g. Fernandez et al., 2014; Regan et al., 2017).

The value of J_{crit} is orders of magnitude higher than the typical strength of the Lyman-Werner background at the relevant redshifts, even if one accounts for clustering of sources (Ahn et al., 2009). Radiation fields of the required strength

will therefore only be encountered in unusual circumstances. One promising way in which a field of the required strength can be produced is the synchronised halo model (Dijkstra et al., 2008; Visbal et al., 2014b; Regan et al., 2017; Agarwal et al., 2017). This model supposes that occasionally two ACHs will be found in close proximity. If both haloes remain chemically pristine until the onset of atomic cooling, and if the collapse times of the haloes are sufficiently similar, then Pop III star formation can begin in the first halo before the second has finished collapsing. The resulting irradiation from the more evolved system provides a sufficiently strong LW radiation field to suppress cooling in the secondary (proto-)galaxy, which therefore becomes an ideal location for the formation of a DCBH. However, for this model to work, it is necessary to suppress H_2 formation in both haloes until they become massive enough to atomically cool. If this is accomplished via LW feedback, the required field strength is $J \gtrsim 100 J_{21}$, which is still somewhat higher than the typical strength of the LW background.

Another, perhaps more natural, mechanism for delaying Pop III star formation is via streaming of the baryons with respect to the dark matter. This effect, elucidated by Tselikhovich and Hirata (2010), is a result of the initial offset between the baryonic velocities and the dark matter velocities after recombination. The velocity offset between baryons and dark matter decays as $\Delta v \propto (1+z)$, but offsets as large as 9 km s^{-1} are still possible at $z \sim 100$. The impact of this streaming motion on Pop III star formation have been investigated by several authors with general agreement that the minimum halo mass required for Pop III star formation is increased in the presence of large-scale streaming velocities (Stacy et al., 2011; Greif et al., 2011b; Naoz et al., 2013, Schauer et al. 2017b in prep) as the baryons require a larger gravitational potential in which they can virialise due to the additional streaming velocity. Therefore, streaming motions are not thought to have a large effect on ACHs illuminated with LW radiation fields with strengths greater than J_{crit} (i.e. haloes which would form DCBHs even without the streaming; see Latif et al. 2014a for details). However, Tanaka and Li (2014) argue that very large streaming velocities may suppress Pop III star formation entirely in some haloes, allowing pristine haloes above the atomic cooling limit to form, thereby providing ideal locations in which DCBHs can form without requiring an extremely strong LW radiation field. This model has been criticised by Visbal et al. (2014a), who concede that streaming can suppress H_2 formation in minihaloes but argue that in ACHs, H_2 formation in dense collapsing gas is inevitable, regardless of the streaming velocity, unless the gas is illuminated by a strong LW radiation field. Other models which

can successfully suppress H_2 cooling and delay PopIII formation have been put forward by [Inayoshi and Omukai \(2012\)](#) (collisional dissociation by shocks), [Fernandez et al. \(2014\)](#) (rapid accretion in a mild LW background) and [Inayoshi et al. \(2015\)](#) (proto-galactic collisions) among other. However, here we focus on streaming velocities as a mechanism for increasing the minimum mass for star formation and hence for creating ideal environments for DCBH formation.

In this Chapter, we re-examine the role of baryonic streaming in the formation of DCBHs. We show that although baryonic streaming by itself cannot produce haloes capable of forming DCBHs, it provides a very natural mechanism for suppressing H_2 formation in pairs of haloes until they reach the atomic cooling regime. It therefore offers a simple way of producing the pristine ACH pairs required by the synchronised halo model without the need for a locally elevated LW background. Furthermore, the risk of metal enrichment from background galaxies is significantly reduced since mini-halo formation is suppressed in the immediate vicinity.

5.2 SIMULATIONS

5.2.1 NUMERICAL METHOD

The simulations described in this Chapter are carried out using the AREPO moving-mesh code ([Springel, 2010](#)). We include both dark matter particles and gas cells. The hydrodynamics of the gas is evolved using a Voronoi grid in which the gas cells move along with the flow. We use a recent version of AREPO that includes improvements to the time integration scheme, spatial gradient reconstruction and grid regularization discussed in [Pakmor et al. \(2016\)](#) and [Mocz et al. \(2015\)](#). We model the thermal and chemical evolution of the gas in our cosmological boxes using an updated version of the chemical network and cooling function implemented in AREPO by [Hartwig et al. \(2015b\)](#), based on earlier work by [Glover and Jappsen \(2007\)](#) and [Clark et al. \(2011\)](#). Our chemical model accounts for the formation of H_2 by the H^- and H_2^+ pathways and its destruction by collisions and by photodissociation. It includes all of the chemical reactions identified by [Glover \(2015\)](#) as being important for accurately tracking the H_2 abundance in simulations of DCBH formation.

Compared to [Hartwig et al. \(2015b\)](#), we have made three significant changes to the chemical network. First, we have included a simplified treatment of deuterium chemistry designed to track the formation and destruction of HD following [Clark et al. \(2011\)](#). Second, we have updated the rate coefficient used for the dielectronic recombination of ionized helium, He^+ ; we now use the rate calculated by [Badnell](#)

(2006). Finally, we have improved our treatment of H^- photodetachment to account for the contribution to the H^- photodetachment rate coming from non-thermal CMB photons produced as a consequence of cosmological recombination (Hirata and Padmanabhan, 2006). We describe this process using the simple analytical expression given in Coppola et al. (2011).

Our treatment of the cooling accounts for all of the processes important at the number densities probed by our simulations, including Lyman- α cooling and H_2 rotational and vibrational cooling. The latter is taken from Glover and Abel (2008) and updated as described in Glover (2015). Further details of our chemical and thermal treatment can be found in Schauer et al. (2017, in prep).

5.2.2 INITIAL CONDITIONS

We initialise our simulations at $z = 200$. We assume a Λ CDM cosmology and use cosmological parameters from the 2015 Planck data release (Planck Collaboration et al., 2016b). Unless we explicitly state otherwise, we use physical units throughout the Chapter. The initial conditions for the dark matter are created with MUSIC (Hahn and Abel, 2011), using the transfer functions of Eisenstein and Hu (1998). The baryons are assumed to initially trace the dark matter density distribution. To account for the supersonic streaming of the baryons relative to the dark matter, we first set up a velocity field in the baryonic component that is the same as that in the dark matter, and then impose a constant velocity offset, v_{stream} . We take the magnitude of this offset to be $v_{\text{stream}} = 18 \text{ km s}^{-1}$ at $z = 200$, corresponding to a value of $3 \sigma_{\text{rms}}$, of the root-mean-squared streaming velocity at this redshift (Tselikhovich and Hirata, 2010).

We carry out two simulations, runs SB (small box) and LB (large box). In run SB, we model a box of size (1 Mpc/ h) in comoving units, while in run LB, we consider a box of size (4 Mpc/ h). Both simulations are performed using 1024^3 dark matter particles and initially represent the gas using 1024^3 Voronoi mesh cells. In run SB, we therefore have a dark matter particle mass of $99.4 M_{\odot}$ and an average initial mesh cell mass of $18.6 M_{\odot}$. In run LB, these values are a factor of 64 larger, as summarised in Table 5.2.1. If we conservatively require 1000 dark matter particles in order to consider a halo to be resolved (Sasaki et al., 2014, Schauer et al. 2017b in prep.), then the corresponding resolution limits are $M_{\text{DM,res}} \simeq 10^5 M_{\odot}$ for run SB and $M_{\text{DM,res}} \simeq 6.4 \times 10^6 M_{\odot}$ for run LB. We note that even in our lower resolution, larger box run, the minimum resolvable halo mass is smaller than the minimum mass

Name	Box length (h^{-1} Mpc)	M_{DM} (M_{\odot})	$M_{\text{gas,init}}$ (M_{\odot})
SB	1	99	18.6
LB	4	6360	1190

Table 5.2.1: Dark matter particle mass and initial mesh cell gas mass in our two simulations.

of an ACH in the range of redshifts considered in this Chapter, $M_{\text{atom}} \sim 10^7 M_{\odot}$.

For gas number densities $n < 100 \text{ cm}^{-3}$, we adopt a “constant mass” refinement criterion, meaning that AREPO refines or de-refines mesh cells as required in order to keep the mass of gas in each cell at its initial value, plus or minus some small tolerance. At $n \geq 100 \text{ cm}^{-3}$, we instead use Jeans refinement, and ensure that the Jeans length is always resolved by at least eight mesh cells. However, in order to prevent run-away collapse to protostellar densities, we switch off refinement once the cell volume becomes less than $0.1 h^{-3} \text{ pc}^3$ in comoving units, corresponding to a density of $n \sim 10^6 \text{ cm}^{-3}$.

5.3 RESULTS

5.3.1 MASSES AND COLLAPSE REDSHIFTS OF HALOES CONTAINING COLD DENSE GAS

We expect runaway collapse for densities exceeding a number density of $n \geq 10^4 \text{ cm}^{-3}$ (Glover, 2005). We therefore call a halo collapsed when this number density is exceeded by at least one gas cell in that halo. In our simulations, the first objects collapse at $z = 19$ in simulation LB and at $z = 14$ in simulation SB. This difference in collapse redshift is an expected consequence of the difference in box size: simulation LB contains more large-scale power and hence naturally forms collapsed objects somewhat earlier than simulation SB.

In Figure 5.3.1, we show the halo mass at collapse as a function of collapse redshift z_{coll} . In our simulations, we produce output snapshots with a redshift spacing $\Delta z = 1$ in order to restrict the volume of data produced to a reasonable level. We can therefore not distinguish between haloes forming at e.g. $z = 19.99$ and $z = 19.01$, leading to the clear clustering of points in the Figure.

In simulation SB, we form only a single collapsed halo by the end of the simulation. This object has a mass of $3 \times 10^7 M_{\odot}$ and a collapse redshift $z_{\text{coll}} = 14$. In run LB, on the other hand, the larger box allows us to form more collapsed haloes. We

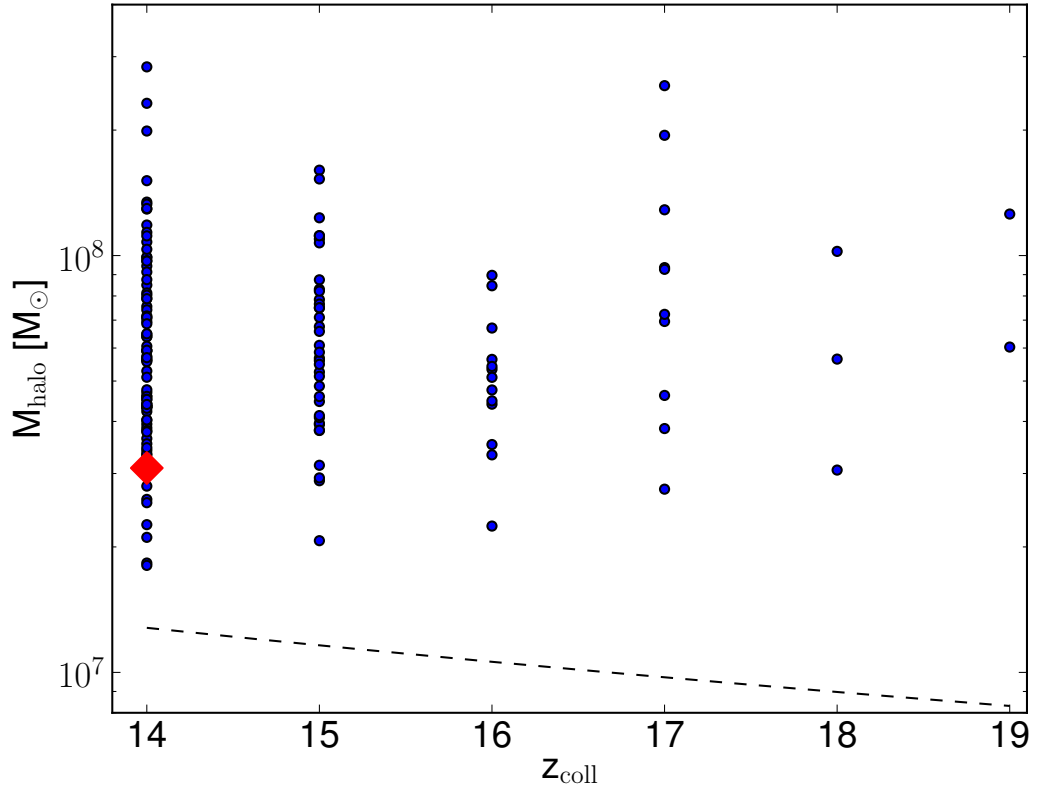


Figure 5.3.1: Masses of haloes containing cold dense gas, plotted at their redshift of collapse z_{coll} , defined as described in Section 5.3. The clustering of points at particular values of z_{coll} reflects the fact that we produce output snapshots with a redshift separation $\Delta z = 1$. The red diamond denotes the halo in simulation SB, and the blue circles denote the haloes in simulation LB. All collapsed haloes have masses larger than the minimum mass of an ACH (denoted by the dashed black line), demonstrating that only ACHs can collapse when $v_{\text{stream}} = 3\sigma_{\text{rms}}$.

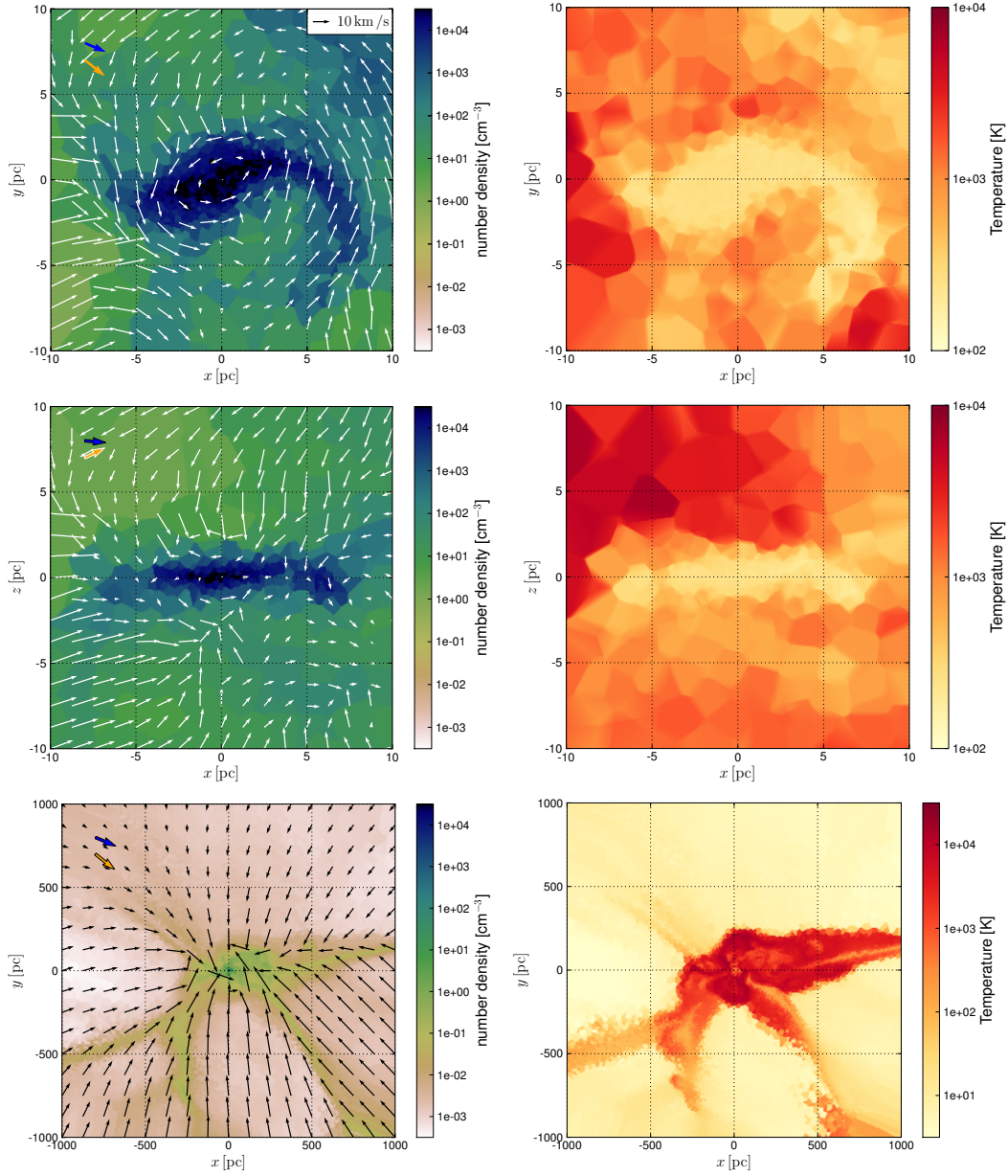


Figure 5.3.2: Number density (left panels) and temperature (right panels) slices of the collapsed halo with $M_{\text{halo}} = 3 \times 10^7 M_{\odot}$ in the SB simulation at redshift $z = 14$. In the upper two rows, we show the central region in face-on and edge-on projections. In the bottom row, we show the larger-scale structure surrounding the halo. The distances shown are in proper units. The black or white arrows in the density slices show the velocity field of the closest cell projected into the plane. (Note that the velocities shown are computed in the centre of mass rest-frame.) In blue, we show the streaming velocity at this redshift, scaled up by a factor of 10, and in orange the velocity of the centre of mass. We can see that the centre of the halo is dense and cold with temperatures around a few hundred K. This is the place where Pop III star formation will eventually take place. On larger scales, the gas flows that feed the halo are visible.

find 2, 3, 10, 13, 37 and 86 haloes that collapse at redshifts $z = 19, 18, 17, 16, 15$ and 14, respectively. In every single case, the halo mass at collapse is larger than the mass of a halo with a virial temperature of 8000 K (indicated by the dashed black line in Figure 5.3.1), which is a reasonable proxy for the minimum mass of an ACH. Previous work has shown that Pop III stars in regions of the Universe with no streaming velocity can form in minihaloes with masses of a few times $10^5 M_{\odot}$ (Machacek et al., 2001; Yoshida et al., 2003; Hirano et al., 2015). We find no cold dense gas in any halo with a mass less than the atomic cooling limit, demonstrating that when the baryonic streaming velocity is very high, the formation of Pop III stars in H_2 -cooled minihaloes is very strongly suppressed.

Our results demonstrate that high baryonic streaming velocities are a viable mechanism for producing a population of chemically pristine ACHs without the need for a high LW background. A sufficient close pair of such haloes collapsing at very similar redshifts would be an ideal site for the formation of a DCBH (Visbal et al., 2014b; Regan et al., 2017). We have carefully examined whether any of the collapsed haloes in the LB simulation have separations of less than 500 pc in proper units, which is a reasonable upper limit on the required separation, but have found no such close pairs. However, this is unsurprising, since their space density is expected to be very small. In their simulations, Visbal et al. (2014b) find two closely synchronized halo pairs in a volume of $\approx 1.7 \times 10^4 \text{ cMpc}^3$, corresponding to a number density of $1.2 \times 10^{-4} \text{ cMpc}^{-3}$, where cMpc denotes comoving Mpc. Since the combined volume of simulations SB and LB is much smaller (209 cMpc^3), the probability of finding a synchronized pair is only $\sim 2.5\%$.

The fraction of the Universe with streaming velocities of $3\sigma_{\text{rms}}$ or higher is $\approx 5.9 \times 10^{-6}$. If we assume that all high-redshift quasars originate from synchronized halo pairs in regions with $v_{\text{stream}} \geq 3\sigma_{\text{rms}}$, then we find a quasar number density of 0.7 cGpc^{-3} . This number is in good agreement with the low number density of quasars observed at redshift $z = 6$ of about 1 cGpc^{-3} (Fan, 2006). This statement is based on the assumption that all observed high-redshift quasars can be well observed and are not quiescent or hidden in a dust cloud. Thus the real number density of quasars could be higher than the value that is observed today.

5.3.2 GAS PROPERTIES WITHIN THE COLLAPSED HALOES

Next, we take a closer look at the collapsed halo in simulation SB. In Figure 5.3.2, we show slices of the number density and the temperature of the central region

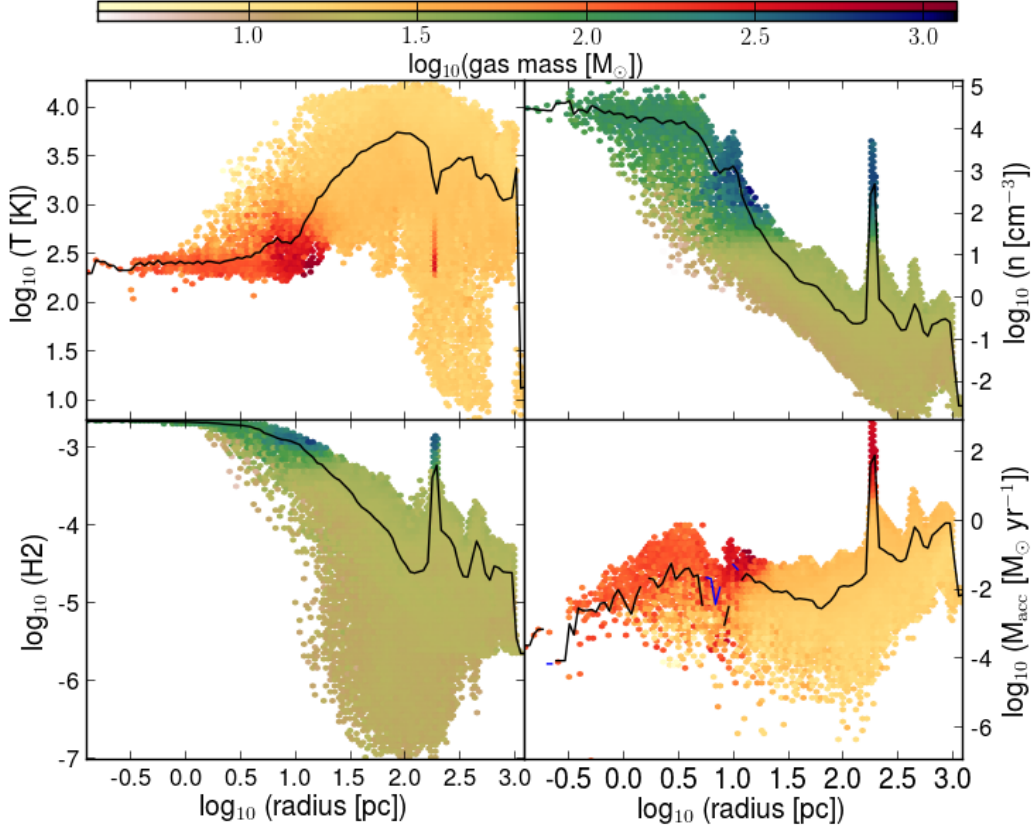


Figure 5.3.3: Properties of the collapsed halo with $M_{\text{halo}} = 3 \times 10^7 M_{\odot}$ in the SB simulation at redshift $z = 14$. From top left to bottom right, we show the temperature, gas number density, H_2 abundance and mass accretion rate as a function of radius, with the radius given in proper units. The colored regions show two dimensional histograms of the distribution of gas cells, the black lines the mass averaged values. For the mass accretion rate, we show a blue line for outflowing masses. In the central, high density halo region, the temperature drops to a few hundred Kelvin due to cooling by H_2 . In the same region, the H_2 abundance reaches values above 10^{-3} . Since the accretion rate is low ($\approx 10^{-2} M_{\odot} \text{yr}^{-1}$), we expect Pop III star formation and not the formation of a supermassive star that eventually collapses into a DCBH.

and the surroundings of our halo at redshift $z = 14$. In the upper left panel, we see the face-on cut-through of the central 20 pc, where all of the dense, collapsed gas can be found. Here, the densities are high enough for efficient formation of H_2 , leading to strong cooling. The dense region thus corresponds to a region of low temperature (upper right panel). In the edge-on cut-through (middle left and middle right panels), one can see a stream of hot, low-density gas flowing onto the halo. The larger-scale structure in which the halo is embedded can be seen in the lower two panels. It is in the middle of several hot gas streams that feed the minihalo. The central 200 pc region is shock-heated up to 10^4 K, except for some high-density streams that already cool efficiently.

In Figure 5.3.3, we can see the radial profiles of our halo in the SB simulation. As can already be seen from the slice plots in Figure 5.3.2, we see a drop in temperature at the centre of the halo, corresponding to a region of high density and high H_2 abundance. Furthermore, in the bottom right hand panel of Figure 5.3.3 we see that the mass inflow rate onto the central region is, on average, well below the threshold value of $\sim 0.1 M_\odot \text{yr}^{-1}$ for forming supermassive stars (e.g. Hosokawa et al., 2013; Schleicher et al., 2013). These results confirm the argument put forward by Visbal et al. (2014a) that high streaming velocities are unable to prevent H_2 formation in dense gas in ACHs, and demonstrate that the suggestion of Tanaka and Li (2014) that streaming velocities alone can create the necessary conditions for DCBH formation is incorrect.

In the top panel of Figure 5.3.4, we show a two-dimensional histogram of all gas cells in simulation LB in a $\log(n)$ – $\log(T)$ diagram. The region with low number density and temperature corresponds to void regions in the simulation, where the gas can cool below the CMB temperature adiabatically. In the bottom panel of Figure 5.3.4, we depict the same histogram, but only for gas cells associated with the collapsed haloes at this redshift. Unsurprisingly, there are no cells in the low density, low temperature regime.

Above gas number densities of $n > 1 \text{ cm}^{-3}$, most of the gas undergoes cooling and settles into temperatures of a few hundred K. There is, however, some gas that occupies the high density, high temperature region in the diagram. We carefully check that this hot ($T > 4000$ K), dense ($n > 10^4 \text{ cm}^{-3}$) gas can be traced back to shock heating of individual cells in the haloes (as predicted by Inayoshi and Omukai, 2012). These cells are typically located at the edge of the high density, cold centre of the halo, where it is intersected by an inflowing gas stream (compare with Latif et al., 2014b, who find a similar behaviour in their low LW halo). In the bottom

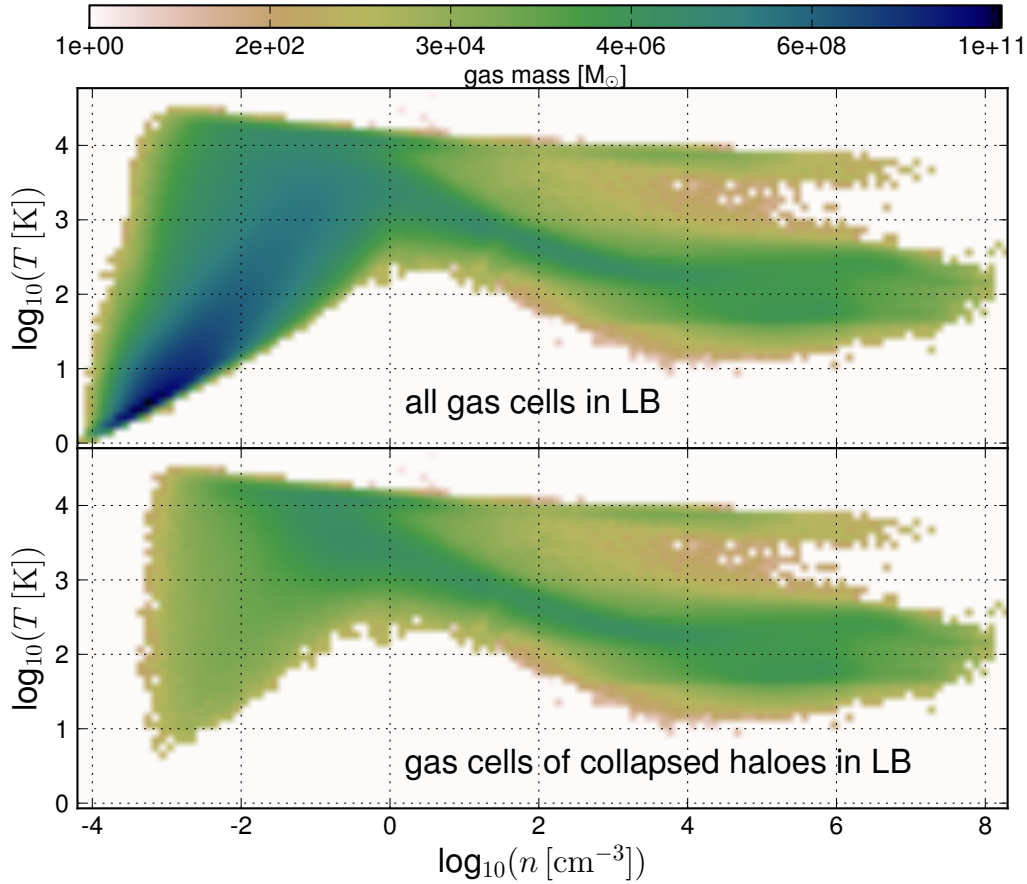


Figure 5.3.4: Two dimensional histograms of all gas cells in $\log(n)$ - $\log(T)$ space at redshift $z = 14$. The upper panel shows all gas cells in simulation LB, the lower panel all gas cells in LB that are associated with the collapsed haloes. Above number densities of $n \gtrsim 1\text{cm}^{-3}$, the majority of the gas cells under-go cooling by H_2 and HD and reach temperatures as low as hundred K. The few high density – high temperature gas cells can be associated with single shocked gas cells in some haloes. We can conclude that all collapsed haloes in simulation LB have cool, dense centres similar to the halo in simulation SB.

panel of Figure 5.3.4 we see that the majority of the dense, collapsed gas in our haloes cools efficiently via H_2 and HD emission down to temperatures of around a hundred K. We can therefore safely conclude that all of the collapsed haloes that form in our simulations have a cold, dense centre, and are therefore unlikely to collapse to form DCBHs in the absence of external LW feedback.

5.4 CONCLUSIONS

In this Chapter, we have investigated the role that high baryonic streaming velocities may play in the formation of DCBHs. We carried out two simulations in which we imposed a constant velocity offset, $v_{\text{stream}} = 3\sigma_{\text{rms}}$, where σ_{rms} is the root-mean-squared streaming velocity. One of these simulations used a volume of side length $1 \text{ cMpc}/h$, giving us very good mass resolution, but producing only a single sample of an ACH. The other simulation used a larger volume with side length $4 \text{ cMpc}/h$, and consequently had worse mass resolution but yielded a much larger sample of ACHs. In both cases, we find that the effect of the large streaming velocity is to suppress H_2 formation (and hence star formation) in minihaloes: the first haloes in which gas is able to cool and collapse to high densities are all ACHs. However, contrary to a suggestion by Tanaka and Li (2014), we find no evidence for the suppression of H_2 cooling in any of the collapsed ACHs. In every case, H_2 forms within the centre of the halo, and so in the absence of additional physics, we would expect all of the haloes to form Pop III stars rather than DCBHs. In the cases where Pop III star formation is the final result and if the Pop III star(s) find themselves at the centre of a convergent flow with high in-fall rates then rapid growth may be possible even when starting from a so-called “lighter seed” (Lupi et al., 2016; Pezzulli et al., 2016).

Nonetheless, our results demonstrate that high streaming velocities cannot by themselves produce the conditions required for DCBH formation. However, they do produce an ideal environment in which the synchronised halo model for DCBH formation can operate. This model requires that star formation be suppressed in a close pair of haloes until both reach masses large enough that they can start to atomically cool (Dijkstra et al., 2008; Visbal et al., 2014b; Regan et al., 2017). Achieving this with LW feedback is possible, but requires a LW radiation field strength that is significantly higher than the typical background value (Visbal et al., 2014b). High streaming velocities provide an alternative means of achieving the same suppression without the need for a locally elevated LW background, and without the risk that the haloes will be enriched with metals from nearby minihaloes. In

addition, if we estimate the comoving number density of synchronised halo pairs that are located in regions with $v_{\text{stream}} \geq 3\sigma_{\text{rms}}$, we find a number of order 1 cGpc^{-3} , in good agreement with the observed comoving number density of $z > 6$ quasars. We conclude that synchronised halo pairs forming in regions of very high baryonic streaming velocity are ideal candidates for forming the seeds of the first quasars.

ACKNOWLEDGMENTS

The authors would like to acknowledge fruitful discussions with Naoki Yoshida and Takashi Hosokawa as well as with Mattis Magg and Mattia Sormani. They would like to thank the anonymous referee for her/his valuable comments that helped to improve the paper. ATPS would like to thank Volker Springel and his team for kindly providing the code AREPO that was used to carry out this simulation. Special thanks goes to Christian Arnold, Rüdiger Pakmor, Kevin Schaal, Christine Simpson and Rainer Weinberger for their help with the code. ATPS, SCOG and RSK acknowledge support from the European Research Council under the European Community's Seventh Framework Programme (FP7/2007 - 2013) via the ERC Advanced Grant "STARLIGHT: Formation of the First Stars" (project number 339177). SCOG and RSK also acknowledge support from the Deutsche Forschungsgemeinschaft via SFB 881 "The Milky Way System" (sub-projects B1, B2 and B8) and SPP 1573 "Physics of the Interstellar Medium" (grant number GL 668/2-1). JR acknowledges the support of the EU Commission through the Marie Skłodowska-Curie Grant - "SMARTSTARS" - grant number 699941. The authors gratefully acknowledge the Gauss Centre for Supercomputing e.V. (www.gauss-centre.eu) for funding this project by providing computing time on the GCS Supercomputer SuperMUC at Leibniz Supercomputing Centre (www.lrz.de). The authors acknowledge support by the state of Baden-Württemberg through bwHPC and the German Research Foundation (DFG) through grant INST 35/1134-1 FUGG.

6

The Influence of Streaming Velocities on the Formation of the First Stars

Distribution of work This chapter is in preparation for publication. Anna T. P. Schauer performed all simulations and scaling tests and wrote the majority of the text. Simon C. O. Glover contributed text to the methods section and the appendix. Both Simon C. O. Glover and Ralf S. Klessen contributed with ideas and comments.

Authors Anna T. P. Schauer¹, Simon C. O. Glover¹, Ralf S. Klessen^{1,2}

¹ Universität Heidelberg, Zentrum für Astronomie, Institut für Theoretische Astrophysik, Albert-Ueberle-Str. 2, 69120 Heidelberg, Germany

² Universität Heidelberg, Interdisziplinäres Zentrum für Wissenschaftliches Rechnen, Im Neuenheimer Feld 205, 69120 Heidelberg, Germany

Abstract How, when and where the first stars formed are fundamental questions that need to be answered if we want to understand the global star formation history of the Universe. A few years ago, a second order effect in the fluid equations was

re-evaluated by [Tseliakhovich and Hirata \(2010\)](#) and found to make a significant contribution: an offset-velocity between gas and dark matter, the so-called streaming velocity. It has been found to delay the formation of the first stars and lower the gas fractions and halo mass function. We present a set of cosmological, hydrodynamical simulations of different regions of the Universe with different streaming velocities performed with the moving mesh code AREPO. A primordial chemistry network is coupled to the hydrodynamical evolution. Our simulations have a very high resolution of 1024^3 dark matter particles and gas cells throughout the whole volume of $(1 \text{ cMpc}/h)^3$. This enables us to study minihaloes down to masses of $10^5 M_\odot$ with more than 1500 dark matter particles / gas cells. With these tools in hand, we find that the minimum halo mass for a halo to contain cold, dense gas that will probably form Population III stars is $M_{\text{halo,min}} = 5 \times 10^5 M_\odot$, independent of redshift. Above a halo mass of $M_{\text{halo,50\%}} = 1.2 \times 10^6 M_\odot$, more than 50% of all haloes possess cold, dense gas. For regions of the Universe with non-zero streaming velocity, the halo mass function and the baryon fraction decrease. This also results in high minimum halo masses for cold, dense gas. For regions with streaming velocities $v_{\text{stream}} \geq 3 \sigma_{\text{rms}}$, only haloes exceeding the atomic cooling limit are able to cool.

Keywords early universe – cosmic background radiation – dark ages, reionisation, first stars – stars: Population III – radiation: dynamics.

6.1 INTRODUCTION

The first stars in the Universe form in minihaloes at high redshifts. Gas in these haloes cools via molecular hydrogen down to temperatures of $T \approx 150 - 200 \text{ K}$, allowing the gas to collapse and form Population III (Pop III) stars (e.g. see reviews by [Bromm, 2013](#); [Glover, 2013](#)). The minimum halo mass required for cooling via H_2 and first star formation is a crucial quantity for understanding the primordial Universe.

The halo mass function scales inversely to the halo mass M_{halo} , giving rise to a strong dependence of the Pop III star number density on the minimum halo mass. The implications reach far and are manifold:

Minihaloes may play a significant role in reionisation. On the one hand, Pop III stars may provide additional radiation that leads to an earlier start of reionization

(Ahn et al., 2012). On the other hand, minihaloes play an important role by absorbing ionising photons, leading to a lower volume-averaged ionising fraction, thus delaying the end of the reionisation epoch (Barkana and Loeb, 2002; Haiman et al., 2001; Ciardi et al., 2006). Minihaloes could even leave an imprint on the 21 cm signal prior to reionization (Shapiro et al., 2006; Yue et al., 2009). In addition, primordial supernova rates depend on the number density of Pop III stars and hence on the minimum halo mass (Magg et al., 2016).

The metal pollution history of the Universe also depends on the minimum halo mass for Pop III star formation. If star formation takes place in lower mass haloes, the ejecta from supernovae can escape from the potential wells of the haloes more easily (Mac Low and Ferrara, 1999).

Two important effects have been discussed in the literature that influence the minimum halo mass. First, Lyman-Werner radiation originating from the first stars and galaxies can photodissociate molecular hydrogen. When H_2 is destroyed, the gas cannot cool down to low temperatures and loses its ability to form stars (see e.g. Haiman et al., 1997, 2000). Unless the star formation efficiency is very low, most of this Lyman-Werner radiation can usually escape the host halo (Schauer et al., 2015, 2017a), following which it can travel for large distances in the early Universe. Consequently, the onset of Pop III star formation is rapidly followed by the build-up of a Lyman-Werner background (LWBG).

On a global scale, a LWBG leads to delayed star formation (Machacek et al., 2001; Wise and Abel, 2007; O’Shea and Norman, 2008) and the halo mass required for star formation increases (Haiman et al., 2000; Yoshida et al., 2003; Wise and Abel, 2007; O’Shea and Norman, 2008; Visbal et al., 2014c). These studies, with the exception of Yoshida et al. (2003), have the drawback that they focus on the one or ten most massive haloes in their simulation volume and do not address the question of where Pop III stars can form quantitatively down to smaller minihalo masses.

Second, it has recently been discovered that relative velocities between baryons and dark matter exist at recombination (Tseliakhovich and Hirata, 2010; Tseliakhovich et al., 2011). These studies show that this relative velocity is coherent over several comoving Mpc with a root-mean-squared value at $z \approx 1100$ of $\sigma_{\text{rms}} \approx 30 \text{ km s}^{-1}$. Although this relative velocity decreases as $v_{\text{stream}} \sim (1+z)$ as the Universe expands, it nevertheless has profound effects on the formation of dark matter minihaloes. Streaming leads to a reduced baryon fraction in the haloes (Naoz et al., 2012) and a lower halo number density (Tseliakhovich et al., 2011; Naoz

et al., 2013), as it is harder for baryons to settle into the host dark matter haloes. As a consequence, Pop III star formation is delayed (Greif et al. 2011b; Fialkov et al. 2012, see however Stacy et al. 2011) and the minimum halo mass required for efficient H₂ cooling is increased. Streaming velocities may even help create the environment required for the formation of direct collapse black holes (Tanaka and Li, 2014; Latif et al., 2014a; Schauer et al., 2017b).

In our study, we run a set of cosmological simulations with a box size of 1 cMpc/ h (where c stands for comoving and h is the Hubble constant in units of $100 \text{ km s}^{-1} \text{ Mpc}^{-1}$) down to a redshift of $z = 14$, leading to several thousand haloes to analyse for each box. We study regions of the Universe with streaming velocities of 0, 1, 2 and 3 times σ_{rms} . In contrast to previous studies (e.g. Naoz et al., 2012, 2013; Popa et al., 2016), we also include a primordial chemistry network in our simulations, allowing us to investigate the thermal evolution of the gas. We can not only investigate the gas fraction in our studies, but also how much cold, dense gas assembles in the haloes that is available for Pop III star formation. Our very high resolution of $20 M_{\odot}$ per gas cell throughout our simulation volume allows us to trace the gas up to very high densities of $n > 10^2 \text{ cm}^{-3}$ in all minihaloes. This allows us to give a quantitative and statistically robust result about the influence of streaming velocities on first star formation. In this chapter, we study regions of the Universe with different streaming velocities and how this influences the formation of Pop III stars. We will consider a LWBG and the combination of these effects in a follow-up study.

This chapter is structured as follows: we present our set of simulations in Section 6.2. In Section 6.3, we analyse the results of our study, starting with the simulation without streaming velocities in Section 6.3.1. In Section 6.3.2 we then present the results for simulations with streaming velocities of 1, 2 or $3\sigma_{\text{rms}}$. We conclude and discuss our findings in Section 6.4. Several Appendices give insight into the numerical methods and analysis tools.

6.2 METHOD

6.2.1 NUMERICAL METHOD

Our cosmological simulations are carried out using the moving-mesh code AREPO (Springel, 2010). AREPO solves the equations of hydrodynamics on an unstructured mesh defined by the Voronoi tessellation of a set of mesh-generating points that move with the flow of the gas. Dark matter is included using a Barnes and Hut

(1986) oct-tree.

To model the chemical and thermal evolution of the gas, we use an updated version of the primordial chemistry network and cooling function implemented in AREPO by Hartwig et al. (2015b), based on earlier work by Glover and Jappsen (2007), Glover and Abel (2008), Clark et al. (2011) and Glover (2015). The main change with respect to Hartwig et al. (2015b) is the inclusion of a simplified model of deuterium chemistry, focussing on the formation and destruction of hydrogen deuteride, HD. This is important for our study because there are indications that HD cooling can become significant in some circumstances in low-mass minihaloes (Ripamonti, 2007; Sasaki, 2015). Our treatment of the deuterium chemistry and HD cooling follows Clark et al. (2011). In addition, we have made two further minor changes to the chemistry network: we have updated the rate coefficient used for the dielectronic recombination of He^+ , and we have accounted for the photodetachment of H^- by photons from the cosmic microwave background. More details concerning both of these changes are given in Appendix 6.A.

6.2.2 INITIAL CONDITIONS

Our simulations are initialised at $z = 200$. Their details are summarised in Table 6.2.1. The initial conditions for the dark matter are created with MUSIC (Hahn and Abel, 2011), using the transfer functions of Eisenstein and Hu (1998). The baryons are assumed to initially trace the dark matter density distribution. We assume a Λ CDM cosmology and use cosmological parameters derived from PLANCK observations of the CMB, namely $h = 0.6774$, $\Omega_0 = 0.3089$, $\Omega_b = 0.04864$, $\Omega_\Lambda = 0.6911$, $n = 0.96$ and $\sigma_8 = 0.8159$ (Planck Collaboration et al., 2016b).

In our runs without streaming, the initial velocity field of the baryons is the same as that of the dark matter. In the runs that include streaming, we add a constant velocity offset, arbitrarily chosen to be in the x -direction, with a magnitude v_{stream} . We run simulations with $v_{\text{stream}} = 6, 12, \text{ and } 18 \text{ km s}^{-1}$, corresponding to values 1, 2 and 3 times σ_{rms} , the root-mean-squared streaming velocity at $z = 200$. In our initial conditions, we ignore the effect of a position shift of the baryons with respect to the dark matter due to the streaming, as Naoz et al. (2012) have shown that this is unimportant at $z \gg 15$ and is completely erased by the time $z \sim 15$.

The naming convention for our simulations is simple. Each simulation has a name of the form vN , where N denotes the streaming velocity in units of σ_{rms} ; thus, $v0$ corresponds to a run with $v_{\text{stream}} = 0$. Most of the simulations are carried

Name	Box size [cMpc/h]	v_{stream} [km s ⁻¹]	M_{gas} [M _⊙]	M_{DM} [M _⊙]
v0	1	0	18.6	99
v1	1	6	18.6	99
v2	1	12	18.6	99
v3	1	18	18.6	99
v3_big	4	18	1190	6360

Table 6.2.1: Overview of our simulations. Note that v_{stream} gives the strength of the streaming velocity at $z = 200$.

out with a box size of $(1 \text{ cMpc}/h)^3$. However, for the case with $v_{\text{stream}} = 3\sigma_{\text{rms}}$, we have carried out an additional simulation with a significantly larger box size, $(4 \text{ Mpc}/h)^3$, which we name v3_big.

All simulations are performed with 1024^3 dark matter particles and initially have 1024^3 Voronoi mesh cells to represent the gas. This corresponds to a dark matter particle mass of $99 M_{\odot}$ and an average initial mesh cell mass of $18.6 M_{\odot}$ in the simulations with a box size of $(1 \text{ Mpc}/h)^3$. The corresponding values in the run with a larger box are larger by a factor of $4^3 = 64$.

For gas number densities lower than $n = 100 \text{ cm}^{-3}$, we allow AREPO to refine or de-refine mesh cells as necessary to keep the mass of gas in the cells close to the initial mass. At higher densities, we switch on Jeans refinement, where we refine cells as required to ensure that the Jeans length λ_{J} is always resolved by at least eight mesh cells. However, to prevent run-away collapse to protostellar densities, we switch off refinement again once the cell volume drops below $0.1 h^{-3} \text{ cpc}^3$. The corresponding maximum density is redshift dependent, but typically a few times 10^6 cm^{-3} .

6.2.3 HALO SELECTION

We select haloes via a standard friends-of-friends algorithm. We have verified that our results do not change much if we look only at the first subhalo in each halo that is actually gravitationally bound (see Appendix 6.C).

At each output redshift, we examine every halo and identify those containing cold gas. In order to be counted as “cold” for our purposes, gas needs to fulfil the following three criteria:

- Temperature $T \leq 500 \text{ K}$,

- Hydrogen nuclei number density $n \geq 100 \text{ cm}^{-3}$,
- Fractional H_2 abundance $x_{\text{H}_2} \geq 10^{-4}$.

These criteria allow us to distinguish between gas which has formed H_2 , cooled and begun to undergo gravitational collapse, and gas which instead has a low temperature simply because it has not yet virialized. Our selection is insensitive to the values chosen for the temperature and molecular hydrogen abundance criteria, provided we choose a temperature lower than the typical halo virial temperature and larger than the minimum temperature reachable by H_2 cooling, $T \sim 200 \text{ K}$, and an H_2 abundance that is considerably larger than the abundance in the undisturbed intergalactic medium, $x_{\text{H}_2} \sim 10^{-6}$ (Hirata and Padmanabhan, 2006). We chose a density threshold $n \geq 100 \text{ cm}^{-3}$, above which we employ a Jeans refinement criterion. We assume that gas denser than this threshold has reached the “point of no return” beyond which the gas cannot be stopped from collapsing, implying that the halo will form stars shortly afterwards. We define the cold mass, M_{cold} , as the sum of the gas masses in all of the mesh cells that fulfil the three criteria above. A halo that contains at least one such gas cell is counted to be “cold” and contributes to the number of cold gas haloes, N_{cold} .

6.3 RESULTS

6.3.1 NO STREAMING VELOCITIES

We begin by analysing the evolution of haloes in a patch of the Universe with zero streaming velocity. Figure 6.3.1 shows the cumulative halo mass function $N(> M)$ plotted for several different redshifts in range $14 \leq z \leq 24$. We also show the cumulative cold halo mass function $N_{\text{cold}}(> M)$ for all haloes that contain at least one cold, dense gas cell. At redshifts $z \leq 20$, the most massive haloes are always cold, whereas smaller haloes $M_{\text{halo}} \approx 10^5 M_{\odot}$ are never cold, independent of redshift.

Figure 6.3.2 shows the cold gas mass M_{cold} against halo mass M_{halo} for all haloes that contain at least one cold gas cell at redshift $z = 15$. The cold gas mass scales with the halo mass as

$$M_{\text{cold}} = 7.55 \times 10^3 M_{\odot} \times \left(\frac{M_{\text{halo}}}{10^6 M_{\odot}} \right)^{1.618}, \quad (6.1)$$

but with scatter of up to two orders of magnitude at the lower mass end. We provide this fit for all simulations in Appendix 6.D of the paper.

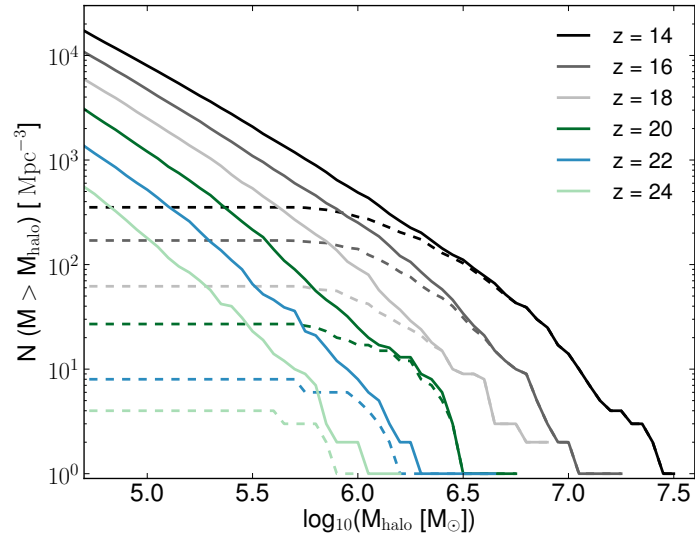


Figure 6.3.1: Cumulative halo mass function for all haloes (solid lines) and cold haloes (dashed lines) for redshifts $z = 24 - 14$ for the simulation without streaming velocity.

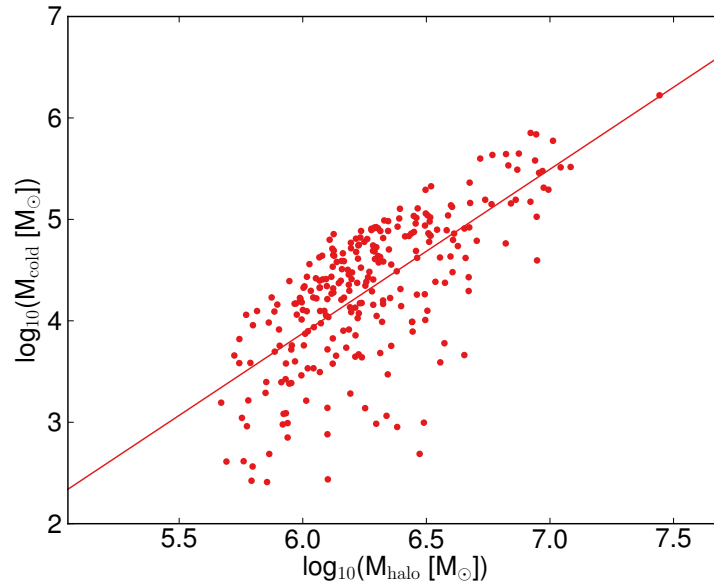


Figure 6.3.2: Cold gas mass M_{cold} plotted as a function of halo mass M_{halo} for the simulation without streaming velocity at $z = 15$. The solid red line provides a fit to the data points.

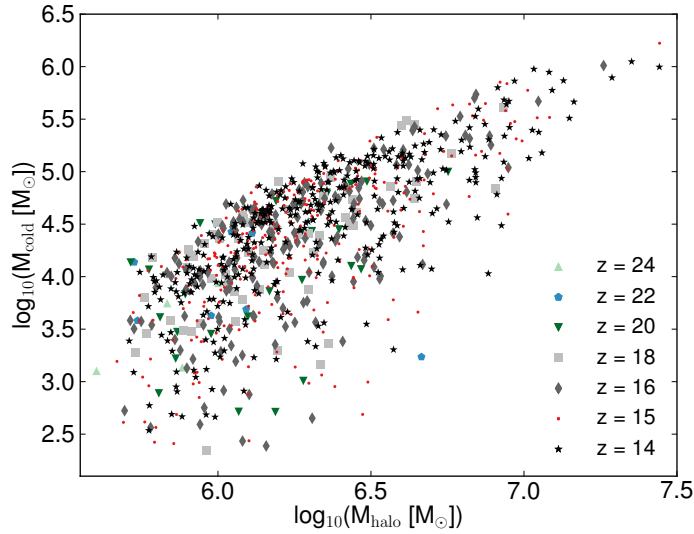


Figure 6.3.3: Cold gas mass M_{cold} plotted as a function of halo mass M_{halo} for the simulation without streaming velocity at redshifts in the range $14 \leq z \leq 24$.

The relation of cold gas mass against halo mass is rather independent of redshift. Figure 6.3.3 shows the cold gas mass – halo mass relation for the same box in the redshift range $14 \leq z \leq 24$. At redshifts $z = 24$ (light green triangles) and $z = 22$ (blue pentagons), we are limited by small number statistics as our simulation sample includes only 4 and 8 haloes that contain cold gas, respectively. For redshifts $z \leq 20$, the cold mass – halo mass relations for different redshifts agree well and the exponent is always in the interval [1.3,1.6].

As expected, larger haloes contain more cold gas, but it is not immediately obvious whether this is because cooling is more efficient in these haloes, or whether it is larger because these haloes contain more gas. It is therefore interesting to examine the cold gas fraction $M_{\text{cold}}/M_{\text{halo}}$ as a function of halo mass M_{halo} , as shown in Figure 6.3.4. We see a weak correlation between cold gas fraction and halo mass. Larger haloes tend to have higher cold gas fractions, but the scatter is large.

The cold gas fraction is similar for higher redshifts as can be seen in Figure 6.3.5. The main difference arises from the fact that the haloes forming at higher redshifts are less massive and thus the diagram is less populated at higher halo masses for higher redshifts.

Another interesting quantity is the minimum halo mass $M_{\text{halo,min}}$ for haloes to harbour cold gas that will be able to form stars. There appears to be a clear edge to the distribution of points on the left-hand side of Figures 6.3.2, 6.3.3, 6.3.4 and 6.3.5

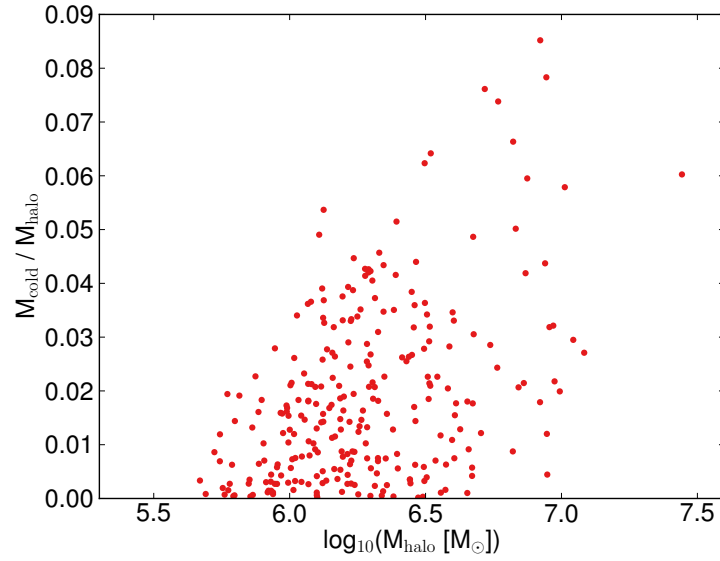


Figure 6.3.4: Cold gas fraction $M_{\text{cold}}/M_{\text{halo}}$ plotted as a function of halo mass M_{halo} for the simulation without streaming velocity at $z = 15$. Values are plotted only for haloes that contain at least one cold gas cell.

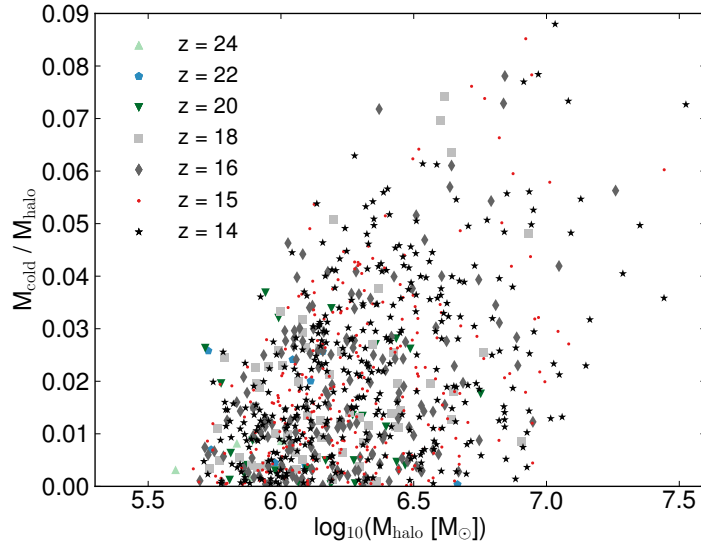


Figure 6.3.5: Cold gas fraction $M_{\text{cold}}/M_{\text{halo}}$ plotted as a function of halo mass M_{halo} for the simulation without streaming velocity for redshifts in the range $14 \leq z \leq 24$. Values are plotted only for haloes that contain at least one cold gas cell.

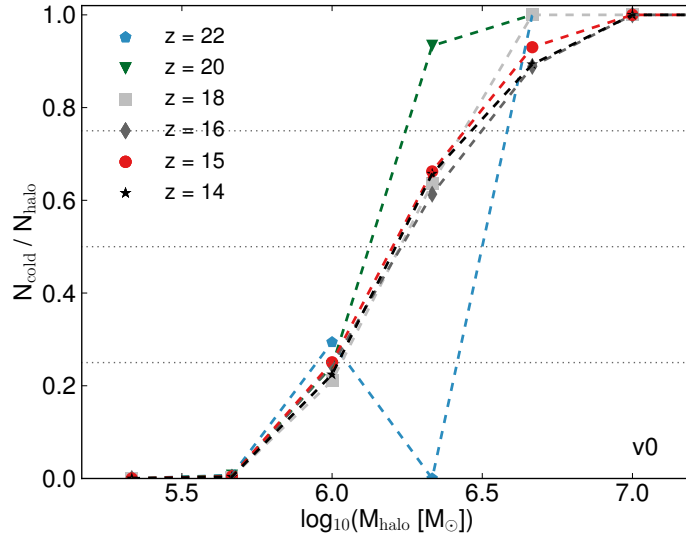


Figure 6.3.6: Fraction of haloes that contain cold gas plotted as function of halo mass for different redshifts in the range $14 \leq z \leq 22$. The dotted, grey horizontal lines mark the 25%, 50% and 75% transitions of $N_{\text{cold}}/N_{\text{halo}}$ from fewer to more cold haloes. $N_{\text{cold}}/N_{\text{all}}$ generally increases with halo mass. At redshift $z = 22$ we are limited by low number statistics.

that corresponds to a minimum halo mass. To quantify this, we show the fraction of haloes with at least one cold gas particle, N_{cold} , over the number of haloes in the mass bin, N_{all} , for different redshifts in Figure 6.3.6. At all times, the fraction $N_{\text{cold}}/N_{\text{all}}$ increases with halo mass M_{halo} . At redshifts $z \leq 22$, there is always a minimum halo mass above which more than 50% of all haloes harbour cold gas. The transition happens at $M_{\text{halo}} \approx 1.6 \times 10^6 M_{\odot}$ and is independent of redshift.

We show these two masses, the minimum halo mass $M_{\text{halo,min}}$ and the average halo mass $M_{\text{halo,50\%}}$ for Pop III star formation in Figure 6.3.7. In addition, we add several models from the literature for comparison.

Simulations by Yoshida et al. (2003, orange dot-dashed line) find a minimum halo mass of $\approx 7 \times 10^5 M_{\odot}$, which is about 50% larger than our value. As they are using a lower resolution (their best resolution is about a factor of lower, $m_{\text{gas}} \approx 42 M_{\odot}$), an earlier and less accurate treatment of the H_2 cooling function, as well as a higher density threshold for their cold gas ($n \geq 5 \times 10^2 \text{ cm}^{-3}$), this small discrepancy is not surprising.

Other authors have used semi-analytic models to predict the minimum halo mass. Trenti and Stiavelli (2009) find the minimum halo mass for gas to cool within a Hubble time to scale as $(z + 1)^{-2.074}$. While we cannot see this redshift depen-

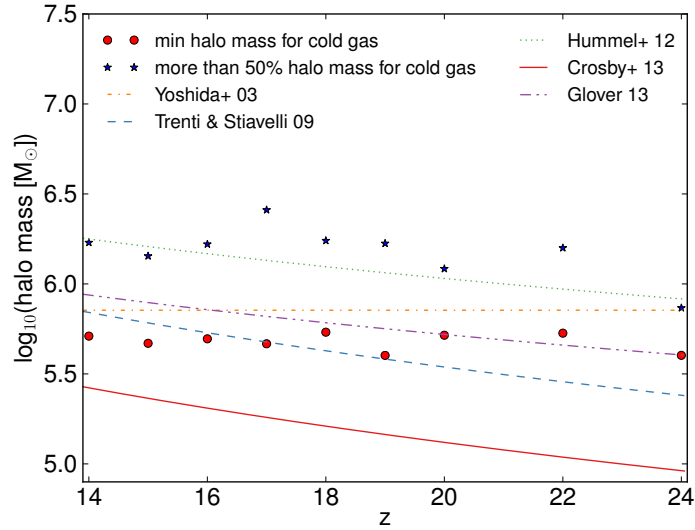


Figure 6.3.7: Minimum halo mass $M_{\text{halo},\text{min}}$ for a halo to contain cold gas and halo mass $M_{\text{halo},50\%}$ above which more than 50% of all haloes harbour cold, dense gas plotted as a function of redshift. Over-plotted are data from the literature from [Yoshida et al. \(2003\)](#), [Trenti and Stiavelli \(2009\)](#), [Hummel et al. \(2012\)](#), [Crosby et al. \(2013\)](#), [Glover \(2013\)](#). Note that the results from [Yoshida et al. \(2003\)](#) are empirical results from a cosmological simulation, while the other values are from toy models of cooling and collapse in high redshift minihaloes.

dence in our data, their predicted values are close to our simulation results, e.g. at redshift $z = 15$: $M_{\text{halo}}^{TS09}(z = 15) \approx 6.1 \times 10^5 M_{\odot}$. The predictions from [Hummel et al. \(2012\)](#) and [Glover \(2013\)](#) overestimate the masses, while [Crosby et al. \(2013\)](#) underestimates them.

6.3.2 STREAMING VELOCITIES

In this section, we study the influence of different streaming velocities on the ability of gas to cool and form stars. We start by looking at two effects that have been studied by other authors before and that we can confirm with our simulations.

Due to streaming velocities, it is harder for baryons to settle into a dark matter halo. We show the baryon fraction $M_{\text{bar}}/M_{\text{halo}}$ as a function of redshift in [Figure 6.3.8](#). Here, we measure the baryon fraction in haloes of $10^5 M_{\odot}$ or higher. For the simulation without streaming velocity and no LW background, the baryon fraction is close to the cosmic mean of $\Omega_b/\Omega_0 \approx 0.16$. However, as we increase the streaming velocity, the baryon fraction decreases, down to values as small as of 0.01 in the `v_3` run. This decrease in gas fraction has been predicted by [Tseliakhovich and Hirata \(2010\)](#) and seen in simulations before by several authors (e.g. [Tseliakhovich et al.](#),

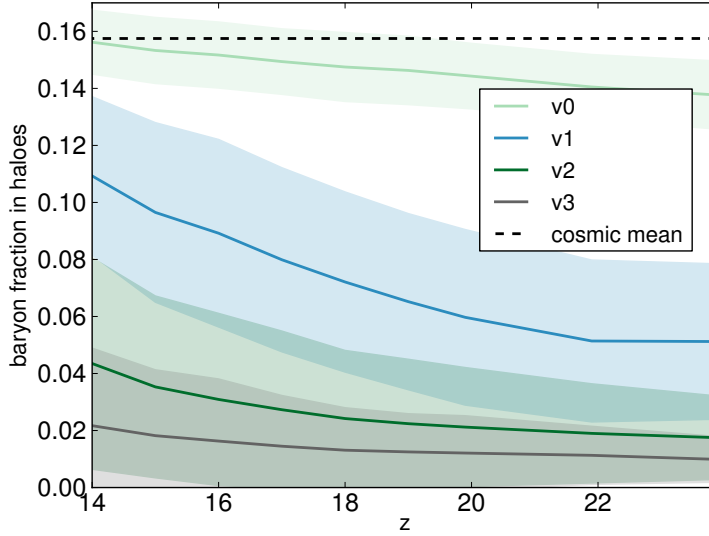


Figure 6.3.8: Baryon fraction in haloes with masses of $M_{\text{halo}} \leq 10^5 M_{\odot}$ as a function of redshift. In the case of zero streaming velocity (light green), the value approaches the cosmic mean (dashed grey line). For all simulations with non-zero streaming velocities (blue, dark green, grey), it is well below that value.

2011; Naoz et al., 2013) and we can confirm the effect for our data.

A second large-scale effect follows as a consequence: the halo mass function decreases in simulations of non-zero streaming velocity regions owing to the decreased contribution of baryons to the self-gravity of overdense regions. We show how the influence of streaming velocities lowers the cumulative halo mass function $N(> M_{\text{halo}})$ at redshift $z = 15$ in Figure 6.3.9 for all simulations in the small box. The suppression in our simulations is on the order of 10% to 25% in the mass range of $M_{\text{halo}} = 10^5 - 10^6 M_{\odot}$ at $z = 15$ per additional σ_{rms} streaming velocity. Naoz et al. (2012) see a decrease by 15% and 50% for $1.7\sigma_{\text{rms}}$ and $3.4\sigma_{\text{rms}}$ regions, respectively at redshift $z = 19$. Popa et al. (2016) find a similar decrease of small objects with $M_{\text{halo}} \leq 10^5 M_{\odot}$ of $\sim 60\%$ at redshift $z = 20$. Our results are therefore in good agreement with other recent studies.

We would like to note that Naoz et al. (2012) find overall lower halo mass functions when comparing to their simulation with normal $\sigma_8 = 0.82$. This may be due to the fact that they use only gas and dark matter within the virial radius to construct their halo masses, while we consider the mass of the whole structure found by the friends-of-friend algorithm.

Our study goes beyond these existing studies as we are able to follow the collapse

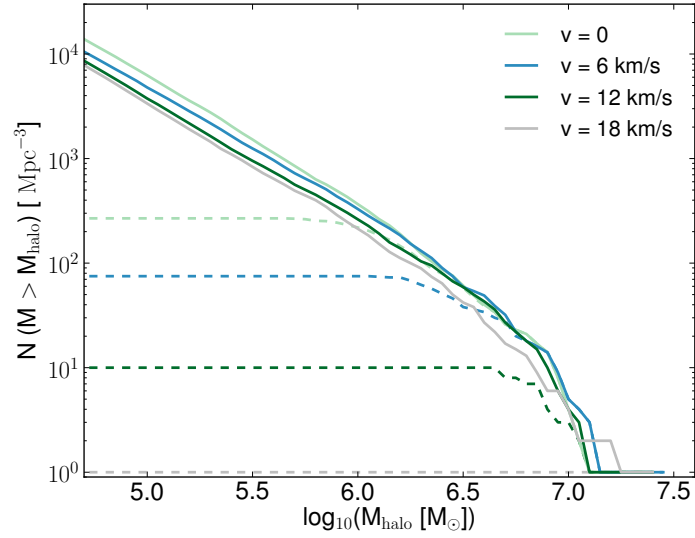


Figure 6.3.9: Cumulative halo mass function $N(> M_{\text{halo}})$ at redshift $z = 15$ for all simulation in the small box and streaming velocities of 0, 1, 2 and 3 σ_{rms} . The total number of haloes is shown as a solid line, the number of cold gas haloes as a dashed line.

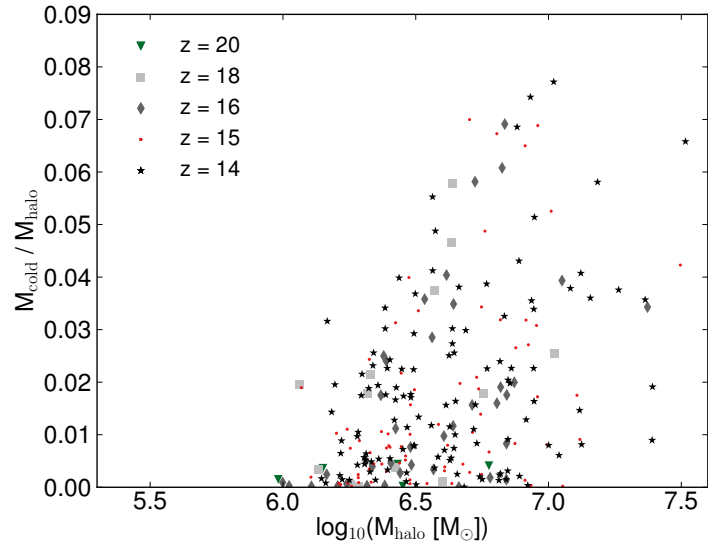


Figure 6.3.10: Cold gas fraction $M_{\text{cold}}/M_{\text{halo}}$ as a function of halo mass for the simulation with a streaming velocity of 1σ for redshifts in the range $14 \leq z \leq 20$. Values are only plotted for haloes that contain at least one cold gas cell.

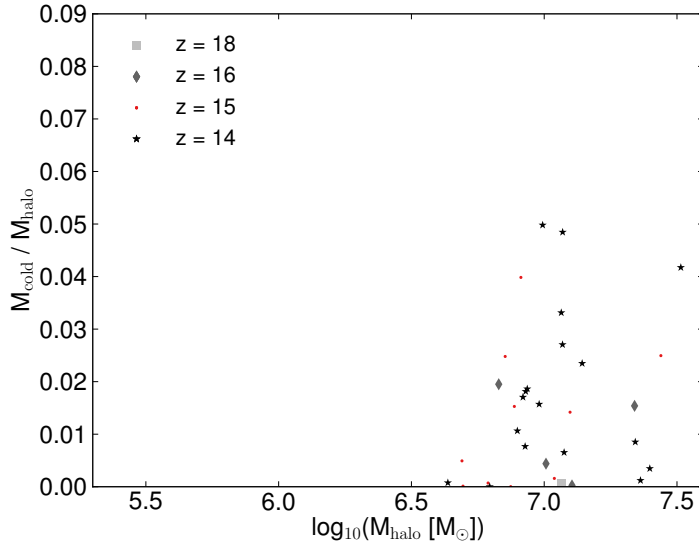


Figure 6.3.11: Cold gas fraction $M_{\text{cold}}/M_{\text{halo}}$ as a function of halo mass for the simulation with a streaming velocity of 2σ for redshifts in the range $14 \leq z \leq 18$. Values are only plotted for haloes that contain at least one cold gas cell.

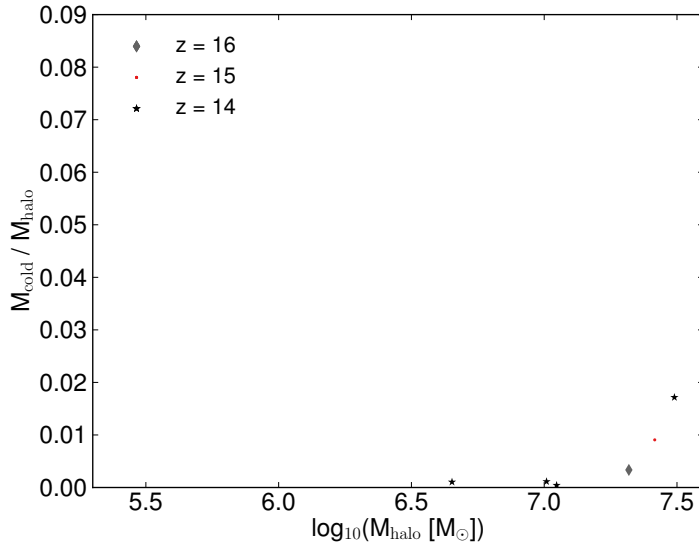


Figure 6.3.12: Cold gas fraction $M_{\text{cold}}/M_{\text{halo}}$ as a function of halo mass for the simulation with a streaming velocity of 3σ in the small box for redshifts in the range $14 \leq z \leq 16$. Values are only plotted for haloes that contain at least one cold gas cell.

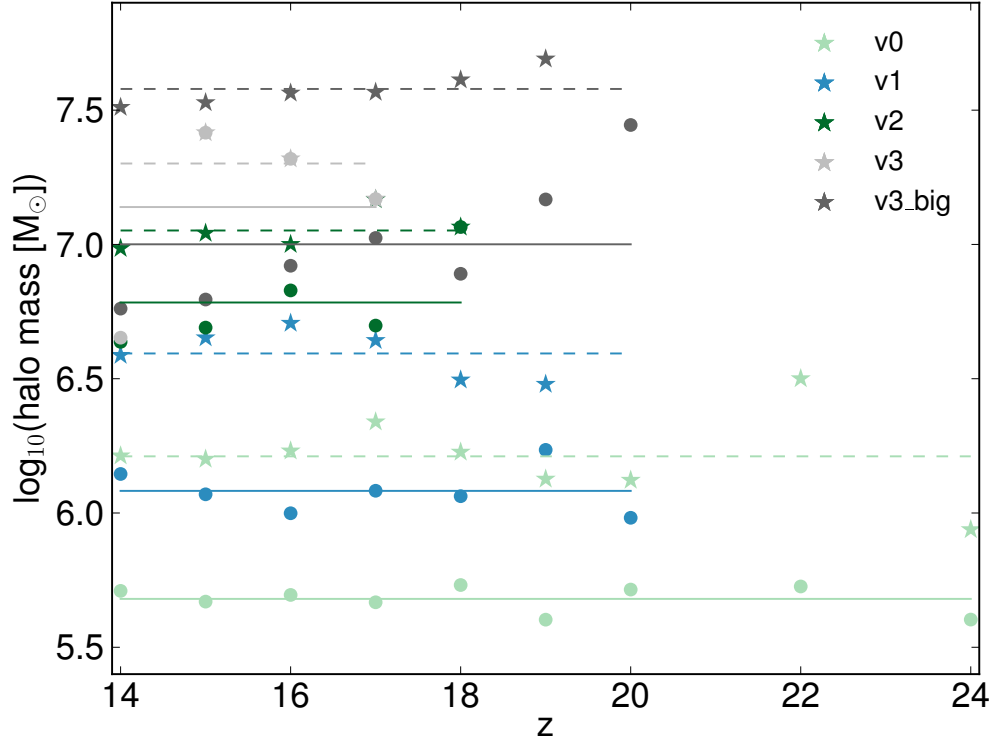


Figure 6.3.13: Halo mass of the first halo to contain cold gas (circles) and halo threshold mass above which more than 50% of all haloes contain cold gas (stars) as a function of redshift. The results for all simulations are shown here. Different colours indicate different streaming velocities. Solid lines show the average halo mass of the first halo to contain cold gas for the different streaming velocities, dashed lines show the average halo mass above which 50% of the haloes contain cold gas.

of gas to cold, dense structures in the centre of a halo. In Figures 6.3.10, 6.3.11 and 6.3.12 we show the cold mass fraction $M_{\text{cold}}/M_{\text{halo}}$ against halo mass M_{halo} for the three different streaming velocity simulations. Compared to the case of zero streaming in Figure 6.3.5, one can immediately see that the number of haloes in the figures decreases with increasing streaming velocity. This effect cannot be reduced to the decrease in halo mass function alone. In regions with high streaming velocity, cold gas can only assemble in more massive objects than in regions with zero streaming. This can be seen from the same figures, as the minimum halo mass for cold gas shifts to higher values.

Similar to Figure 6.3.7, we can give quantitative values for simulations of the different streaming velocity regions. Figure 6.3.13 shows the mass of the first cold halo and the halo mass threshold above which most of the haloes are cold. One can

see that the redshift for the first halo to contain cold gas decreases with increasing streaming velocity: for v1, the first halo with cold gas forms at redshift $z = 20$, for v2, it forms at $z = 18$ and for v3, it forms at $z = 17$.

The halo mass, above which more than 50% of the haloes contain cold gas, is independent of redshift and moves to higher halo masses for higher streaming velocities. The minimum halo mass $M_{\text{halo,min}}$ increases from $1.2 \times 10^6 M_{\odot}$ at 1σ by a factor of five to $6.1 \times 10^6 M_{\odot}$ at 2σ and by another factor of two to $1.4 \times 10^7 M_{\odot}$ at 3σ . The increase in halo mass $M_{\text{halo,50\%}}$ above which more than 50% of all haloes harbour cold gas is a factor of 1.3 larger, from $M_{\text{halo,50\%}} = 3.4 \times 10^6 M_{\odot}$ at 1σ to $1.3 \times 10^7 M_{\odot}$ at 2σ to $2.1 \times 10^7 M_{\odot}$ at 3σ .

Simulation v3 contains only four haloes with cold, dense gas at our final redshift $z = 14$. We therefore include the results from the large box v3_big in Figure 6.3.7. Due to the simulation volume that is increased by a factor of 64, we have many more and also more massive objects forming. The first halo in this simulation to contain cold gas is at redshift $z = 20$.

This offset in halo mass has been observed by Greif et al. (2011b), who find an average increase in halo mass by a factor of three for a streaming velocity of $1\sigma_{\text{rms}}$. This is very similar to our results, as we find an increase in the minimum halo mass by a factor of 2.5 and in the average halo mass by a factor of 2.4. Since we do not study the evolution of individual haloes, we do not see a delay of these haloes when becoming star forming. It is worthwhile noting that studies like Greif et al. (2011b) and Stacy et al. (2011) studied only the most massive object forming in their simulation volume. We, on the contrary, study all haloes in our simulation volume and thus have a statistically more valuable sample. We find an offset of a factor of four between the least massive halo that harbours cold gas and the 50% threshold for haloes to host cold gas in halo mass.

6.4 DISCUSSION AND CONCLUSION

We have performed five cosmological hydrodynamical simulations using the code AREPO, including a primordial chemistry network. They target different regions of the Universe with zero, 1, 2 and 3 σ_{rms} streaming velocity to understand the influence of the streaming velocity value on first star formation. Our employed resolution is very high throughout the box, leading to thousands of well-resolved minihaloes.

In a region of the Universe with zero streaming velocity, we find that the min-

imum mass above which a halo forms cold, dense gas in its centre is $M_{\text{halo,min}} \approx 4.8 \times 10^5 M_{\odot}$. At halo masses of $M_{\text{halo,50\%}} \approx 1.6 \times 10^6 M_{\odot}$ and above, more than 50% of the minihaloes contain cold, dense gas. In contrast to predictions from analytical studies, we do not see a dependence of this mass on redshift. Our minimum halo mass is a factor of $\sim 50\%$ larger than the value found by [Yoshida et al. \(2003\)](#).

In follow-up work, we will study the implications of LWBG radiation on the formation of cold gas in minihaloes for regions of the Universe with 0, 1, 2 and $3\sigma_{\text{rms}}$ streaming velocity. We will then be able to give consistent results for the suppression of Pop III star formation due to a LWBG in our large sample of highly resolved minihaloes. We will be able to determine which effect dominates the delay of Pop III star formation.

Furthermore, X-rays might play an important role, as they provide additional free electrons to trigger formation of molecular hydrogen and possibly enhance star formation (see e.g. [Glover and Brand, 2003](#)). In the future, we plan to include X-ray radiation as well to get a consistent picture of first star formation in the Universe.

ACKNOWLEDGMENTS

A. T. P. S. acknowledges support from the European Research Council under the European Community’s Seventh Framework Programme (FP7/2007 - 2013) via the ERC Advanced Grant “STARLIGHT: Formation of the First Stars” (project number 339177). S. C. O. G. and R. S. K. also acknowledge support from the Deutsche Forschungsgemeinschaft via SFB 881, “The Milky Way System” (sub-projects B1, B2 and B8) and SPP 1573, “Physics of the Interstellar Medium” (grant number GL 668/2-1).

6.A UPDATES TO THE CHEMICAL MODEL

The primordial chemistry model used in this study is based on the model implemented in AREPO by [Hartwig et al. \(2015b\)](#), but has been updated in several respects. The most significant difference is the inclusion of a simplified treatment of deuterium chemistry designed to track the formation and destruction of HD. Our treatment of the deuterium chemistry follows that in [Clark et al. \(2011\)](#) and full details can be found in that paper. In the interests of brevity, we do not repeat them here.

The second update involves our treatment of the dielectronic recombination of

ionized helium, He^+ . In [Hartwig et al. \(2015b\)](#) we used a rate for this process taken from [Aldrovandi and Pequignot \(1973\)](#). In our present study, we use instead the more recent determination by [Badnell \(2006\)](#). In practice, we expect this change to have no significant impact on our results, as at the gas temperatures probed in this study, very little ionized helium is present, and the small amount that is created recombines primarily via radiative recombination rather than dielectronic recombination.

Finally, we have also updated our treatment of H^- photodetachment. In all of our runs, we account for photodetachment of H^- by CMB photons. The rate for this process is given by the sum of two contributions, one describing the influence of the thermal CMB photons and a second describing the influence of the non-thermal radiation background produced by cosmic recombination at $z \sim 1100$ ([Hirata and Padmanabhan, 2006](#)). For the thermal contribution, we adopt the following rate coefficient from [Galli and Palla \(1998\)](#):

$$R_{\text{H}^-, \text{th}} = 0.11 T_{\text{r}}^{2.13} \exp\left(\frac{-8823\text{K}}{T_{\text{r}}}\right) \text{ s}^{-1} \quad (6.2)$$

where $T_{\text{r}} = T_{\text{CMB}} = 2.73(1+z)$ K. For the non-thermal contribution, we adopt the expression ([Coppola et al., 2011](#))

$$R_{\text{H}^-, \text{nth}} = 8 \times 10^{-8} T_{\text{r}}^{1.3} \exp\left(\frac{-2300\text{K}}{T_{\text{r}}}\right) \text{ s}^{-1}. \quad (6.3)$$

The total H^- photodetachment rate is simply the sum of these two terms.

6.B NUMERICAL CONVERGENCE OF BOX SIZES

We want to provide robust results that are numerically converged. Therefore, we test our fiducial resolution of 2×1024^3 particles in $(1 \text{ cMpc}/h)^3$ against larger and smaller mass resolutions with otherwise identical initial conditions. For simulations with box length of $500 \text{ ckpc}/h$, we vary the number of particles from 2×128^3 to 2×1024^3 in steps of eight. Therefore, the mass resolution changes between each simulation by a factor of 8. As a test case, we present variations of the simulation without feedback.

In [Figure 6.B.1](#) we show the cold gas mass against halo mass for the four realisations. One can see that for the two lower resolutions of 2×128^3 particles and 2×256^3 particles, the cold gas mass is lower than for the two higher resolution

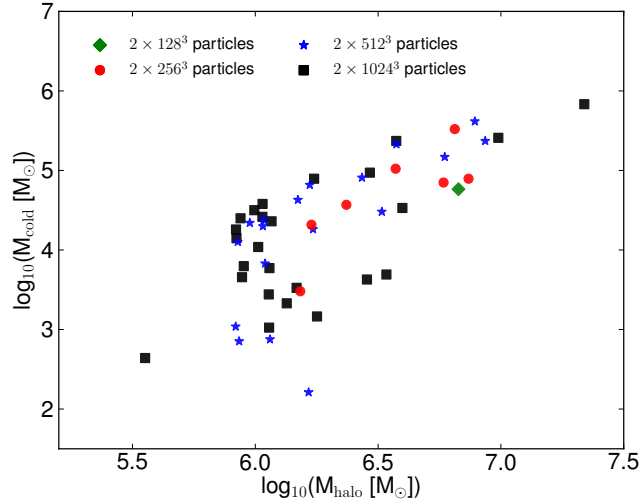


Figure 6.B.1: Resolution test: different number of particles and Voronoi cells for a cosmological box with the side length of $500 \text{ ckpc}/h$. There are many fewer red circles (2×256^3 particles) and only one green diamond (2×128^3 particles) than blue stars (2×512^3 particles) or black squares (2×1024^3 particles). Except for one halo at $\approx 10^{5.6} M_\odot$, the onset of efficient cooling at a halo mass $\approx 10^{5.8} M_\odot$ is the same for the 2×512^3 and 2×1024^3 runs.

cases. Our fiducial resolution of 2×512^3 particles agrees well with an even higher resolution of 2×1024^3 particles. We are therefore confident our simulations are well converged.

6.C COMPARISON OF FRIENDS-OF-FRIENDS RESULTS WITH SUBFIND

In the high-redshift Universe, minihaloes tend not to be spherical but instead are very elongated and irregular (see also [Sasaki et al., 2014](#)). Our results could therefore depend on the halo finding algorithm. In this Appendix, we provide a check to show that our results are independent of the halo selection algorithm. In this paper, we have considered all cold gas particles that were associated to a halo by the standard friends-of-friends (fof) algorithm. Another possibility is to consider only gas that belongs to the most bound subhalo in the fof structure. For this test, we use the halo finding algorithm subfind ([Springel et al., 2001](#)).

In [Figure 6.C.1](#), we show the cold gas mass as a function of halo mass for the simulation without LWBG or streaming at redshift $z = 15$ (red circles). Overplotted are the cold gas masses in the most bound subhaloes (black stars). The cold gas mass found in the most bound subhalo agrees very well with the cold gas mass found

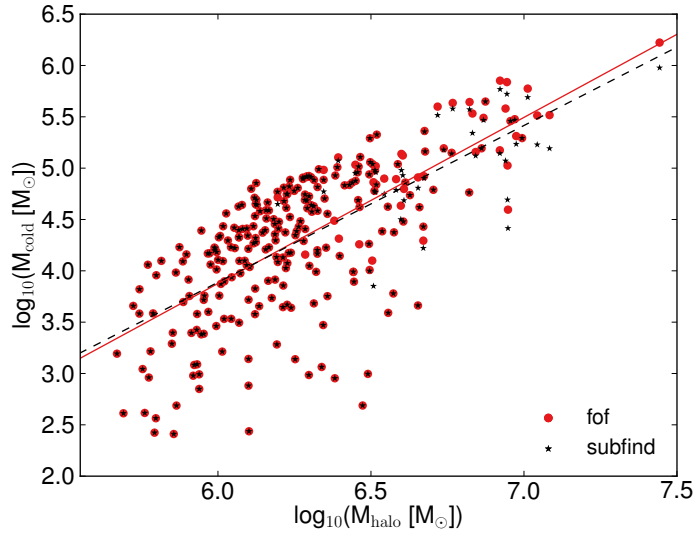


Figure 6.C.1: Cold gas mass against halo mass for the simulation without LWBG or streaming at redshift $z = 15$. We show the cold gas mass selected by two different halo finders: cold gas found in the whole fof structure (red circles) and cold gas only found in the most massive subhalo (black stars).

in the whole fof structure. At the highest halo masses, some halos contain more cold gas when considering only the most bound subhalo. We therefore conclude that for this study, our results are not sensitive to the halo finding algorithm.

6.D COLD MASS - HALO MASS RELATION

In Section 6.3.1, we have provided a fit for the cold gas mass - halo mass relation. As can be seen in Figure 6.3.2, the scatter is significant and should not be neglected when using our fitting approximation. Despite this caveat, we provide fits to all our simulations in Table 6.D.1 that could be used for semi-analytical calculations. The data in this table is given in the form

$$\log_{10}(M_{\text{cold}}) = a \times \log_{10}(M_{\text{halo}}) - b. \quad (6.4)$$

Name	a	b	a	b
z	15	15	20	20
v0	1.618	5.830	1.296	3.984
v1	1.771	7.229	1.161	3.759
v2	3.086	16.965	–	–
v3_big	1.739	7.658	2.815	15.988

Table 6.D.1: Cold gas mass - halo mass relation for all simulations at redshifts 15 and 20. Simulation v3 does not have enough data points at redshifts $z = 15$ or $z = 20$ to provide a fit.

7

Conclusion and Outlook

In this thesis, we have studied two effects that can delay the formation of the first stars: streaming velocities and Lyman-Werner radiation. We started by computing the escape fractions of LW photons from the first stars in minihaloes in Chapter 3 and from stellar populations in the first galaxies in Chapter 4.

With our one dimensional models, we are able to properly resolve the very thin shell of molecular hydrogen that can build up in front of the ionization front. This shell can lead to complete self-shielding of H_2 , preventing LW radiation from escaping from the source halo.

We distinguish two different regimes: the near-field and the far-field. In the near-field, we are sitting in the rest frame of the source and therefore in the line centres of the LW lines and can use self-shielding functions to describe the escape fraction. In the far-field, we assume that we are shifted out of resonance and consider how much radiation in the LW range from 11.2 eV to 13.6 eV has been absorbed.

We find that a massive $10^7 M_\odot$ halo can shield radiation even from a $120 M_\odot$ Pop III star completely in the near-field and reduces the escape fraction in the far-field to $\sim 70\%$. For lower-mass minihaloes, the escape fraction is usually larger, and increases with the mass of the stellar radiation source. Another important result is that shielding of H_2 by neutral hydrogen plays an important role; in

some cases, it can reduce the escape fraction by up to a factor of three.

In the follow-up study presented in Chapter 4, we investigate time-dependent spectra from stellar populations that are assumed to form in an instantaneous starburst. We consider initial mass functions for the stellar radiation sources that range from very extreme with a Salpeter slope and a minimum and maximum mass of 50 and $500 M_{\odot}$, to normal and similar to present day with a Kroupa shape and a minimum and maximum mass of 0.1 and $100 M_{\odot}$. Except for a very small star formation efficiency of 0.1%, the flux-averaged LW escape fraction is always larger than 50%. The build-up of the LWBG from stellar populations in their host galaxies is therefore efficient.

The results from these chapters have already been included in a semi-analytical merger tree model that uses a self-consistent LWBG. This code has been used for applications ranging from modelling the Pop III supernovae rate (Magg et al., 2016) to studies of the luminous Lyman α emitter CR7 (Hartwig et al., 2015c).

In Chapters 5 and 6, we studied the other important effect to delay first star formation: streaming of baryons relative to the dark matter. We performed cosmological hydrodynamical simulations with different streaming velocities that represent different regions of the Universe. We find that the minimum halo mass for cooling in a halo is $M_{\text{halo}} \sim 7 \times 10^5 M_{\odot}$ in regions with no streaming velocity. This value increases with higher streaming velocities. This minimum halo mass shows no dependence on redshift, contrary to expectations from simple toy models.

For regions with the highest streaming velocity values we investigate, three times the root-mean-squared value, the halo mass required for effective cooling shifts above the atomic cooling mass¹. We have studied whether these regions of the Universe are good sources for direct collapse black holes (see Chapter 5). We investigate all haloes whose centres have collapsed to number densities of $n \geq 10^4 \text{ cm}^{-3}$. All of them contain molecular hydrogen and their centres are cold. As H_2 formation is not suppressed, gas in these haloes will not collapse without fragmentation and form a supermassive star (and subsequently a very massive black hole). Instead, the gas will cool and fragment, giving rise to Pop III star formation.

In the synchronized halo model (as e.g. discussed by Agarwal et al., 2016; Regan et al., 2017), two neighbouring haloes are needed for DCBH formation that need to be well-synchronized in time and distance. One needs to collapse a few kyr to Myr earlier than the other, igniting a large star burst. The resulting LW radiation is then incident on the neighbouring halo, destroying its H_2 . When this second halo

¹The mass scale at which cooling is dominated initially by atomic hydrogen rather than H_2

collapses, it then forms one massive object as fragmentation is suppressed. The tight constraint on timing and the distance come from the fact that the LW flux seen by the second halo must be very large, but the haloes must be distant enough to avoid the first polluting the second with metals.

For this scenario to work, it is crucial that neither of the haloes are pre-enriched by metals. This means that their progenitor minihaloes must be prevented from forming stars. This can be achieved by a large LWBG (Regan et al., 2017), although this still leaves one with the problem of producing a sufficiently high background. However, we find in our study that in $3\sigma_{\text{rms}}$ streaming velocity regions, Pop III star formation in minihaloes is also suppressed. We conclude that these small haloes stay pristine and metal-free. Consequently, close pairs of atomic cooling haloes forming in regions of the Universe with $v_{\text{stream}} \geq 3\sigma_{\text{rms}}$ are good candidates for the formation sites of direct collapse black holes. Combining the number densities of the synchronized halo pairs estimated by Visbal et al. (2014b) and the volume fraction of the Universe with streaming velocity of $3\sigma_{\text{rms}}$ or higher, we find a number density for DCBHs of $\sim 1 \text{ cGpc}^{-3}$. This value is very close to the observed number density of high redshift quasars that has been estimated to be $\sim 0.7 \text{ cGpc}^{-3}$ (Fan et al., 2006). We therefore might explain the existence of these massive, early quasars with our model.

A lot of exciting future work is expecting us. We plan to continue the cosmological simulations run with AREPO, under the influence of a LWBG. We will use two uniform backgrounds of $0.1J_{21}$ and $0.01J_{21}$ and turn them on at high redshift $z = 40$. This simple model will let us determine the effect of LW radiation directly. We will study the same LWBG radiation in regions of the Universe with different streaming velocities. This will allow us to determine how large the delay of LWBG is on first star formation and whether the local streaming velocity or the LWBG plays a dominant role in delaying Pop III star formation.

With these numbers in hand, we can then develop a semi-analytic model for the LWBG that incorporates the suppression of Pop III star formation in regions with different streaming velocities and due to the LWBG itself. This new self-consistent model for the LWBG can then be employed in a simulation to yield realistic results for the star formation history of the Dark Ages. In the future, we would then like to combine these two negatives effects with X-rays, that are predicted to enhance star formation (see e.g. Glover and Brand, 2003).

To built upon our results, SPRAI, a new tool for the transport of ionizing photons in AREPO has been developed (Jaura et al. in prep). It is build upon the

Simplex (Paardekooper et al., 2010) algorithm, which transports ionizing photon packages between the cells of a Voroni mesh and can be used as a post-processing tool on a snapshot. With SPRAI, the ionizing photons will be transported on every hydrodynamical time step of the simulation.

With this new tool, we plan to determine the escape fractions of ionizing photons from minihaloes with the highest resolution up to date; simulations like FiBY or Renaissance can resolve minihaloes with ~ 100 gas particles (FiBY; Paardekooper et al., 2015) or even fewer gas cells (Renaissance; O’Shea et al., 2015; Xu et al., 2016). We will be able to increase that resolution by a factor of 50 – 200. We also plan to properly include binaries into our stellar radiation sources as their contribution might increase the escape fraction by a factors of 4-10 (Ma et al., 2016).

Following up on that project, I will further supervise a master student studying the spread of metals from supernova explosions in the previously photoevaporated minihaloes. We will be able to study many minihaloes at the same time, and develop a global picture of metal spreading in the early Universe and the transition to Pop II stars throughout the entire simulation volume of 1 cMpc^3 with high resolution.

Acknowledgments

First of all, I would like to thank my two supervisors, Ralf Klessen and Simon Glover, for their help and guidance through the last three years. I learned a lot during my PhD and am very grateful for their unlimited support and the possibility to present my results at many conferences.

I would also like to thank Volker Springel and his whole group for giving me opportunity to work with AREPO, the code I used for part of my thesis.

Thank you, Daniel Whalen, for supervising me when I started my PhD and for the nice projects we worked on together. And thank you, John Regan, for the good collaborative work on DCBHs.

Furthermore, I would like to thank my old group in Munich with Andi Burkert and Rhea-Silvia Remus for staying in touch, inviting me to the fabulous CAST-outings and continuing talking about the σ -bump.

My time here in Heidelberg is a blast, thanks to my friends and colleges at ITA and the great IMPRS program. Special thanks to my former and present office mates Mattis, Robin, Juan, Mattia, Bhakskar, Christian, Daniel, Eric, Sam, Utte, Onix, Poldo et al. I truly enjoyed the board game evenings, barbecues, mountains of ice cream and little pranks and am looking forward to your company for another year.

I would like to thank my dear friends inside and outside of Heidelberg for all the fun and good times and the support during bad times. Flo, Johannes, Inés, Martina, Maria, Caro, Chiara, Christian, Clio, Sara, Peter and Reza, I don't know what I would have done without you.

Abschliessend möchte ich mich ganz herzlich bei meinen Eltern, meiner Oma und meinem Flo für ihre uneingeschränkte Unterstützung während der gesamten Zeit, nicht nur hier in Heidelberg, bedanken.

List of Publications

The following publications have been used in this thesis:

1. **Schauer, A. T. P.**, Regan, J., Glover, S. C. O., and Klessen, R. S.
“The formation of direct collapse black holes under the influence of streaming velocities”.
ArXiv e-prints 1705.02347, accepted by MNRAS, May 2017b
doi: 10.1093/mnras/stx1915.
2. **Schauer, A. T. P.**, Agarwal, B., Glover, S. C. O., Klessen, R. S., Latif, M. A., Mas-Ribas, L., Rydberg, C.-E., Whalen, D. J., and Zackrisson, E.
“Lyman-Werner escape fractions from the first galaxies”.
MNRAS, 467:2288–2300, May 2017a.
doi: 10.1093/mnras/stx264.
3. **Schauer, A. T. P.**, Whalen, D. J., Glover, S. C. O., and Klessen, R. S.
“Lyman-Werner UV escape fractions from primordial haloes”.
MNRAS, 454:2441–2450, December 2015.
doi: 10.1093/mnras/stv2117.

The following publications have not been used in this thesis:

4. **Schauer, A. T. P.**, Schulze, F., Remus, R.-S., and Burkert, A.
“The σ -bump in elliptical galaxies - a signature of major mergers?”
In Gil de Paz, A., Knapen, J. H., and Lee, J. C., editors, *Formation and Evolution of Galaxy Outskirts*, volume 321 of *IAU Symposium*, pages 122–122, March 2017c.
doi: 10.1017/S1743921316009467.
5. **Schauer, A. T. P.**, Remus, R.-S., Burkert, A., and Johansson, P. H.
“The Mystery of the σ -Bump: A New Signature for Major Mergers in Early-type Galaxies?”
ApJ, 783:L32, March 2014.
doi: 10.1088/2041-8205/783/2/L32.

References

- Abbott, B. P., Abbott, R., Abbott, T. D., Abernathy, M. R., Acernese, F., Ackley, K., Adams, C., Adams, T., Addesso, P., Adhikari, R. X., and et al. Properties of the Binary Black Hole Merger GW150914. *Physical Review Letters*, 116(24):241102, June 2016a. doi: 10.1103/PhysRevLett.116.241102.
- Abbott, B. P., Abbott, R., Abbott, T. D., Abernathy, M. R., Acernese, F., Ackley, K., Adams, C., Adams, T., Addesso, P., Adhikari, R. X., and et al. GW151226: Observation of Gravitational Waves from a 22-Solar-Mass Binary Black Hole Coalescence. *Physical Review Letters*, 116(24):241103, June 2016b. doi: 10.1103/PhysRevLett.116.241103.
- Abbott, B. P., Abbott, R., Abbott, T. D., Acernese, F., Ackley, K., Adams, C., Adams, T., Addesso, P., Adhikari, R. X., Adya, V. B., and et al. GW170104: Observation of a 50-Solar-Mass Binary Black Hole Coalescence at Redshift 0.2. *Physical Review Letters*, 118(22):221101, June 2017. doi: 10.1103/PhysRevLett.118.221101.
- Abel, T., Bryan, G. L., and Norman, M. L. The Formation and Fragmentation of Primordial Molecular Clouds. *ApJ*, 540:39–44, September 2000. doi: 10.1086/309295.
- Abel, T., Bryan, G. L., and Norman, M. L. The Formation of the First Star in the Universe. *Science*, 295:93–98, January 2002. doi: 10.1126/science.1063991.
- Abel, T., Wise, J. H., and Bryan, G. L. The H II Region of a Primordial Star. *ApJ*, 659:L87–L90, April 2007. doi: 10.1086/516820.
- Abgrall, H. and Roueff, E. Wavelengths, oscillator strengths and transition probabilities of the H₂ molecule for Lyman and Werner systems. *A&AS*, 79:313–328, September 1989.
- Abgrall, H., Le Bourlot, J., Pineau Des Forets, G., Roueff, E., Flower, D. R., and Heck, L. Photodissociation of H₂ and the H/H₂ transition in interstellar clouds. *A&A*, 253:525–536, January 1992.
- Agarwal, B. and Khochfar, S. Revised rate coefficients for H₂ and H⁻ destruction by realistic stellar spectra. *MNRAS*, 446:160–168, January 2015. doi: 10.1093/mnras/stu1973.

- Agarwal, B., Khochfar, S., Johnson, J. L., Neistein, E., Dalla Vecchia, C., and Livio, M. Ubiquitous seeding of supermassive black holes by direct collapse. *MNRAS*, 425:2854–2871, October 2012. doi: 10.1111/j.1365-2966.2012.21651.x.
- Agarwal, B., Dalla Vecchia, C., Johnson, J. L., Khochfar, S., and Paardekooper, J.-P. The First Billion Years project: birthplaces of direct collapse black holes. *MNRAS*, 443:648–657, September 2014. doi: 10.1093/mnras/stu1112.
- Agarwal, B., Johnson, J. L., Zackrisson, E., Labbe, I., van den Bosch, F. C., Natarajan, P., and Khochfar, S. Detecting Direct Collapse Black Holes: making the case for CR7. *ArXiv: 1510.01733*, October 2015.
- Agarwal, B., Smith, B., Glover, S., Natarajan, P., and Khochfar, S. New constraints on direct collapse black hole formation in the early Universe. *MNRAS*, 459:4209, April 2016.
- Agarwal, B., Regan, J., Klessen, R. S., Downes, T. P., and Zackrisson, E. An analytic resolution to the competition between Lyman-Werner radiation and metal winds in direct collapse black hole hosts. *MNRAS*, *submitted*; *arXiv:1703.08181*, March 2017.
- Ahn, K., Shapiro, P. R., Iliev, I. T., Mellema, G., and Pen, U. The Inhomogeneous Background Of H₂-Dissociating Radiation During Cosmic Reionization. *ApJ*, 695:1430–1445, April 2009. doi: 10.1088/0004-637X/695/2/1430.
- Ahn, K., Iliev, I. T., Shapiro, P. R., Mellema, G., Koda, J., and Mao, Y. Detecting the Rise and Fall of the First Stars by Their Impact on Cosmic Reionization. *ApJ*, 756:L16, September 2012. doi: 10.1088/2041-8205/756/1/L16.
- Ahn, K., Xu, H., Norman, M. L., Alvarez, M. A., and Wise, J. H. Spatially Extended 21 cm Signal from Strongly Clustered Uv and X-Ray Sources in the Early Universe. *ApJ*, 802:8, March 2015. doi: 10.1088/0004-637X/802/1/8.
- Aldrovandi, S. M. V. and Pequignot, D. Radiative and Dielectronic Recombination Coefficients for Complex Ions. *A&A*, 25:137, May 1973.
- Alexander, T. and Natarajan, P. Rapid growth of seed black holes in the early universe by supra-exponential accretion. *Science*, 345:1330–1333, September 2014. doi: 10.1126/science.1251053.
- Ali, Z. S., Parsons, A. R., Zheng, H., Pober, J. C., Liu, A., Aguirre, J. E., Bradley, R. F., Bernardi, G., Carilli, C. L., Cheng, C., DeBoer, D. R., Dexter, M. R., Grobelaar, J., Horrell, J., Jacobs, D. C., Klima, P., MacMahon, D. H. E., Maree, M., Moore, D. F., Razavi, N., Stefan, I. I., Walbrugh, W. P., and Walker, A. PAPER-64 Constraints on Reionization: The 21 cm Power Spectrum at $z = 8.4$. *ApJ*, 809:61, August 2015. doi: 10.1088/0004-637X/809/1/61.

- Alizadeh, E. and Hirata, C. M. Molecular hydrogen in the cosmic recombination epoch. *Phys. Rev. D*, 84(8):083011, October 2011. doi: 10.1103/PhysRevD.84.083011.
- Alvarez, M. A., Bromm, V., and Shapiro, P. R. The H II Region of the First Star. *ApJ*, 639:621–632, March 2006. doi: 10.1086/499578.
- Alvarez, M. A., Wise, J. H., and Abel, T. Accretion onto the First Stellar-Mass Black Holes. *ApJ*, 701:L133–L137, August 2009. doi: 10.1088/0004-637X/701/2/L133.
- Anninos, P., Zhang, Y., Abel, T., and Norman, M. L. Cosmological hydrodynamics with multi-species chemistry and nonequilibrium ionization and cooling. *New Astronomy*, 2:209–224, August 1997. doi: 10.1016/S1384-1076(97)00009-2.
- Badnell, N. R. Dielectronic recombination data for dynamic finite-density plasmas. X. The hydrogen isoelectronic sequence. *A&A*, 447:389–395, February 2006. doi: 10.1051/0004-6361:20053269.
- Baker, J. G., McWilliams, S. T., van Meter, J. R., Centrella, J., Choi, D.-I., Kelly, B. J., and Koppitz, M. Binary black hole late inspiral: Simulations for gravitational wave observations. *Phys. Rev. D*, 75(12):124024, June 2007. doi: 10.1103/PhysRevD.75.124024.
- Barkana, R. and Loeb, A. Effective Screening Due to Minihalos during the Epoch of Reionization. *ApJ*, 578:1–11, October 2002. doi: 10.1086/342313.
- Barkana, R. and Loeb, A. In the beginning: the first sources of light and the reionization of the universe. *Phys. Rep.*, 349:125–238, July 2001. doi: 10.1016/S0370-1573(01)00019-9.
- Barnes, J. and Hut, P. A hierarchical $O(N \log N)$ force-calculation algorithm. *Nature*, 324:446–449, December 1986. doi: 10.1038/324446a0.
- Becker, R. H., Fan, X., White, R. L., Strauss, M. A., Narayanan, V. K., Lupton, R. H., Gunn, J. E., Annis, J., Bahcall, N. A., Brinkmann, J., Connolly, A. J., Csabai, I., Czarapata, P. C., Doi, M., Heckman, T. M., Hennessy, G. S., Ivezić, Ž., Knapp, G. R., Lamb, D. Q., McKay, T. A., Munn, J. A., Nash, T., Nichol, R., Pier, J. R., Richards, G. T., Schneider, D. P., Stoughton, C., Szalay, A. S., Thakar, A. R., and York, D. G. Evidence for Reionization at $z \sim 6$: Detection of a Gunn-Peterson Trough in a $z=6.28$ Quasar. *AJ*, 122:2850–2857, December 2001. doi: 10.1086/324231.
- Beers, T. C. and Christlieb, N. The Discovery and Analysis of Very Metal-Poor Stars in the Galaxy. *ARA&A*, 43:531–580, September 2005. doi: 10.1146/annurev.astro.42.053102.134057.

- Begelman, M. C., Volonteri, M., and Rees, M. J. Formation of supermassive black holes by direct collapse in pre-galactic haloes. *MNRAS*, 370:289–298, July 2006. doi: 10.1111/j.1365-2966.2006.10467.x.
- Belafhal, A. The shape of spectral lines: widths and equivalent widths of the Voigt profile. *Opt. Comm.*, 177:111–118, April 2000.
- Bocquet, S., Saro, A., Dolag, K., and Mohr, J. J. Halo mass function: baryon impact, fitting formulae, and implications for cluster cosmology. *MNRAS*, 456:2361–2373, March 2016. doi: 10.1093/mnras/stv2657.
- Bowler, R. A. A., McLure, R. J., Dunlop, J. S., McLeod, D. J., Stanway, E. R., Eldridge, J. J., and Jarvis, M. J. No evidence for Population III stars or a Direct Collapse Black Hole in the $z = 6.6$ Lyman- α emitter 'CR7'. *ArXiv 1609.00727*, September 2016.
- Bromm, V. Formation of the first stars. *Reports on Progress in Physics*, 76(11):112901, November 2013. doi: 10.1088/0034-4885/76/11/112901.
- Bromm, V. and Loeb, A. Formation of the First Supermassive Black Holes. *ApJ*, 596:34–46, October 2003. doi: 10.1086/377529.
- Bromm, V., Coppi, P. S., and Larson, R. B. Forming the First Stars in the Universe: The Fragmentation of Primordial Gas. *ApJ*, 527:L5–L8, December 1999. doi: 10.1086/312385.
- Bromm, V., Coppi, P. S., and Larson, R. B. The Formation of the First Stars. I. The Primordial Star-forming Cloud. *ApJ*, 564:23–51, January 2002. doi: 10.1086/323947.
- Bryan, G. L., Norman, M. L., O’Shea, B. W., Abel, T., Wise, J. H., Turk, M. J., Reynolds, D. R., Collins, D. C., Wang, P., Skillman, S. W., Smith, B., Harkness, R. P., Bordner, J., Kim, J.-h., Kuhlen, M., Xu, H., Goldbaum, N., Hummels, C., Kritsuk, A. G., Tasker, E., Skory, S., Simpson, C. M., Hahn, O., Oishi, J. S., So, G. C., Zhao, F., Cen, R., Li, Y., and Enzo Collaboration. ENZO: An Adaptive Mesh Refinement Code for Astrophysics. *ApJS*, 211:19, April 2014. doi: 10.1088/0067-0049/211/2/19.
- Chandrasekhar, S. The Dynamical Instability of Gaseous Masses Approaching the Schwarzschild Limit in General Relativity. *ApJ*, 140:417–+, August 1964.
- Ciardi, B. and Ferrara, A. The First Cosmic Structures and Their Effects. *Space Sci. Rev.*, 116:625–705, February 2005. doi: 10.1007/s11214-005-3592-0.
- Ciardi, B., Scannapieco, E., Stoehr, F., Ferrara, A., Iliev, I. T., and Shapiro, P. R. The effect of minihaloes on cosmic reionization. *MNRAS*, 366:689–696, February 2006. doi: 10.1111/j.1365-2966.2005.09908.x.

- Clark, P. C., Glover, S. C. O., and Klessen, R. S. The First Stellar Cluster. *ApJ*, 672:757-764, January 2008. doi: 10.1086/524187.
- Clark, P. C., Glover, S. C. O., Klessen, R. S., and Bromm, V. Gravitational Fragmentation in Turbulent Primordial Gas and the Initial Mass Function of Population III Stars. *ApJ*, 727:110, February 2011. doi: 10.1088/0004-637X/727/2/110.
- Clark, P. C., Glover, S. C. O., Smith, R. J., Greif, T. H., Klessen, R. S., and Bromm, V. The Formation and Fragmentation of Disks Around Primordial Protostars. *Science*, 331:1040–, February 2011b. doi: 10.1126/science.1198027.
- Coppola, C. M., Longo, S., Capitelli, M., Palla, F., and Galli, D. Vibrational Level Population of H_2 and H^+_2 in the Early Universe. *ApJS*, 193:7, March 2011. doi: 10.1088/0067-0049/193/1/7.
- Crosby, B. D., O’Shea, B. W., Smith, B. D., Turk, M. J., and Hahn, O. Population III Star Formation in Large Cosmological Volumes. I. Halo Temporal and Physical Environment. *ApJ*, 773:108, August 2013. doi: 10.1088/0004-637X/773/2/108.
- Cyburt, R. H., Fields, B. D., and Olive, K. A. An update on the big bang nucleosynthesis prediction for ${}^7\text{Li}$: the problem worsens. *J. Cosmology Astropart. Phys.*, 11:012, November 2008. doi: 10.1088/1475-7516/2008/11/012.
- Dijkstra, M., Haiman, Z., Mesinger, A., and Wyithe, J. S. B. Fluctuations in the high-redshift Lyman-Werner background: close halo pairs as the origin of supermassive black holes. *MNRAS*, 391:1961–1972, December 2008. doi: 10.1111/j.1365-2966.2008.14031.x.
- Dijkstra, M., Ferrara, A., and Mesinger, A. Feedback-regulated supermassive black hole seed formation. *MNRAS*, 442:2036–2047, August 2014. doi: 10.1093/mnras/stu1007.
- Dijkstra, M., Gronke, M., and Sobral, D. $\text{Ly}\alpha$ Signatures from Direct Collapse Black Holes. *ApJ*, 823:74, June 2016. doi: 10.3847/0004-637X/823/2/74.
- Dopcke, G., Glover, S. C. O., Clark, P. C., and Klessen, R. S. On the Initial Mass Function of Low-metallicity Stars: The Importance of Dust Cooling. *ApJ*, 766:103, April 2013. doi: 10.1088/0004-637X/766/2/103.
- Draine, B. T. and Bertoldi, F. Structure of Stationary Photodissociation Fronts. *ApJ*, 468:269–+, September 1996. doi: 10.1086/177689.
- Eisenstein, D. J. and Hu, W. Baryonic Features in the Matter Transfer Function. *ApJ*, 496:605–614, March 1998. doi: 10.1086/305424.
- Eisenstein, D. J. and Loeb, A. Origin of quasar progenitors from the collapse of low-spin cosmological perturbations. *ApJ*, 443:11–17, April 1995. doi: 10.1086/175498.

- Ekström, S., Meynet, G., and Maeder, A. Can Very Massive Stars Avoid Pair-Instability Supernovae? In Bresolin, F., Crowther, P. A., and Puls, J., editors, *Massive Stars as Cosmic Engines*, volume 250 of *IAU Symposium*, pages 209–216, June 2008. doi: 10.1017/S1743921308020516.
- Fan, X. Evolution of high-redshift quasars. *New A Rev.*, 50:665–671, November 2006. doi: 10.1016/j.newar.2006.06.077.
- Fan, X., Strauss, M. A., Richards, G. T., Hennawi, J. F., Becker, R. H., White, R. L., Diamond-Stanic, A. M., Donley, J. L., Jiang, L., Kim, J. S., Vestergaard, M., Young, J. E., Gunn, J. E., Lupton, R. H., Knapp, G. R., Schneider, D. P., Brandt, W. N., Bahcall, N. A., Barentine, J. C., Brinkmann, J., Brewington, H. J., Fukugita, M., Harvanek, M., Kleinman, S. J., Krzesinski, J., Long, D., Neilsen, E. H., Jr., Nitta, A., Snedden, S. A., and Voges, W. A Survey of $z > 5.7$ Quasars in the Sloan Digital Sky Survey. IV. Discovery of Seven Additional Quasars. *AJ*, 131:1203–1209, March 2006. doi: 10.1086/500296.
- Ferland, G. J., Porter, R. L., van Hoof, P. A. M., Williams, R. J. R., Abel, N. P., Lykins, M. L., Shaw, G., Henney, W. J., and Stancil, P. C. The 2013 Release of Cloudy. *Rev. Mexicana Astron. Astrofis.*, 49:137–163, April 2013.
- Fernandez, R., Bryan, G. L., Haiman, Z., and Li, M. H_2 suppression with shocking inflows: testing a pathway for supermassive black hole formation. *MNRAS*, 439:3798–3807, April 2014. doi: 10.1093/mnras/stu230.
- Fialkov, A. Supersonic relative velocity between dark matter and baryons: A review. *International Journal of Modern Physics D*, 23:1430017, July 2014. doi: 10.1142/S0218271814300171.
- Fialkov, A., Barkana, R., Tseliakhovich, D., and Hirata, C. M. Impact of the relative motion between the dark matter and baryons on the first stars: semi-analytical modelling. *MNRAS*, 424:1335–1345, August 2012. doi: 10.1111/j.1365-2966.2012.21318.x.
- Fialkov, A., Barkana, R., Visbal, E., Tseliakhovich, D., and Hirata, C. M. The 21-cm signature of the first stars during the Lyman-Werner feedback era. *MNRAS*, 432:2909–2916, July 2013. doi: 10.1093/mnras/stt650.
- Field, G. B., Somerville, W. B., and Dressler, K. Hydrogen Molecules in Astronomy. *ARA&A*, 4:207, 1966. doi: 10.1146/annurev.aa.04.090166.001231.
- Finkelstein, S. L., Dunlop, J., Le Fevre, O., and Wilkins, S. The Case for a James Webb Space Telescope Extragalactic Key Project. *ArXiv e-prints*, December 2015.
- Fixsen, D. J., Cheng, E. S., Gales, J. M., Mather, J. C., Shafer, R. A., and Wright, E. L. The Cosmic Microwave Background Spectrum from the Full COBE FIRAS Data Set. *ApJ*, 473:576, December 1996. doi: 10.1086/178173.

- Frebel, A. Stellar archaeology: Exploring the Universe with metal-poor stars. *Astronomische Nachrichten*, 331:474–488, May 2010. doi: 10.1002/asna.201011362.
- Frebel, A., Johnson, J. L., and Bromm, V. Stellar Archaeology: Using Metal-Poor Stars to Test Theories of the Early Universe. In Hunt, L. K., Madden, S. C., and Schneider, R., editors, *IAU Symposium*, volume 255 of *IAU Symposium*, pages 336–340, December 2008. doi: 10.1017/S1743921308025039.
- Frebel, A., Johnson, J. L., and Bromm, V. The minimum stellar metallicity observable in the Galaxy. *MNRAS*, 392:L50–L54, January 2009. doi: 10.1111/j.1745-3933.2008.00587.x.
- Frebel, A. et al. Nucleosynthetic signatures of the first stars. *Nature*, 434:871–873, April 2005. doi: 10.1038/nature03455.
- Friedmann, A. Über die Krümmung des Raumes. *Zeitschrift für Physik*, 10:377–386, 1922. doi: 10.1007/BF01332580.
- Fryer, C. L., Woosley, S. E., and Heger, A. Pair-Instability Supernovae, Gravity Waves, and Gamma-Ray Transients. *ApJ*, 550:372–382, March 2001. doi: 10.1086/319719.
- Fryxell, B., Olson, K., Ricker, P., Timmes, F. X., Zingale, M., Lamb, D. Q., MacNeice, P., Rosner, R., Truran, J. W., and Tufo, H. FLASH: An Adaptive Mesh Hydrodynamics Code for Modeling Astrophysical Thermonuclear Flashes. *ApJS*, 131:273–334, November 2000. doi: 10.1086/317361.
- Galli, D. and Palla, F. The chemistry of the early Universe. *A&A*, 335:403–420, July 1998.
- Gebhardt, K., Adams, J., Richstone, D., Lauer, T. R., Faber, S. M., Gültekin, K., Murphy, J., and Tremaine, S. The Black Hole Mass in M87 from Gemini/NIFS Adaptive Optics Observations. *ApJ*, 729:119, March 2011. doi: 10.1088/0004-637X/729/2/119.
- Gillessen, S., Eisenhauer, F., Trippe, S., Alexander, T., Genzel, R., Martins, F., and Ott, T. Monitoring Stellar Orbits Around the Massive Black Hole in the Galactic Center. *ApJ*, 692:1075–1109, February 2009. doi: 10.1088/0004-637X/692/2/1075.
- Glover, S. The First Stars. In Wiklund, T., Mobasher, B., and Bromm, V., editors, *The First Galaxies*, volume 396 of *Astrophysics and Space Science Library*, page 103, 2013. doi: 10.1007/978-3-642-32362-1_3.
- Glover, S. The Formation Of The First Stars In The Universe. *Space Sci. Rev.*, 117: 445–508, April 2005. doi: 10.1007/s11214-005-5821-y.

- Glover, S. C. O. Simulating the formation of massive seed black holes in the early Universe. III: The influence of X-rays. *arXiv:1610.05679*, October 2016.
- Glover, S. C. O. Simulating the formation of massive seed black holes in the early Universe - I. An improved chemical model. *MNRAS*, 451:2082–2096, August 2015. doi: 10.1093/mnras/stv1059.
- Glover, S. C. O. and Abel, T. Uncertainties in H₂ and HD chemistry and cooling and their role in early structure formation. *MNRAS*, 388:1627–1651, August 2008. doi: 10.1111/j.1365-2966.2008.13224.x.
- Glover, S. C. O. and Brand, P. W. J. L. On the photodissociation of H₂ by the first stars. *MNRAS*, 321:385–397, March 2001. doi: 10.1046/j.1365-8711.2001.03993.x.
- Glover, S. C. O. and Brand, P. W. J. L. Radiative feedback from an early X-ray background. *MNRAS*, 340:210–226, March 2003. doi: 10.1046/j.1365-8711.2003.06311.x.
- Glover, S. C. O. and Jappsen, A.-K. Star Formation at Very Low Metallicity. I. Chemistry and Cooling at Low Densities. *ApJ*, 666:1–19, September 2007. doi: 10.1086/519445.
- Glover, S. C. O. and Savin, D. W. Is H⁺₃ cooling ever important in primordial gas? *MNRAS*, 393:911–948, March 2009. doi: 10.1111/j.1365-2966.2008.14156.x.
- Gould, R. J. and Salpeter, E. E. The Interstellar Abundance of the Hydrogen Molecule. I. Basic Processes. *ApJ*, 138:393, August 1963. doi: 10.1086/147654.
- Grand, R. J. J., Gómez, F. A., Marinacci, F., Pakmor, R., Springel, V., Campbell, D. J. R., Frenk, C. S., Jenkins, A., and White, S. D. M. The Auriga Project: the properties and formation mechanisms of disc galaxies across cosmic time. *MNRAS*, 467:179–207, May 2017. doi: 10.1093/mnras/stx071.
- Greif, T. H., Johnson, J. L., Klessen, R. S., and Bromm, V. The observational signature of the first HII regions. *MNRAS*, 399:639–649, October 2009. doi: 10.1111/j.1365-2966.2009.15336.x.
- Greif, T. H., Glover, S. C. O., Bromm, V., and Klessen, R. S. The First Galaxies: Chemical Enrichment, Mixing, and Star Formation. *ApJ*, 716:510–520, June 2010. doi: 10.1088/0004-637X/716/1/510.
- Greif, T. H., Springel, V., White, S. D. M., Glover, S. C. O., Clark, P. C., Smith, R. J., Klessen, R. S., and Bromm, V. Simulations on a Moving Mesh: The Clustered Formation of Population III Protostars. *ApJ*, 737:75, August 2011a. doi: 10.1088/0004-637X/737/2/75.
- Greif, T. H., White, S. D. M., Klessen, R. S., and Springel, V. The Delay of Population III Star Formation by Supersonic Streaming Velocities. *ApJ*, 736:147, August 2011b. doi: 10.1088/0004-637X/736/2/147.

- Greif, T. H., Bromm, V., Clark, P. C., Glover, S. C. O., Smith, R. J., Klessen, R. S., Yoshida, N., and Springel, V. Formation and evolution of primordial protostellar systems. *MNRAS*, 424:399–415, July 2012. doi: 10.1111/j.1365-2966.2012.21212.x.
- Haehnelt, M. G. and Rees, M. J. The formation of nuclei in newly formed galaxies and the evolution of the quasar population. *MNRAS*, 263:168–178, July 1993.
- Hahn, O. and Abel, T. Multi-scale initial conditions for cosmological simulations. *MNRAS*, 415:2101–2121, August 2011. doi: 10.1111/j.1365-2966.2011.18820.x.
- Haiman, Z., Rees, M. J., and Loeb, A. Destruction of Molecular Hydrogen during Cosmological Reionization. *ApJ*, 476:458–, February 1997. doi: 10.1086/303647.
- Haiman, Z., Abel, T., and Rees, M. J. The Radiative Feedback of the First Cosmological Objects. *ApJ*, 534:11–24, May 2000. doi: 10.1086/308723.
- Haiman, Z., Abel, T., and Madau, P. Photon Consumption in Minihalos during Cosmological Reionization. *ApJ*, 551:599–607, April 2001. doi: 10.1086/320232.
- Hartwig, T., Bromm, V., Klessen, R. S., and Glover, S. C. O. Constraining the primordial initial mass function with stellar archaeology. *MNRAS*, 447:3892–3908, March 2015a. doi: 10.1093/mnras/stu2740.
- Hartwig, T., Glover, S. C. O., Klessen, R. S., Latif, M. A., and Volonteri, M. How an improved implementation of H₂ self-shielding influences the formation of massive stars and black holes. *MNRAS*, 452:1233–1244, September 2015b. doi: 10.1093/mnras/stv1368.
- Hartwig, T., Latif, M. A., Magg, M., Bromm, V., Klessen, R. S., Glover, S. C. O., Whalen, D. J., Pellegrini, E. W., and Volonteri, M. Exploring the nature of the Lyman- α emitter CR7. *ArXiv: 1512.01111*, December 2015c.
- Hartwig, T., Volonteri, M., Bromm, V., Klessen, R. S., Barausse, E., Magg, M., and Stacy, A. Gravitational waves from the remnants of the first stars. *MNRAS*, 460: L74–L78, July 2016. doi: 10.1093/mnrasl/slw074.
- Hasegawa, K., Umemura, M., and Susa, H. Radiative regulation of Population III star formation. *MNRAS*, 395:1280, April 2009. doi: 10.1111/j.1365-2966.2009.14639.x.
- Hayes, J. C., Norman, M. L., Fiedler, R. A., Bordner, J. O., Li, P. S., Clark, S. E., ud-Doula, A., and Mac Low, M.-M. Simulating Radiating and Magnetized Flows in Multiple Dimensions with ZEUS-MP. *ApJS*, 165:188–228, July 2006. doi: 10.1086/504594.
- Heger, A. and Woosley, S. E. The Nucleosynthetic Signature of Population III. *ApJ*, 567:532–543, March 2002. doi: 10.1086/338487.

- Helfand, D. J. and Moran, E. C. The Hard X-Ray Luminosity of OB Star Populations: Implications for The Contribution of Star Formation to the Cosmic X-Ray Background. *ApJ*, 554:27–42, June 2001. doi: 10.1086/321368.
- Hirano, S., Hosokawa, T., Yoshida, N., Umeda, H., Omukai, K., Chiaki, G., and Yorke, H. W. One Hundred First Stars: Protostellar Evolution and the Final Masses. *ApJ*, 781:60, February 2014. doi: 10.1088/0004-637X/781/2/60.
- Hirano, S., Hosokawa, T., Yoshida, N., Omukai, K., and Yorke, H. W. Primordial star formation under the influence of far ultraviolet radiation: 1540 cosmological haloes and the stellar mass distribution. *MNRAS*, 448:568–587, March 2015. doi: 10.1093/mnras/stv044.
- Hirata, C. M. and Padmanabhan, N. Cosmological production of H_2 before the formation of the first galaxies. *MNRAS*, 372:1175–1186, November 2006. doi: 10.1111/j.1365-2966.2006.10924.x.
- Holmberg, E. On the Clustering Tendencies among the Nebulae. II. a Study of Encounters Between Laboratory Models of Stellar Systems by a New Integration Procedure. *ApJ*, 94:385, November 1941. doi: 10.1086/144344.
- Hosokawa, T., Omukai, K., Yoshida, N., and Yorke, H. W. Protostellar Feedback Halts the Growth of the First Stars in the Universe. *Science*, 334:1250–, December 2011. doi: 10.1126/science.1207433.
- Hosokawa, T., Yoshida, N., Omukai, K., and Yorke, H. W. Protostellar Feedback and Final Mass of the Second-generation Primordial Stars. *ApJ*, 760:L37, December 2012. doi: 10.1088/2041-8205/760/2/L37.
- Hosokawa, T., Yorke, H. W., Inayoshi, K., Omukai, K., and Yoshida, N. Formation of Primordial Supermassive Stars by Rapid Mass Accretion. *ApJ*, 778:178, December 2013. doi: 10.1088/0004-637X/778/2/178.
- Hosokawa, T., Hirano, S., Kuiper, R., Yorke, H. W., Omukai, K., and Yoshida, N. Formation of Massive Primordial Stars: Intermittent UV Feedback with Episodic Mass Accretion. *ApJ*, 824:119, June 2016. doi: 10.3847/0004-637X/824/2/119.
- Hummel, J. A., Pawlik, A. H., Milosavljević, M., and Bromm, V. The Source Density and Observability of Pair-instability Supernovae from the First Stars. *ApJ*, 755:72, August 2012. doi: 10.1088/0004-637X/755/1/72.
- Iliev, I. T., Shapiro, P. R., and Raga, A. C. Minihalo photoevaporation during cosmic reionization: evaporation times and photon consumption rates. *MNRAS*, 361:405–414, August 2005. doi: 10.1111/j.1365-2966.2005.09155.x.
- Inayoshi, K. and Omukai, K. Supermassive black hole formation by cold accretion shocks in the first galaxies. *MNRAS*, 422:2539–2546, May 2012. doi: 10.1111/j.1365-2966.2012.20812.x.

- Inayoshi, K. and Tanaka, T. L. The suppression of direct collapse black hole formation by soft X-ray irradiation. *MNRAS*, 450:4350–4363, July 2015. doi: 10.1093/mnras/stv871.
- Inayoshi, K., Visbal, E., and Kashiyama, K. Direct collapse black hole formation via high-velocity collisions of protogalaxies. *MNRAS*, 453:1692–1700, October 2015. doi: 10.1093/mnras/stv1654.
- Inayoshi, K., Haiman, Z., and Ostriker, J. P. Hyper-Eddington accretion flows on to massive black holes. *MNRAS*, 459:3738–3755, July 2016. doi: 10.1093/mnras/stw836.
- Jarosik, N., Bennett, C. L., Dunkley, J., Gold, B., Greason, M. R., Halpern, M., Hill, R. S., Hinshaw, G., Kogut, A., Komatsu, E., Larson, D., Limon, M., Meyer, S. S., Nolte, M. R., Odegard, N., Page, L., Smith, K. M., Spergel, D. N., Tucker, G. S., Weiland, J. L., Wollack, E., and Wright, E. L. Seven-year Wilkinson Microwave Anisotropy Probe (WMAP) Observations: Sky Maps, Systematic Errors, and Basic Results. *ApJS*, 192:14, February 2011. doi: 10.1088/0067-0049/192/2/14.
- Jeon, M., Pawlik, A. H., Greif, T. H., Glover, S. C. O., Bromm, V., Milosavljević, M., and Klessen, R. S. The First Galaxies: Assembly with Black Hole Feedback. *ApJ*, 754:34, July 2012. doi: 10.1088/0004-637X/754/1/34.
- Joggerst, C. C., Almgren, A., Bell, J., Heger, A., Whalen, D., and Woosley, S. E. The Nucleosynthetic Imprint of 15-40 M_{sun} Primordial Supernovae on Metal-Poor Stars. *ApJ*, 709:11–26, January 2010. doi: 10.1088/0004-637X/709/1/11.
- Johnson, J. L. and Bromm, V. The cooling of shock-compressed primordial gas. *MNRAS*, 366:247–256, February 2006. doi: 10.1111/j.1365-2966.2005.09846.x.
- Johnson, J. L. and Bromm, V. The aftermath of the first stars: massive black holes. *MNRAS*, 374:1557–1568, February 2007. doi: 10.1111/j.1365-2966.2006.11275.x.
- Johnson, J. L., Greif, T. H., and Bromm, V. Occurrence of metal-free galaxies in the early Universe. *MNRAS*, 388:26–38, July 2008. doi: 10.1111/j.1365-2966.2008.13381.x.
- Johnson, J. L., Greif, T. H., Bromm, V., Klessen, R. S., and Ippolito, J. The first galaxies: signatures of the initial starburst. *MNRAS*, 399:37–47, October 2009. doi: 10.1111/j.1365-2966.2009.15158.x.
- Kippenhahn, R., Weigert, A., and Weiss, A. *Stellar Structure and Evolution*. 2012. doi: 10.1007/978-3-642-30304-3.
- Kitayama, T., Yoshida, N., Susa, H., and Umemura, M. The Structure and Evolution of Early Cosmological H II Regions. *ApJ*, 613:631–645, October 2004. doi: 10.1086/423313.

- Koopmans, L., Pritchard, J., Mellema, G., Aguirre, J., Ahn, K., Barkana, R., van Bemmell, I., Bernardi, G., Bonaldi, A., Briggs, F., de Bruyn, A. G., Chang, T. C., Chapman, E., Chen, X., Ciardi, B., Dayal, P., Ferrara, A., Fialkov, A., Fiore, F., Ichiki, K., Illiev, I. T., Inoue, S., Jelic, V., Jones, M., Lazio, J., Maio, U., Majumdar, S., Mack, K. J., Mesinger, A., Morales, M. F., Parsons, A., Pen, U. L., Santos, M., Schneider, R., Semelin, B., de Souza, R. S., Subrahmanyam, R., Takeuchi, T., Vedantham, H., Wagg, J., Webster, R., Wyithe, S., Datta, K. K., and Trott, C. The Cosmic Dawn and Epoch of Reionisation with SKA. *Advancing Astrophysics with the Square Kilometre Array (AASKA14)*, art. 1, April 2015.
- Koushiappas, S. M., Bullock, J. S., and Dekel, A. Massive black hole seeds from low angular momentum material. *MNRAS*, 354:292–304, October 2004. doi: 10.1111/j.1365-2966.2004.08190.x.
- Kroupa, P. On the variation of the initial mass function. *MNRAS*, 322:231–246, April 2001. doi: 10.1046/j.1365-8711.2001.04022.x.
- Latif, M. A. and Volonteri, M. Assessing inflow rates in atomic cooling haloes: implications for direct collapse black holes. *MNRAS*, 452:1026–1044, September 2015. doi: 10.1093/mnras/stv1337.
- Latif, M. A., Schleicher, D. R. G., Schmidt, W., and Niemeyer, J. Black hole formation in the early Universe. *MNRAS*, 433:1607–1618, August 2013. doi: 10.1093/mnras/stt834.
- Latif, M. A., Niemeyer, J. C., and Schleicher, D. R. G. Impact of baryonic streaming velocities on the formation of supermassive black holes via direct collapse. *MNRAS*, 440:2969–2975, June 2014a. doi: 10.1093/mnras/stu489.
- Latif, M. A., Schleicher, D. R. G., Bovino, S., Grassi, T., and Spaans, M. The Formation of Massive Primordial Stars in the Presence of Moderate UV Backgrounds. *ApJ*, 792:78, September 2014b. doi: 10.1088/0004-637X/792/1/78.
- Latif, M. A., Schleicher, D. R. G., Bovino, S., Grassi, T., and Spaans, M. The Formation of Massive Primordial Stars in the Presence of Moderate UV Backgrounds. *ApJ*, 792:78, September 2014a. doi: 10.1088/0004-637X/792/1/78.
- Latif, M. A., Bovino, S., Van Borm, C., Grassi, T., Schleicher, D. R. G., and Spaans, M. A UV flux constraint on the formation of direct collapse black holes. *MNRAS*, 443:1979–1987, September 2014b. doi: 10.1093/mnras/stu1230.
- Leitherer, C., Schaerer, D., Goldader, J. D., Delgado, R. M. G., Robert, C., Kune, D. F., de Mello, D. F., Devost, D., and Heckman, T. M. Starburst99: Synthesis Models for Galaxies with Active Star Formation. *ApJS*, 123:3–40, July 1999. doi: 10.1086/313233.

- Lodato, G. and Natarajan, P. Supermassive black hole formation during the assembly of pre-galactic discs. *MNRAS*, 371:1813–1823, October 2006. doi: 10.1111/j.1365-2966.2006.10801.x.
- Loeb, A. and Rasio, F. A. Collapse of primordial gas clouds and the formation of quasar black holes. *ApJ*, 432:52–61, September 1994a. doi: 10.1086/174548.
- Loeb, A. and Rasio, F. A. Collapse of primordial gas clouds and the formation of quasar black holes. *ApJ*, 432:52–61, September 1994b. doi: 10.1086/174548.
- Lupi, A., Haardt, F., Dotti, M., Fiacconi, D., Mayer, L., and Madau, P. Growing massive black holes through supercritical accretion of stellar-mass seeds. *MNRAS*, 456:2993–3003, March 2016. doi: 10.1093/mnras/stv2877.
- Ma, X., Hopkins, P. F., Kasen, D., Quataert, E., Faucher-Giguère, C.-A., Kereš, D., Murray, N., and Strom, A. Binary stars can provide the ‘missing photons’ needed for reionization. *MNRAS*, 459:3614–3619, July 2016. doi: 10.1093/mnras/stw941.
- Mac Low, M.-M. and Ferrara, A. Starburst-driven Mass Loss from Dwarf Galaxies: Efficiency and Metal Ejection. *ApJ*, 513:142–155, March 1999. doi: 10.1086/306832.
- Machacek, M. E., Bryan, G. L., and Abel, T. Simulations of Pregalactic Structure Formation with Radiative Feedback. *ApJ*, 548:509–521, February 2001. doi: 10.1086/319014.
- Machacek, M. E., Bryan, G. L., and Abel, T. Effects of a soft X-ray background on structure formation at high redshift. *MNRAS*, 338:273–286, January 2003. doi: 10.1046/j.1365-8711.2003.06054.x.
- Madau, P. and Rees, M. J. Massive Black Holes as Population III Remnants. *ApJ*, 551:L27–L30, April 2001. doi: 10.1086/319848.
- Magg, M., Hartwig, T., Glover, S. C. O., Klessen, R. S., and Whalen, D. J. A new statistical model for Population III supernova rates: discriminating between Λ CDM and WDM cosmologies. *MNRAS*, 462:3591–3601, November 2016. doi: 10.1093/mnras/stw1882.
- Marigo, P., Girardi, L., Chiosi, C., and Wood, P. R. Zero-metallicity stars. I. Evolution at constant mass. *A&A*, 371:152–173, May 2001. doi: 10.1051/0004-6361:20010309.
- Marri, S. and White, S. D. M. Smoothed particle hydrodynamics for galaxy formation simulations: improved treatments of multiphase gas, of star formation and of supernovae feedback. *MNRAS*, 345:561–574, October 2003. doi: 10.1046/j.1365-8711.2003.06984.x.

- Mas-Ribas, L., Dijkstra, M., and Forero-Romero, J. E. Boosting Ly α and He II λ 1640 Line Fluxes from Population III Galaxies: Stochastic IMF Sampling and Departures from Case-B. *ApJ*, 833:65, December 2016. doi: 10.3847/1538-4357/833/1/65.
- McKee, C. F. and Tan, J. C. The Formation of the First Stars. II. Radiative Feedback Processes and Implications for the Initial Mass Function. *ApJ*, 681: 771–797, July 2008. doi: 10.1086/587434.
- McLure, R. J. and Dunlop, J. S. The cosmological evolution of quasar black hole masses. *MNRAS*, 352:1390–1404, August 2004. doi: 10.1111/j.1365-2966.2004.08034.x.
- Mizusawa, H., Omukai, K., and Nishi, R. Primordial Molecular Emission in Population III Galaxies. *PASJ*, 57:951–967, December 2005. doi: 10.1093/pasj/57.6.951.
- Mocz, P., Vogelsberger, M., Pakmor, R., Genel, S., Springel, V., and Hernquist, L. Reducing noise in moving-grid codes with strongly-centroidal Lloyd mesh regularization. *MNRAS*, 452:3853–3862, October 2015. doi: 10.1093/mnras/stv1598.
- Mortlock, D. J., Warren, S. J., Venemans, B. P., Patel, M., Hewett, P. C., McMahon, R. G., Simpson, C., Theuns, T., González-Solares, E. A., Adamson, A., Dye, S., Hambly, N. C., Hirst, P., Irwin, M. J., Kuiper, E., Lawrence, A., and Röttgering, H. J. A. A luminous quasar at a redshift of $z = 7.085$. *Nature*, 474:616–619, June 2011. doi: 10.1038/nature10159.
- Nakamura, F. and Umemura, M. On the Initial Mass Function of Population III Stars. *ApJ*, 548:19–32, February 2001. doi: 10.1086/318663.
- Naoz, S., Yoshida, N., and Gnedin, N. Y. Simulations of Early Baryonic Structure Formation with Stream Velocity. I. Halo Abundance. *ApJ*, 747:128, March 2012. doi: 10.1088/0004-637X/747/2/128.
- Naoz, S., Yoshida, N., and Gnedin, N. Y. Simulations of Early Baryonic Structure Formation with Stream Velocity. II. The Gas Fraction. *ApJ*, 763:27, January 2013. doi: 10.1088/0004-637X/763/1/27.
- Navarro, J. F., Frenk, C. S., and White, S. D. M. A Universal Density Profile from Hierarchical Clustering. *ApJ*, 490:493–508, December 1997.
- Oh, S. P. Reionization by Hard Photons. I. X-Rays from the First Star Clusters. *ApJ*, 553:499–512, June 2001. doi: 10.1086/320957.
- Oh, S. P. and Haiman, Z. Second-Generation Objects in the Universe: Radiative Cooling and Collapse of Halos with Virial Temperatures above 10^4 K. *ApJ*, 569: 558–572, April 2002. doi: 10.1086/339393.

- Omukai, K. Primordial Star Formation under Far-Ultraviolet Radiation. *ApJ*, 546: 635–651, January 2001. doi: 10.1086/318296.
- Omukai, K., Schneider, R., and Haiman, Z. Can Supermassive Black Holes Form in Metal-enriched High-Redshift Protogalaxies? *ApJ*, 686:801–814, October 2008. doi: 10.1086/591636.
- O’Shea, B. W. and Norman, M. L. Population III Star Formation in a Λ CDM Universe. I. The Effect of Formation Redshift and Environment on Protostellar Accretion Rate. *ApJ*, 654:66–92, January 2007. doi: 10.1086/509250.
- O’Shea, B. W. and Norman, M. L. Population III Star Formation in a Λ CDM Universe. II. Effects of a Photodissociating Background. *ApJ*, 673:14–33, January 2008. doi: 10.1086/524006.
- O’Shea, B. W., Wise, J. H., Xu, H., and Norman, M. L. Probing the Ultraviolet Luminosity Function of the Earliest Galaxies with the Renaissance Simulations. *ApJ*, 807:L12, July 2015. doi: 10.1088/2041-8205/807/1/L12.
- Osterbrock, D. E. *Astrophysics of gaseous nebulae and active galactic nuclei*. 1989.
- Paardekooper, J.-P., Kruip, C. J. H., and Icke, V. SimpleX2: radiative transfer on an unstructured, dynamic grid. *A&A*, 515:A79, June 2010. doi: 10.1051/0004-6361/200913821.
- Paardekooper, J.-P., Khochfar, S., and Dalla Vecchia, C. The First Billion Years project: the escape fraction of ionizing photons in the epoch of reionization. *MNRAS*, 451:2544–2563, August 2015. doi: 10.1093/mnras/stv1114.
- Pacucci, F., Loeb, A., and Salvadori, S. Gravitational Wave Sources from Pop III Stars are Preferentially Located within the Cores of their Host Galaxies. *ArXiv e-prints*, June 2017.
- Pakmor, R., Springel, V., Bauer, A., Mocz, P., Munoz, D. J., Ohlmann, S. T., Schaal, K., and Zhu, C. Improving the convergence properties of the moving-mesh code AREPO. *MNRAS*, 455:1134–1143, January 2016. doi: 10.1093/mnras/stv2380.
- Palla, F., Salpeter, E. E., and Stahler, S. W. Primordial star formation - The role of molecular hydrogen. *ApJ*, 271:632–641, August 1983. doi: 10.1086/161231.
- Pallottini, A., Ferrara, A., Pacucci, F., Gallerani, S., Salvadori, S., Schneider, R., Schaerer, D., Sobral, D., and Matthee, J. The brightest Ly α emitter: Pop III or black hole? *MNRAS*, 453:2465–2470, November 2015. doi: 10.1093/mnras/stv1795.
- Park, K. and Ricotti, M. Accretion onto Intermediate-mass Black Holes Regulated by Radiative Feedback. I. Parametric Study for Spherically Symmetric Accretion. *ApJ*, 739:2, September 2011. doi: 10.1088/0004-637X/739/1/2.

- Parsons, A. R., Backer, D. C., Foster, G. S., Wright, M. C. H., Bradley, R. F., Gugliucci, N. E., Parashare, C. R., Benoit, E. E., Aguirre, J. E., Jacobs, D. C., Carilli, C. L., Herne, D., Lynch, M. J., Manley, J. R., and Werthimer, D. J. The Precision Array for Probing the Epoch of Re-ionization: Eight Station Results. *AJ*, 139:1468–1480, April 2010. doi: 10.1088/0004-6256/139/4/1468.
- Patil, A. H., Yatawatta, S., Koopmans, L. V. E., de Bruyn, A. G., Brentjens, M. A., Zaroubi, S., Asad, K. M. B., Hatéf, M., Jelić, V., Mevius, M., Offringa, A. R., Pandey, V. N., Vedantham, H., Abdalla, F. B., Brouw, W. N., Chapman, E., Ciardi, B., Gehlot, B. K., Ghosh, A., Harker, G., Iliev, I. T., Kakiichi, K., Majumdar, S., Mellema, G., Silva, M. B., Schaye, J., Vrbanec, D., and Wijnholds, S. J. Upper Limits on the 21 cm Epoch of Reionization Power Spectrum from One Night with LOFAR. *ApJ*, 838:65, March 2017. doi: 10.3847/1538-4357/aa63e7.
- Pawlik, A. H., Milosavljević, M., and Bromm, V. The First Galaxies: Assembly under Radiative Feedback from the First Stars. *ApJ*, 767:59, April 2013. doi: 10.1088/0004-637X/767/1/59.
- Pezzulli, E., Valiante, R., and Schneider, R. Super-Eddington growth of the first black holes. *MNRAS*, 458:3047–3059, May 2016. doi: 10.1093/mnras/stw505.
- Planck Collaboration, Ade, P. A. R., Aghanim, N., Armitage-Caplan, C., Arnaud, M., Ashdown, M., Atrio-Barandela, F., Aumont, J., Baccigalupi, C., Banday, A. J., and et al. Planck 2013 results. XVI. Cosmological parameters. *arXiv:1303.5076*, March 2013.
- Planck Collaboration, Adam, R., Aghanim, N., Ashdown, M., Aumont, J., Baccigalupi, C., Ballardini, M., Banday, A. J., Barreiro, R. B., Bartolo, N., Basak, S., Battye, R., Benabed, K., Bernard, J.-P., Bersanelli, M., Bielewicz, P., Bock, J. J., Bonaldi, A., Bonavera, L., Bond, J. R., Borrill, J., Bouchet, F. R., Boulanger, F., Bucher, M., Burigana, C., Calabrese, E., Cardoso, J.-F., Carron, J., Chiang, H. C., Colombo, L. P. L., Combet, C., Comis, B., Couchot, F., Coulais, A., Crill, B. P., Curto, A., Cuttaia, F., Davis, R. J., de Bernardis, P., de Rosa, A., de Zotti, G., Delabrouille, J., Di Valentino, E., Dickinson, C., Diego, J. M., Doré, O., Douspis, M., Ducout, A., Dupac, X., Elsner, F., Enßlin, T. A., Eriksen, H. K., Falgarone, E., Fantaye, Y., Finelli, F., Forastieri, F., Frailis, M., Fraisse, A. A., Franceschi, E., Frolov, A., Galeotta, S., Galli, S., Ganga, K., Génova-Santos, R. T., Gerbino, M., Ghosh, T., González-Nuevo, J., Górski, K. M., Gruppuso, A., Gudmundsson, J. E., Hansen, F. K., Helou, G., Henrot-Versillé, S., Herranz, D., Hivon, E., Huang, Z., Ilić, S., Jaffe, A. H., Jones, W. C., Keihänen, E., Keskitalo, R., Kisner, T. S., Knox, L., Krachmalnicoff, N., Kunz, M., Kurki-Suonio, H., Lagache, G., Lähteenmäki, A., Lamarre, J.-M., Langer, M., Lasenby, A., Lattanzi, M., Lawrence, C. R., Le Jeune, M., Levrier, F., Lewis, A., Liguori, M., Lilje, P. B., López-Caniego, M., Ma, Y.-Z., Macías-Pérez, J. F., Maggio, G., Mangilli, A., Maris, M., Martin, P. G., Martínez-González, E., Matarrese, S., Mauri, N.,

- McEwen, J. D., Meinhold, P. R., Melchiorri, A., Mennella, A., Migliaccio, M., Miville-Deschênes, M.-A., Molinari, D., Moneti, A., Montier, L., Morgante, G., Moss, A., Naselsky, P., Natoli, P., Oxborrow, C. A., Pagano, L., Paoletti, D., Partridge, B., Patanchon, G., Patrizii, L., Perdureau, O., Perotto, L., Pettorino, V., Piacentini, F., Plaszczyński, S., Polastri, L., Polenta, G., Puget, J.-L., Rachen, J. P., Racine, B., Reinecke, M., Remazeilles, M., Renzi, A., Rocha, G., Rossetti, M., Roudier, G., Rubiño-Martín, J. A., Ruiz-Granados, B., Salvati, L., Sandri, M., Savelainen, M., Scott, D., Sirri, G., Sunyaev, R., Suur-Uski, A.-S., Tauber, J. A., Tenti, M., Toffolatti, L., Tomasi, M., Tristram, M., Trombetti, T., Valiviita, J., Van Tent, F., Vielva, P., Villa, F., Vittorio, N., Wandelt, B. D., Wehus, I. K., White, M., Zacchei, A., and Zonca, A. Planck intermediate results. XLVII. Planck constraints on reionization history. *A&A*, 596:A108, December 2016a. doi: 10.1051/0004-6361/201628897.
- Planck Collaboration, Ade, P. A. R., Aghanim, N., Arnaud, M., Ashdown, M., Aumont, J., Baccigalupi, C., Banday, A. J., Barreiro, R. B., Bartlett, J. G., and et al. Planck 2015 results. XIII. Cosmological parameters. *A&A*, 594:A13, September 2016b. doi: 10.1051/0004-6361/201525830.
- Popa, C., Naoz, S., Marinacci, F., and Vogelsberger, M. Gas-rich and gas-poor structures through the stream velocity effect. *MNRAS*, 460:1625–1639, August 2016. doi: 10.1093/mnras/stw1045.
- Pritchard, J. R. and Loeb, A. 21 cm cosmology in the 21st century. *Reports on Progress in Physics*, 75(8):086901, August 2012. doi: 10.1088/0034-4885/75/8/086901.
- Raiter, A., Schaerer, D., and Fosbury, R. A. E. Predicted UV properties of very metal-poor starburst galaxies. *A&A*, 523:A64, November 2010. doi: 10.1051/0004-6361/201015236.
- Regan, J. A. and Haehnelt, M. G. Pathways to massive black holes and compact star clusters in pre-galactic dark matter haloes with virial temperatures $> \sim 10000\text{K}$. *MNRAS*, 396:343–353, June 2009a. doi: 10.1111/j.1365-2966.2009.14579.x.
- Regan, J. A. and Haehnelt, M. G. The formation of compact massive self-gravitating discs in metal-free haloes with virial temperatures of $\sim 13000\text{--}30000\text{K}$. *MNRAS*, 393:858–871, March 2009b. doi: 10.1111/j.1365-2966.2008.14088.x.
- Regan, J. A., Johansson, P. H., and Wise, J. H. The Direct Collapse of a Massive Black Hole Seed under the Influence of an Anisotropic Lyman-Werner Source. *ApJ*, 795:137, November 2014. doi: 10.1088/0004-637X/795/2/137.
- Regan, J. A., Johansson, P. H., and Wise, J. H. Forming Super-Massive Black Hole Seeds under the Influence of a Nearby Anisotropic Multi-Frequency Source. *MNRAS*, April 2016a. doi: 10.1093/mnras/stw899.

- Regan, J. A., Johansson, P. H., and Wise, J. H. Positive or negative? The impact of X-ray feedback on the formation of direct collapse black hole seeds. *MNRAS*, 461:111–125, September 2016b. doi: 10.1093/mnras/stw1307.
- Regan, J. A., Visbal, E., Wise, J. H., Haiman, Z., Johansson, P. H., and Bryan, G. L. Rapid formation of massive black holes in close proximity to embryonic proto-galaxies. *Nature Astronomy*, 1:0075, March 2017. doi: 10.1038/s41550-017-0075.
- Ricotti, M. X-ray twinkles and Population III stars. *MNRAS*, 462:601–609, October 2016. doi: 10.1093/mnras/stw1672.
- Ricotti, M., Gnedin, N. Y., and Shull, J. M. Feedback from Galaxy Formation: Production and Photodissociation of Primordial H₂. *ApJ*, 560:580–591, October 2001. doi: 10.1086/323051.
- Ricotti, M., Gnedin, N. Y., and Shull, J. M. The Fate of the First Galaxies. II. Effects of Radiative Feedback. *ApJ*, 575:49–67, August 2002. doi: 10.1086/341256.
- Ripamonti, E. The role of HD cooling in primordial star formation. *MNRAS*, 376:709–718, April 2007. doi: 10.1111/j.1365-2966.2007.11460.x.
- Ritter, J. S., Safranek-Shrader, C., Gnat, O., Milosavljević, M., and Bromm, V. Confined Population III Enrichment and the Prospects for Prompt Second-generation Star Formation. *ApJ*, 761:56, December 2012. doi: 10.1088/0004-637X/761/1/56.
- Rodgers, C. D. and Williams, A. P. Integrated Absorption of a Spectral Line with the Voigt Profile. *J. Quant. Spec. Radiat. Transf.*, 14:319–323, April 1974.
- Rydberg, C. E., Zackrisson, E., and Scott, P. Can the James Webb Space Telescope detect isolated population III stars? In M. Raue, T. Kneiske, D. Horns, D. Elsaesser, & P. Hauschildt, editor, *Cosmic Radiation Fields: Sources in the early Universe (CRF 2010)*, page 26, 2010.
- Rydberg, C.-E., Zackrisson, E., Lundqvist, P., and Scott, P. Detection of isolated Population III stars with the James Webb Space Telescope. *MNRAS*, 429:3658–3664, March 2013. doi: 10.1093/mnras/sts653.
- Rydberg, C.-E., Zackrisson, E., Zitrin, A., Guaita, L., Melinder, J., Asadi, S., Gonzalez, J., Östlin, G., and Ström, T. A Search for Population III Galaxies in CLASH. I. Singly-imaged Candidates at High Redshift. *ApJ*, 804:13, May 2015. doi: 10.1088/0004-637X/804/1/13.
- Safranek-Shrader, C., Agarwal, M., Federrath, C., Dubey, A., Milosavljević, M., and Bromm, V. Star formation in the first galaxies - I. Collapse delayed by Lyman-Werner radiation. *MNRAS*, 426:1159–1177, October 2012a. doi: 10.1111/j.1365-2966.2012.21852.x.

- Safranek-Shrader, C., Agarwal, M., Federrath, C., Dubey, A., Milosavljević, M., and Bromm, V. Star formation in the first galaxies - I. Collapse delayed by Lyman-Werner radiation. *MNRAS*, 426:1159–1177, October 2012b. doi: 10.1111/j.1365-2966.2012.21852.x.
- Salvadori, S., Schneider, R., and Ferrara, A. Cosmic stellar relics in the Galactic halo. *MNRAS*, 381:647–662, October 2007. doi: 10.1111/j.1365-2966.2007.12133.x.
- Sasaki, M. PhD thesis, University of Heidelberg, 2015.
- Sasaki, M., Clark, P. C., Springel, V., Klessen, R. S., and Glover, S. C. O. Statistical properties of dark matter mini-haloes at $z \geq 15$. *MNRAS*, 442:1942–1955, August 2014. doi: 10.1093/mnras/stu985.
- Schaerer, D. On the properties of massive Population III stars and metal-free stellar populations. *A&A*, 382:28–42, January 2002. doi: 10.1051/0004-6361:20011619.
- Schauer, A. T. P., Whalen, D. J., Glover, S. C. O., and Klessen, R. S. Lyman-Werner UV escape fractions from primordial haloes. *MNRAS*, 454:2441–2450, December 2015. doi: 10.1093/mnras/stv2117.
- Schauer, A. T. P., Agarwal, B., Glover, S. C. O., Klessen, R. S., Latif, M. A., Mas-Ribas, L., Rydberg, C.-E., Whalen, D. J., and Zackrisson, E. Lyman-Werner escape fractions from the first galaxies. *MNRAS*, 467:2288–2300, May 2017a. doi: 10.1093/mnras/stx264.
- Schauer, A. T. P., Regan, J., Glover, S. C. O., and Klessen, R. S. The formation of direct collapse black holes under the influence of streaming velocities. *ArXiv e-prints*, May 2017b.
- Schleicher, D. R. G., Galli, D., Palla, F., Camenzind, M., Klessen, R. S., Bartelmann, M., and Glover, S. C. O. Effects of primordial chemistry on the cosmic microwave background. *A&A*, 490:521–535, November 2008. doi: 10.1051/0004-6361:200809861.
- Schleicher, D. R. G., Palla, F., Ferrara, A., Galli, D., and Latif, M. Massive black hole factories: Supermassive and quasi-star formation in primordial halos. *A&A*, 558:A59, October 2013. doi: 10.1051/0004-6361/201321949.
- Shang, C., Bryan, G. L., and Haiman, Z. Supermassive black hole formation by direct collapse: keeping protogalactic gas H_2 free in dark matter haloes with virial temperatures $T_{\text{vir}} > \text{rsm}10^4$ K. *MNRAS*, 402:1249–1262, February 2010. doi: 10.1111/j.1365-2966.2009.15960.x.
- Shapiro, P. R., Iliiev, I. T., and Raga, A. C. Photoevaporation of cosmological minihaloes during reionization. *MNRAS*, 348:753–782, March 2004. doi: 10.1111/j.1365-2966.2004.07364.x.

- Shapiro, P. R., Ahn, K., Alvarez, M. A., Iliev, I. T., Martel, H., and Ryu, D. The 21 cm Background from the Cosmic Dark Ages: Minihalos and the Intergalactic Medium before Reionization. *ApJ*, 646:681–690, August 2006. doi: 10.1086/504972.
- Smidt, J., Whalen, D. J., Chatzopoulos, E., Wiggins, B. K., Chen, K.-J., Kozyreva, A., and Even, W. Finding the First Cosmic Explosions. IV. 90 - 140 Msol Pair-Instability Supernovae. *ArXiv e-prints*, November 2014.
- Smith, R. J., Glover, S. C. O., Clark, P. C., Greif, T., and Klessen, R. S. The effects of accretion luminosity upon fragmentation in the early universe. *MNRAS*, 414: 3633–3644, July 2011. doi: 10.1111/j.1365-2966.2011.18659.x.
- Smith, R. J., Hosokawa, T., Omukai, K., Glover, S. C. O., and Klessen, R. S. Variable accretion rates and fluffy first stars. *MNRAS*, 424:457–463, July 2012. doi: 10.1111/j.1365-2966.2012.21211.x.
- Sobral, D., Matthee, J., Darvish, B., Schaerer, D., Mobasher, B., Röttgering, H. J. A., Santos, S., and Hemmati, S. Evidence for PopIII-like Stellar Populations in the Most Luminous Lyman- α Emitters at the Epoch of Reionization: Spectroscopic Confirmation. *ApJ*, 808:139, August 2015. doi: 10.1088/0004-637X/808/2/139.
- Springel, V. E pur si muove: Galilean-invariant cosmological hydrodynamical simulations on a moving mesh. *MNRAS*, 401:791–851, January 2010. doi: 10.1111/j.1365-2966.2009.15715.x.
- Springel, V. and Hernquist, L. Cosmological smoothed particle hydrodynamics simulations: the entropy equation. *MNRAS*, 333:649–664, July 2002. doi: 10.1046/j.1365-8711.2002.05445.x.
- Springel, V., White, S. D. M., Tormen, G., and Kauffmann, G. Populating a cluster of galaxies - I. Results at $z=0$. *MNRAS*, 328:726–750, December 2001. doi: 10.1046/j.1365-8711.2001.04912.x.
- Stacy, A. and Bromm, V. The First Stars: A Low-mass Formation Mode. *ApJ*, 785: 73, April 2014. doi: 10.1088/0004-637X/785/1/73.
- Stacy, A., Greif, T. H., and Bromm, V. The first stars: formation of binaries and small multiple systems. *MNRAS*, 403:45–60, March 2010. doi: 10.1111/j.1365-2966.2009.16113.x.
- Stacy, A., Bromm, V., and Loeb, A. Effect of Streaming Motion of Baryons Relative to Dark Matter on the Formation of the First Stars. *ApJ*, 730:L1, March 2011. doi: 10.1088/2041-8205/730/1/L1.

- Stacy, A., Greif, T. H., and Bromm, V. The first stars: mass growth under protostellar feedback. *MNRAS*, 422:290–309, May 2012. doi: 10.1111/j.1365-2966.2012.20605.x.
- Stacy, A., Bromm, V., and Lee, A. T. Building up the Population III initial mass function from cosmological initial conditions. *ArXiv e-prints*, March 2016.
- Stecher, T. P. and Williams, D. A. Photodestruction of Hydrogen Molecules in H I Regions. *ApJ*, 149:L29, July 1967a.
- Stecher, T. P. and Williams, D. A. Photodestruction of Hydrogen Molecules in H I Regions. *ApJ*, 149:L29, July 1967b. doi: 10.1086/180047.
- Stone, J. M. and Norman, M. L. ZEUS-2D: A radiation magnetohydrodynamics code for astrophysical flows in two space dimensions. I - The hydrodynamic algorithms and tests. *ApJS*, 80:753–790, June 1992. doi: 10.1086/191680.
- Sugimura, K., Omukai, K., and Inoue, A. K. The critical radiation intensity for direct collapse black hole formation: dependence on the radiation spectral shape. *MNRAS*, 445:544–553, November 2014. doi: 10.1093/mnras/stu1778.
- Susa, H. Photodissociation Feedback of Population III Stars onto Neighboring Prestellar Cores. *ApJ*, 659:908–917, April 2007. doi: 10.1086/512670.
- Susa, H. and Umemura, M. Secondary Star Formation in a Population III Object. *ApJ*, 645:L93–L96, July 2006. doi: 10.1086/506275.
- Susa, H., Umemura, M., and Hasegawa, K. Formation Criteria and the Mass of Secondary Population III Stars. *ApJ*, 702:480–488, September 2009. doi: 10.1088/0004-637X/702/1/480.
- Tanaka, S. J., Chiaki, G., Tominaga, N., and Susa, H. Blocking metal accretion onto population III stars by stellar wind. *ArXiv e-prints*, July 2017.
- Tanaka, T. L. and Li, M. The formation of massive black holes in $z \approx 30$ dark matter haloes with large baryonic streaming velocities. *MNRAS*, 439:1092–1100, March 2014. doi: 10.1093/mnras/stu042.
- Teyssier, R. Cosmological hydrodynamics with adaptive mesh refinement. A new high resolution code called RAMSES. *A&A*, 385:337–364, April 2002. doi: 10.1051/0004-6361:20011817.
- Trenti, M. and Stiavelli, M. Formation Rates of Population III Stars and Chemical Enrichment of Halos during the Reionization Era. *ApJ*, 694:879–892, April 2009. doi: 10.1088/0004-637X/694/2/879.
- Tsaliakhovich, D. and Hirata, C. Relative velocity of dark matter and baryonic fluids and the formation of the first structures. *Phys. Rev. D*, 82(8):083520, October 2010. doi: 10.1103/PhysRevD.82.083520.

- Tseliakhovich, D., Barkana, R., and Hirata, C. M. Suppression and spatial variation of early galaxies and minihaloes. *MNRAS*, 418:906–915, December 2011. doi: 10.1111/j.1365-2966.2011.19541.x.
- Tumlinson, J. Chemical Evolution in Hierarchical Models of Cosmic Structure. I. Constraints on the Early Stellar Initial Mass Function. *ApJ*, 641:1–20, April 2006. doi: 10.1086/500383.
- Turk, M. J., Abel, T., and O’Shea, B. The Formation of Population III Binaries from Cosmological Initial Conditions. *Science*, 325:601–, July 2009. doi: 10.1126/science.1173540.
- van Haarlem, M. P., Wise, M. W., Gunst, A. W., Heald, G., McKean, J. P., Hessels, J. W. T., de Bruyn, A. G., Nijboer, R., Swinbank, J., Fallows, R., Brentjens, M., Nelles, A., Beck, R., Falcke, H., Fender, R., Hörandel, J., Koopmans, L. V. E., Mann, G., Miley, G., Röttgering, H., Stappers, B. W., Wijers, R. A. M. J., Zaroubi, S., van den Akker, M., Alexov, A., Anderson, J., Anderson, K., van Ardenne, A., Arts, M., Asgekar, A., Avruch, I. M., Batejat, F., Bähren, L., Bell, M. E., Bell, M. R., van Bemmelen, I., Bennema, P., Bentum, M. J., Bernardi, G., Best, P., Bîrzan, L., Bonafede, A., Boonstra, A.-J., Braun, R., Bregman, J., Breitling, F., van de Brink, R. H., Broderick, J., Broekema, P. C., Brouw, W. N., Brüggen, M., Butcher, H. R., van Cappellen, W., Ciardi, B., Coenen, T., Conway, J., Coolen, A., Corstanje, A., Damstra, S., Davies, O., Deller, A. T., Dettmar, R.-J., van Diepen, G., Dijkstra, K., Donker, P., Doorduyn, A., Dromer, J., Drost, M., van Duin, A., Eislöffel, J., van Enst, J., Ferrari, C., Frieswijk, W., Gankema, H., Garrett, M. A., de Gasperin, F., Gerbers, M., de Geus, E., Griesmeier, J.-M., Grit, T., Gruppen, P., Hamaker, J. P., Hassall, T., Hoeft, M., Holties, H. A., Horneffer, A., van der Horst, A., van Houwelingen, A., Huijgen, A., Iacobelli, M., Intema, H., Jackson, N., Jelic, V., de Jong, A., Jette, E., Kant, D., Karastergiou, A., Koers, A., Kollen, H., Kondratiev, V. I., Kooistra, E., Koopman, Y., Koster, A., Kuniyoshi, M., Kramer, M., Kuper, G., Lambropoulos, P., Law, C., van Leeuwen, J., Lemaître, J., Loose, M., Maat, P., Macario, G., Markoff, S., Masters, J., McFadden, R. A., McKay-Bukowski, D., Meijering, H., Meulman, H., Mevius, M., Middelberg, E., Millenaar, R., Miller-Jones, J. C. A., Mohan, R. N., Mol, J. D., Morawietz, J., Morganti, R., Mulcahy, D. D., Mulder, E., Munk, H., Nieuwenhuis, L., van Nieuwpoort, R., Noordam, J. E., Norden, M., Noutsos, A., Offringa, A. R., Olofsson, H., Omar, A., Orrú, E., Overeem, R., Paas, H., Pandey-Pommier, M., Pandey, V. N., Pizzo, R., Polatidis, A., Rafferty, D., Rawlings, S., Reich, W., de Reijer, J.-P., Reitsma, J., Renting, G. A., Riemers, P., Rol, E., Romein, J. W., Roosjen, J., Ruiter, M., Scaife, A., van der Schaaf, K., Scheers, B., Schellart, P., Schoenmakers, A., Schoonderbeek, G., Serylak, M., Shulevski, A., Sluman, J., Smirnov, O., Sobey, C., Spreeuw, H., Steinmetz, M., Sterks, C. G. M., Stiepel, H.-J., Stuurwold, K., Tagger, M., Tang, Y., Tasse, C., Thomas, I., Thoudam, S., Toribio, M. C., van der Tol, B., Usov, O., van Veelen, M., van der Veen, A.-J., ter Veen, S., Verbiest, J. P. W., Vermeulen, R., Vermaas, N., Vocks, C., Vogt,

- C., de Vos, M., van der Wal, E., van Weeren, R., Weggemans, H., Weltevrede, P., White, S., Wijnholds, S. J., Wilhelmsson, T., Wucknitz, O., Yatawatta, S., Zarka, P., Zensus, A., and van Zwieten, J. LOFAR: The LOw-Frequency ARray. *A&A*, 556:A2, August 2013. doi: 10.1051/0004-6361/201220873.
- van Leer, B. Towards the Ultimate Conservative Difference Scheme. IV. A New Approach to Numerical Convection. *Journal of Computational Physics*, 23:276–+, March 1977. doi: 10.1016/0021-9991(77)90095-X.
- Vestergaard, M. and Osmer, P. S. Mass Functions of the Active Black Holes in Distant Quasars from the Large Bright Quasar Survey, the Bright Quasar Survey, and the Color-selected Sample of the SDSS Fall Equatorial Stripe. *ApJ*, 699: 800–816, July 2009. doi: 10.1088/0004-637X/699/1/800.
- Visbal, E., Haiman, Z., and Bryan, G. L. A no-go theorem for direct collapse black holes without a strong ultraviolet background. *MNRAS*, 442:L100–L104, July 2014a. doi: 10.1093/mnras/slu063.
- Visbal, E., Haiman, Z., and Bryan, G. L. Direct collapse black hole formation from synchronized pairs of atomic cooling haloes. *MNRAS*, 445:1056–1063, November 2014b. doi: 10.1093/mnras/stu1794.
- Visbal, E., Haiman, Z., Terrazas, B., Bryan, G. L., and Barkana, R. High-redshift star formation in a time-dependent Lyman-Werner background. *MNRAS*, 445: 107–114, November 2014c. doi: 10.1093/mnras/stu1710.
- Volonteri, M. Formation of supermassive black holes. *A&A Rev.*, 18:279–315, July 2010. doi: 10.1007/s00159-010-0029-x.
- Wadsley, J. W., Stadel, J., and Quinn, T. Gasoline: a flexible, parallel implementation of TreeSPH. *New A*, 9:137–158, February 2004. doi: 10.1016/j.newast.2003.08.004.
- Whalen, D. and Norman, M. L. A Multistep Algorithm for the Radiation Hydrodynamical Transport of Cosmological Ionization Fronts and Ionized Flows. *ApJS*, 162:281–303, February 2006. doi: 10.1086/499072.
- Whalen, D. and Norman, M. L. Ionization Front Instabilities in Primordial H II Regions. *ApJ*, 673:664–675, February 2008a. doi: 10.1086/524400.
- Whalen, D., Abel, T., and Norman, M. L. Radiation Hydrodynamic Evolution of Primordial H II Regions. *ApJ*, 610:14–22, July 2004. doi: 10.1086/421548.
- Whalen, D., O’Shea, B. W., Smidt, J., and Norman, M. L. How the First Stars Regulated Local Star Formation. I. Radiative Feedback. *ApJ*, 679:925–941, June 2008. doi: 10.1086/587731.

- Whalen, D., Hueckstaedt, R. M., and McConkie, T. O. Radiative and Kinetic Feedback by Low-Mass Primordial Stars. *ApJ*, 712:101–111, March 2010. doi: 10.1088/0004-637X/712/1/101.
- Whalen, D. J. and Fryer, C. L. The Formation of Supermassive Black Holes from Low-mass Pop III Seeds. *ApJ*, 756:L19, September 2012. doi: 10.1088/2041-8205/756/1/L19.
- Whalen, D. J. and Norman, M. L. Three-Dimensional Dynamical Instabilities in Galactic Ionization Fronts. *ApJ*, 672:287–297, January 2008b. doi: 10.1086/522569.
- Whalen, D. J., Smidt, J., Even, W., Woosley, S. E., Heger, A., Stiavelli, M., and Fryer, C. L. Finding the First Cosmic Explosions. III. Pulsational Pair-instability Supernovae. *ApJ*, 781:106, February 2014. doi: 10.1088/0004-637X/781/2/106.
- Whalen, D. J. et al. Finding the First Cosmic Explosions. I. Pair-instability Supernovae. *ApJ*, 777:110, November 2013a. doi: 10.1088/0004-637X/777/2/110.
- Whalen, D. J. et al. Finding the First Cosmic Explosions. II. Core-collapse Supernovae. *ApJ*, 768:95, May 2013b. doi: 10.1088/0004-637X/768/1/95.
- Wise, J. H. and Abel, T. Suppression of H_2 Cooling in the Ultraviolet Background. *ApJ*, 671:1559–1567, December 2007. doi: 10.1086/522876.
- Wise, J. H. and Abel, T. Resolving the Formation of Protogalaxies. III. Feedback from the First Stars. *ApJ*, 685:40–56, September 2008. doi: 10.1086/590417.
- Wise, J. H., Turk, M. J., Norman, M. L., and Abel, T. The Birth of a Galaxy: Primordial Metal Enrichment and Stellar Populations. *ApJ*, 745:50, January 2012. doi: 10.1088/0004-637X/745/1/50.
- Wise, W. L. and Fuhr, J. R. Accurate Atomic Transition Probabilities for Hydrogen, Helium, and Lithium. *JPCRD*, 38:565, 2009.
- Wolcott-Green, J. and Haiman, Z. Suppression of HD cooling in protogalactic gas clouds by Lyman-Werner radiation. *MNRAS*, 412:2603–2616, April 2011. doi: 10.1111/j.1365-2966.2010.18080.x.
- Wolcott-Green, J., Haiman, Z., and Bryan, G. L. Photodissociation of H_2 in protogalaxies: modelling self-shielding in three-dimensional simulations. *MNRAS*, 418: 838–852, December 2011. doi: 10.1111/j.1365-2966.2011.19538.x.
- Wolcott-Green, J., Haiman, Z., and Bryan, G. L. Beyond J_{crit} : a critical curve for suppression of H_2 -cooling in protogalaxies. *MNRAS*, 469:3329–3336, August 2017. doi: 10.1093/mnras/stx167.

- Wong, W. Y., Moss, A., and Scott, D. How well do we understand cosmological recombination? *MNRAS*, 386:1023–1028, May 2008. doi: 10.1111/j.1365-2966.2008.13092.x.
- Wu, X.-B., Wang, F., Fan, X., Yi, W., Zuo, W., Bian, F., Jiang, L., McGreer, I. D., Wang, R., Yang, J., Yang, Q., Thompson, D., and Beletsky, Y. An ultraluminous quasar with a twelve-billion-solar-mass black hole at redshift 6.30. *Nature*, 518: 512–515, February 2015. doi: 10.1038/nature14241.
- Xu, H., Wise, J. H., Norman, M. L., Ahn, K., and O’Shea, B. W. Galaxy Properties and UV Escape Fractions during the Epoch of Reionization: Results from the Renaissance Simulations. *ApJ*, 833:84, December 2016. doi: 10.3847/1538-4357/833/1/84.
- Yoshida, N., Abel, T., Hernquist, L., and Sugiyama, N. Simulations of Early Structure Formation: Primordial Gas Clouds. *ApJ*, 592:645–663, August 2003. doi: 10.1086/375810.
- Yue, B., Ciardi, B., Scannapieco, E., and Chen, X. The contribution of the IGM and minihaloes to the 21-cm signal of reionization. *MNRAS*, 398:2122–2133, October 2009. doi: 10.1111/j.1365-2966.2009.15261.x.
- Zackrisson, E., Rydberg, C.-E., Schaerer, D., Östlin, G., and Tuli, M. The Spectral Evolution of the First Galaxies. I. James Webb Space Telescope Detection Limits and Color Criteria for Population III Galaxies. *ApJ*, 740:13, October 2011. doi: 10.1088/0004-637X/740/1/13.